Claquage Electrique et Optique d'Allotropes du Carbone : Mécanismes et Applications pour le Stockage de Données

Loïc Loisel

NNT : 2016SACLX021

THESE DE DOCTORAT DE

LA NANYANG TECHNOLOGICAL UNIVERSITY
ET DE L'UNIVERSITE PARIS-SACLAY

préparée à

LA NANYANG TECHNOLOGICAL UNIVERSITY

et à

L'ECOLE POLYTECHNIQUE

ÉCOLE DOCTORALE

Interfaces - Approches interdisciplinaires: fondements, applications et innovations

Spécialité de doctorat : Physique

par

Loïc LOISEL

Optical and Electrical Breakdown of Carbon Allotropes: Mechanisms and Applications for Data Storage

Thèse présentée et soutenue à l'Ecole Polytechnique, le 13 avril 2016

Composition du jury :

M. Qing ZHANG	Président	Nanyang Technological University
M. Daniel CHUA	Examinateur	National University of Singapore
M. Henri-Jean DROUHIN	Examinateur	Ecole Polytechnique
M. RUSLI	Examinateur	Nanyang Technological University

Titre : Claquage Electrique et Optique d'Allotropes du Carbone: Mécanismes et Applications pour le Stockage de Données

Mots clés : stockage de données, mémoires, recuit laser, carbone, graphène, commutateur électro-mécanique

Résumé : Aujourd'hui, les applications de stockage de donnés utilisent principalement deux types de matériaux: les chalcogénures pour le stockage optique (*e.g.* Blu-Ray) et le silicium pour le stockage électronique (*e.g.* mémoires Flash). Malgré le fait qu'ils se soient avérés les plus efficaces pour des applications répandues, ces matériaux ont des limitations. Récemment, avec la montée en puissance du graphène, les allotropes du carbone ont été étudiés à la fois pour leurs propriétés intrinsèques et pour des applications; ils ont des propriétés électroniques, thermiques et mécaniques très intéressantes qui peuvent rendre ces matériaux plus efficaces que les chalcogénures ou le silicium pour certaines applications. Dans cette thèse, nous étudions la faisabilité et le potentiel du carbone comme matériau pour le stockage de données.

Nous nous concentrons d'abord sur le développement de stockage optique. Nous découvrons que les lasers continus et pulsés peuvent être utilisés pour induire des changements de phase réversibles dans des couches minces de carbone, confirmant la possibilité d'utiliser le carbone comme un matériau pour le stockage optique. De plus, nous découvrons plusieurs nouveaux phénomènes, que nous expliquons en utilisant des techniques de caractérisation avancées et la modélisation par ordinateur de la propagation thermique dans le carbone.

Ensuite, nous nous concentrons sur le stockage de données électronique en développant des mémoires à base de graphène qui peuvent être dans deux états de résistance bien séparés pour un grand nombre de cycles. Pour évaluer le potentiel de cette technologie, on caractérise le mécanisme de changement de résistance et on développe un modèle électromécanique qui permet de prédire les meilleures performances atteignables : ces mémoires ont le potentiel de commuter bien plus rapidement que les mémoires Flash tout en étant non-volatiles.

Title : Optical and Electrical Breakdown of Carbon Allotropes: Mechanisms and Applications for Data Storage

Keywords : data storage, memory, laser annealing, graphene, electro-mechanical switch

Abstract : Today, data storage applications rely mainly on two types of materials: chalcogenides for optical storage (*e.g.* Blu-Ray) and silicon for electronic storage (*e.g.* Flash memory). While these materials have proven to be the most efficient for widespread applications, both have limitations. Recently, with the rise of graphene, carbon allotropes have been studied both for their intrinsic properties and for applications; graphene and other carbon allotropes have very interesting electronic, thermal and mechanical properties that can make these materials more efficient than either chalcogenides or silicon for certain applications. In this thesis, we study the feasibility and potential of the usage of carbon as a data storage material.

Firstly, we focus on developing optical data storage. It is found that both continuous-wave and pulsed lasers can be used to induce reversible phase changes in carbon thin films, thus opening the way toward carbon-based data storage. Along the way, several phenomena are discovered, shown and explained by using advanced characterization techniques and thermal modelling.

Secondly, we focus on electronic data storage by developing graphene-based memories that are found to switch reliably between two well-separated resistance states for a large number of cycles. To assess the potential of this new technology, we characterize the switching mechanism and develop an electro-mechanical model enabling to predict the best performances attainable: these memories would potentially be much faster than Flash memories while playing the same role (non-volatile storage).

Université Paris-Saclay
Espace Technologique / Immeuble Discovery
Route de l'Orme aux Merisiers RD 128 / 91190 Saint-Aubin, France

Résumé

Les technologies informatiques ont un impact important sur les sociétés actuelles et sur leur évolution. Elles ont des besoins importants en termes de stockage de données. Il existe plusieurs façons de stocker des données qui sont plus ou moins adaptées à des besoins spécifiques. En particulier, on peut distinguer deux familles de technologies: le stockage de données électronique et le stockage optique. Un exemple de stockage de données optique est la technologie Blu-Ray, pour laquelle un laser est utilisé pour écrire et/ou lire des données sur un disque. Un exemple de stockage de données électronique est la technologie Flash, pour laquelle une tension électrique est appliquée aux deux bornes d'un transistor, et la quantité de courant électrique qui est lue dépend de son état: soit "ON" soit "OFF" (lecture). Pour modifier la quantité de courant qui passe (écriture), on applique une tension à une troisième partie du transistor appelée "la grille".

Les matériaux les plus utilisés pour ces deux types de technologie sont le silicium (stockage électronique) et les chalcogénures (stockage optique). Jusqu'à aujourd'hui, le silicium a été le meilleur compromis pour le stockage électronique pour plusieurs raisons: grande disponibilité, oxydation aisée pour créer l'oxyde de grille du transistor, progrès rapides liés au grand rythme de miniaturisation du transistor (loi de Moore), etc...

Les chalcogénures, quant à eux, sont utilisées pour des applications de stockage optique grâce aux basses températures nécessaires pour changer leur état de cristallinité (température de cristallisation ou de fusion). Des températures d'écriture plus basses mènent à des besoins énergétiques plus faibles, et donc à une baisse du coût de la technologie. Néanmoins, il existe des domaines dans lesquels ces matériaux n'excellent pas, et sur

lesquels des efforts de recherche se concentrent aujourd'hui.

Jusqu'à présent, pour le stockage de données électronique, il a été nécessaire d'utiliser plusieurs technologies complémentaires afin d'obtenir les meilleurs performances car il n'y a pas de composant électronique qui soit à la fois peu cher, rapide, non volatile (qui garde l'information même quand le système est éteint), et qui permette de stocker de très grande densités d'information sur une petite surface. Ainsi l'architecture des ordinateurs comprend plusieurs types de mémoires à plusieurs endroits et qui ont plusieurs rôles complémentaires. Aujourd'hui, il n'y a donc pas de moyen de se passer de cette complexité. Mais de nombreux instituts de recherche et entreprises sont à la recherche d'une technologie qui soit à la fois peu chère, rapide, non volatile et qui permette de stocker de larges quantités de données. La découverte d'une telle technologie permettrait de grandement améliorer les architectures informatiques, en minimisant grandement leur complexité.

Un autre problème lié à l'utilisation du silicium est qu'à force de miniaturiser les transistors pour améliorer leurs performances, leurs dimensions se rapprochent de la limite atomique, ce qui mène à plusieurs problèmes liés à des phénomènes quantiques (courants de fuite, variabilité des implantations de dopants...) et, de toute manière, la limite de l'atome est une limite qui ne pourra pas être dépassée avec les approches actuelles. Bien que les technologies à base de silicium soient mâtures, des défis importants existent toujours aujourd'hui, qu'il semble difficile de résoudre en n'utilisant qu'elles.

Pour ce qui est du stockage optique, la principale qualité des chalcogénures peut aussi s'avérer être un défaut: comme leurs températures de changements de structure (cristallisation, fusion) sont basses, ils peuvent s'avérer instables dans des conditions extrêmes, telles que l'espace (exposition à des rayonnements énergétiques, températures et variations de températures extrêmes). Trouver des matériaux plus stables à hautes températures peut donc s'avérer intéressant pour des applications dans l'aérospatiale, par exemple.

Dans cette thèse, on se propose d'explorer le potentiel du carbone comme matériau de base pour le stockage de données optique et électronique.

Pour les applications optiques, la température de fusion du carbone est bien plus élevée que celle des chalcogénures ; ainsi, sa structure devrait être plus résistante à des conditions extrêmes. Pour ce qui est des applications électroniques, certains allotropes du carbone ont été synthétisés pour la première fois assez récemment (par exemple le graphène, en 2004), et il a été montré que certaines de leurs propriétés électroniques sont supérieures à celles du silicium (par exemple, la mobilité des porteurs de charge).

Pour le stockage optique, l'état de l'art sur les interactions laser-carbone montre qu'il n'y a pour l'instant pas de démonstration de changement de phase réversible, ce qui est un défi à relever si on veut réaliser des mémoires optiques réversibles. On réalise également que les mécanismes de changement de phase sont assez peu compris, que ce soit dans le cas de recuits laser continus (application d'un flux lumineux continu) ou dans le cas de recuits laser pulsés (applications de "pulses" de lumière très rapides).

En premier lieu (Chapter 3), on étudie les recuits laser continus de couches minces de graphite nanocristallin. Bien qu'un changement de phase réalisé par un laser continu soit, par définition, plus long qu'un changement de phase réalisé par un laser pulsé, on estime que les phénomènes observés seront plus aisés à comprendre, et on pourra donc ensuite se baser sur cette compréhension pour travailler avec des lasers pulsés (Chapter 4). On utilise des couches minces de graphite nanocristallin car la structure de ce matériau peut être classée entre celle du carbone amorphe et du graphite: des cristaux de graphite sont entourés de carbone amorphe. C'est une structure cristalline idéale pour étudier des changements de phase car elle permet de les étudier dans les deux directions: changements de phase vers une structure plus cristalline ou vers une structure plus amorphe.

On découvre que l'application d'une puissance laser suffisante mène à plusieurs phénomènes: pour les plus hautes énergies, une perte de matière ainsi qu'une amorphisation de la structure, tous deux observés par microscopie électronique à transmission (MET). Pour des énergies plus faible, bien qu'il n'y ait pas de changements cristallin directement observables par MET à haute résolution, localement la conductivité électrique est grandement augmentée (microscopie à force atomique en mode conduction) ; ce changement est couplé à une légère augmentation de la hauteur moyenne de la couche. Ces deux faits

suggèrent qu'un phénomène de graphitisation a lieu pendant le recuit, car le graphite est plus conducteur électriquement que le carbone amorphe, et il est également moins dense (il prend plus de place). Nous contrôlons également l'évolution du signal Raman réémis par le matériau in-situ (durant le recuit), ce qui nous permet d'obtenir des informations sur la structure cristalline pendant le recuit. L'évolution des pics I(D)/I(G) et de la largeur du pic G indiquent un phénomène d'amorphisation, ce qui va dans le sens de ce qu'on observe au MET. En revanche, l'évolution de la position du pic G semble indiquer un phénomène de graphitisation. Or, le pic G est sensible à d'autres paramètres que la structure cristalline, tels que la température ou encore la concentration de dopants. De plus, le carbone peut être dopé positivement quand il interagit avec de l'oxygène. On décide donc d'étudier la présence d'éléments chimiques dans les couches recuites grâce à un spectromètre dispersif en énergie, et on observe en effet une plus forte présence d'oxygène aux endroits recuits, jusqu'à des profondeurs proches de la profondeur du phénomène d'amorphisation observé au MET. Ainsi, ces résultats suggèrent que l'amorphisation ainsi que l'évolution de la position du pic G pendant le recuit sont tous deux dus à des phénomènes d'oxydation. La perte de matière est certainement également provoquée par des réactions avec l'oxygène ambiant, car la température d'oxydation (par émission de molécules gazeuses de CO et de CO_2) du carbone est bien inférieure à sa température de fusion (environ 4450K). De plus, on n'observe aucun dommage sur la couche de titane présente sous le carbone, ce qui suggère que des températures supérieures à la température de fusion du titane (environ 1941K) ne sont pas atteintes durant le recuit.

Dans cette étude, on a donc montré qu'il est possible d'obtenir des changements de phase dans les deux directions (amorphisation et graphitisation) *via* l'application d'un faisceau laser continu. L'amorphisation et la perte de matière sont liés à des réactions avec l'oxygène environnant, et tous les changements se font à l'état solide. On a également montré que cette technique peut être utilisée pour écrire des motifs conducteurs. Mais les échelles de temps nécessaires étant longues, on cherche dans le chapitre suivant (Chapter 4) à utiliser un laser pulsé pour induire des changements dans des couches minces de carbone de même nature.

Au début de notre étude sur les recuits laser pulsés, l'état de l'art suggérait qu'il était très difficile, voire impossible, d'amorphiser le carbone. Notre premier but était donc d'amorphiser le graphite nanocristallin. Pour cela, on décide d'utiliser des pulses lumineux plus énergétiques que ceux généralement utilisés dans la littérature. On réalise une étude systématique de recuits laser en augmentant peu à peu l'énergie jusqu'à un maximum de 15.4 J.cm^2. Pour des énergies faibles, on observe un phénomène de graphitisation qui est déjà décrit dans la littérature. Néanmoins, en augmentant l'énergie, on atteint un plateau de graphitisation, et l'application de pulses plus énergétiques mène graduellement à un matériau plus amorphe. Ces résultats sont confirmés par MET à haute résolution et par spectroscopie Raman. Le premier objectif de l'étude étant réalisé, on teste l'endurance du processus réversible (car on peut graphitiser et amorphiser). On trouve que l'endurance est très limitée, à deux ou trois cycles (un cycle = graphitisation puis amorphisation), et on décide donc d'étudier l'état de la surface après les recuits, afin d'étudier les dégradations causées par les recuits énergétiques. Grâce à un microscope électronique à balayage, on observe différentes formes de dégradations apparaissant à différentes énergies: la croissance de grains (signe de fusion), cracks, vagues, sphères, piliers pleins ou creux, et enfin la présence de structures labyrinthiques qui suggèrent qu'aux hautes énergies nécessaires pour l'amorphisation, des phénomènes de fusion explosive apparaissent. Une grande partie de ces dégradations sont irréversibles et expliquent donc la faible endurance que l'on a observé. Elles montrent également que même aux plus faibles densités d'énergie utilisées dans cette étude, au moins une partie du carbone est fondue. Ce fait contraste fortement avec les résultats que nous avons obtenus avec un laser continu (Chapter 3). Nous effectuons des simulations par éléments finis, qui nous permettent d'estimer les températures atteintes et les durées nécessaires pour les atteindre: on trouve que la température en surface monte très rapidement (en moins de 10 nanosecondes) à des températures suffisantes pour fusionner le carbone, tandis que les durées nécessaires à l'oxydation du carbone qui sont rapportées dans la littérature sont bien plus longues. L'oxydation ne joue donc pas un rôle prépondérant ici, contrairement au cas du recuit laser continu (Chapter 3). Les simulations nous permettent également de comparer les vitesses de refroidissement après avoir atteint la température maximale, et les gradients thermiques dans les couches lors du refroidisse-

ment. Cela nous permet de savoir si l'amorphisation se fait par refroidissement rapide (comme pour le verre) ou par solidification homogène (comme, dans certains cas, pour le silicium). On trouve que la solidification homogène est le phénomène qui mène à l'amorphisation ici: la solidification se fait de manière homogène quand le carbone reste à l'état liquide assez longtemps pendant le refroidissement pour que les gradients de température soient faibles quand la température de solidification est atteinte. Dans ce cas, il n'y a pas (ou peu) de noyaux de cristallisation solides restants dans la matière pour agir comme catalyseurs de la cristallisation du matériau liquide. La graphitisation, quant à elle, est obtenue à des énergies plus faibles pour lesquels des gradients de température existent lors de la solidification: il y a donc une solidification hétérogène, et le carbone liquide devient solide en contact avec du carbone solide qui agit comme catalyseur de la cristallisation.

On a donc démontré que le carbone a un potentiel comme matériau de base pour stocker des données. Pour améliorer l'endurance, il faudrait trouver un moyen de graphitiser et d'amorphiser avec moins de dégradations. Une piste est l'utilisation de pulses femtoseconde au lieu de pulses nanoseconde: certains articles de la littérature mentionnent qu'il est possible d'amorphiser de la matière de façon "non thermique" en utilisant des pulses femtoseconde. On a mis en place un banc optique de recuit laser femtoseconde, et pour l'instant, nous avons obtenu des résultats préliminaires qui sont décrits dans ce manuscrit.

Le deuxième objectif de cette thèse est d'étudier la possibilité de fabriquer des mémoires électroniques à base de carbone, qui seraient à la fois rapides, non-volatiles, et qui pourraient être fabriquées avec de fortes densités de surface.

En particulier, ici nous avons décidé de nous concentrer sur un type de dispositif à base de graphène, un allotrope du carbone consistant en une couche d'atomes de carbone arrangée en nids d'abeilles. Il y a un débat dans la littérature sur un certain type de dispositif en particulier ; ces dispositifs sont faits de deux électrodes posées sur une bande de graphène, et auxquels on a appliqué une très forte tension qui a mené à leur claquage électrique. Il a été montré que le claquage est dû à l'apparition d'un crack qui se propage perpendiculairement au champ électrique, et qui coupe la bande de graphène en deux,

ce qui mène à une conductivité nulle (mis à part des effets tunnels pour lesquels les électrons traversent le vide). Ensuite, il a été démontré qu'il est possible de revenir à un état de résistance bien plus basse, et *vice-versa*. Ces états de résistance réversibles sont non volatils, et des vitesses de commutation de 100 ns ont été démontrées. Bien que ce ne soit pas aussi rapide que la commutation des mémoires vives statiques ou dynamiques, ces résultats préliminaires sont très encourageants. Néanmoins, la compréhension du mécanisme de commutation n'est pas complète: deux modèles s'opposent. Certains auteurs proposent qu'à partir du claquage électrique, le graphène n'est plus le matériau actif, mais que le changement de résistance se fait dans le substrat d'oxyde de silicium (SiO_2). La commutation se ferait donc par création/destruction de filaments de silicium dans le SiO_2 ou réduction/oxydation du SiO_2. D'autres auteurs proposent que le graphène est bien le matériau actif: il ferme/ouvre le crack en se déplaçant de manière réversible. Bien qu'il y ait des indices favorisant fortement les deux hypothèses, certains chercheurs pensent que le premier modèle (SiO_2) est plus solide, car le second modèle propose peu d'explications pour les phénomènes décrits. En particulier, on ne sait pas quelles forces contrôlent l'ouverture/fermeture du crack, ni la non-volatilité.

Ici, on cherche à fabriquer des mémoires non-volatiles à base de graphène et à comprendre leur mécanisme de commutation, en prenant en compte ce débat (Chapter 5). En premier lieu, on montre que l'on obtient des dispositifs qui commutent de manière non-volatile, pour 500 cycles dans le meilleur des cas, et avec des contrastes de résistance aussi élevés que 10^4 (pour 125 cycles). Ensuite, on observe le crack par microscopie à force atomique: quand un dispositif conduit (état "ON"), on trouve qu'à certains endroits du crack, des "ponts" de graphène sont présents, ce qui explique la plus grande conductivité. A l'état "OFF", nous ne trouvons pas de trace de ces ponts. Ainsi, il semble que dans notre cas, l'hypothèse de commutation par mouvements du graphène peut être privilégiée. De plus, les performances de nos dispositifs, surtout en termes de temps de commutation (aux alentours d'une seconde), sont similaires aux autres dispositifs dont la commutation est expliquée par le mouvement du graphène. Les deux mécanismes de commutation pourraient donc bien coexister dans différents dispositifs.

Néanmoins, ici il est important de comprendre comment le graphène se déplace si on

veut pouvoir estimer le potentiel de cette technologie, et trouver des moyens pour l'améliorer. En appliquant des bilans d'énergie au système graphène + crack, on montre qu'un modèle purement électro-mécanique permet d'expliquer le déplacement dans les deux sens (fermeture du crack par les forces d'attraction de Coulomb lorsqu'on applique une tension électrique, ouverture du crack par les forces élastiques du graphène en l'absence de tension électrique). En revanche, ce modèle ne permet pas d'expliquer la non-volatilité et les performances limitées en termes de vitesse de commutation et d'endurance: une mémoire purement électro-mécanique peut commuter à des vitesses proches de la nanoseconde. A cause de ces performances contradictoires, jusqu'à maintenant, les chercheurs n'ont pas réussi à expliquer complètement le fonctionnement de leurs mémoires. En se focalisant sur ces données apparemment contradictoires et en surveillant la littérature, on trouve une explication qui permet d'expliquer les phénomènes observés ici. En effet, des chercheurs ont montré, en 2012, que l'application d'un courant au travers de deux couches de graphène déposées l'une sur l'autre pouvait mener à leur fusion. On propose que ce phénomène complète le modèle: la commutation est bien électro-mécanique, mais c'est la fusion partielle des deux côtés du graphène (formation de liaisons covalentes) qui mène à la non-volatilité. Ce phénomène permet d'expliquer les performances limitées des dispositifs: il faut des durées bien plus longues (de l'ordre de la seconde) que celle de la commutation seule pour chauffer assez le graphène afin que deux couches fusionnent. De plus, s'il est nécessaire de créer puis détruire des liaisons covalentes, des quantités non négligeables de carbone doivent être perdues à chaque cycle, menant aux endurances limitées que nous observons ici.

Une mémoire à base de graphène purement électro-mécanique démontrerait plusieurs attributs de la mémoire idéale: non-volatilité, vitesse, endurance, etc... Pour l'obtenir, il faudrait pouvoir commuter de manière non-volatile sans former de liaisons covalentes. Notre modèle électro-mécanique suggère que cela est théoriquement possible car les forces de friction entre le graphène et le substrat s'opposent aux mouvements du graphène. Mais pour pouvoir rester à l'état conducteur, il faut que celles-ci soient plus fortes que les forces élastiques qui mènent à l'ouverture du crack (ON -> OFF). On calcule que les forces de friction sont suffisantes quand la largeur du crack est inférieure à 1

nm. Bien qu'il semble difficile d'obtenir des cracks aussi petits par claquage électrique, en 2013, une étude a montré qu'il était possible de diminuer la taille moyenne des cracks obtenus par claquage électrique en contrôlant précisément l'application de la tension avant et lors du claquage. C'est une piste qui pourrait être explorée afin de fabriquer les premières mémoires électroniques planaires à base de matériau 2D.

Pour finir, en termes d'applications, cette thèse démontre que le carbone a un potentiel intéressant pour le stockage de données, tant pour le stockage optique que pour le stockage électronique. De plus, on propose des pistes concrètes pour améliorer les technologies, et des jalons de ces améliorations ont déjà été posés (mise en place d'un banc de recuit femtoseconde). Sur le plan scientifique, cette thèse montre qu'il est parfois intéressant de travailler à des énergies qui sont *a priori* trop élevées pour développer des applications: cela permet de mettre à jour de nouveaux phénomènes, d'améliorer notre compréhension de la physique (*e.g.* des changements de phase) et enfin de proposer de nouvelles solutions pour des applications.

Acknowledgements

First, I must thank Florian Longnos, who made all of this possible by forwarding the thesis proposal to me and introducing me to Dominique Baillargeat, the former director of CINTRA. So thank you for impacting my life so greatly, Florian.

I must then thank Dominique, who is a strong leader who cares for his students and post-docs; he hired me and got me started on the joint PhD programme with Ecole Polytechnique, which greatly impacted both my research and my life.

My thoughts then go to prof. Tay Beng Kang, my main supervisor in Singapore, who also cares deeply for his students and tries to provide help whenever needed. I could not have achieved what I did without his support and trust: the joint PhD programme, my talks at conferences abroad, and some expensive characterization experiments, were all supported by him. He let me try and go whatever and wherever I thought was best for my research. With great patience, he also accepted and helped setup the collaboration of NTU with Ecole Polytechnique, which I believe and hope will continue to be fruitful.

I thank my supervisors at Ecole Polytechnique: prof. Bernard Drévillon, and Costel-Sorin Cojocaru, who both took care of getting me started well at the LPICM. Costel introduced me to Bérengère, and with her, both advised me to start working on graphene based electronic memories which are the subject of Chapter 5. A simple month-long attempt with devices fabricated in one week (with the help of Waleed, thank you Waleed) became a full research project, on which I devoted a great amount of time and energy. Costel is always ready to help and advise me on my research and career, and he provided graphene samples when I needed them, with the help of Iléana.

I am VERY grateful to Bérengère Lebental, with who I started collaborating three years ago but who later became my official co-supervisor at LPICM. She is without a doubt the one who spent

the most time helping me on every aspect of my thesis, which is especially impressive considering the fact that she was not officially supervising me when we started working together. She provided the guidance I needed, and after I started working with her I never felt lost. I (and I am not alone) still wonder how she can devote so much time on greatly helping all of her students and post-docs.

At LPICM, I got to work with other great people who devoted a lot of their time to help me settle there and move on with my research: Iléana (thanks for the ride to LPN and the TEM and EDX characterization!), Pere, Marc Châtelet, Laurence Bodelot, Andrei Constantinescu, Garry, Jean-Charles, Jérôme, Eric, Jacqueline, Cyril, Marc Chaigneau, Laurence Corbel.

Even though I was not directly working with them, there are a lot of people at LPCIM and Ecole Polytechnique I must thank for making me feel happy to go to work, even in the cold French winters: Fulvio, Thomas, Louis, Salomé, Alice, Leandro, Benjamin, Cai, Yaowu, Lucie, Dennis Lange, Fatme, Mariam, Anna, Edoardo, Alfredo, Heechul, Luka, Chiara, Federico, Sanghyuk, Fatima, Martin, Wanghua, Mallesham, Soumyadeep, Alba.

In hot Singapore, it was not necessarily easy to start a new life at NTU, but it quickly became my new home, and for that I must thank many people, with who I shared many discussions during coffee breaks and outside of work: from CINTRA, Etienne, Mathieu Cometto, Mathieu Bergont, Olivier, Charles (thanks for the interesting discussions. I still don't understand much of your PhD topic but I'm getting better!), Denis Le Goff (for opening our eyes on geopolitics), Stéphane, Naiyun, Jing Fei, Qi Jia, Ouyang, Shuwen, Nazia, Christophe Wilhelm, Sébastien, Aurélien, Pierre Baudin; from Nanoelectronics 1, Dunlin (thanks for the Chai tea latte!), Majid (I recall fondly the late Ramen diners), Liang Kun, Xingli, Chong Wei (my FCVA mentor), Wai Leong, Li Hong, Cong Xiang. Thanks to Philippe and Quyen for keeping on improving the work initiated by Dominique at CINTRA. Neither from CINTRA nor Nanoelectronics 1: Jun, Chong Guan, Victor, who are awesome fellows that I hope to meet somewhere in the world very soon!

Of course, a very special thanks to Aliénor and Pierre who became some of my best friends, and made my life in Singapore much more enjoyable, both in and out of work. Both cared deeply about... well, everything, and we helped each other many times in "tough" times. I am happy that we still live close to each other and see each other often. I hope it will continue.

Another very special thanks to Ange, who is the person I collaborated most during my PhD. Without him, I would clearly not have gone that far in the work described in Chapter 5. Many of the experimental results come from his work. He is a passionate researcher and I look forward

to reading and discussing about his future results. I hope I will get to work with him again in the future. He is also a great friend, with a great humor; his positive mindset enabled to brighten many lunch meals when nobody seemed to be talkative.

I also enjoyed collaborating with the specialists of quantum optics: Christophe Couteau and Stefano Vezzoli. They both were curious and hard-working enough to try and help me setup the femtosecond laser annealing experiment, even though the purpose clearly was not to entangle pairs of photons, but rather to blast billions of atoms at each shot. I really hope we will get to work together again in the future. Stefano was also very helpful in understanding what was going on in the graphene memories when we had no clue.

I must also thank my two final-year-project students: Yi Xiang and Fairus, who helped Ange and I deal with the wealth of data coming from electrical characterization on tens of graphene-based devices of varying qualities, dimensions, and characterization conditions.

All these people made the last four years of my life a treat, proving that research is not done by solitary lab rats but rather by international people who enjoy sharing experiences (and not only lab experiments).

On a more personal note, I want to thank my family, who accepted my choice to live abroad and supports me in any choice I make. Both my parents had a deep impact on who I am and the choices I make in my life, and without the influence they had on me I would clearly not have dared to go to Singapore for four years of research! I must thank my younger brothers and sister, who are growing up so fast and do not seem to be following my lead; I look forward to the architect (Brice), the artist (Marie), and the aerospace engineer (Rémy)?!

I also want to thank all my friends outside of work, with who I remained close despite my leaving France. The list is too long, but they will recognize themselves!

And finally, I want to thank Juliette, who I love. Without her my life would not feel fullfilled.

Contents

Acronyms

Table 1: List of acronyms

AFM	Atomic Force Microscopy
a-C	amorphous Carbon
CNT	Carbon Nanotube
CW	Continuous-Wave
EDX	energy dispersive X-ray spectroscopy
FCVA	Filtered Cathodic Vacuum Arc
FIB	Focused Ion Beam
FWHM	Full Width at Half Maximum
HRS	High Resistance State (Chapter 5)
HRTEM	High Resolution Transmission Electron Microscopy
LRS	Low Resistance State (Chapter 5)
MOSFET	Metal Oxide Semiconductor Field Effect Transistor
PCM	Phase Change Memory
RESET	"LRS -> HRS" step (Chapter 5)
SAED	Selected Area Electron Diffraction
SEM	Scanning Electron Microscopy
SET	"HRS -> LRS" step (Chapter 5)
ta-C	tetrahedral amorphous Carbon (high sp^3)

Chapter 1

Introduction

1.1 Optical and electronic memories: key enablers of the ongoing technological disruptions

Thanks to the Internet - enabling anyone and anything to be connected - and the constant shrinking of transistors following Moore's law - enabling ever faster and ever-more energy-efficient computers - the amount of data to process is constantly increasing. This trend is not expected to end soon, as other technological advances such as big data analytics, deep learning, cloud technologies, the internet of things (the IoT) are booming, and require increasing data storage capabilities.

It is large disruptions in hardware technologies that give rise to such developments. Moore's law enables computers to increase processing power exponentially, and quicker internet is made possible through the development of fast and efficient communication hardware such as optical fibers.

Big data, deep learning, cloud computing and the IoT all rely on the ability to store huge

amounts of data in data centers all over the world.

These data may need to be accessed and modified regularly, rapidly, at low energetic costs, or stored reliably for very long periods.

Thus, data storage is a critical enabler for such new disruptive technologies, opening new markets and leading semiconductor companies to invest heavily in research and development.

In fact, despite a shrinkage of the market for traditional non-volatile memory approaches in the period 2014-2020, the whole non-volatile memory market (including tranditional and non-traditional approaches) is expected to grow by 1.18% annually, to $40.2 bn, driven by non-traditional approaches [1]. During the same period, the market for **non-traditional approaches** to memory (both volatile and non-volatile) is expected to grow by $\approx 40\%$ annually [2].

As will be discussed in this thesis, there are several approaches to data storage at the single data bit level.

For data that has to be stored cheaply, for a long time, and easily transported, optical disks are the standard. One example of ubiquitous use of optical disks is Blu-Ray technology. Constant efforts are made to improve the performance of optical disks, as demonstrated by the ongoing transition from DVD to Blu-Ray and Ultra-HD Blu-Ray.

For personal computers, there exist several kinds of memory. Computer memory architecture is complex: large amounts of data are stored on the hard disk but cannot be accessed quickly. Smaller amounts of data are stored in the dynamic random access memory (DRAM), which is faster to access but at a larger cost. Finally, smaller amounts of data are stored in the cache, which is even faster but has an even larger cost per bit.

So far, all such technologies rely mainly on two types of materials: chalcogenides for optical disks (because of their low crystallization and melting temperatures), and silicon for computer memory architecture (because constant improvements to silicon transistors are being made in accordance with Moore's law).

However, in optical disks, the use of chalcogenides renders the disks useless at high temperatures or faulty in rough conditions (*e.g.* in Space). Moreover, Moore's law is expected to fail soon, as the size of silicon transistors gets closer to the size of an atom. Therefore, it is of interest to look for new materials that could be used as the basis of innovative memory technologies.

For example, since carbon nanotubes were first synthesized in 1991 [3], carbon allotropes have been the focus of relentless attention from research institutions and semiconductor industries. The versatility of their bonding structure and available dimensionalities (0D fullerenes, 1D carbon nanotubes, 2D graphene, 3D graphite and diamond) leads to a wide range of tunable physical properties for many applications including electronics [4].

In this thesis, we explore the use of two carbon allotropes - textured carbon and graphene - for memory applications, both optically (*e.g.* for optical disks) and electrically controlled (*e.g.* for computers).

a Memories: state of the art

a.1 Optical memories

In 1971, Feinleib, Ovshinsky *et al.* demonstrated reversible phase change in amorphous chalcogenide films ($Te_{81}Ge_{15}Sb_2S_2$) [5] using a pulsed argon-ion laser (wavelength 514.5 nm) with pulse durations varying between 1 and 16 μs. Depending on the pulse energy, the structure of the chalcogenide can be changed from amorphous (State 0) to crystalline (State 1) or from crystalline to amorphous (Figure 1.1 (a)). After this first achievement, the technology of laser-induced phase change was continuously developed and adopted by the industry. It eventually led to technologies such as Blu-Ray, the ubiquitous technology for movie recording and viewing (Figure 1.1 (b)).

To increase the density of information that can be recorded on a disk, the surface area of a bit of information must be decreased. This shrinking is achieved by decreasing the

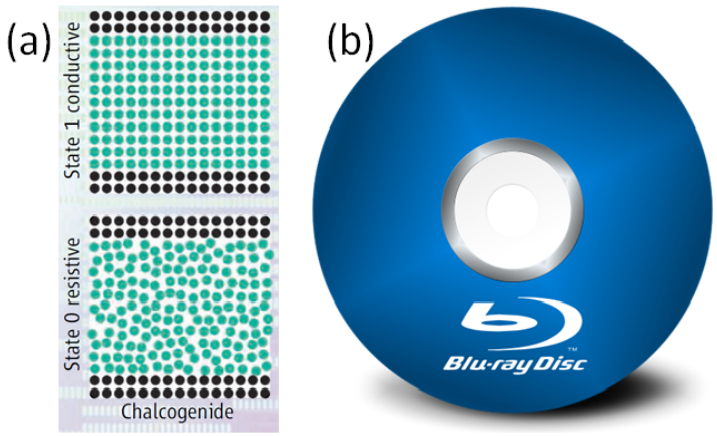

Figure 1.1: Phase change memory technology for electronic and optical memory applications. (a) Switching from a disordered (bottom) to an ordered (top) state in a reversible manner enables to reversibly change the properties of matter, such as its electrical resistivity or optical reflectivity. Reproduced from [6]. (b) A Blu-Ray disk. The phase change is induced by laser pulses (405 nm) of smaller wavelength than those used to induce phase changes in DVDs, resulting in a higher information density.

wavelength of the excitation light, which is the rationale behind the transition from DVD (light wavelength = 650 nm) to Blu-Ray (405 nm).

a.1.1 Mechanism of data storage in optical memories

During the excitation of matter by the laser light, photons are absorbed in matter, leading to the excitation of electrons, which then interact with other free electrons and with lattice vibrations (phonons).

The generation of heat *via* the transfer of energy from the electrons to the lattice vibrations is called "thermalization" [7]. Thermalization occurs on the timescale of picoseconds (10^{-12} s, see Figure 1.2). By being heated to higher temperatures, atoms move more freely and take new configurations, possibly leading to phase changes.

As the lattice temperature increases due to the thermalization process, thermal and structural effects such as phase changes or surface damage occur, on timescales on the order of picoseconds to μs (Figure 1.2).

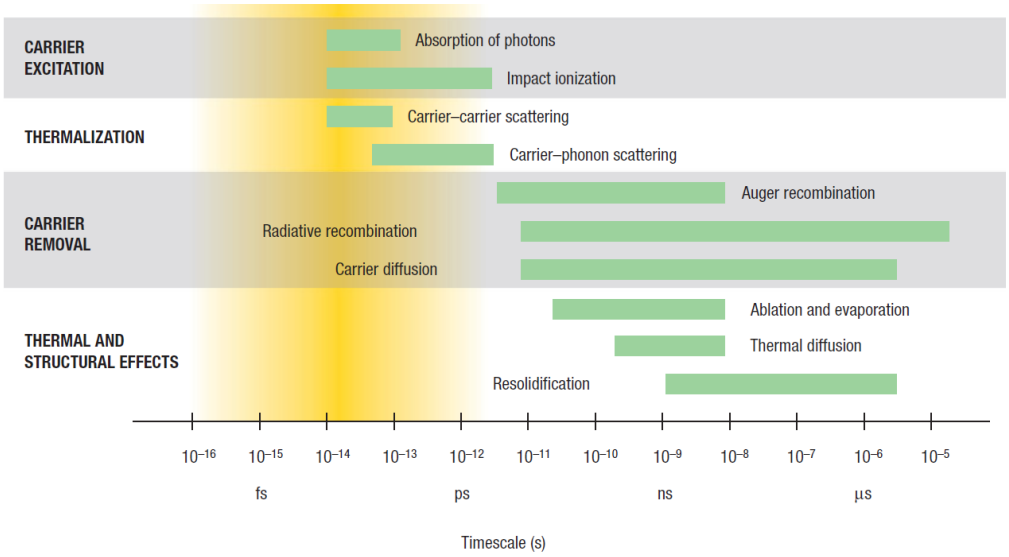

Figure 1.2: Timescales of various processes occuring during and after laser-matter interactions. Reproduced from [7].

Depending on a number of factors that we will discuss, the resulting matter after cooling may be more amorphous or more crystalline, hence impacting its physical properties (optical, electrical, thermal...) which can later be used as means to "read" the state of a phase change memory device.

a.1.2 Reversible phase change in chalcogenides

Chalcogenides are the chemical compounds used as the memory material in DVD or Blu-Ray disks. They contain at least one chalcogen anion (group 16 elements such as Se and Te) and at least one more electropositive element.

Switching mechanism A simple switching model exists for the reversible phase change in chalcogenides (Figure 1.3) [8, 9].

The important characteristic temperatures of a chalcogenide are its melting temperature T_m and its crystallization temperature T_c (Figure 1.3). The crystallization temperature is the temperature above which, given enough time, the structure of the chalcogenide will

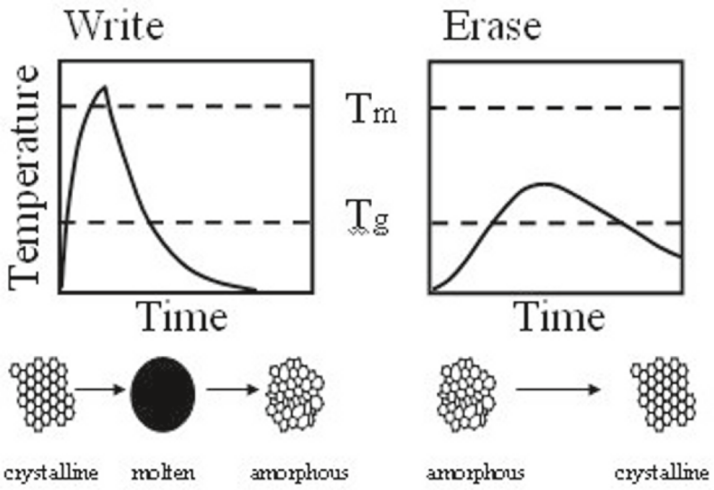

Figure 1.3: Switching mechanism for optical phase change of chalcogenides showing the Write (crystalline to amorphous) and the Erase (amorphous to crystalline) transitions. Both the temperature and the cooling and heating rates are important. For the Write process, matter must be molten (high temperature) then quenched (high cooling rate). For the Erase process, matter must stay long enough at temperatures between the crystallization and melting temperatures. Reproduced from [8].

crystallize. Hence, there is a "crystallization range of temperatures" between T_c and T_m, whereby crystallization occurs.

Amorphous to crystalline

During laser annealing, the transition from the amorphous to the crystalline state occurs when the temperature of the material remains between its crystallization temperature T_c and its melting temperature T_m for a sufficient amount of time (Figure 1.3, right). For the chalcogenide described in [5] ($Te_{82}Ge_{15}Sb_2S_2$), temperatures of $T_c \approx 125°C$ and $T_m \approx 380°C$ are given for the crystallization and melting temperatures, respectively.

Crystalline to Amorphous: quenching

On the other hand, the transition from the crystalline to the amorphous state occurs through rapid quenching from the liquid state. The temperature must reach higher temperatures than the melting point of matter (here 380°C), resulting in complete fusion, and then it must decrease to room temperature fast enough to avoid crystallization in the temperature region between the crystalline and melting temperatures T_c and T_m (Figure 1.3, left). For example, in [5], a cooling rate of at least -50°C/min is a suggested requirement to avoid re-crystallization during quenching.

a.1.3 Criteria for phase-change materials for optical recording

To decrease the power consumption (the power consumption is roughly determined by the power of the laser), melting and crystallization temperatures must be as low as possible. However, to provide long-term stability at room and operational temperatures, T_c and T_m must be much higher than the operational temperature (to avoid unintended writing). So choosing the right phase change material is a matter of compromise.

Materials other than chalcogenides for which phase-change reversibility has been demonstrated are less performant for an ubiquitous use (*e.g.* Blu-Ray) because their melting temperature is higher. For example, silicon melts at $\approx 1414°C$, much higher than tellurium, which melts at 450°C.

But amorphous Te is very unstable at room temperature, easily crystallizing [8]. To make the amorphous structure more stable, it can be compounded with other elements such

as Ge or Sb. We recall that the chalcogenide used by Feinleib to demonstrate optical phase-change contained both Te, Ge and Sb ($Te_{81}Ge_{15}Sb_2S_2$) [5]. To date, chalcogenides are still considered one of the best materials for phase change.

a.1.4 Laser annealing of silicon

For the reasons highlighted in the previous section (too high melting temperature), silicon is not used for optical memory applications. However, there have been many studies on optically induced phase changes in silicon, which are relevant to understand the physics of optically-induced phase changes in materials other than chalcogenides.

Moreover, carbon is more similar to silicon than to chalcogenides in terms of structure and physical properties, so silicon laser annealing results provide us with useful information. Both laser-induced crystallization and amorphization of silicon are reported.

Contrary to the case of chalcogenides, most reports on silicon crystallization by lasers discuss crystallization directly from the melt [10–18]. We recall that in the case of chalcogenides, the solid material has to remain at temperatures between T_c and T_m (hence below the melting temperature T_m) long enough for crystallization to occur.

There are two main routes for laser-induced amorphization of silicon: one in which low (but still higher than the melting threshold) energy densities are used (amorphization *via* quenching) and another in which much higher energy densities are used (amorphization *via* homogeneous solidification).

Amorphization *via* quenching The first reports on laser-induced amorphization of silicon describe an amorphization mechanism controlled by the rate of solidification of the melt (quenching), expressed in terms of the melt front velocity [11, 12] (threshold velocity ≈ 15 m/s). If the melt front velocity is higher than the threshold velocity, the matter ends up in an amorphous, metastable state. This is a similar amorphization mechanism as that of chalcogenides (Section a.1.2, page 27).

The melt front velocity, that control the phase change, is found to depend strongly on the energy density, and also on the wavelength and thickness of the film.

Because higher energy densities lead to higher maximum temperatures, there is more time for the temperature to homogeneize spatially during cooling back down to the solidification temperature; hence, at the solidification temperature, the spatial thermal gradient is lower for higher energy densities, leading to slower solification velocities and to more time for crystallization processes.

Thus, lower energy densities lead to higher melt front velocities, hence to better amorphization [11–14, 19, 20], which is why low energy densities just above the melting threshold lead to amorphization.

These studies on laser-induced silicon phase change were so successful that some reported limited cycle ability studies [20], providing a proof of principle that silicon could be used as an optical memory material, just like chalcogenides.

Amorphization *via* homogeneous solidification There are two routes to minimize the crystalline content during cooling of a material from the melt.

In the previous section, we talked about quenching, whereby the temperature drops fast below the crystallization temperature, resulting in the matter retaining its disordered structure. In this case, the success of the amorphization process is impacted by the crystallization kinetics of the material, the crystallization temperature T_c and the presence of solid-state catalysts. Solid-state catalysts are remaining solid crystals that can act as a crystallization template for the solidifying liquid [21].

Another route toward minimizing the crystalline content during cooling from the melt is to minimize the amount of such solid catalysts during solidification. Solid crystals that have not melted may act as such catalysts (*type 1* catalyst). Moreover, neighboring matter that has just solidified may also act as a crystallization catalyst (*type 2* catalyst). A way to minimize the amount of both types of catalysts during solidification is to use very high power densities to increase the maximum temperature reached during the process. It enables full melting, hence removing type 1 catalysts. Moreover, in the molten matter,

the temperature field has more time to homogeneize. If the temperature field is perfectly homogeneous at the solidification temperature, the material solidifies everywhere simultaneously (**homogeneous solidification**), hence minimizing the impact of type 2 catalysts.

In [17], Sameshima *et al.* report reversible phase changes in silicon by means of laser-annealing at high energy densities. After carefully modeling and simulating the temperature distribution in the thin film during melting, and by comparing these data with experimental results, they proposed a model for the amorphization process based on homogeneous solidification rather than quenching. They provided precise values describing the environment in which matter solidifies and the consequences of that environment. They found that, for amorphization to occur:

- all the silicon (resting on a quartz susbtrate) must melt.

- it must remain in the molten state for at least 70 nanoseconds (70x10^{-9} s).

- the thermal gradient at the Si/quartz interface must be lower than 1.0*10^5 K/cm.

These requirements are related to the presence of solid catalysts during solidification: all the silicon must be molten so that no remaining solid (type 1 catalyst) is present during solidification to act as a catalyst; it must remain in the molten state for a significant amount of time so that its temperature homogeneizes spatially, hence providing low thermal gradients. The low thermal gradients are needed to prevent heterogeneous solidification, whereby one region solidifies first, hence serving as a crystallization catalyst (type 2 catalyst) for the remaining solidifying matter.

Crystallization Silicon crystallization occurs when the silicon is annealed at an energy density in-between the thresholds for *quenching* (low energy) and for *homoegeneous solidification* (high energy). All three phase change processes (sorted by increasing energy of the laser pulse: amorphization *via* quenching, crystallization, amorphization *via* homogeneous solidification) start from the melt.

In terms of catalysts, the requirements for crystallization are opposite to those of quenching and homogeneous solidification. Crystallization occurs through slow, heteroge-

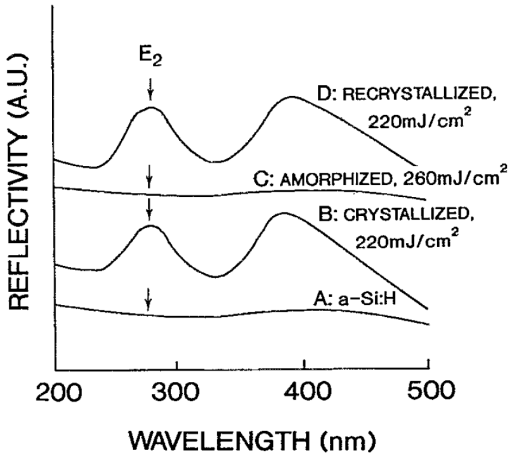

Figure 1.4: Optical reflectivity spectra of laser-annealed a-Si:H showing reversible phase changes between an amorphous phase (required energy density = 260 mJ/cm^2) and a crystalline phase (required energy density = 220 mJ/cm^2). Reproduced from [15].

neous, interface controlled solidification (the interface being the interface between the solid and the liquid, and acting as a type 2 catalyst).

Using the energy thresholds they determined in their studies, Sameshima *et al.* [15, 17] were able to demonstrate cycling ability (Figure 1.4), with low reported damages.

Summary To summarize this section, current optical memory technologies rely mostly on chalcogenides because their low crystallization and melting temperatures enable low power switching. However, in rough conditions (*e.g.* for space or defense applications), data may be lost easily because chalcogenides cannot withstand high temperatures. Materials with higher melting points may be used for such niche applications. For example, silicon has been shown to switch reversibly between two crystalline state *via* single pulse laser annealing.

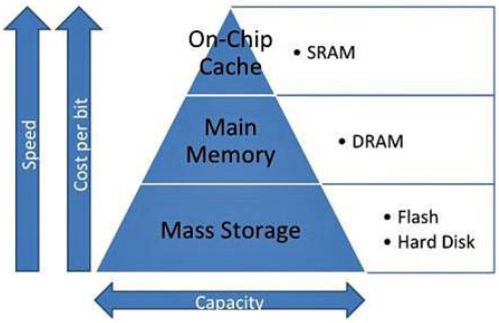

Figure 1.5: The four main memory technologies are all used in a complementary way. Reproduced from [22].

a.2 Electronic memories

Electronic memories are ubiquitous and essential to our computing and communication systems. Mainstream approaches to memory include hard disk drives, Flash (solid state drives), DRAM and SRAM. They differ by their performances and cost, and all are used in computers at different levels of the computing architecture (Figure 1.5 and Table 1.1).

In this section, we first describe the most common memory devices used for computing and data storage, and then we describe approaches to memory that are still in development and have the potential to replace or complement current approaches in the near future.

a.2.1 Non-volatile memory: hard disk drives

Hard disk drives are the cheapest (cost per bit) form of memory in the computer architecture. They are used to store the largest amounts of data.

On the other hand, hard disk drives are also the slowest form of memory in the computer architecture (Table 1.1), mainly because moving mechanical parts (a moving head and a spinning disk) are needed.

At the bit level, the storage mechanism relies on the magnetic properties of a material:

Table 1.1: Comparison of the performances of mainstream electronic memory technologies. Data obtained from [23] (all but phase change and metal oxide), [24] (phase change), [25] (Table 4, second column from the right, metal oxide)

Technology	Energy pJ	Read time ns	Write time ns	Retention	Cycles	I_{ON}/I_{OFF}
Flash	0.00002	100,000	100,000	years	10^4	–
DRAM	0.005	10	10	« s	$> 10^{16}$	–
SRAM	0.0005	0.1-0.3	0.1-0.3	= power time	10^{16}	–
Hard Disk	1 - 10*10^9	5 - 8*10^6	5 - 8*10^6	years	10^4	–
Phase Change	–	60 ns	120 ns	> 10 years	10^9	> 100
Redox	7.5*10^7	10 ns	10 ns	3hr at 200°C	10^{12}	> 100

reading consists in characterizing the orientation of the magnetic field generated locally by the material, while writing consists in changing the orientation of that magnetic field. Because the magnetic properties are retained even when the hard disk is not powered, a hard disk is a non-volatile data storage technology.

a.2.2 Non-volatile memory: Flash memories

Flash memory is another form of non-volatile memory. The cost per bit is higher than that of hard disk drives, but Flash memories are still sometimes used to store large amounts of data in solid state drives.

At the bit level, the operation of a Flash memory relies on a floating gate transistor architecture (Figure 1.6). A typical transistor requires only one gate (control gate) that is used to enable or block the flow of current in the channel. In a floating gate transistor, there is an extra (floating) gate between the control gate and the channel: depending on the electric charges it contains, the floating gate may or may not screen (cancel) the electric field provided to the channel by the control gate. Whether the field is screened or not enables to determine the state of the floating gate (charged or un-charged; 0 or 1).

Screening is achieved by charging the floating gate, which is a conductive material sandwiched between the gate and the channel and is electrically insulated from them by two

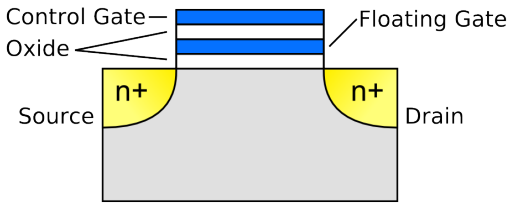

Figure 1.6: Schematic of a floating-gate-transistor (Flash). Reproduced from `http://elec424.rice.edu/gigamesh/blog/index.php?m=01&y=09&d=18&entry=entry090122-181953`.

oxide layers (Figure 1.6). Charging the floating gate is done *via* Fowler-Nordheim tunneling: when a large electric field is applied accross a thin oxide layer, electrons can "leak" through it due to their wave properties. Thus, writing a Flash memory is done by charging/discharging the floating gate.

As the leakage of charges from the floating gate in the absence of an electric field is low, Flash memory is a non-volatile technology. It can retain its information even when powered off for years (Table 1.1).

Flash memories are used in many applications relying on the easy transport of large amounts of data, such as USB Flash drives or memory sticks for cameras. As their cost goes down with improving technologies, they are now sometimes used as a faster replacement to hard disk drives in solid state drives.

a.2.3 Volatile memory: dynamic random access memories

Data writing,reading, and transfer rates in non-volatile memories are very slow as compared to the operating frequencies of computers. As computers require to constantly store and read data during their calculations, they cannot rely on non-volatile memories to gain from their high operating frequencies.

For this reason, when turned on, computing units communicate mainly with volatile memories, which require constant power to retain information but are considerably faster than non-volatile memories (Table 1.1).

Each dynamic random access memory (DRAM) cell is composed of a capacitor and a transistor. The information is retained in the capacitor as an electric charge, while the transistor is used to control when the capacitor is read or written. Because the capacitor is constantly leaking its charge, DRAM need to be refreshed constantly, making them more power-hungry than non-volatile memories. They are also more costly, so typically a limited amount of DRAM is present in the computer architecture: only the information used frequently is retained there, while other less accessed informations are stored in the hard disk drive or the solid state drive.

a.2.4 Volatile memory: static random access memories

Static random access memories (SRAM) are the fastest memory devices (Table 1.1). They can operate roughly at the same frequency as the processing units. On the other hand, they are much more costly, as each bit is stored in four to six transistors.

Consequently, there is an even lower (than DRAM) amount of SRAM in the processing unit, and it is typically placed very near the processor, in the "cache". When the processor is doing operations, it stores the crucial, frequently accessed information in the cache.

SRAM retain their information as long as the power is on, but lose it instantly when it is turned off (volatile).

a.2.5 Non-volatile memory: phase-change

Switching mechanism In 1968, three years before their demonstration of a reversible phase change induced optically [5], Ovshinsky *et al.* induced reversible phase changes in disordered semiconductors by using electrical pulses [26]. In that case, instead of providing heat via the thermalization of photons, the Joule effect is used.

Except from the heat source, the principle of switching is the same (Figure 1.7 (b)): a high voltage is applied for a short amount of time to melt and quench the material, resulting in the amorphization (RESET, red curve in Figure 1.7 (b)) of the phase change memory

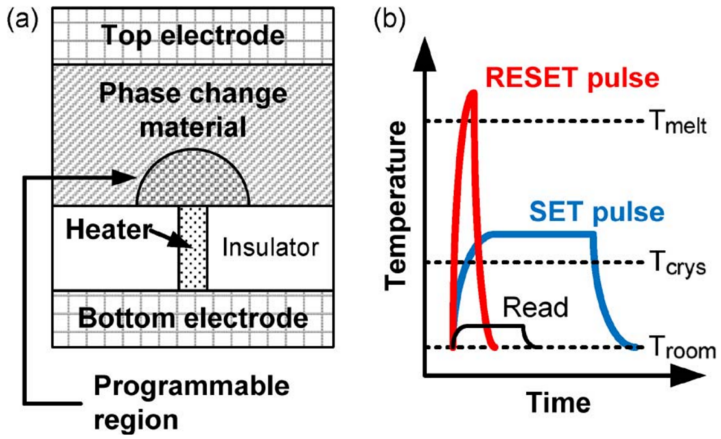

Figure 1.7: Electronic phase change memory. (a) Cross-section of the most common architecture called a "mushroom cell". (b) Switching is achieved by current pulses resulting in heating of the phase change material. Reproduced from [24].

(PCM); a smaller voltage is applied for a longer duration, resulting in the crystallization (SET, blue curve in Figure 1.7 (b)) of the material. The polarization (electric field direction) is not important: PCM devices display a unipolar electrical behavior (Figure 1.8 (b)).

Device architecture The architecture for electronic phase change memories (PCM) comprises the phase change material (typically a chalcogenide) sandwiched between two electrodes. The bottom electrode is sometimes fabricated smaller than the upper one to provide a localized heating source, hence decreasing the amount of matter to crystallize/amorphize at each cycle (Figure 1.7 (a)).

State of the art For the last decades, because silicon-based technologies were deemed more performant for electronic data storage applications, PCM were not used in common computers. However, many researchers and engineers believe that this is about to change [24, 27, 28] as current PCMs are much faster non-volatile memory devices than Flash and hard disk drives (Table 1.1). Recently, very impressive improvements have been demonstrated, with switching speeds faster than 1 ns [29] and energies per bit as small as 100 fJ (20 ns switching speed) [30]. While the metric that keeps semiconductor

industries away from widely adopting PCM as a replacement to Flash is the cost, it is acknowledged that PCM may soon end up being a cheaper technology than Flash memory [31].

a.2.6 Non-volatile memory: binary metal oxide (redox)

Switching mechanism As such, metal oxides are highly insulating (OFF state). However, if a strong electric field is applied to a metal oxide, the oxygen atoms diffuse away from the positive side of the electric field because oxygen is more electronegative than the metal atoms [32]. When the oxygen atoms are repelled (reduction), the remaining atoms are metallic, hence conductive (ON state).

Applying this concept to a metal oxide sandwiched between two electrodes, it is possible to create reduced metal oxide filaments extending from one electrode to the other, hence establishing electrical conduction (OFF to ON).

This process can be reverted (ON to OFF) by applying a negative (opposite direction) electric field, hence attracting the oxygen atoms to the filament location, oxidizing the metal again and restoring the high resistance state. Because electric fields of opposite directions are needed for the full switching cycle of a redox memory, such devices are called bipolar (Figure 1.8 (c)).

It is interesting to note that Redox memories have been described [33] as the fourth missing passive circuit element predicted by Leon Chua in 1971 [34].

Device architecture Devices are fabricated with insulating metal oxide (*e.g.* TiO_2, HfO_2) layers sandwiched between two electrodes (Figure 1.8 (a)). The writing is done by applying voltage pulses of opposite polarities, and the reading is done at low voltages to avoid unintended writing.

State of the art Redox memories are a candidate technology for use as an ubiquitous "universal" memory [35]. They are scalable, offer possibilities for multi-level storage (more than one bit per cell) and endurant. Recently, very high performances have been

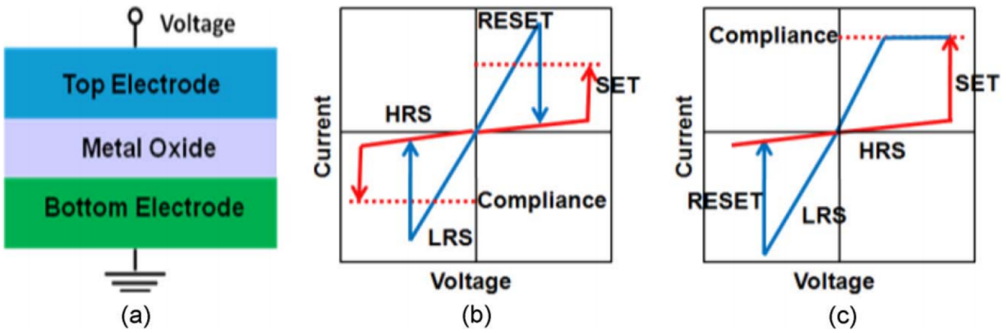

Figure 1.8: Redox phase change memory. (a) Cross-section of the most common architecture for redox memories. (b) Unipolar switching characteristic of phase change memories. (c) Bipolar switching characteristic of redox memories. Reproduced from [25].

demonstrated with HfO_x [36] and TaO_x [37] systems, with endurances larger than 10^{10} (5 ns switching speed), and 10^{12} (< 1 ns switching speed), respectively. The main issue with redox memories for their integration into the computer architecture is their low I_{ON}/I_{OFF} current ratio values. For example, in Ref. [25], a table is provided with the best performances of 11 metal oxide memory devices, and the best performances in terms of I_{ON}/I_{OFF} is a ratio above 100.

a.2.7 Non-volatile memory: Magnetoresistive Random Access Memories

The typical architecture of a Magnetoresistive Random Access Memory (MRAM) is shown in Figure 1.9. It consists in a tunnel junction sandwiched between two magnetic layers: one fixed layer and one free layer. The fixed layer has a fixed magnetization (Left to Right in Figure 1.9), while the magnetization of the free layer can be changed.

The reading of the memory state is done by measuring the amount of current flowing through the cell for a given voltage. If the two magnetic layers are oriented in the same direction (*i.e.* the free layer magnetization is also oriented from Left to Right in Figure 1.9), the device is in a low resistance state and the bit is "1". On the other hand, if the two magnetic domains are oriented in an anti-parallel manner, very little current flows and

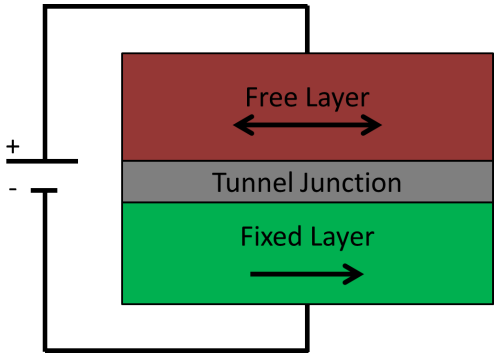

Figure 1.9: Architecture of a magnetoresistive random access memory

the device is in a high resistance state: the bit is "0".

There are several strategies that can be used to change the orientation of the magnetic domains of the free layer, that is, to "write" the memory. Historically, the first approach that was used was to use the electrical currents running through adjacent conductive lines of memory cells to generate magnetic fields that could be used to switch the device state [38]. Even though this approach is functional, it requires large amounts of currents, making MRAM un-competitive with mainstream approaches such as SRAM or DRAM.

In 1996, it was discovered that the magnetization of a free layer could be controlled by flowing an electrical current through it. This phenomenon is called "spin-transfer torque" and is the basis of the latest generations of MRAM, called spin-transfer torque memories [39].

Currently, thanks to these improvements, MRAM stand as one of the most promising approaches to memory, with properties comparing to the best of SRAM, DRAM and Flash combined [38].

Some reasons for industries not to use MRAM as a mainstream technology yet include the huge investment costs that come with implementing a new technology in a semiconductor factory: as long as no company starts investing, it is possible to keep on producing SRAM, DRAM and Flash while remaining competitive. On the other hand, starting to develop a new approach to mainstream memory is risky, so being the prime mover

is not necessarily deemed as a good approach. Usually, as we will see below with the 3D XPoint technology, INTEL is the prime mover which dictates the pace of development.

a.2.8 Non-volatile memory: 3D XPoint

In July of 2015, INTEL and Micron announced the development of a new memory technology that they call "3D XPoint". It is said to be non-volatile, to switch 1,000 times faster than Flash memory and to have higher densities than DRAM (Source: `http://www.eetimes.com/document.asp?doc_id=1327289`).

Many details have been kept secret, however it is known that this approach does require only one cell per bit with no selection transistor, therefore increasing the memory density. Moreover, the main material is a chalcogenide (Source: `http://www.theregister.co.uk/2016/01/29/xpoint_examination/`), which is the same material that is used for phase change memories.

Even though phase change memories are one of the most promising approaches to non-volatile memory, both INTEL and Micron have so far denied that the 3D XPoint technology relies on a phase change mechanism.

Keeping the memory technology secret as long as possible enables both INTEL and Micron to confirm their leadership in the memory industry. As with other developments (*e.g.* the FINFet transistor), other semiconductor factories will follow the lead of INTEL, which is the company most capable of taking risks and invest heavily in new, disruptive technologies.

b Current and future challenges

b.1 Optical memories

b.1.1 Optical memories in rough conditions

A problem with current technologies is that they mostly rely on chalcogenides, that may contain elements that are either rare and/or toxic (*e.g.* tellurium). Moreover, the main advantage of chalcogenides for memory applications, namely, that they are easy to transform, can be a drawback if these memory technologies are used in rougher conditions (*e.g.* defense or aerospace applications).

b.1.2 Heat-induced damages

Using materials with higher melting points such as silicon may be interesting in order to obtain a better stability in rougher conditions (*e.g.* higher temperatures); however, the higher energy densities required for transformations may lead to large degradations.

Bubbles and sputtering When the temperature of a solid reaches its melting point (*e.g.* 1,685 K for silicon), a phase change takes place, from solid to liquid. During the phase change, an amount of energy is absorbed at a fixed temperature, the latent heat of fusion. After enough heat has been absorbed, the temperature rises again until it reaches the boiling point. At boiling, the liquid phase transforms into a gaseous phase escaping the material (vaporization). During this process, bubbles form continuously. As the material cools down to temperatures lower than the melting point, these bubbles freeze in a solid form, and they can be observed long after the laser-annealing process.

Bubble formation in itself does not result in matter loss, so depending on the type of phase change memory, it might not inhibit the cycling ability. However, if enough energy is provided, the bubbles may vaporize, resulting in matter loss (sputtering). In that case,

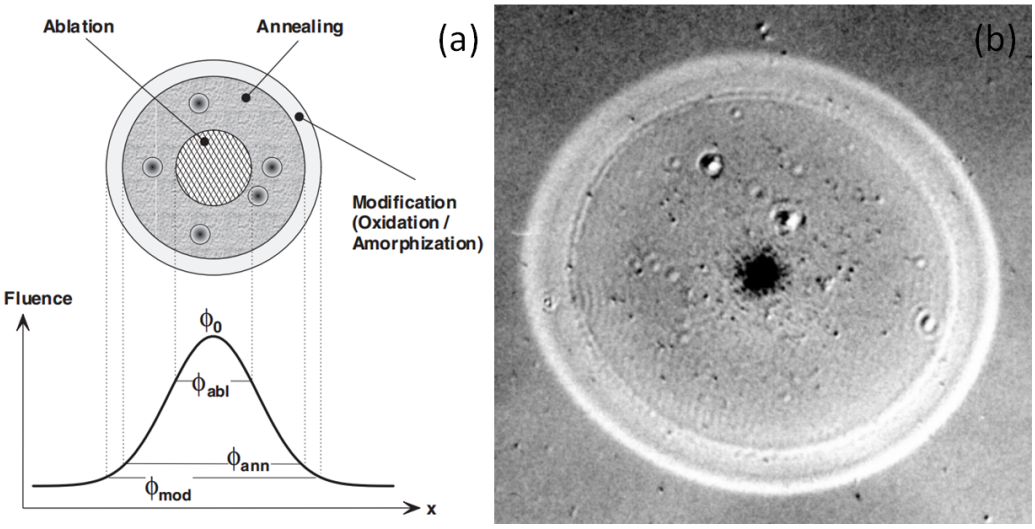

Figure 1.10: Degradations induced by femtosecond laser annealing of silicon. (a) Schematic showing a spot annealed by a femtosecond laser with the energetic centre at the centre of the disk. At high energy densities, ablation occurs, while at lower energy densities, crystallization and then amorphization may occur. (b) Optical micrograph of the surface of silicon after annealing by a single laser pulse in air (wavelength = 800 nm, duration = 130 fs, energy density = 1.5 J/cm^2). Reproduced from [18].

the cycling ability will be reduced, depending on how much matter is sputtered at each cycle.

Ripples One feature commonly encountered after laser-annealing of Si surfaces is wave-like patterns often called periodic "ripples". They were explained after scientists uncovered the dependence of their period on the wavelength of the light (period = wavelength for a normal incidence) and the dependence of their orientation on the polarization of the incoming light. Laser-induced ripples are due to interactions between the incoming electromagnetic field and surface electronic waves called "plasmons". Because a large number of free electrons are needed for these waves to arise, ripples are typically found after laser-annealing of metals or low-bandgap semiconductors only. It is much more difficult to form these periodic structures while annealing an insulating material (such as amorphous carbon). In silicon, ripples usually arise when the surface starts melting [40].

Ablation and explosive boiling We recall that one of the principal industrial applications of lasers is laser cutting. Laser cutting mostly occurs through ablation, which may itself involve rather complicated physical phenomena depending on the laser and on the annealed matter.

At moderate energy densities, laser annealing results in the phase change from solid to liquid, followed by the formation of bubbles and their sputtering. However, at higher energy densities, when the surface temperature rises very rapidly (in less than 1 μs [41]) to temperatures much higher than the melting point, catastrophic nucleation of bubbles occur, resulting in huge matter losses [41]. This process is called "explosive boiling" or "phase explosion" and is responsible for the large matter losses observed during high energy density laser annealing. It is the mechanism enabling to use short pulse lasers as cutting tools (ablation) or as energy sources during pulsed laser deposition.

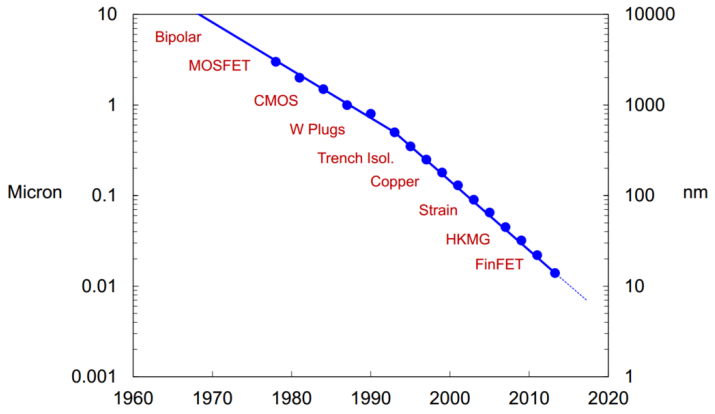

Figure 1.11: Evolution of the gate length of the transistor over the years. The labels state the engineering innovations that helped sustain this evolution. Source: INTEL. Meaning of the acronyms: "Bipolar": Bipolar transistors. MOSFET: Metal Oxide Semiconductor Field Effect Transistor. CMOS: Complementary Metal Oxide Semiconductor. W plugs: Tungsten plugs. Trench Isol.: Trench Isolation. Copper: Copper interconnects. Strain: Strain engineering of the channel. HKMG: High-K Metal Gate. FinFET: Gate all Around Field Effect Transistor, see Figure 1.12 (b).

b.2 Electronic memories

b.2.1 The end of Moore's law

For years, miniaturization was the preferred choice of semiconductor companies all over the world to enhance the performance of their electronic chips. Moore's law states that the number of transistors in an unit area doubles roughly every two years, and this prediction proved sustainable for decades (Figure 1.11). However, due to several challenges that are increasingly complex to address, this is about to change [42].

This fact is well-reflected in the development of the last "technological node". Typically, each new technological node corresponds to a shrinking size of the transistor gate. However, the last jump in performances was not provided by these means but rather by the development of a new transistor architecture (FinFET, see Figure 1.12 (b)). The fact that developing a new architecture of transistors proves easier than shrinking their size highlights the increasing difficulties in reaching smaller dimensions.

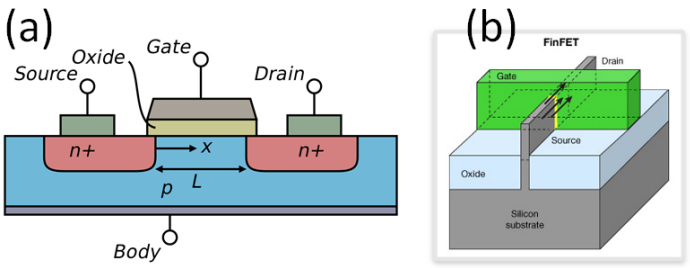

Figure 1.12: The evolution of the architecture of high-performance transistors. (a) Schematic showing the typical configuration of a MOSFET transistor. The current flows from the source to the drain, and its amount is controlled by the gate voltage. The gate oxide prevents charges from flowing from the channel into the gate. Reproduced from Wikimedia Commons. (b) Schematic of the architecture of a gate-all-around field effect transistor (FINFet). The principle of operation is the same. The difference comes from the fact that the channel is surrounded by the gate, thus making it more effective at controlling the current flow. Reproduced from Synopsys webpage (www.synopsys.com).

Moreover, the leading semiconductor company INTEL acknowledged issues with scaling further to the 7 nm node, and stated that another material than silicon, possibly indium gallium arsenide, will be used for that node [43].

Decreasing the wavelength of the light for optical lithography The fabrication of electronic chips is based on optical lithography, a technique that uses masks and light sources to draw patterns onto photo-sensitive polymers called "photoresists". As the patterns in the masks decrease in size, the light source must emit smaller wavelength light. For the 14 nm node (the node refers to the gate length of the field-effect transistor), for example, deep-ultraviolet lithography is used. It requires power-consuming deep-ultraviolet laser sources (248 and 193 nm). For smaller pattern sizes, extreme ultraviolet sources are expected to be needed (EUV, 10-15 nm), leading to even larger power consumption. Recently, IBM demonstrated a chip with 7 nm transistors; to fabricate these transistors, an EUV source was used. However, the development of such sources is costly and difficult. The achievement of a demonstrator does not mean this technology is ready to be commercialized.

Besides their huge power consumption, the problem with EUV light sources is that they are very sensitive to the environment. It might not be financially viable to fabricate new plants with EUV sources, as financial margins are small in the semiconductor industry.

Getting closer to the atomic limit To read the difference between a "0" bit or a "1" bit, the amount of current flowing from the Source to the Drain is measured (Figure 1.12 (a)). The amount of current is controlled by applying a voltage onto the Gate. A threshold gate voltage V_T is defined above which the transistor is conductive and below which the device is insulating. This threshold voltage is a very important value because it must be homogeneous for the millions or billions of transistors on a chip, as current processors do not tolerate errors.

Variability

Therefore, all the transistors on a chip must have very similar threshold voltages. Until now, this homogeneity has been achieved for every new generation of processing chips as every step of the fabrication of a transistor was controlled with a high accuracy.

However, some fabrication processes are intrinsically random. The implantation is such a process: it consists in implanting dopants in silicon to make it conductive with either electrons (n-doped) or holes (p-doped). Depending on the needed properties, hole dopants or electron dopants are implanted. Implantation is a necessary fabrication step for making silicon field effect transistors because silicon is not intrinsically conductive. Until recently, the randomness associated to the implantation process was not an issue because a very large number of dopants was implanted in "large" transistors. However, as the size of the transistor scales down, so does the number of implanted dopants, until the intrinsic randomness of the implantation process results in large variabilities in the number of implanted dopants from device to device. These variations are an issue because changing the dopant concentration of a silicon transistor changes its threshold voltage, which in turn leads to errors when measuring the state of a transistor.

Gate oxide tunneling

The role of the Gate oxide (Figure 1.12 (a)) is to prevent charge carriers from flowing from the channel into the Gate upon application of a Gate voltage. For large transistors, using thick Gate oxide layers works well. On the other hand, smaller transistors require smaller voltage therefore the Gate oxide must be smaller in order not to screen the controlling Electric Field. Due to quantum mechanics, at small dimensions, the charge carriers flowing in the channel are both particle and wave: they have a wave function with a certain size. If the size of the wavefunction is significantly larger than the Gate oxide thickness, then a charge carrier can tunnel through the Gate oxide and leak into the Gate. This forced the semiconductor industry to consider "high-κ" dielectrics as a replacement to SiO_2 for last generation transistors. This solution works now but will eventually fail as well, as the Gate oxide thickness keeps on shrinking.

Punchthrough

As the device size is decreased, the channel length scales faster than the depletion layer widths of both the source-channel and drain-channel junctions. When these widths have the same order of magnitude as the channel length, short-channel-effects start occuring.

The starkest effect occurs when the two depletion regions are so large as compared to the channel length that they end up contacting each other, therefore setting the effective channel length to 0. As the current flow in the channel is critical to the operation of the transistor, punchthrough results in failure of the transistors.

Drain-induced barrier lowering

In "large size" transistors, to a first approximation the potential barrier is controlled entirely by the Gate voltage (vertical electric field). Therefore, the only relevant parameter is the threshold voltage V_T. At smaller sizes, it is necessary to account for the horizontal electric field as well (Drain-Source voltage) because it also impacts the potential barrier permitting or inhibitting the flow of charge carriers in the channel. Therefore, at a fixed Gate voltage, the Drain voltage will impact the potential barrier faced by the electrons, resulting in large subthreshold currents, for example (which means one would read a "0" when one should read a "1").

Surface scattering of the carriers

One of the most important properties of charge carriers in transistors is their mobility. It characterizes how fast they can move, and therefore the operating frequency of the transistors (and ultimately the computing power). The mobility of charge carriers depends on a large number of parameters, such as the material, its crystalline configuration, the doping type and concentration, etc... Therefore, defects can largely impact the mobility of charge carriers. In silicon transistors, charge carriers flow in the channel. The channel forms an interface with the Gate oxide above it (Figure 1.12 (a)): at these interfaces there are defects (scattering centers) than can decrease the mobility of charge carriers. As the size of devices shrink, so does the inversion layer in the channel, which means that on average, the charge carriers travel closer to the Channel-Gate oxide interface, therefore decreasing their average mobility.

All these issues result in an urgent need to find new architectures and new materials for field effect transistors. More information on scaling challenges for the silicon industry can be found in [42, 44].

b.2.2 The complexity of the computer architecture

The current architecture of computing systems is far from ideal (Figure 1.5): at least four types of memories (Flash, Hard Disk, SRAM, DRAM) are used at different locations, resulting in high complexity and communication delays between the data storage and computing systems, and between the data storage systems themselves.

With the current technologies, using all these different approaches to memory is the best compromise, because no memory technology is simultaneously cheap, fast and non-volatile. But, to quote the International Technology Roadmap for Semiconductors (ITRS): [35], "development of electrically accessible non-volatile memory with high speed and high density would initiate a revolution in computer architecture [...]".

For all these reasons (large market driven by innovation, Moore's law failing, the complexity of the computing architecture), research on new approaches to electronic memories is intense. In this thesis, we contribute to the research on this topic by developing

carbon-based electronic memories.

1.2 Carbon as an alternative to chalcogenides and silicon for optical and electronic memories

a Forms of carbon

While semiconductor companies are struggling to deliver the new technological nodes, researchers are actively developing new approaches. They include developing silicon-based more performant architectures (*e.g.* the FinFET, see Figure 1.12 (b)) or using new materials (*e.g.* carbon).

Carbon is considered a material of choice for developing new approaches. Since the discovery of CNTs in 1991 [3], large efforts have been led to develop technological products based on carbon. Today, researchers and industries alike focus on both carbon nanotubes (CNTs) and graphene to develop new transistors, sensors, etc...

There are several reasons why carbon attracts so much attention. First, it is widely available, non-toxic and compatible with the ubiquitous complementary metal oxide semi-conductor (CMOS) technology. Moreover, its atomic structure can be stable or metastable in many crystalline structures (Figure 1.13) ranging from graphite (electrically conductive, opaque, can be used as a lubriquant) to diamond (electrically insulating, transparent, the hardest known material), with the possibility of tuning the bonding arrangement to develop a wide range of allotropes with properties in-between those of diamond and graphite.

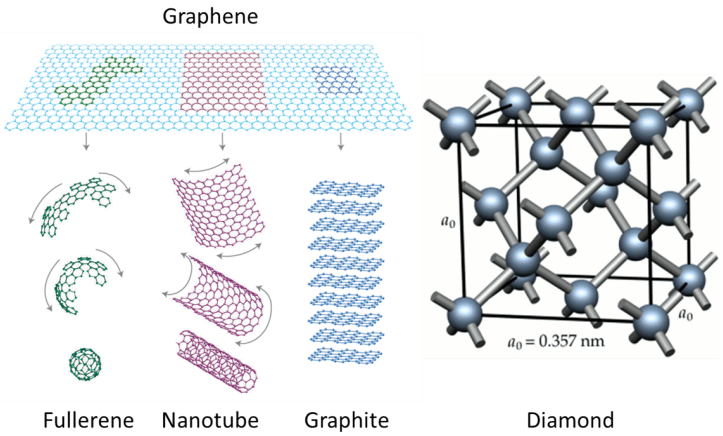

Figure 1.13: The different crystalline structures and dimensions of carbon crystals. 3D crystals are graphite (100% sp^2) and diamond (100% sp^3). Graphene (2D) can be folded to form fullerenes (0D) or nanotubes (1D). Stacking graphene layers on top of each other leads to graphite. Reproduced from [45] and `http://www.stevesque.com/diamond/structure/`.

a.1 Carbon nanotubes

CNTs were first experimentally synthesized by Iijima [3] in 1991. Entirely made of carbon, they are the first quasi-1D structures to be synthesized, leading to interesting quantum effects such as ballistic transport. Most interestingly for semiconductor industries, they were shown to conduct electricity with mobilities > 100,000 $cm^2/V.s$ [46], and heat with thermal conductivities > 6,000 W/(m.K) [47]. Moreover, their electrical properties depend on their size, number of walls, and chirality, with some nanotubes behaving as metals while others behave as semiconductors. Their small sizes enable scientists to imagine entire circuits made of carbon nanotubes - with semiconducting nanotubes for field-effect transistors and metallic nanotubes for connections [48] - and scaling performances rivaling those of silicon-based circuits, as nanotube diameters can be as small as 1.5 nm.

a.2 Graphene

Graphene is a monolayer of graphite. While some of its properties had been theoretically predicted before that, it was first experimentally isolated in 2004 [49] by two researchers at the University of Manchester: Andre Geim and Kostya Novoselov. For this achievement, they earned the Nobel Prize in Physics in 2010.

The reason for the Nobel Prize is twofold: first, graphene is the first 2D material that can be readily tested in the lab, enabling quantum physics experiments [50]. Second, its properties are extraordinary, be it electrical (charge mobility of 200,000 $cm^2/V.s$ [51]), thermal (thermal conductivity of > 4,000 W/m.K [52]), mechanical [53], optical, etc...

Since its discovery, industries and research institutes work hard at using graphene as an electronics materials. The motivation is huge: moving beyond silicon to move beyond Moore's law, enabling a continuity in the improvements we have seen in the last 50 years.

a.3 Textured carbon

Textured carbon is deposited as a thin film in a filtered cathodic vacuum arc, a plasma deposition technique described in Section a, page 78. Its structure is composed of vertical (perpendicular to the substrate) graphitic planes embedded in an amorphous matrix (Figure 1.14). Its fabrication [54], intrinsic properties [55, 56] and their modifications *via* external energetic sources [57, 58] have been studied in detail by current or former members of our research group at NTU. Our group is also a leader in the fabrication and characterization of FCVA systems which are used to deposit the carbon thin films described in this thesis [59–63].

In absolute values, the properties of textured carbon, be it electrical or thermal, are nowhere near those of high-quality graphene or CNTs [55]. Nevertheless, its anisotropic properties make it an interesting material for niche applications. Relative to that of graphene, its thermal conductivity is low (at most 17 W/(m.K) [56]) but it is much better

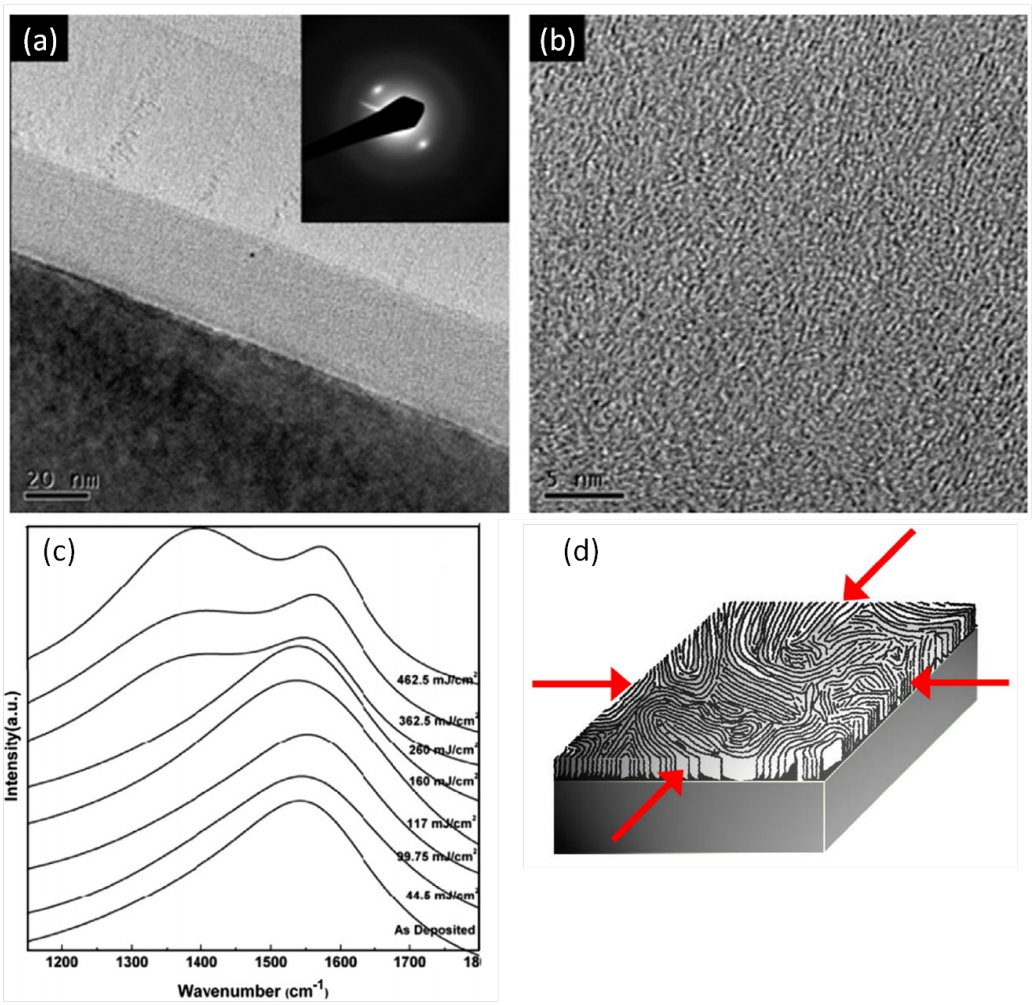

Figure 1.14: Structure of textured carbon. (a) Low-magnification TEM image of a textured carbon film deposited at -500V. *Inset*: corresponding SAED pattern. (b) HRTEM image of the carbon film. Both (a) and (b) are reproduced from [54]. (c) Raman spectra of an amorphous carbon film annealed by 23-ns laser pulses at varying energy densities. After annealing by a 462.5 mJ/cm^2 (top spectrum), the structure is that of textured carbon. Reproduced from [57] (d) Schematic of the crystalline structure of textured carbon. Reproduced from [64].

than that of thermal pastes, so it has been proposed for thermal management applications [56].

Moreover, its electrical properties can be tuned drastically by applying a strong electric current, leading to resistance variations of as much as 10,000 [58]. Fast laser pulses can also be used to tune its properties, be it electrical or thermal, enabling applications such as localized *via*s or heat sinks [57].

Importantly for the work conducted in this thesis where phase changes are studied, the structure of textured carbon is neither fully crystalline nor amorphous. It is in-between crystalline and amorphous, as evidenced by Raman and TEM data (Figure 1.14). Such a structure is of interest because it enables probing of the phase changes in both direction: more crystalline and more amorphous.

Finally, contrary to the cases of graphene and CNT, textured carbon can be deposited at room temperature, which may prove critical if it is to be used as a complement to silicon in electronic chips.

a.4 Thin films with other atomic bonding arrangements

Depending on the deposition conditions, different crystalline structures of carbon thin films may be obtained. From fully graphitic to fully amorphous, carbon thin films display a wide range of properties; moreover, two 100% amorphous films can have widely different properties depending on their sp^2/sp^3 atomic bond ratio. sp^2 bonds are the bonds found in graphite and sp^3 (tetrahedral arrangement) bonds are the bonds found in diamond. When a large fraction of bonds are sp^3 (more than 80%), the film structure is called "tetrahedral amorphous carbon" (ta-C). On the other hand, we call a film containing a large fraction of sp^2 bonds a "high-sp^2" film.

Theoretically, it is possible to tune the optical, electrical, thermal, properties of carbon thin films between those of diamond and graphite by tuning the sp^2/sp^3 and the amount of sp^2 clustering. The intrinsic properties of carbon thin films can be tuned further by absorption of hydrogen, transforming amorphous carbon (a-C) into "hydrogrenated amor-

phous carbon" (a-C:H) [65] and tetrahedral amorphous carbon into "hydrogenated tetrahedral amorphous carbon" (ta-C:H) [66].

b Carbon memories: state of the art

In this thesis, we wish to study how carbon allotropes can be used to develop new approaches to memory. As discussed above, carbon may display extremely different properties depending on its atomic structure: contrasting properties are the basis of data storage in matter.

b.1 Carbon-based optical memories

Lasers provide energy under the form of heat, that can distabilize the atomic structure of the carbon allotrope and lead to a phase change. So far, no optical memory technology based on carbon has been developed, however the literature contains a wealth of studies on the effect of heat on the atomic structure and the properties of carbon allotropes.

b.1.1 Thermal annealing of carbon thin films

We first focus on carbon thermal annealing in an oven. Thermal annealing is a slow process, therefore it may enable to predict some of the effects of continuous-laser annealing that is the topic of Chapter 3.

Most of the experiments described here are conducted in vacuum or in a neutral atmosphere. In the presence of oxygen, carbon films tend to oxidize [67].

Graphitization A range of phenomena occur when carbon thin films are slowly annealed in an oven (Table 1.2). One such phenomenon is graphitization. It occurs first (at lower temperatures) through the clustering of sp^2 bonds (which is the formation of sp^2 clusters via the migration of sp^2 bonds), hence it is in general easier to graphitize

Table 1.2: Temperatures (in °C) at which structural changes are found to occur in carbon thin films during thermal annealing

Ref	Material	Stress Reduction	Graphitization	sp^3 -> sp^2
[70]	ta-C	600	800 - 1300	1100
[66]	ta-C:H	–	500 - 700	–
[68]	high-sp^2 a-C	–	600	1300
[72]	ta-C	500 - 600	500 (sp^2 clustering)	–
[69]	a-C	200 (Stress increase!)	600	–

high-sp^2 a-C because it already contains a large concentration of sp^2 bonds. Typical graphitization temperatures for high-sp^2 a-C are around 600°C [68, 69], while they tend to be a bit higher for ta-C [66, 70]. Considering the melting point of carbon ($\approx$ 4,500 K [71]), it is clear that the graphitization process uncovered in these studies occurs in the solid-state.

For ta-C, the graphitization is accompanied by sp^3 to sp^2 conversion as the fraction of sp^2 bonds in the structure is initially low. sp^3 to sp^2 conversion is generally found to occur at higher temperatures than sp^2 clustering [68, 70], even though some references suggest that it may occur at very low temperatures [69].

Stress relief Because carbon thin films are often considered for coating applications that require high mechanical stability, internal stress values are often extracted. In several cases, internal stresses are found to decrease during thermal annealing [70, 72]. These changes are explained in terms of small structural changes enhanced by the high temperatures (such as sp^2 clustering or sp^3 -> sp^2 conversion). Typically, stress relase occurs at temperatures around 600°C [70, 72]. In one case only, we found a reference discussing a stress *increase* during annealing [69].

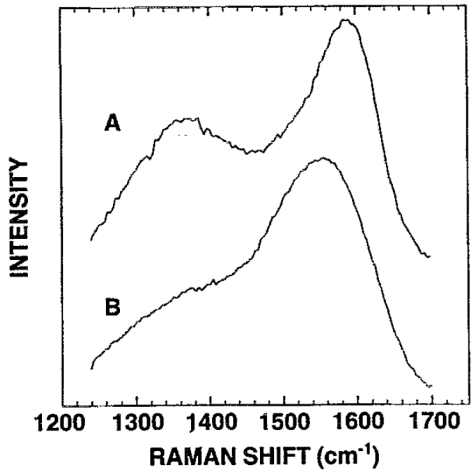

Figure 1.15: Raman spectra of a rf-plasma deposited a-C:H film before (B) and after (A) continuous laser annealing by an ar-ion laser. Reproduced from [73].

b.1.2 Continuous laser annealing

In the case of continuous laser annealing, researchers mainly use micro-Raman characterization to study the impact of laser annealing on the atomic structure.

As is the case for thermal annealing, graphitization is repeatedly found to occur, as evidenced by a rising D peak and a shifted G peak in Raman spectra (Figure 1.15 and see Section a.2, page 97 for a discussion on the 3-Stage model of Ferrari *et al.* [74]). In only one study, amorphization and ablation are found to occur [75].

These studies show that laser-induced heating of the lattice may lead to graphitization and amorphization, which is a pre-requisite for the development of a phase-change memory. However, the mechanisms by which these structural changes occur are not explained. In this thesis, we study the changes induced by a continuous laser in a carbon thin film, and characterize them by advanced and varied characterization techniques, hence attempting to provide a clearer view of the physics behind continuous laser induced phase changes (Chapter 3).

Table 1.3: Power densities (in W.mm^{-2}) at which structural changes are found to occur in carbon thin films during continuous-laser annealing

Ref	Material	Wavelength (nm)	Graphitization
[73]	a-C:H	514.5	1,500
[76]	a-(C:H/Si:O)	514.5	5,000
[75]	a-C:H	514.5	9,000 (with ablation)
		632.8	3,000 (with ablation)

b.1.3 Pulsed laser annealing

Much of the older literature on pulsed-laser annealing of carbon allotropes focuses on inducing a transient phase change in graphite and studying the properties of this ephemeral phase. While graphite is known to sublimate when subjected to high temperatures for long durations, it is found to melt when subjected to a high energy laser pulse (Table 1.4).

After those early studies, researchers started focusing on the state of matter after the annealing, that is, long after the excitation. Most studies found that, in a similar manner as thermal annealing and continuous laser annealing, fast pulse annealing leads to graphitization.

More precisely, it is reported that first, the sp^2 cluster density tends to increase, followed by their coalescence to form graphitic crystals. Raman characterization and transmission electron microscopy (TEM) are shown to be very complementary techniques, as Raman is better at detecting very small sp^2 clusters (less than 2 nm in size), while TEM enables to visualize the orientation of large crystals. This will be discussed in more details in Chapter 3, when comparing TEM and Raman data after continuous laser annealing of textured carbon.

Some research groups characterized the properties of the annealed material for applications. Laser-induced graphitization is found to enhance the electrical properties (electrical conductivity [82, 84] and field emission [55]) and thermal conductivity of carbon

Table 1.4: Impact of pulsed-laser annealing on the structure of carbon thin films

Ref	Material	Duration	λ (nm)	Impact
[77]	Graphite	30 ns	694.3	Partial melting (0.6 J/cm^2)
[78]	Graphite	20 ps	532	Phase change (0.14 J/cm^2)
[79]	Graphite	90 fs	620	Phase change (0.13 J/cm^2)
[80]	Graphite	30 ns 20 ps	694.3 or 532	**Microstructure study:** 0.1 μm diameter spheroids Torn layers Surface upheavals Partial melting (0.8 J/cm^2)
[81]	a-C:H	15 ns	248	$\nearrow$ sp^2 cluster density (<0.1 J/cm^2) Graphitization (0.1 J/cm^2) Ablation (from 0.25 J/cm^2)
[82]	a-C	25 ns	248	$\nearrow$ sp^2 cluster density (0.12 J/cm^2) sp^2 cluster growth (0.12 J/cm^2) $\searrow$ electrical resistivity (0.03 J/cm^2) No roughness $\nearrow$ (up to 0.12 J/cm^2)
[83]	a-C 8 ns 8 ns	 355 532	**10 Hz, 300 to 1200 pulses** Graphitization (0.05 J/cm^2) Graphitization (0.165 J/cm^2) Ablation (films < 50 nm thick)
[57]	a-C	23 ns	248	sp^2 clustering (< 0.117 J/cm^2) cluster coalescence (> 0.117 J/cm^2)
[84]	a-C	23 ns	248	Graphitization (0.362 J/cm^2) $\searrow$ electrical resistance $\nearrow$ surface roughness (0.40 J/cm^2)

films [56].

Finally, some researchers characterized the damages caused by pulsed-laser annealing (if reversible memories are to be developed, the amount of damage must be minimized). A first study showed that a critical parameter is the thickness of the carbon film: when laser-annealing thin films, a significant fraction of the light goes directly into the substrate underneath the carbon film (typically silicon), which is less heat-resistant than carbon, resulting in rapid failure [83]. A simple solution is to use thicker films, for which laser-induced graphitization is successful. Another study [84] conjointly reports the electrical and surface properties of laser-annealed a-C. It is found that while the roughness increases with the pulse energy density (from less than 0.2 nm for the un-annealed film up to $\approx$ 3.5 nm for a film annealed with a 0.65 J/cm^2 pulse), the enhanced electrical properties are retained.

To summarize, there are a number of studies reporting laser-induced graphitization of carbon allotropes, which can be, for example, a transition from the state 0 (amorphous) to the state 1 (graphitic) of an optical memory. So far however, there are no reports on the 1 to 0 transition, that is, laser-induced amorphization. It is a major challenge that has to be addressed if carbon is used as a basis for optical memories.

b.2 Carbon-based electronic memories

To keep on improving data storage technologies, a range of carbon-based electronic memory approaches have been developed.

b.2.1 Redox memories

Research groups have fabricated graphene-based redox memories with two non-volatile resistance states. However, they also demonstrate low endurances and low ON/OFF ratio (Table 1.5). The amount of work conducted so far on graphene oxide redox memories is negligible as compared to efforts conducted on TiO_2 redox memories, for example. However, this trend is not expected to change as preliminary results do not suggest that

Table 1.5: Graphene approaches to electrical memory. In the "Mechanism" column, "Nano-gap filament" refers to the creation/destruction of graphitic filaments bridging a nano-sized gap in the device. "Nano-gap redox SiO_2" refers to reduction/oxidation reactions in the substrate under a nano-sized gap in the graphene. "EM" refers to electro-mechanical switching.

Ref	I_{ON}/I_{OFF}	Cycles	Speed	Device size	Volatile?	Mechanism
[85]	≈50-100	10^5	100 ms	≈ 1 μm	No	Nano-gap filament
[86]	10^4	10^4	500 ns	500 nm	No	Nano-gap redox SiO_2
[87]	40	300	1 s	1 μm	No	Nano-gap EM filament
[88]	2.5	–	–	0.8-20 μm	No	Ferroelectric
[89]	100	100	–	50 μm	No	Redox
[90]	20	100	–	100 μm	No	Redox
[91]	10^3	100	–	180 μm	No	Redox
[92]	10^4	120	100 ms	≈ 3 μm	No	Flash
[93]	–	–	–	–	No	Flash
[94]	10^6	8	80 us (reset)	4 μm	No	Chemical modification
[95]	10^5	18	–	≈ 100s nm	–	EM probe
[96]	10	Several times	–	≈ 100s μm	Yes	EM
[97]	1000	6	40 ns	20 μm	–	EM
[98]	–	–	17 ns	2 μm	Yes	EM
[99]	10^4	500	–	2 μm	No	EM

graphene oxide memories could be competitive with other redox memory approaches (Section a.2.6, page 39).

b.2.2 Filamentary mechanisms

Another approach to memory consists in sandwiching an insulating material between two electrodes and using diffusion mechanisms to create a conductive path through the insulating material, from an electrode to another. For this process to work, the matter in the electrodes must diffuse rapidly in the insulator. Usually, a very small filament diffuses from an electrode, driven by the electric field, in a similar manner as the reduced metal oxide filament in redox memories. Despite the very small size of the filament, very high I_{ON}/I_{OFF} ratio values can be achieved [100].

Another way to induce filamentary conduction in an insulator is through phase-change. Contrary to the approach we discussed just above, the filament is not made of matter from the electrodes but rather of matter from the insulating material that becomes conductive through a phase change. Starting from an electrically insulating structure (*e.g.* amorphous carbon), a filament of conductive matter forms inside of it (a graphitic filament). This process has been documented several times [101–103] and the developed memories display promising performances.

b.2.3 Electro-mechanical switches

Nano-electro-mechanical (NEM) switches typically rely on a suspended conductive nanostructure (*e.g.* a CNT) that can reversibly move between two positions, hence opening or closing an electrical contact.

Despite being intrinsically limited for high-frequency applications as compared to FETs (for example, they are less efficient at frequencies higher than $\approx$ 134 MHz for 32-bit adders [104]), NEM switches possess a range of desirable attributes that pushed the International Technology Roadmap for Semiconductors to acknowledge these devices as a possible replacement or complement for CMOS-based technologies. They are already in

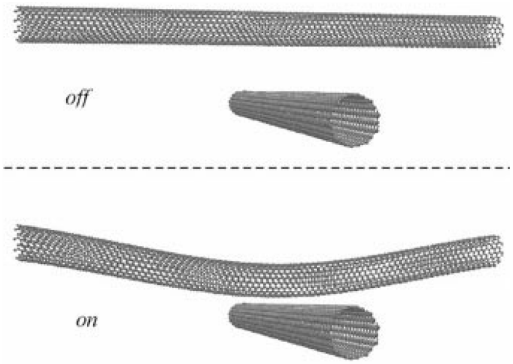

Figure 1.16: Mechanism of a nanotube NEM switch. In the "off" state, the two nanotubes are far apart, hence no current is flowing between them. In the "on" state, the two nanotubes are close, so current may flow. Reproduced from [107].

use in hybrid NEM-CMOS technologies [105].

NEM devices tend to be very resistant to rough conditions (radiation, high-temperature, external electric fields) which make them attractive for aerospace and defense applications [106]. Moreover, they tend to possess lower leakage currents (current in the OFF state), as electrons are forced to flow by tunneling through vacuum (or air), with dimensions of the vacuum gap varying depending on the NEM architecture. Hence, for very low I_{OFF} currents, it is better to have a larger gap, but it generally comes at the price of a larger pull-in voltage and lower reliability. For the same reason, very high I_{ON}/I_{OFF} ratio values may be achieved. Finally, it has been demonstrated that some logic gates can be achieved with less NEM switches than transistors. For example, only two NEM switches are required to make a four-terminal XOR gate, while more than ten CMOS transistors are needed [104].

In 2000, a paper by Rueckes *et al.* [107] opened the eyes of the research community about the potential of carbon-based NEM memories (Figure 1.16) by demonstrating CNT NEM switches. Thomas Rueckes, the lead author, then co-founded a company that develops chips of "NRAM" (nanotube random access memory) for commercial applications.

Due to the fact that experimental research on graphene started only recently, research

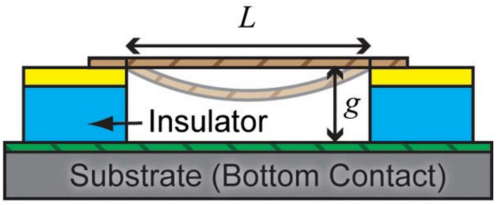

Figure 1.17: Schematic of a graphene-based NEM. The graphene (brown) is suspended over the substrate, which must be a conductive material. Applying an electric field between the graphene and the substrate should lead to closing of the gap. Reproduced from [96].

on graphene NEM switches is still in its infancy. Only very recently were studies on the mechanical properties of graphene conducted [95–99] and many key aspects are still unclear.

Typically, NEM switches open and close the electrical contact *via* electrostatic attraction/repulsion of the suspended structure. Thus, the first step toward the development of a graphene based NEM switch is to probe that electrostatic forces are strong enough to overcome the elastic forces of a suspended graphene membrane, without tearing it. The most obvious choice is to use suspended graphene as a top electrode that may or may not contact a bottom, fixed electrode, leading to the 0 and 1 bit states of a memory (Figure 1.17).

Studies report that electric fields reached at reasonable voltage values (*e.g.* 1.85 V [97]) enable attraction and contact of a moving graphene flake with a fixed electrode. However, the cycle ability is limited due to the mechanical stresses under which the moving graphene flakes must operate. The architecture with suspended graphene is not as ideal for graphene as it is for CNTs.

b.2.4 Graphene planar nano-gap switches

In 2008, Standley *et al.* reported the development of graphene-based nano-gap switches [85]. First, they fabricated planar two-terminal resistive devices based on graphene (Figure 1.18 (a)) and then applied high voltage sweeps accross their electrodes, resulting in electrical breakdown. Electrical breakdown of graphene and CNTs is a known phe-

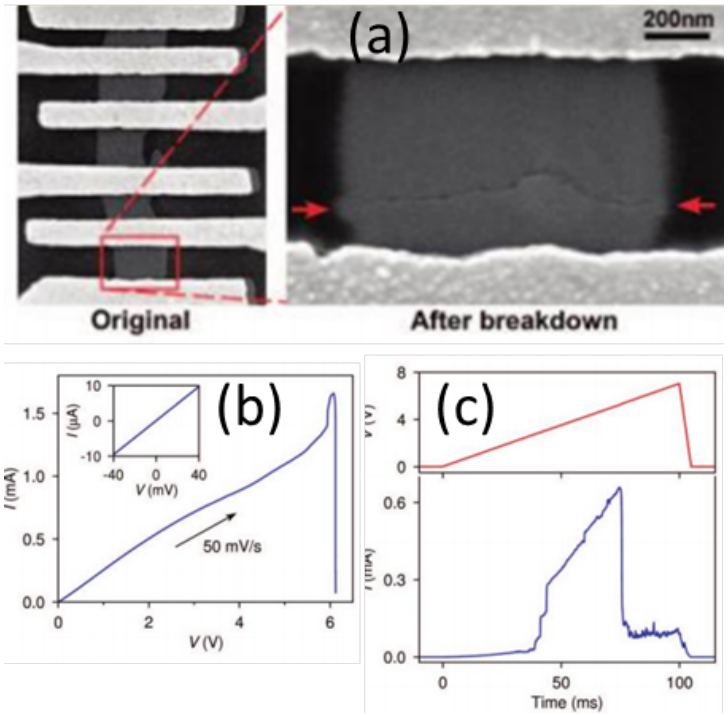

Figure 1.18: Graphene-based nano-gap switch. (a) SEM images of a device before (left, "Original") and after (right, "After breakdown") electrical breakdown of the graphene. (b) I-V curve of the electrical breakdown process. (c) Voltage as a function of time (top) and the corresponding current as a function of time (bottom) during a forward voltage sweep after breakdown, showing a SET process followed by a RESET process. Reproduced from [85].

nomenon driven by Joule heating and resulting in the formation of a continuous physical gap perpendicular to the direction of the current [4, 108–111] (Figure 1.18 (a)).

Then, Standley *et al.* discovered that applying an electric field to the broken device in vacuum enables to recover part of its conductivity in a non-volatile manner (Figure 1.18 (c)). Moreover, applying another voltage sweep to the device in its low resistance state results again in a breakdown process that sets the device back to a high resistance state. This process was shown to be reversible, and over hundreds of cycles were demonstrated.

At the time, an explanation based on the creation/destruction of atomic-scale carbon filaments bridging the nano-gap was proposed. This model was supported by electrical

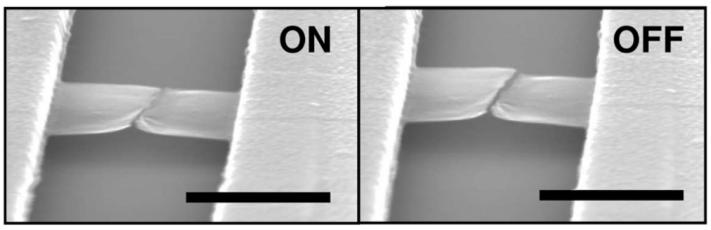

Figure 1.19: A graphene nano-gap system suspended above the substrate can switch the device ON and OFF. The scale bar is 1 μm. Reproduced from [87].

data showing conductance jumps roughly equaling the quantum conductance.

Following up on this study, Zhang *et al.* demonstrated reversible switching in a nano-gap system based on a suspended graphene architecture [87] (Figure 1.19).

The main purpose of that study was to demonstrate that the switching is occurring through reversible movements of the graphene flakes opening and closing an electrical contact. In fact, in 2009 [112], a study revealed that nano-gap systems could switch reversibly through the growth/shrinking of silicon nanocrystals in the SiO_2 substrate, thus questioning the fact that nano-gap systems switch through reversible movements of the material on top of the SiO_2 substrate.

We discuss the arguments for both switching mechanisms (movement of the graphene flakes versus silicon nanocrystals in the SiO_2 substrate) in Section c.2.1, page 70.

b.2.5 SiO_x nano-gap switches

In 2009, Yao *et al.* reported fast (2 μs tested limit) [112] non-volatile switching in a nano-gap system obtained *via* electrical breakdown of amorphous carbon on SiO_2.

Compared to nano-gap systems based on graphene (see previous section, page 65), while the mechanism of formation of the nano-gap is the same (electrical breakdown) and non-volatile switching is also achieved, the demonstrated switching speed of SiO_x nano-gap switches is much faster ($\approx$ 500 ns vs 10 ms) and I_{ON}/I_{OFF} ratio values are much larger. A more comprehensive comparison between those two approaches is provided in Table 1.6, page 72.

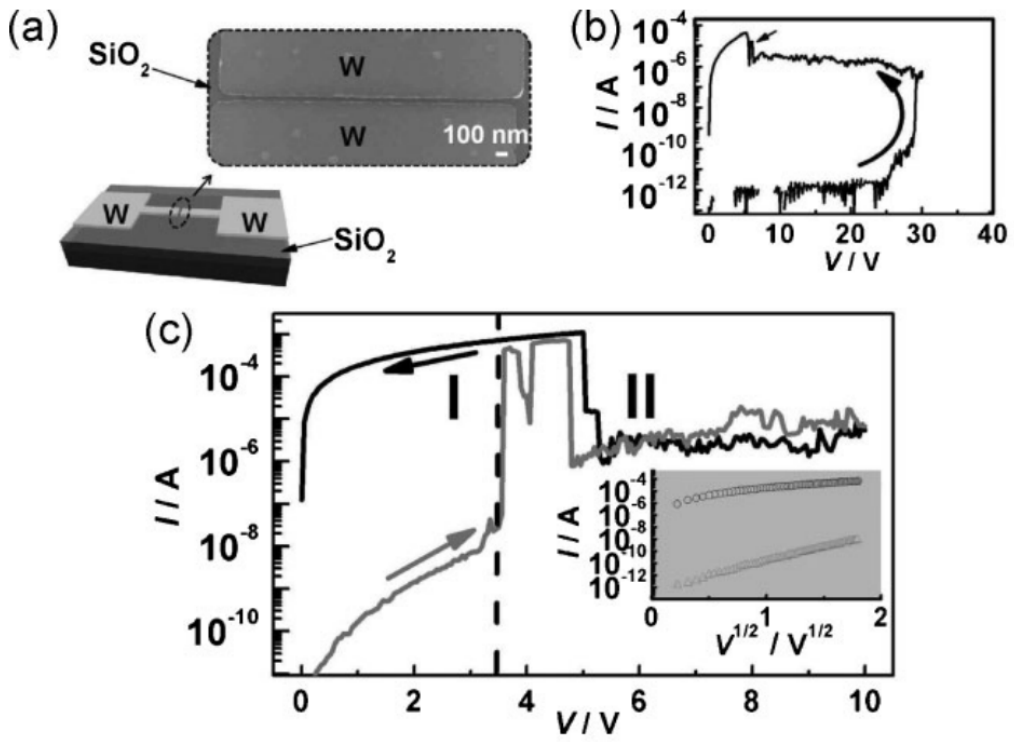

Figure 1.20: Reversible non-volatile switching is achieved in a nano-gap on SiO_2 with Pt/Pt electrodes. (a) Device architecture. (b) I-V curve of the electroforming process. (c) Switching cycle from the high resistance state (grey) to the low resistance state (black). *Inset*: I-$V^{1/2}$ plot for Poole-Frenkel fitting. Reproduced from [112].

Interestingly, in the same study, Yao *et al.* [112] reported that this switching behavior could be obtained by forming a nano-gap in another material than amorphous carbon. They reported similar results with Pt (metal, see Figure 1.20) on SiO_2, TiN (semiconductor) on SiO_2 and multi-walled CNTs on SiO_2.

This fact was suggested as evidence that the switching was occurring not in the material on top of the substrate, but rather in the substrate itself (in SiO_2). The fact that the SiO_2 substrate was damaged during the electroforming process was proposed as further evidence. Several studies from the same group [113–116] and from other groups followed [86, 117].

In these studies, it was found that during a process called electroforming driven by the electric field, silicon nanocrystals were forming in the SiO_2 substrate. These crystals are made of a rare crystalline structure of silicon called silicon-III [116], whose properties are semimetallic, hence enabling the large observed ON current levels.

c Carbon memories: challenges

c.1 Carbon-based optical memories

Achieving amorphization of carbon allotropes *via* laser-annealing To develop optical memories based on carbon, the first challenge to address is to induce a reversible phase change. Most published data on laser-annealing of carbon allotropes report graphitization (Figure 1.21). In order to induce a reversible change, it is necessary to induce amorphization as well.

Minimizing laser induced damages for better cycling ability We discussed laser induced damages in silicon (see Section b.1.2, page 43). While laser-induced damages remain low at energy densities required to achieve graphitization [84], higher energy laser-annealing may induce extensive damage to the surface [80].

A thorough review of the surface degradations created by high energy pulse laser an-

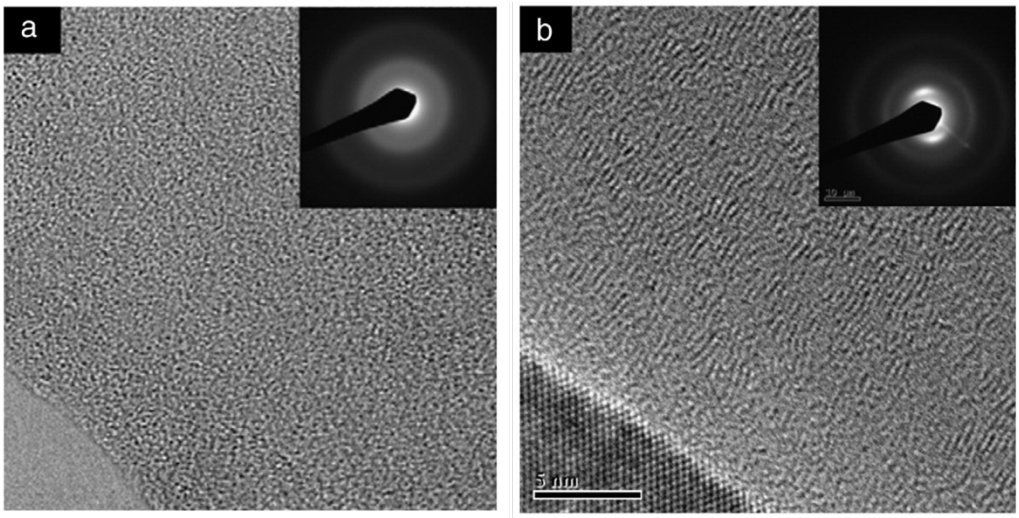

Figure 1.21: HRTEM images of an amorphous carbon thin film before and after annealing. (a) Before annealing, there is no order detected, and this is confirmed by the SAED pattern displaying no anisotropy (inset). (b) After annealing by a 665 mJ.cm^{-2} pulse, graphitic planes perpendicular to the substrate are observed. The SAED pattern (inset) shows two arcs corresponding to the (002) graphite planes. Reproduced from [84].

nealing of graphite was conducted [80], in which it is described that laser-annealing may induce the formation of torn layers, surface upheavals, and ≈ 0.1 μm spheroids. All these artefacts are created by thermal effects, be it mechanical failure (tearing and upheavals) or phase changes (spheroids).

If high energy densities are required for the amorphization process, it will be necessary to conduct a study on the degradations induced in the process, as these degradations may largely impede the cycle ability of a carbon-based optical memory.

c.2 Graphene-based electronic memories

c.2.1 Graphene switching versus SiO_x switching: an on-going debate

Graphene nano-gap devices do not suffer from graphene's lack of a bandgap as they are not controlled by a gate effect. However, one big challenge is to understand exactly the

switching mechanism in such devices.

In 2011, Yao *et al.* published a paper suggesting that many previously encountered switching phenomena in nano-gap systems were due to the SiO_x substrate rather than the proposed active material [114]. For example, the graphene-based devices described in 2008 by Standley *et al.* [85] (Figure 1.18) could switch *via* the creation/shrinking of silicon nanocrystals in the SiO_2 substrate, instead of the proposed formation of atomic sized carbon filaments.

Indeed, the evidence for SiO_x switching in nano-gap systems is convincing (see discussion page 67).

Nevertheless, in 2012, a study by Zhang *et al.* [87] showed that a suspended nano-gap system could switch between two states as well, with switching speeds comparable with those of the 2008 study by Standley *et al.* [85].

An argument in favor of the SiO_x model that could be put forward is that the suspended graphene device is fabricated on a SiO_2 substrate. However, a calculation of the electric field for the SET process enables to conclude that switching ON does not occur through electroforming of silicon nanocrystals in the substrate: the SET process occurs at voltages as low as ≈ 4 V, while the distance between the electrodes is ≈ 1 μm (Figure 1.19). Hence, the SET electric field equals roughly 0.04 MV.cm^{-1} (in the substrate). On the other hand, electric fields that are required for the formation of silicon nanocrystals are reported to equal roughly 6 MV.cm^{-1} [112], that is, 150 times larger than the actual field in the substrate. Thus, the study by Zhang *et al.* is convincing in showing that graphene nano-gap devices can switch ON and OFF *via* the reversible movements of the graphene. SEM characterization of the device in the OFF and ON state supports this idea, as the two flakes are found to be further apart in the OFF state as compared to the ON state (Figure 1.19).

A comparison of the performances of the devices developed by Standley *et al.* [85] and Zhang *et al.* [87] with the devices based on SiO_x switching and mainly developed by Yao *et al.* [112, 113, 115] shows that there are large differences in terms of switching speed and I_{ON}/I_{OFF} ratio (Table 1.6). While the slowest devices based on SiO_x switching demon-

Table 1.6: Comparison of the performances of devices based on graphene switching versus devices based on SiO_x switching

Ref	Active Material	I_{ON}/I_{OFF}	Cycles	Speed
[85]	graphene	$\approx$ 50-100	10^5	0.1 s
[87]	graphene	40	300	1 s
[112]	SiO_x	10^5	10^3	2 μs (tested limit)
[113]	SiO_x	$> 10^5$	10^4	< 100 ns
[86]	SiO_x	$> 10^7$	10^4	500 ns
[115]	SiO_x	10^3 to 10^6	–	50 ns (reset) 50 - 500 ns (set)

strate switching speeds on the order of 500 ns, devices based on graphene switching demonstrate switching not faster than 0.1 s, that is, at least 200,000 times slower. Moreover, demonstrated I_{ON}/I_{OFF} ratio values in graphene devices do not rise much higher than 100, while those achieved in SiO_x devices vary between 10^3 and 10^7.

This supports the idea that these two categories of devices switch differently: while many nano-gap systems on SiO_2 switch through the growth and shrinking of silicon nanocrystals, graphene nano-gap systems may switch through the opening and closing of the nano-gap by the movements of the graphene flakes. This may be due to the mechanical properties of graphene as compared to other nano-gap electrode materials: its thinness may enable easier stretching as compared to thicker electrode materials such as Pt or TiN [112].

A detailed discussion on an electro-mechanical model for the switching of graphene devices is provided in Chapter 5. Moreover, we provide more evidence that the switching is through the reversible movements of the graphene by comparing AFM images of the nano-gap obtained in the HRS and in the LRS (Chapter 5).

c.2.2 Performances of graphene nano-gap mechanical switches

If graphene nano-gap switches are switching *via* the opening and closing of a nano-gap, it is the first demonstration of a planar mechanical switch. Such devices could avoid several issues encountered in mechanical switches based on suspended structures, such as mechanical failure (Section b.2.3, page 63).

However, the performances demonstrated so far in terms of switching speed and I_{ON}/I_{OFF} ratios are lagging behind many of their competitors, including SiO_x switches (Table 1.6).

Hence, for the future developments of graphene nano-gap based mechanical switches, it is important to know what determines these "poor" performances. This will enable to assess the potential of this technology, and to know which steps could be taken to reach that potential.

In Chapter 5, we provide a comprehensive model of the switching of graphene nano-gap switches that enables to understand what limits the switching speed and the I_{ON}/I_{OFF} ratio values.

1.3 Goals of the thesis

a Optical memories: study of the phase changes and study of the degradations

The major challenge in the development of optical memories based on carbon is to induce amorphization. This is necessary to obtain reversible control of the structure of a material through laser annealing.

As discussed before in Section a.1.4, page 30, there are a number of reports revealing that silicon amorphization *via* laser-annealing is possible, and discussing two main amorphization mechanisms.

In many respects, silicon is similar to carbon. Both have the same valency configuration ($2p^2$ for carbon and $3p^2$ for silicon), leading to similar chemical reactivities; moreover, while they have very different melting points (1,687 K for silicon, 4,300 K for carbon), they share a stable crystalline structure (diamond cubic).

If this comparison can be drawn further, we expect laser-induced amorphization to be achievable, either *via* quenching at low energy densities, or via homogeneous solidification.

Some studies mention the possibility of inducing amorphization of carbon allotropes through laser annealing, in particular through continuous laser annealing [75] or by using a femtosecond laser to study the thermodynamic properties of graphite [77]. However, these processes were not studied thoroughly.

In this thesis, we address this challenge to the development of carbon-based optical memories by focusing first on the process of amorphization, then on the study of the surface degradations induced by this laser-induced amorphization process.

b Graphene-based electronic memories: development of a model for the switching

If the switching in planar graphene nano-gap memories is through the reversible movement of the graphene, it should be possible to visualize this movement, as was done by Zhang *et al.* [87] with SEM images of suspended graphene. However, SEM characterization does not have the necessary resolution to visualize nanometre-size displacements in planar devices on SiO_2 [85]. Techniques such as atomic force microscopy (AFM) enable the probing of matter at smaller scales, therefore it should enable the direct visualization of the nano-sized gap, hence enabling to probe its size in both the HRS and the LRS. Hence, in this thesis we use an AFM to probe the state of the nano-gap in both the HRS and the LRS. If the switching is driven by movements of the graphene, the size of the gap should vary.

Confirming that the switching occurs through reversible movements of the graphene is not sufficient to assess the potential of this approach to compete with more traditional approaches to memory. For this purpose, it is necessary to understand the switching in details. This would enable to develop a quantitative model of switching that could predict the potential of such switches. By considering the electro-mechanical forces acting on the graphene flakes in the presence of an electric field, we should be able to predict critical operational characteristics, such as the switching speed, the I_{ON}/I_{OFF} ratio, the cycling ability and the non-volatility.

c Organization of the dissertation

In Chapter 3, we report on the continuous laser-annealing of textured carbon. The goal of this chapter is to understand optically-induced phase changes in carbon, including amorphization. We study the impact of laser irradiation on the surface morphology and on the crystalline phase and chemical composition. We find that amorphization is indeed possible by using a continuous laser, and that it is driven mostly by oxidation.

We also graphitize matter, suggesting that a reversible phase change may be possible. However, a reversible memory using a continuous laser would not perform well as compared to other memories using pulsed lasers. Therefore, we then set out to use a pulsed laser.

In Chapter 4, we achieve a reversible phase change in carbon by using a nanosecond laser. The goal is to demonstrate the development of a fast optical reversible phase change memory based on a carbon allotrope. We find that amorphization is possible by using a nanosecond pulse, however the mechanism of amorphization differs from that using a continuous laser because oxidation does not occur during fast pulse annealing. We also demonstrate partial cycle ability; nevertheless, the endurance is low, and we explain it by characterizing the surface state. Laser annealing results in important damages to the thin film. Energy densities required for amorphization are larger than those leading to important surface damages. Another approach may be required to develop larger endurance memories. In particular, we discuss the feasibility of using femtosecond laser pulses to induce disorder in carbon allotropes at temperatures much lower than the melting point. We demonstrate preliminary results on the femtosecond laser-annealing of textured carbon, including setting-up an optical bench with control of the delivered power and confocal imaging. Another approach to memories is electrical control, and we discuss the development of an electrical memory in the next chapter.

In Chapter 5, we report the development of an electronic memory based on graphene. While our reasoning is the same (change the applied power to obtain different phases), the power source (Joule heating) and the material (2D-graphene vs 3D-textured carbon) are different. We are able to achieve a better memory behavior than with optical control; however, by characterizing the material state, we find that the mechanism controlling the resistance is very different. Rather than being based on a phase change, our graphene two-terminal memories switch by an electro-mechanical mechanism. The first electrical pulse (or sweep) generates enough heat for a nano-sized gap to form, effectively separating the graphene stripe into two pieces. Then, by applying electrical pulses or sweeps, this gap may close or open, leading to drastic non-volatile resistance changes. To predict the optimal performances of such a device, we develop a quantitative electro-mechanical

model explaining the reversible switching cycles.

Chapter 2

Experimental methods

In this section, we describe the experimental methods that are critical to the work described in this thesis. First, we describe the fabrication techniques, necessary to prepare the materials (textured carbon films) and devices (two-terminal graphene devices). Then, we describe the characterization techniques that are used to characterize the state of matter (its crystalline structure and its morphology) during our experiments. We also describe the sources of optical (lasers) and electrical (semiconductor analyser) energy that are used to transform matter during our experiments.

2.1 Fabrication techniques

a Filtered cathodic vacuum arc

The filtered cathodic vacuum arc is a plasma deposition system, whereby a plasma is created and guided to the susbtrate for deposition. After vacuuming the chamber to pressures < 2.10^{-6} Torr, a plasma is generated by creating a strong electric field between an anode and the solid-state cathode made of the desired material (here, graphite) (Figure 2.1 (c) lower-left), hence resulting in an electric arc.

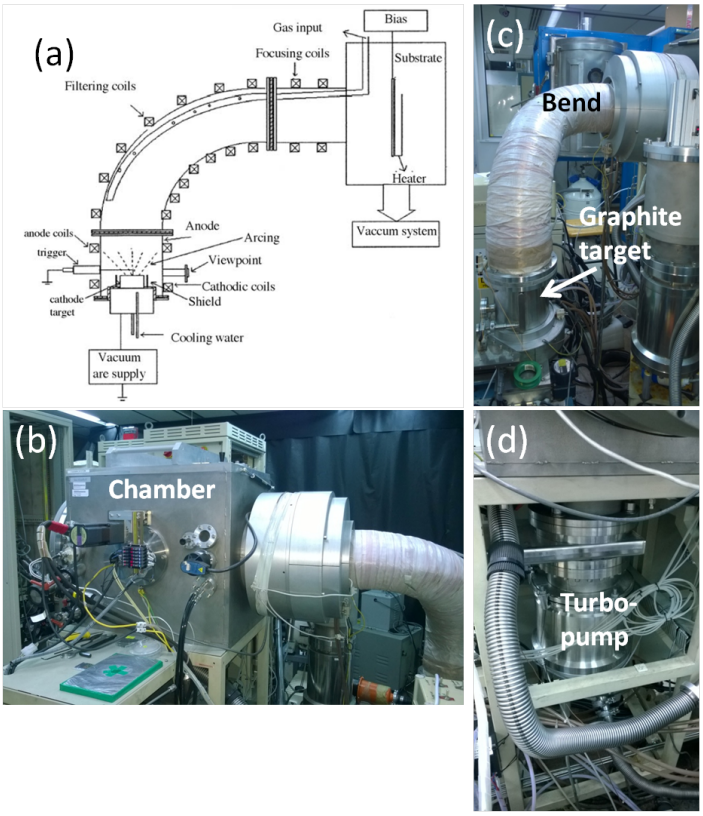

Figure 2.1: The filtered cathodic vacuum arc system used in this thesis. (a) Schematic of a filtered cathodic vacuum arc. Reproduced from [118]. (b) The chamber, containing the substrate holder. (c) The magnetic bend, guiding the charged particles while filtering the macro-particles. (d) The turbo-pump, creating a high vacuum in the chamber.

When it was first developed, the main issue with this method of arc deposition was the generation of neutral (not charged) macroparticles along with the charged plasma, leading to non-uniform deposition of matter onto the substrate. This issue was solved by the utilization of a bent pipe wrapped in a coil generating a magnetic field (Figure 2.1 (c)). The intensity of the magnetic field and its direction are optimized to guide the plasma through the bent path until it reaches the substrate (in the chamber Figure 2.1, (b)), while neutral (hence insensitive to the magnetic field) macroparticles follow a straight path and get "filtered" away.

Control of the crystalline structure

While the purpose of the magnetic field is to guide the plasma to the substrate, an electric field is used to accelerate the carbon ions, hence controlling their kinetic energy. It is done by applying a voltage to the substrate: in our case, a negative voltage is applied to accelerate the positive carbon ions (typically C^+ [57]). The kinetic energy of the ions has a huge impact onto the resulting material structure and properties [64].

Amorphous carbon can be classified into two sub-structures that are: high sp^2 and high sp^3 amorphous carbon. High sp^2 amorphous carbon has a lower density than high sp^3 amorphous carbon. For sp^3/sp^2 fractions higher than 75 %, amorphous carbon is regularly referred to as tetrahedral amorphous carbon or diamond-like carbon.

In crystalline allotropes of carbon, the transformation from graphite to diamond can be achieved by applying a large pressure to graphite; similarly, for amorphous carbon, it is found that a transition from high sp^2 to high sp^3 amorphous carbon occurs when the internal stresses, which are analogous to pressure, get larger than 6 GPa [64] (Figure 2.2).

The control of the internal stress is achieved by controlling the kinetic energy of the ions *via* the electric field that is applied to the substrate. A maximum internal stress (» 6 GPa, see (Figure 2.2)) is achieved for substrate voltages of $\approx$ -100V. At such large stresses, the density is high and the bonds are mainly sp^3: the application of a voltage of -100V enables the deposition of tetrahedral amorphous carbon thin films.

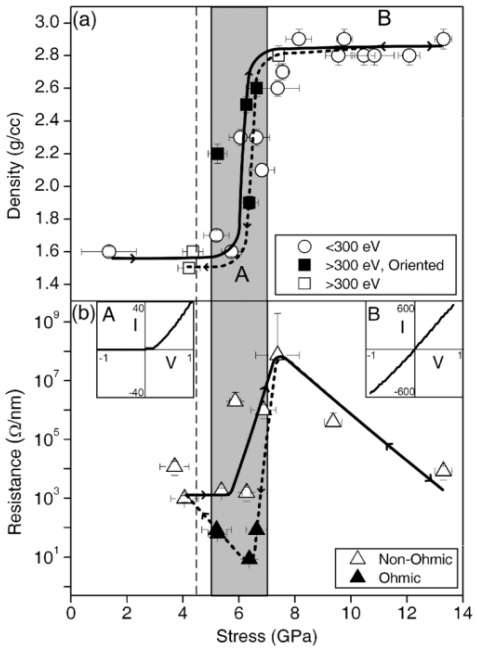

Figure 2.2: Impact of the stress on the structure and electrical properties of amorphous carbon. (a) Density as a function of stress. (b) Electrical resistance as a function of stress. Reproduced from [64].

Increasing the kinetic energy of the ions further results in a decrease of the compressive stresses in the film, and eventually, at stresses around 6 GPa, the electrical resistivity of the film is found to decrease drastically, due to the formation of graphite planes that are perpendicular to the substrate, effectively resulting in textured carbon. There is a range of stresses around 6 GPa for which textured carbon forms, and in this thesis we use two different voltages to obtain such structures: -300 V (Chapter 3) and -500 V (Chapter 4).

The crystal structure of the resulting textured carbon is discussed in both chapters, and it differs slightly due to the different voltages. However, what remains constant is the fact that it is mostly made of nano-sized graphitic crystals perpendicular to the substrate in an amorphous carbon matrix. To study phase changes, the fact that the material is part-amorphous part-crystalline is a huge advantage.

Control of the thickness

The thickness of the deposited film can be controlled by monitoring the deposition time. The application of a higher arc current to the graphite target can also result in the formation of a denser plasma, therefore in a faster deposition rate. In any event, the deposition rates we obtain here are sufficient for the desired film thicknesses, and our deposition time typically never goes beyond 9 minutes.

There is an upper bound to the thickness of the carbon films we can deposit by using the filtered cathodic vacuum arc. It is typically around 500 nm. This limitation is due to internal stresses in the film, which tend to rise with the thickness, and eventually result in a loss of adhesion between the film and the silicon substrate for large thicknesses. Ways around this issue exist, such as a deposition in several steps [119].

However, this upper bound is not an issue for the work conducted in this thesis, as what matters most for optical data storage or laser writing is the contrast we can obtain between two phases (here, amorphous versus graphitic): inducing a phase change requires energy, so film thicknesses smaller than 500 nm are desired.

Theoretically, there is no lower bound on the thickness we can obtain by deposition *via* the filtered cathodic vacuum arc. In the literature, thicknesses typically reported are $\approx$ 100 nm (90 nm [55], 150 nm [54], 100 nm [58]). Therefore, to facilitate comparisons with the literature, in Chapters 3 and 4, we use thicknesses of 140 nm and 110 nm, respectively. Moreover, we deposit a second film approximately three times thicker in Chapter 4 to study the impact of the thickness on the annealing process.

b Electron beam evaporation

Electron beam evaporation is a deposition technique that we use to deposit the Ti/Au electrodes on top of the graphene in Chapter 5. It enables the deposition of precise thicknesses of matter (up to 0.1 nm resolution thanks to a controller measuring the oscillation frequency of a crystal) in a very homogeneous manner.

A solid-state crucible made of the desired material (titanium or gold here) is hit by a beam of accelerated electrons, resulting in heating and melting of the crucible material, until part of the matter evaporates and forms a gaseous phase that spreads and condensates onto the substrate.

Details about the e-beam evaporation conducted during this thesis are:

- Evaporator brand and model: Edwards model Auto306

- Vacuum: 2.10^{-6} Torr (base vacuum)

2 to 6.10^{-6} Torr (during evaporation)

- Accelerating voltage for the electron beam: 5 kV

- Electric current: 50-100 mA

- Deposition rate: 0.5 to 1 Å/s

c Optical lithography

c.1 Principle

During the first step of optical photolithography, a photosensitive polymer called photoresist is spin-coated on the surface of the substrate to pattern. Exposing this polymer to UV light makes it resistant to a special chemical solution called developer. The un-exposed photoresist is not resistant to this solution, resulting in its removal during immersion.

After UV-light exposure, the sample is immersed in the developer solution, leading to the selective removal of the un-exposed photoresist. This step is called development, and it typically results in a sample that is partially protected against the next processing steps (*e.g.* etching) by the remaining photoresist. When the desired steps (*e.g.* etching of the un-protected matter or deposition) have been conducted, the remaining photoresist can be simply removed by immersing the sample in acetone. Then, another photolithography step can be conducted.

To selectively expose the sample to UV light, a mask made of soda lime glass partly covered with a layer of chrome (which absorbs the UV light, therefore enabling the patterning) is used. The photoresist we use resists to development **after exposure**: it is called a "negative" photoresist. "Positive" photoresists do the opposite: they are resistant to the developer **when they are not exposed** to the UV light. The mask must be designed by taking into account the type of photoresist that is to be used.

c.2 Fabrication of two-terminal memory devices

Here, we describe the fabrication of the graphene-based two-terminal devices used in Chapter 5.

We purchase graphene samples from Graphene Supermarket. They consist in polycrystalline monolayer graphene on a SiO_2 film (thickness 285 nm) which itself rests on

Table 2.1: Specifications of the Si/SiO_2 substrate supporting the graphene

Property	Value
Oxide thickness	285 nm
Wafer thickness	525 μm
Wafer resistivity	0.001 - 0.005 ohm-cm
Type	P (boron)

a silicon substrate (specifications in Table 2.1). Before shipping, the graphene is grown on a copper substrate [120]. Then, it is transferred on top of the SiO_2 film *via* a standard transfer method [121].

The first fabrication step is to define graphene bands with varying widths by using UV lithography and O_2 plasma etching (Figure 2.3).

Then, the electrodes are defined and deposited by evaporating Ti (10 nm)/Au (100 nm) on top of patterned resist and lifting-off (Figure 2.4).

We obtain resistive two-terminal devices made of two Ti/Au electrodes bridged by a graphene band.

d Surelite I-10 Nd-YAG 532 nm laser

We discuss specifics of the nanosecond laser we use in Chapter 4, which is a Surelite I-10 Nd-YAG laser (Figure 2.5). The amplification medium is a crystal of neodymium-doped yttrium aluminum (Nd-YAG), which is excited optically. The wavelength of the photons it emits is centered at 1,064 nm (infrared).

The excitation cavity is coupled to a "Q-switch" that opens only when the maximum population inversion is attained, enabling to generate very fast pulses at very high powers.

Several wavelengths are accessible thanks to non-linear crystals. In this project, the frequency of the photons is doubled in a crystal to obtain 532 nm photons.

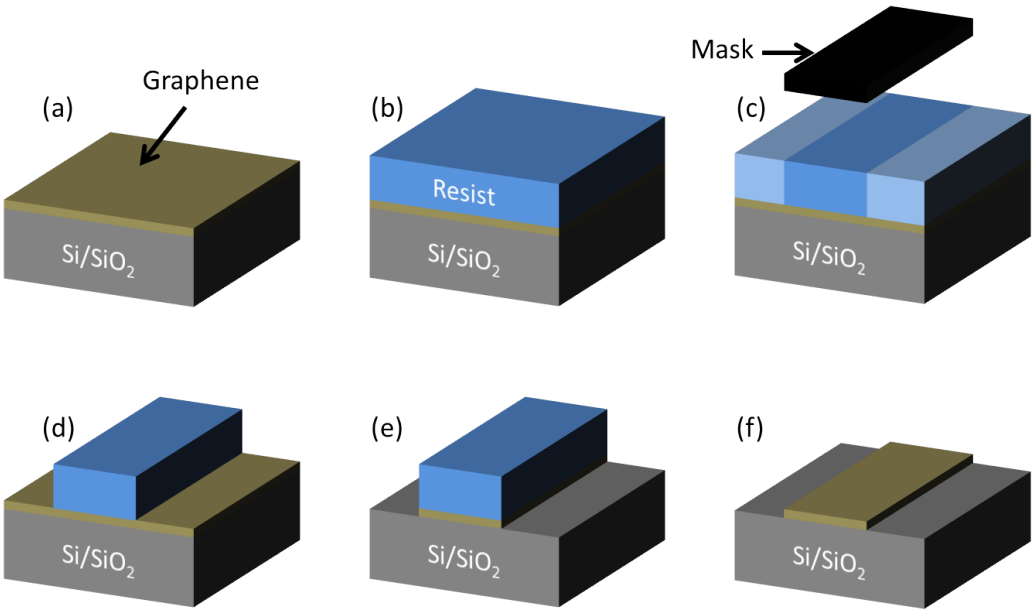

Figure 2.3: Patterning of graphene bands. (a) Graphene on SiO_2/Si. (b) Spin-coating of negative photoresist. (c) UV light exposure with mask. (d) Development. (e) Graphene O_2 plasma etching. (f) Resist removal with acetone.

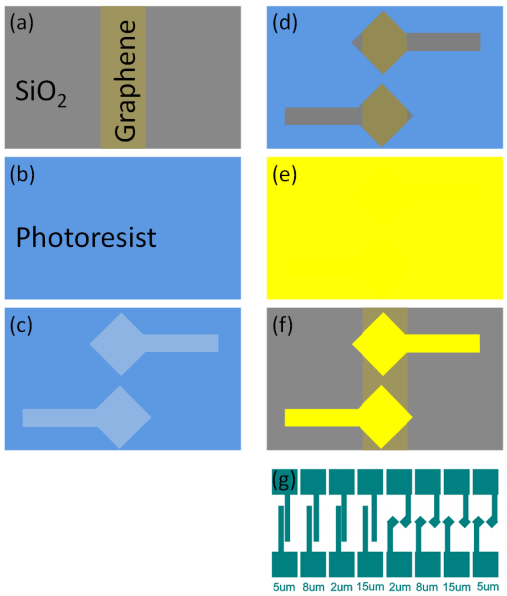

Figure 2.4: Patterning of the electrodes. (a) Graphene band on SiO_2. (b) Spin-coating of negative photoresist. (c) UV light exposure through the mask. (d) Development. (e) Electron beam evaporation of Ti/Au. (f) Lift-off. (g) Design of the mask for electrode patterning.

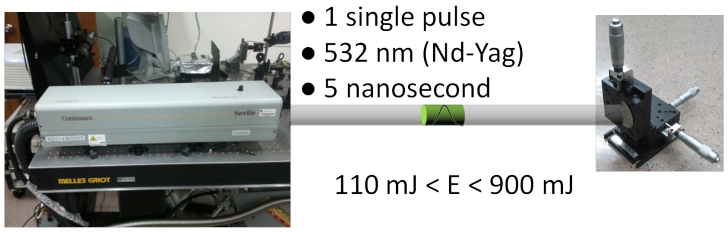

Figure 2.5: The Surelite I-10 Nd-YAG laser used in Chapter 4.

At 532 nm, the Surelite I-10 generates single 532 nm pulses with full width at half maximum (FWHM) duration of ≈ 4 - 6 ns and energy up to 900 mJ (peak power ≈ 0.2 GW). It can be operated at 10 Hz or in single pulse mode; we use the single-pulse mode.

d.1 Measurement of the beam profile and energy density calculation

The total energy contained in a pulse (in J), which can be controlled manually, is measured using a Labmax_Top power meter which is placed normally to the beam.

To calculate the energy density at a specific location, it is necessary to know the surface area on which this energy is applied (because energy density (J/cm^2) = energy (J)/area (cm^2)). We use an Ophir M2-200s beam profiler to characterize the spatial profile of the beam.

The beam profile resembles an ellipse with two high-energy peaks (Figure 2.6 (a)). By using a SEM (Figure 2.6 (b)) or an optical microscope, it is possible to match the two high-energy locations measured by the profiler with surfaces on the textured carbon film.

To estimate the energy density corresponding to each energy and location, we estimate the surface area A of the beam by estimating the area of the affected surface of a textured carbon thin film annealed at a high energy density (≈ 0.13 cm^2). Then, we compute the total number of counts N_{count} and of pixels N_{px} corresponding to the elliptic shape of

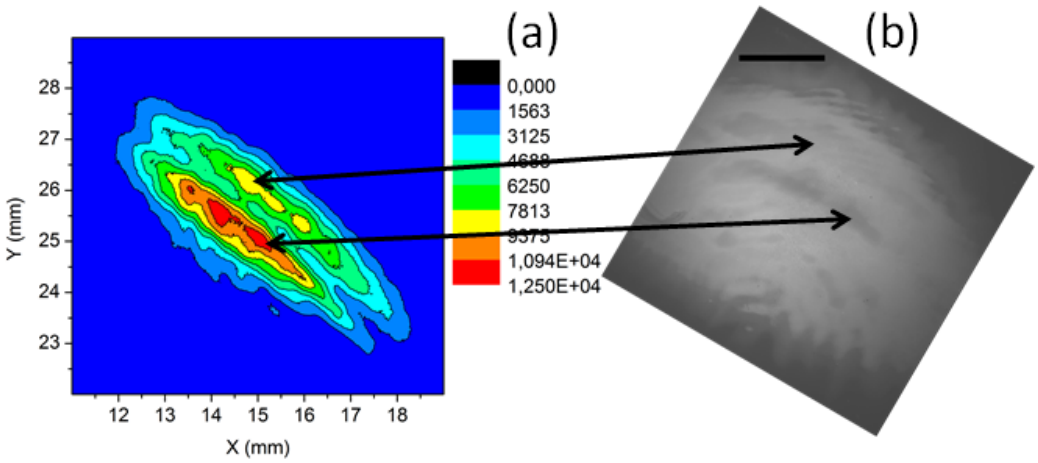

Figure 2.6: (a) Spatial beam profile of the laser beam. (b) SEM image of textured carbon annealed by a single pulse containing 0.39 J of energy.

Figure 2.6 (a). By dividing the number of pixels by the surface area of the beam, we obtain the area per pixel.

$$A_{px} = \frac{N_{px}}{A} \tag{2.1}$$

We also count the energy per count by dividing the total energy of the pulse E by the total number of counts.

$$E_{ph} = \frac{E}{N_{count}} \tag{2.2}$$

Then, for a given pixel, we can estimate the energy density:

$$E_{density} = \frac{n_{count} E_{count}}{A_{px}} \tag{2.3}$$

Unless otherwise specified, in Chapter 4 the characterization is conducted at the centre of energy (highest energy density).

The Nd-YAG laser enables to tune the energy density between 1.95 and 15.40 J/cm^2, with steps of $\approx$ 0.3 to 0.5 J/cm^2.

Table 2.2: Specifications of the Coherent Chameleon Ultra II.

Wavelength	680 nm to 1,080 nm
Maximum power	4W at 800 nm
Pulse frequency	80 MHz
Pulse width	140 fs
Polarization	Horizontal
Beam diameter	$\approx$ 2 mm

e Coherent Chameleon Ultra II

The main specifications of the Coherent Chameleon Ultra II are given in Table 2.2. This laser operates at 80 MHz (80 million pulses/second), forbidding a direct comparison with the results obtained with the nanosecond laser (single pulse). Moreover, there is no direct way to control the output power of the laser. An indirect way to control it is to tune the emission wavelength (Figure 2.7), which is a far from ideal solution, because it forbids parametric studies with only one parameter varying (such as the output power, or the wavelength). The emission wavelength of the laser can be set from 680 to 1080 nm with a step of 1 nm.

e.1 Power control setup

To control the output power, we use a $\lambda/2$ waveplate and a Glan laser polarizer. The signal output from the laser cavity is polarized horizontally. After going through the $\lambda/2$ waveplate, the beam is still polarized linearly, however its angle relative to the horizontal direction is changed; how much it varies depends on the orientation of the $\lambda/2$ waveplate. Any linear polarization is practically achievable by turning the waveplate, which is graduated with angles from 0 to 360 °(Figure 2.8 (a)). Right after the waveplate, we add the linear Glan laser polarizer, which splits the beam in two: the fraction of the beam whose polarization is parallel to the polarizer goes through, while the fraction of the beam whose polarization is perpendicular to the polarizer is reflected perpendicu-

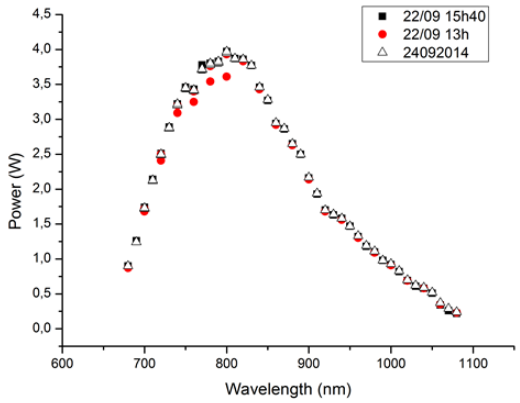

Figure 2.7: Output power as a function of the emission wavelength. These spectra were taken at three different times (two times on the 22^{nd} of September 2014, once on the 24^{th} of September 2014).

larly and is eventually absorbed by the safety enclosure wall (black box surrounding the annealing setup).

With this technique, by coupling a $\lambda/2$ waveplate with a Glan laser polarizer, we are theoretically able to control the power going through the polarizer, from 0% to 100%. In practice, such values are never reached because the beam output from the laser cavity is not 100% horizontally polarized. Nevertheless, for the purpose of this study, the available range of powers enable annealing of textured carbon or of silicon from powers leading to no observable changes to powers leading to strong modifications.

e.2 Alignment

The alignment of the laser beam is perhaps the most critical step in setting up the annealing experiment. It enables to minimize the power losses in the optical components (the laser beam should cross optical components, for example a lens, at their center), to obtain a good focusing of the beam (*e.g.* as the output of a microscope objective) and to avoid damages to some other components (*e.g.* by slightly mis-aligning the beam, it is possible to avoid a return of the reflected beam in the laser cavity, which may lead to some damages).

To mimize risks, alignment must be done at very low powers, as the operator has to look at the beam incident on an item used to aid during the alignment process. For this purpose, after the polarizer, we often add an optical density (Figure 2.8 (a)), which absorbs a fixed fraction of the power, independent of the light polarization.

Three mirrors are used to obtain three degrees of freedom for the beam direction (Figure 2.8 (a)).

e.3 Focusing the beam for laser annealing

After the mirrors, the beam goes through a telescope composed of two lenses (first lens shown in Figure 2.8 (a) and second lens shown in Figure 2.8 (b)), whose goal is to increase the beam size while keeping it collimated. A large collimated beam is required to obtain a good focus with the microscope objective (shown in Figure 2.8 (b)).

e.4 Setting-up a confocal microscope

The annealed features are very small in size (few μm), not resolvable with the naked eye. However, it is necessary to directly image them in order to avoid mistakingly annealing the same location twice, or to aim at specific locations, therefore speeding up the annealing experiments.

For that purpose, we setup a confocal imaging system (Figure 2.8 (b)). For that purpose, two 50/50 beam splitters, a lamp, a lens and a CCD camera are used. The camera is connected to a computer for real-time monitoring of the signal.

The lamp provides light, a fraction of which is directed toward the microscope objective, focused on the sample surface, reflected, and passes through another beam splitter. Finally a fraction of the reflected light is directed toward the CCD camera, enabling direct imaging of the surface (Figure 2.8 (b)). This technique is called confocal imaging.

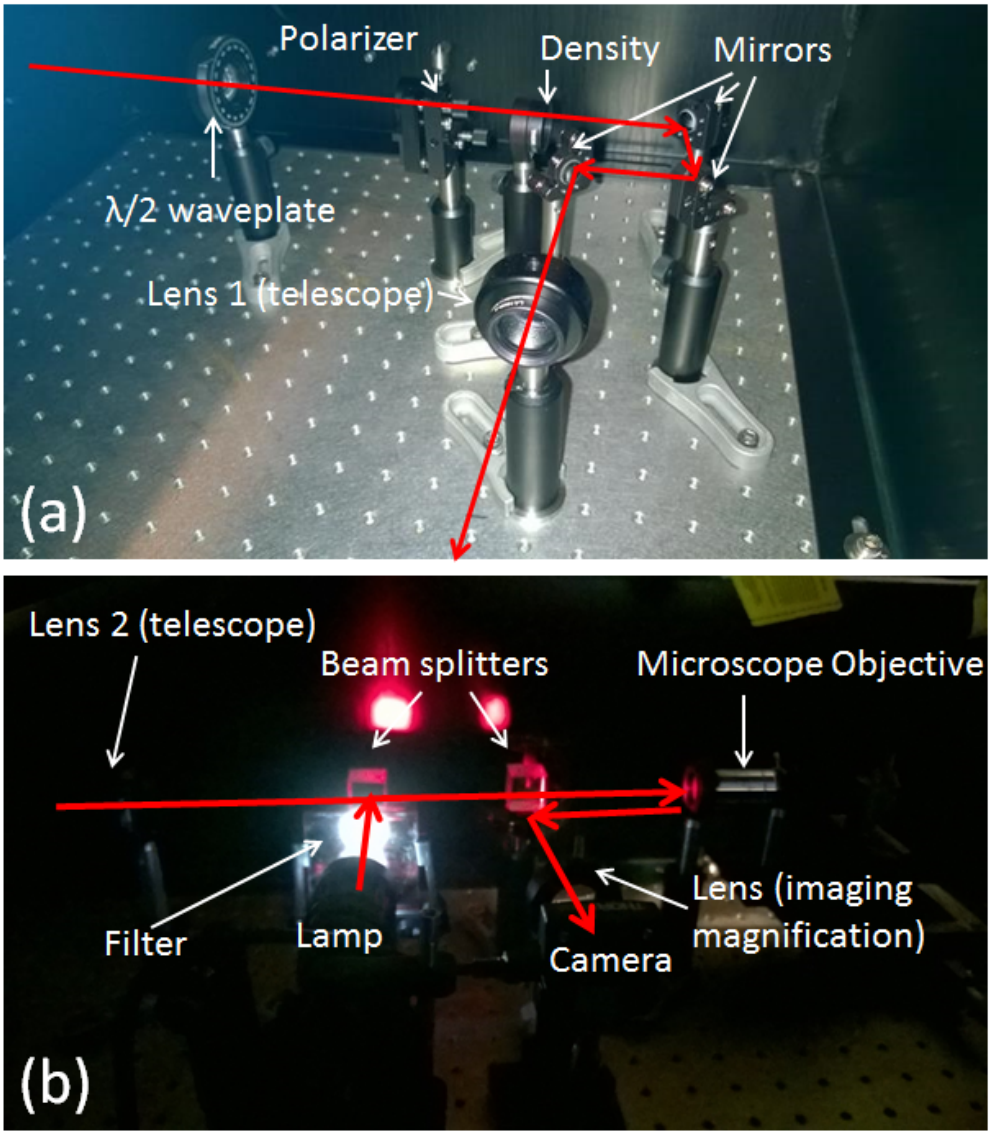

Figure 2.8: Femtosecond laser-annealing setup. (a) Control of the power via the $\lambda/2$ waveplate, the polarized and the density. (b) Confocal imaging system and annealing setup.

e.5 Beam profile

Figure 2.9 shows the profile of the laser beam, which determines the energy distribution that is received by the sample, hence the energy density at each location.

Because the unfocused laser beam is too large to achieve the power densities required for laser-annealing, we focus it with a microscope objective. If a parallel beam enters a microscope objective, the beam is focused into a small disk at the focal distance. Then, if the sample to be annealed is placed at the focal distance, the surface corresponding to this disk of light is imaged after reflection by using the confocal imaging system (2.9 (b)). When the laser is turned OFF, we can directly image the surface of the sample with the lamp: the image is sharp when the sample is at the focal distance of the microscope objective.

The focal distance determined by looking at the sharp image with the confocal system should be the same for both the laser beam and the light coming from the lamp. However, this is true only if both the laser beam and the light coming from the lamp are both collimated beams (parallel) before entering the microscope objective. If a beam is not parallel, the effective distance at which a sharp image (of the laser beam or of the sample surface) is obtained **is not** the focal distance of the microscope objective.

This can result in discrepancies between the obtained laser beam profiles obtained when the focus is on the sample surface (sharp image of the surface) and when the focus is done to obtain the best beam profile, as observed in Figure 2.9. The best focus of the laser beam is obtained in Figure 2.9 (b), however the actual beam profile during our experiments is shown in Figure 2.9 (a) because during our laser-annealing experiments, we focus on the sample surface.

e.6 Calculating the power reaching the sample

Any calculation of the power density must take into account the beam profile. Moreover, we note that the power received by the sample is not equal to the power at the exit of the polarizer (or the optical density) shown in Figure 2.8 (a).

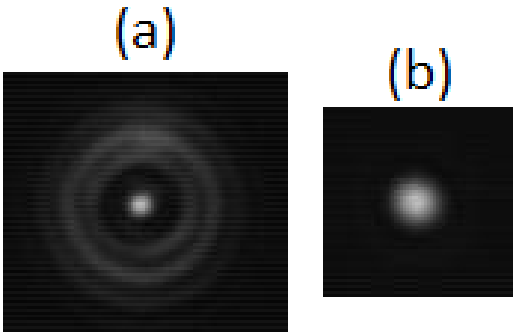

Figure 2.9: Laser beam profile. (a) Beam profile obtained when the distance between the sample and the microscope objective is such that the sample surface appears sharp in the camera. (b) Beam profile obtained when the distance between the sample and the microscope objective is such that the beam profile appears sharp in the camera.

Table 2.3: Power losses in the optical components of the annealing setup. To obtain the output power of an optical component, we divide the input power by the Division factor, which is always larger than 1

Component	Division factor
Mirrors	1.04
Lens 1 (telescope)	1.06
Lens 2 (telescope)	1.10
50/50 Beam splitter 1	2.21 (should be 2.00)
50/50 Beam splitter 2	2.17 (should be 2.00)
Microscope objective	1.32

To start, roughly half of the power is lost in each beam splitter. During annealing, the beam splitters are removed, however significant fractions of the power are still lost in the mirrors, the telescope (two lenses) and the microscope objective. Power losses in each component are shown in Table 2.3.

2.2 Characterization techniques

a Raman spectroscopy

Raman spectroscopy is a powerful tool to obtain information on the crystalline structure ([74]), composition, temperature [122], strain [22] (and so on) of a material.

Laser light is shined on a material, which partially scatters the light, both elastically (no energy change, Rayleigh scattering) and inelastically (energy loss or gain). The scattered light is then collected in a spectrometer. A significant part of the scattered light has lost (Stokes shift) or gained energy (anti-Stokes shift). This energy shift is measured by the spectrometer and a Raman spectrum is plotted: the y-axis corresponds to the number of detected photons, while the x-axis is the energy shift from initial wavelength (in cm^{-1}).

The detected wavelength shifts are due to the interaction of photons with lattice vibrations (phonons) which have well-defined resonant frequencies. These frequencies depend on the crystalline structure, composition, temperature, strain, and so on, so determining them provides critical information about the material.

In the course of this study, we used a Raman WITec setup (Figure 2.10), which comprises three sources of light: 488 (blue), 532 (green) and 633 (red) nm lasers. It is sometimes useful to use different excitation wavelengths because some bonds may interact more or less strongly with different wavelengths. Moreover, depending on the material properties, some characteristic Raman peaks may be dispersive, which means that their energy shifts depending on the excitation wavelength. For example, in carbon, the G peak (cen-

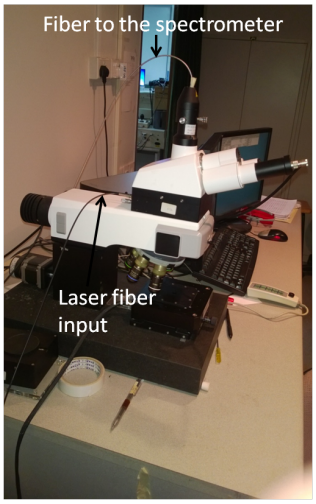

Figure 2.10: The Raman WITec setup.

tred at *ca.* 1,580 cm^{-1}) is more or less dispersive depending on the crystalline content of the carbon allotrope [74]. Therefore, the G peak dispersion can be used as a means to characterize the crystalline content.

In this thesis, for Raman characterization, we use the 532 nm laser (Chapters 4 and 5), because it tends to be the most-studied wavelength for Raman characterization of carbon allotropes. However, we use the 488 nm source in Chapter 3 because if modifies the structure of carbon films more effectively as compared to the 532 nm source, perhaps due to a smaller penetration depth (higher energy photons are absorbed first).

a.1 Measurement of the output power of the laser during Raman characterization

As will be discussed in Chapter 3, Raman lasers are powerful enough to induce structural and morphological changes in carbon allotropes. For this reason, the power is measured each day using a THORLABS S121C Photodiode connected to a THORLABS PM100D display. The laser power fluctuates significantly from day to day, which can partly be assigned to varying ambient temperatures. Moreover, the objective of the microscope through which the laser beam is guided has a large impact on the power deliv-

Table 2.4: Measured power values for different microscope objectives and laser wavelengths

Objective	Power (mW) at 532 nm	Power (mW) at 488 nm
x5	26	21.9
x20	23.6	20.7
x50	20.8	20.1
x100	8	13.2

ered to the sample.

Typical measured laser powers for different wavelengths and microscope objectives can be found in Table 2.4. These values are the maximum values. A knob enables to vary the delivered power between these values and zero.

a.2 Impact of the crystalline structure on Raman signal: the 3-Stage model

The interpretation of Raman spectra for carbon allotropes is done following the framework of Ferrari *et al.* [74]. In carbon-based materials, there are two main windows of interest for the Raman shifts: a first range of waveshifts between 600 and 2000 cm^{-1}, where the D (1350 cm^{-1}) and G peak (1580 cm^{-1}) lie, and a second range of waveshifts centred on the 2D peak (*ca.* 2680 cm^{-1}). In Chapters 3 and 4, as the 2D peak intensity is low for disordered carbon allotropes, we focus on the D and G peaks.

The 2D peak can be used to monitor the quality of graphene, so we monitor its values in Chapter 5.

The G peak is almost always present in carbon allotropes because it corresponds to vibrations of pairs of sp^2 bonds. Because of the consistency of the G peak intensity, we calculate I(D)/I(G) ratio values to characterize the D peak intensity.

D-peak vibrations are active in **defective graphitic rings**. Consequently, they are not found in the presence of defect-free graphitic rings, nor are they found in highly de-

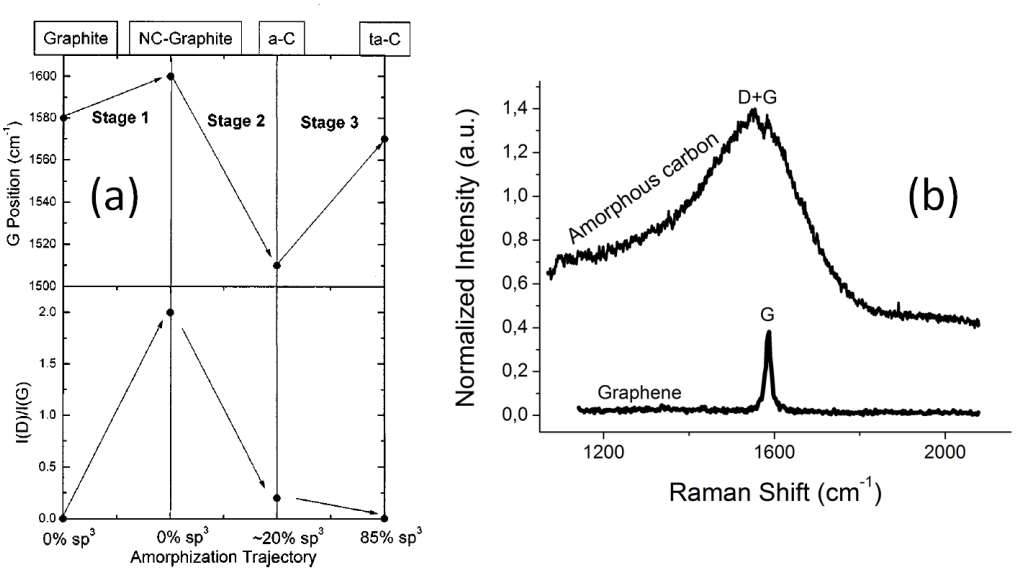

Figure 2.11: Raman characterization of the crystalline content in carbon allotropes. (a) 3-Stage model developed by Ferrari *et al.* [74]. Reproduced from [74]. (b) Raman spectra of graphene (bottom) and ta-C (top) deposited in a FCVA with an accelerating voltage of -100V.

fective materials without graphitic rings. Perfect graphene has an I(D)/I(G) ratio value equal to 0, and so does ta-C [74].

Hence, the I(D)/I(G) ratio value alone does not enable to characterize the crystalline quality of a carbon sample. Ferrari *et al.* [74] devised a three-stage model for the interpretation of carbon Raman spectra (see Figure 2.11 (a)).

a.2.1 Stage 1: from Graphite to nano-crystalline graphite

In Stage 1 (from Graphite to nano-crystalline graphite), by following an amorphization trajectory, the I(D)/I(G) ratio values increase from 0 to 2.0 (Figure 2.11 (a)). It is because defects are introduced in the initially perfect graphitic rings of graphite. The average crystal size decreases from infinity (perfect graphite) to *ca.* 2 nm (in nano-crystalline graphite). In this range of crystal sizes, the formula of Tuinstra and Koenig may be used to estimate the average crystal size L_a (in Å) [123]:

$$\frac{I(D)}{I(G)} = \frac{C(\lambda)}{L_a} \tag{2.4}$$

with C(λ) a constant depending on the wavelength (C(515.5 nm) = 44 Å).

a.2.2 Stage 2: from nano-crystalline graphite to amorphous carbon (high sp^2)

When the average crystal size decreases to sizes below 2 nm, the Stage-2 starts (from nano-crystalline graphite to a-C). As the number of available graphitic rings keeps on decreasing, the intensity of the D peak starts to decrease as well, despite an increasing amount of defects (we recall that the lattice vibrations responsible for the D peak are found in **defective graphitic rings**). I(D)/I(G) peak intensity values decrease to *ca.* 0.2 for a-C (20% sp^3, see Figure 2.11 (a)). Because of the high quantity of sp^2-bonded atoms, there still is a significant amount of graphitic rings, which explains the nonzero ratio.

In Stage 2, another equation may be used to estimate the average crystal size [74]:

$$\frac{I(D)}{I(G)} = C'(\lambda) * L_a^2 \tag{2.5}$$

with C'(λ) a constant depending on the wavelength (C'(515.5 nm) = 0.0055 $Å^{-2}$).

a.2.3 Stage 3: from amorphous carbon (high sp^2) to tetrahedral amorphous carbon (high sp^3)

When the amount of sp^3-bonded atoms relative to the sp^2-bonded atoms increases in a-C, the probability that a graphitic ring forms decreases, hence in Stage-3 (from a-C to ta-C), the I(D)/I(G) ratio values tend to decrease to 0.

In Figure 2.11 (a), the G peak position is also shown to be sensitive to the amount of crystalline content (at all stages) and to the hybridization (sp^2 or sp^3). Hence, the G peak position can be used as a means to confirm I(D)/I(G) data.

In order to determine clearly to which Stage the sample belongs to, using the I(D)/I(G) or G peak position values alone is difficult.

Fortunately, extracting the width of the peaks enables to disciminate between the 3 Stages in a non ambiguous way: as the amount of disorder increases, the G peak tends to broaden monotonically as the average crystal size decreases. The G peak of perfect graphene (or graphite) tends to be very sharp (full width at half maximum ≈ 12 cm^{-1} for high grain size graphite [124], see Figure 2.11 (b), bottom, for a spectrum of mono layer graphene) while the G peak of a-C tends to be very broad (up to ≈ 300 cm^{-1} [124], see Figure 2.11 (b) top spectrum).

a.3 Impact of the oxygen content on the Raman signal

Because most of the experiments reported in this thesis are conducted in air, it is important to assess the impact of oxygen on the Raman spectra of carbon allotropes.

At high temperatures, the oxygen interacts with the lattice and degrades it [125, 126]. This degradation can be detected in Raman spectra by an increase of the I(D)/I(G) ratio values in CNTs (Stage-1 material) [125, 126]. In the case of Stage-2 materials, a degradation of the crystalline order should translate into a decrease of the I(D)/I(G) ratio as well as the G peak position values.

However, when monitoring the position of the G peak during oxidation, another factor must be taken into account. Oyxgen atoms absorbed in the lattice during oxidation may act as hole dopants, which are known to impact the G peak position: the higher the concentration of hole dopants, the higher the frequency of the G peak [22]. Hence, for Stage-2 materials, oxidation simultaneously results in a decrease (degradation of the crystalline structure) and an increase (hole doping) of the G peak position.

a.4 Scilab extraction of Raman parameters

As discussed above, in the case of disordered carbons, we focus on the range of waveshifts from 600 to 2000 cm^{-1}.

To systematically and automatically extract values of the I(D)/I(G) ratio, I(T)/I(G) ratio, G peak position and G peak width parameter values, we fit each Raman spectrum with three Lorentzian curves and a baseline. To do so, we use Scilab [127], a free software similar to Matlab.

The code for curve fitting is provided in Appendix A (Listing A.1 page 241).

a.5 Estimation of standard errors: the Boostrap method

To estimate the standard errors due to the noise in the signal, we use the Bootstrap method [128].

a.5.1 Presentation of the Bootstrap method

Any measurement of a property of the physical world has a finite accuracy resulting in a finite, non-zero error. If this error is large, then the measurement does not describe the physical world well.

Therefore, there are two questions one must ask when trying to characterize a property of the world by measuring a parameter P [128]. 1) What estimator $\hat{P}$ should be used? 2) How accurate is the value of $\hat{P}$ to describe P?

The goal of the Bootstrap method is to answer the second question about the accuracy of the chosen estimator.

In our case, what we want to characterize is the crystalline state of textured carbon. For that, we use Raman spectroscopy. After shining light on a given sample, the spectrometer measures how many photons are bouncing back at given wavelenghts. Because the

measurement with the spectrometer is not perfect, we want to estimate the degree of accuracy of the measurement of the number of photons at each wavelength. In particular, we want to estimate the accuracies of the estimators I(D)/I(G), G peak position, G peak width, etc... that are obtained by fitting Raman spectra. The standard errors we measure *via* this technique enable us to assess whether our measurement accuracy is good enough to produce data that can be significantly interpreted.

a.5.2 Principle of the Bootstrap method

The principle of the Bootstrap method is the following: we generate random subsets of data from the Raman data obtained experimentally. Each subset contains as many data points as the initial data set, except that these data points are extracted randomly from the initial data set, resulting in some data points being present more than once, while some are not replicated in the subset.

We then fit each subset with three Lorentzian peaks for the T, D and G peaks using the code in Listing A.1, page 241 and extract values of the estimators I(D)/I(G), G peak position, G peak width, etc... We then have as many values of each estimator as there are subsets, which means we can calculate a standard deviation on these values. The standard deviation enables to estimate the accuracy of the value of the estimator to describe the "real" parameter which would be measured with a perfect instrument in perfect conditions.

a.5.3 Application and Results

We applied the Bootstrap method to estimate standard errors on the values of relevant parameters extracted from the Raman spectra. The corresponding Scilab code for generation of random subsets is provided in Appendix A (Listing A.2, page 242).

In Chapter 4, the maximum standard deviations on I(D)/I(G), I(T)/I(G) and the G peak position are 0.04, 0.02 and 4 cm^{-1}, respectively. Variations of the values of I(D)/I(G), I(T)/I(G) and the G peak position that are larger than the standard deviations cannot

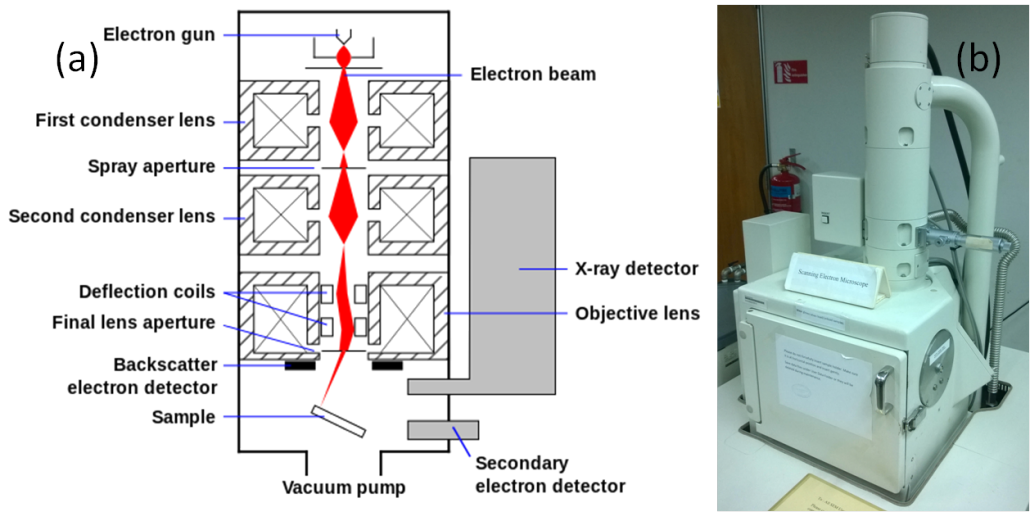

Figure 2.12: (a) Schematic of a scanning electron microscope. Source: Wikipedia. (b) The JEOL JSM-5910LV SEM used to get some pictures displayed in this thesis.

be explained by the finite accuracy of the measurement alone, therefore are significant.

b Scanning electron microscope

In some cases, optical microscopes are not powerful enough to resolve fine details at the surface of a thin film. The resolving power can be improved by changing the optics (lenses) however it is intrinsically limited by the wavelength of the light, due to the diffraction of light by small objects. Thus, even the best optical microscopes cannot directly resolve features smaller than 100 nm.

When a higher resolution is needed, material scientists use electron microscopes. Instead of using light to probe matter, these microscopes can use electrons, which have much smaller wavelengths than visible photons. Consequently, diffraction becomes an issue at much smaller sizes, and the resolution of common electron microscopes can be as small as 0.4 nm.

Scanning electron microscopes (SEM) operate under vacuum. Their main parts are (Fig-

ure 2.12 (a)):

- an electron gun that generates the electron beam

- condenser lenses that are used to focus the beam

- deflection coils enabling to move the electron beam to scan the regions of interest

- a sample holder that can move preferentially in all of space (x, y, z) and be tilted respective to the beam

- detectors able to detect particles of different energies for the different modes of operation of the SEM. The most-used mode is secondary electrons.

In this thesis, SEM images were taken primarily with two models of SEM:

- a LEO 1550 Gemini Field Emission SEM.

- a JEOL JSM-5910LV (Figure 2.12 (b)).

Often, a SEM is used in secondary electron mode, which means that the quantity of secondary electrons emitted by the surface while it is scanned, are detected and used to make an image.

Secondary electrons are emitted when a surface atom is ionized by the incident electron beam. This mode of imaging can be used to image the topography of a sample with a good resolution and depth of field.

c Transmission electron microscope

To obtain even better resolution images than SEM and achieve atomic resolution (in some cases), transmission electron microscopes (TEM) can be used.

Instead of detecting electrons reflected by the surface (like in a SEM), a TEM detects electrons transmitted through the sample. For this reason, samples must be thin (few hundreds of nm at most), and sample preparation is a critical step when conducting TEM experiments.

c.1 Factors limiting the resolution

There are two ways a TEM can be used, reflecting the dual nature of particles such as electrons, which also behave as waves at very small scales. The wavelength of electrons accelerated by a voltage V can be calculated using the equation:

$$\lambda = \frac{h}{\sqrt{2eVm(1 + \frac{eV}{2E_0})}}$$

with h the Planck constant ($6.63.10^{-34}$ m^2kg/s), λ the wavelength (in m), e the electron charge ($1.602.10^{-19}$ C), V the voltage, m the electron mass ($9.11.10^{-31}$ kg) and E_0 the kinetic energy of the electron at rest ($= mc^2 = 511keV$ with c the velocity of light in vacuum).

An electron accelerated at 80 kV behaves like a wave with a wavelength of $\approx 4.10^{-12}$ m, much smaller than the distance between atoms, hence minimizing the diffraction of the electrons by the atoms.

The main factors limiting the resolution in a TEM with an ideal incident flux of electrons (homogeneous kinetic energies of the electrons) are the wavelength of the electrons λ and the spherical aberration coefficient C_s of the objective lens [129]. The theoretical resolution limit of electron microscopes is given by the *point resolution* d_s, calculated as:

$$d_s = 0.65 C_s^{1/4} \lambda^{3/4} \tag{2.6}$$

In practice however, the incident electron flux is not homogeneous, so an extra term called the chromatic aberration C_c (because it is due to variations of the wavelength of the electrons) limiting the resolution must be accounted for. The resulting limitation in resolution is due to fluctuations in the focusing distance, such that:

$$\Delta = C_c[(\Delta V_r/V_r)^2 + (2\Delta I/I)^2]^{1/2} \tag{2.7}$$

With Δ the fluctutations in the focusing distance, V_r the acceleration voltage and ΔV_r its fluctuations, I the electron current and ΔI its fluctuations.

Consequently, to improve on the resolution of TEM, it is necessary to either accelerate the electrons with higher accelerating voltages, to decrease the spherical aberration and/or decrease the chromatic aberration.

c.2 Two imaging modes

The two ways a TEM can be used is by direct visualization of the electrons that went through the sample and by visualization of the diffracted electrons. In the case of direct visualization, the particle-like nature of electrons is used: if the incident electron beam encounters an atom, it is stopped, thus the detector below does not detect electrons at this location. On the other hand, if the electron beam encounters a void (*i.e.* a space between atoms), it goes through and the detector below detects electrons. Thus, a contrast is achieved between the locations containing atoms and those that do not.

In the case of diffracted electrons, the wave-like nature of electrons is used. The electron beam acts as a wave, and if the material is crystalline, it contains periodic arrays of atoms; multiple reflections and transmissions of the incoming wave with these arrays of atoms lead to interference phenomena, resulting in constructive and destructive interferences. The resulting diffraction pattern depends on the crystalline content of the sample, the orientation of the crystals, the distance between the crystalline planes, hence providing critical information about the material.

In the case of diffraction by reflexion, Bragg's equation can be used to calculate the incident angles for which the reflected beam interferes constructively (Figure 2.13):

$$2dsin\theta = n\lambda \tag{2.8}$$

with θ the incident angle, d the inter-planar distance and λ the wavelength of the electrons.

This reasoning can be applied to transmitted electron beams as well: electron beams are scattered multiple times by the atomic planes until they are transmitted, resulting in constructive and destructive interference patterns. These patterns can be detected,

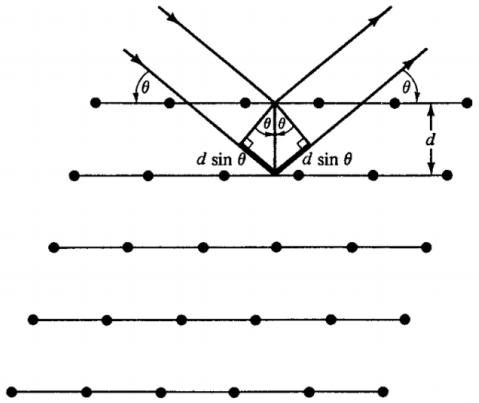

Figure 2.13: Schematic showing parallel atomic planes separated by the distance d, onto which an incident electron beam is reflected with an angle θ. Reproduced from `http://instructor.physics.lsa.umich.edu/adv-labs/Electron_Diffraction/electron_diffraction2.pdf`.

giving information about the crystalline structure of the matter that has been crossed. For example, by examining the angles θ at which constructive interference occurs, and if one knows the wavelength λ of the electrons that are diffracted, one can extract the inter-plane distance d by using Equation 2.8.

Typically, both the direct visualization of the image and the diffraction patterns are used when characterizing a crystalline material (Figure 2.14).

Like a SEM, a TEM contains an electron gun, guiding optics, a sample holder and detectors. The main difference is that the detector is placed "below" the sample on the path of the electron beam which is emitted above the sample (Figure 2.15).

While a very fine sample (at most few hundreds of nm in thickness) is always needed to let the electrons pass through it, the preparation of the sample depends on the needs. In the case of carbon thin films deposited on top of silicon, there might be a need to see the atomic structure in plane view or in cross-sectional view (see Figure 2.14). In plane view, the sample is seen "from above" (top view), while in cross-sectional view, a cross-section of the sample is observed.

In this thesis, we observe cross-sections of thin films. We extract a fine lamellae from the

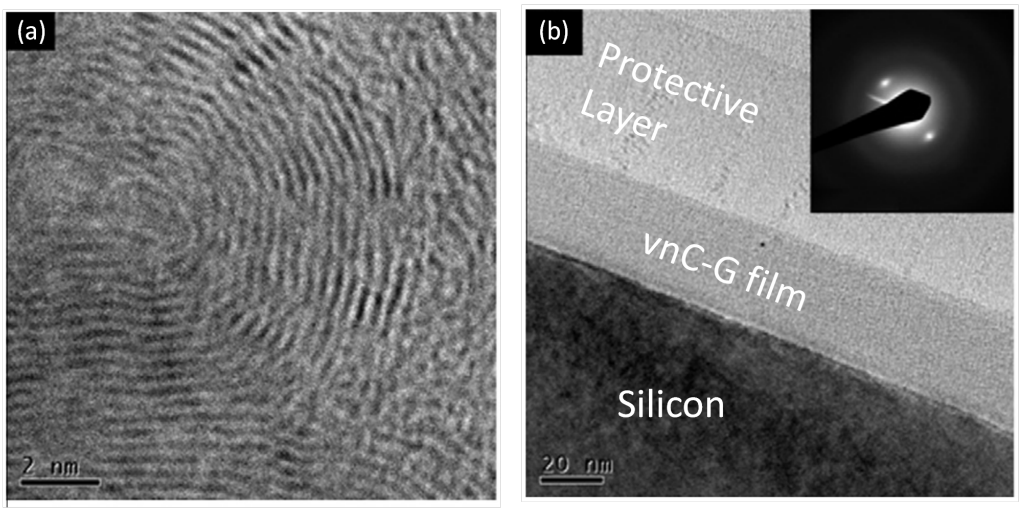

Figure 2.14: (a) Plane-view HRTEM image of a textured carbon film on a silicon substrate showing the graphitic planes. (b) Cross-section TEM image of a textured carbon film on a silicon substrate. *Inset*: SAED pattern showing two (002) diffraction peaks. Reproduced from [57].

bulk of the film using a focused-ion-beam (FIB). The steps involved in the preparation of cross-sections *via* a FIB are:

- deposition of a protective layer (seen in Figure 2.14 (b)) on top.

- milling of a large trapezoid trench and extraction of a thick lamellae.

- fine milling of the lamellae until it is thin enough for TEM imaging.

The TEM/FIB equipments used in this thesis are:

- a FIB/Scios dual beam microscope for preparation of the samples of Chapter 3. A Titan-Themis electron microscope operating at 200 kV, equipped with a Cs probe corrector and a SuperX detector, is used to characterize the samples of Chapter 3.

- a FIB Helios 450S at 30 kV for coarse milling and 5 kV for the final fine milling for samples studied in Chapter 4. Bright field and HRTEM analysis are conducted at 300 kV with a FEI Titan TEM.

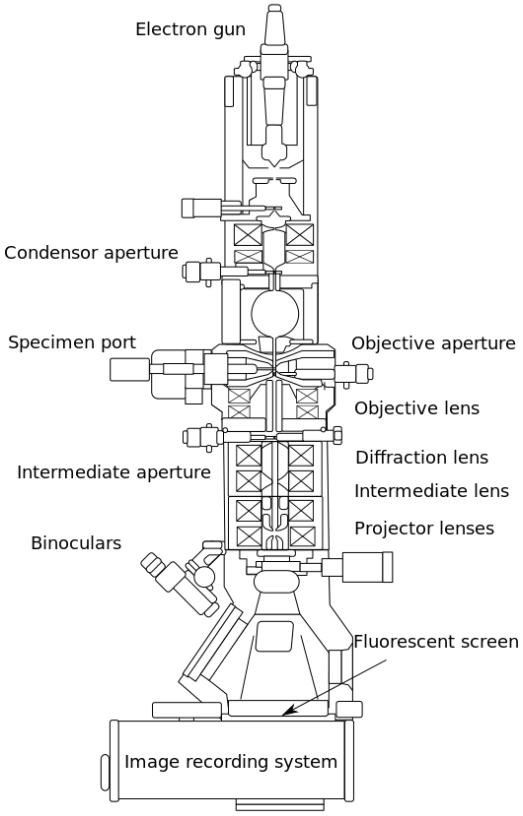

Figure 2.15: Schematic of a transmission electron microscope. Source: Wikipedia.

d Atomic force microscope

Contrary to the case of optical and electron microscopes, the atomic force microscope does not rely on an energetic beam to probe the state of matter. Instead, a cantilever terminated by a micrometer-sized tip and controlled by piezoelectric motors interacts with the surface, and this interaction is monitored by a laser beam.

The laser beam is aimed at the metallic cantilever and is reflected by it. The reflected light is detected by four photodiodes arranged as corners of a square. When the cantilever is deflected, either up or down, either the upper or lower diodes receive more reflected light.

This change in signal is recorded and the piezoelectric motors are used to move the cantilever up or down, back to its equilibrium state. Hence, by monitoring the height of the cantilever as a function of position, an image can be drawn.

There are several modes of functioning for the interaction between the tip and the surface. We use two in particular:

- the contact mode. The tip is constantly touching the surface, with a force previously set by the user. When the cantilever is scanned over the desired region, the deflection of the cantilever is measured by the reflection of the laser beam onto the photodiodes. The deflection can be translated into height data, because a larger deflection means a higher feature. Moreover, thanks to a feedback loop, the piezoelectric motors can be used to adjust the height of the cantilever depending on the height of the features.

- the tapping mode. The cantilever is not constantly in contact with the surface. Instead, it vibrates at its resonant frequency (typically on the order of few tens of kHz). When it interacts with the surface, it leads to a change in the amplitude of the vibrations, which is recorded by the laser. The data on the amplitude of the vibrations is used to draw a 2D map of the height of the features.

In this thesis (Chapter 3 and 5), the AFM we use is an Asylum Research Cypher S (Figure 2.16 (b) and (c)) in tapping mode for topography measurement. When used to obtain electrical information, we use the AFM in contact mode with a Pt-coated silicon

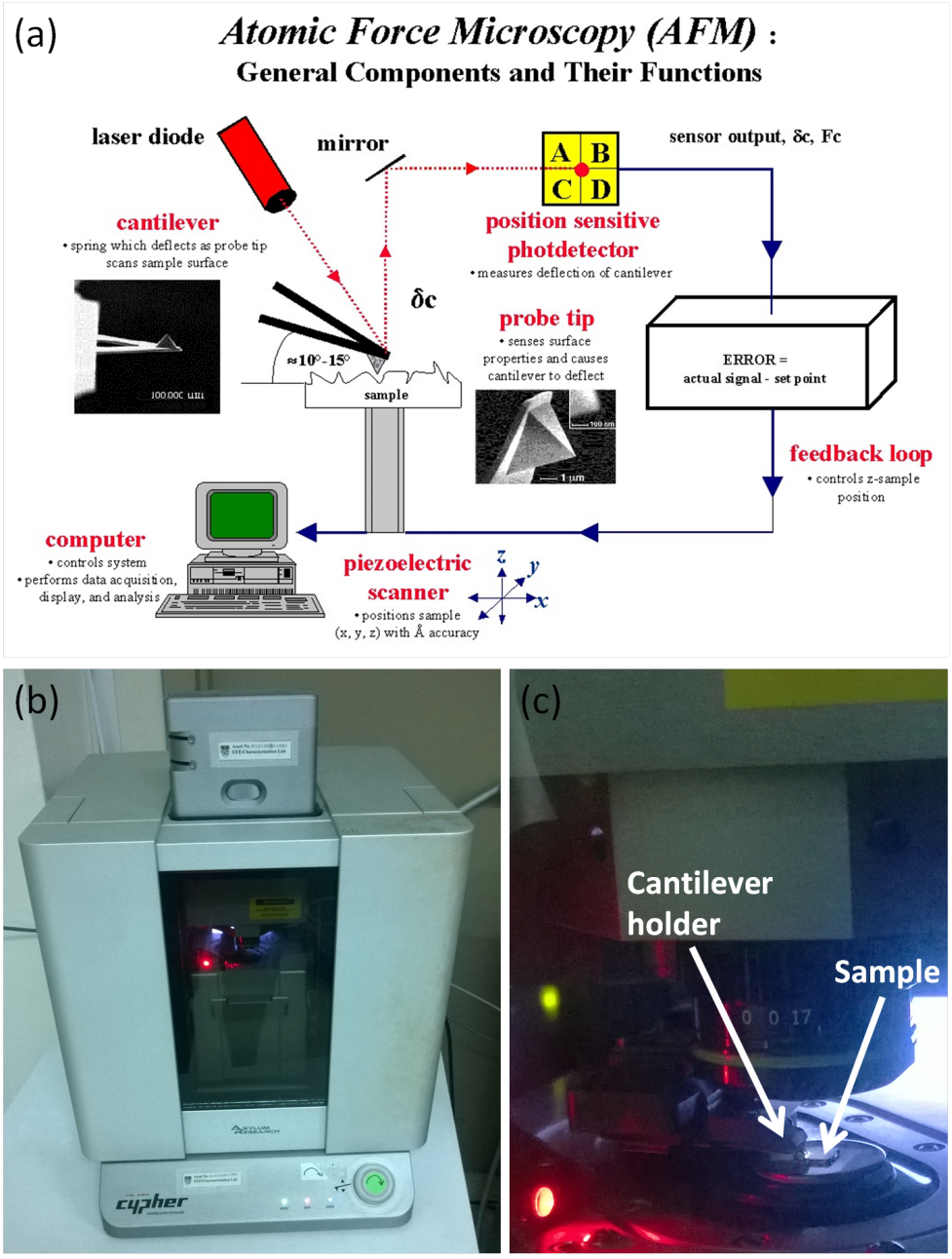

Figure 2.16: (a) General components of an AFM. Source: http://blog.nus.edu.sg/me4105precisionengineering2012/state-of-the-art-research/microscopy-scanning-electron/. (b) Asylum Research Cypher S. (c) Zooming on the cantilever holder.

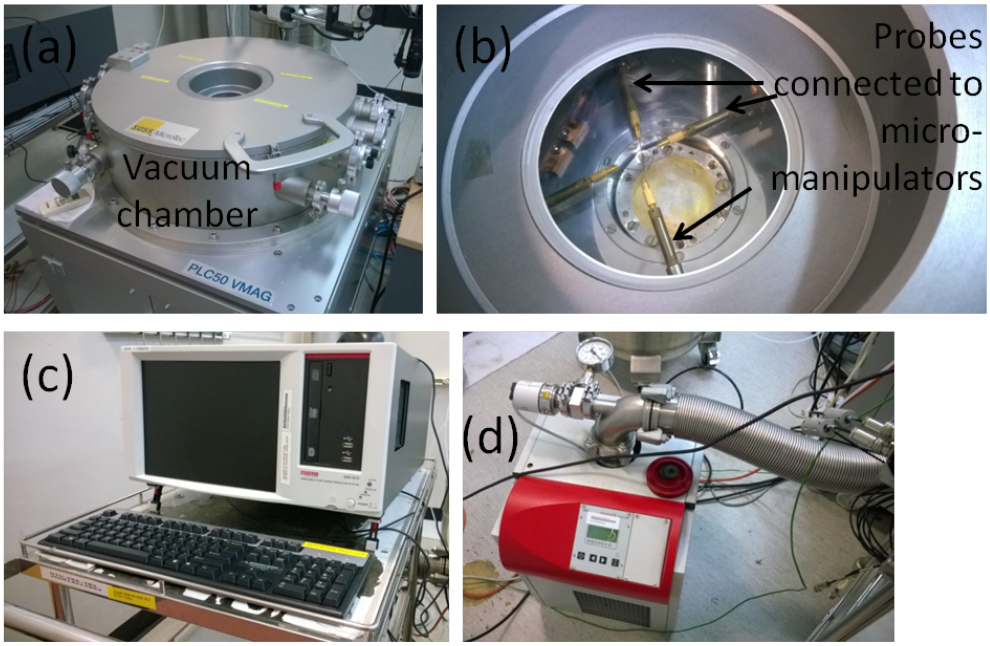

Figure 2.17: The probe station used in Chapter 5. (a) The chamber, sealed for controlled environement. (b) Inside the chamber: four probes are connected to micro-manipulators. (c) The acquisition system. (d) The pump, used to create vacuum in the chamber.

cantilever.

e Keithley 4200-SCS semiconductor characterization system

In Chapter 5, a Keithley 4200-SCS Semiconductor Characterization System is used to apply voltages and measure currents both in air and in vacuum (Figure 2.17). In vacuum, the pressure is typically $\approx 2.10^{-5}$ mBar. It is obtained after several purging cycles with nitrogen.

The probes through which the current flows are attached to micromanipulators enabling a precise control of their movements (Figure 2.17 (b)).

Chapter 3

Continuous laser annealing of textured carbon

3.1 Goals

Recently, direct laser writing has been used as a technique to draw patterns in carbon allotropes. In particular, pulsed lasers have been used to graphitize amorphous carbon [57, 84] or reduce graphite oxide [130–132].

Considering the fact that pulsed lasers are more expensive than continuous-wave (CW) lasers, it is surprising that the literature on pulsed-laser annealing is more abundant than that on CW annealing . Other drawbacks of pulsed laser annealing include the high complexity of the energy dissipation process (because short excitation timescales cause exotic nonlinear effects that are difficult to predict [7]) and very high peak power densities (because the energy must be deposited in the time of the pulse, shorter pulses lead to larger powers for the same deposited energy) which may lead to degradations. Lastly, pulsed-laser annealing has not been showed to induce amorphization of crystalline carbon, impeding the development of applications such as reversible optical memories [133].

In comparison, CW lasers enable the deposition of optical energy in a more gentle manner, as timescales are much longer, resulting in more easily understood phase and morphology changes. Taking advantage of this simplicity, research groups compare the results of CW laser-annealing experiments with those of thermal annealing experiments [75, 76]. Moreover, both the graphitization of amorphous carbon [73, 75, 76] and reducing of graphite oxide [134, 135] have also been demonstrated with CW lasers. And contrary to pulsed-lasers, there is some evidence that CW laser exposure of crystalline carbon may lead to amorphization [75], possibly opening the way toward optical data storage with carbon allotropes even though, for performant data storage applications, pulsed lasers are preferred because they enable fast data writing and reading.

Despite the growing literature on CW laser-annealing of carbon allotropes, there are still several areas that need to be clarified.

First of all, despite evidence of structural changes induced by CW laser-annealing, it is not clear what mechanisms are driving the phase changes from amorphous to crystalline and from crystalline to amorphous, and the matter removal that is observed at high energy densities. For applications, it is critical to estimate the temperatures reached during these processes, and to know what is the impact of the working environment (for example, for aerospace applications).

Secondly, despite indirect (Raman) evidence of a transformation from amorphous carbon to graphitic carbon [73, 75, 76], it is not confirmed that this transformation translates into an enhanced electrical conductivity, which would be critical for a number of applications (*e.g.* drawing of conductive lines).

Finally, and also critically for applications, we would like to assess whether the surface morphology is drastically modified by the annealing process. One advantage of CW laser annealing is that damaging effects such as sputtering and phase explosion [41] are not expected to occur as the energy is deposited in long timescales.

A better understanding of phenomena occuring on long timescales, and especially of the amorphization mechanism, should help us in determining whether an optically-controlled carbon based memory can be developed.

3.2 Crystalline structure of as-deposited textured carbon

A titanium layer was deposited onto a silicon substrate using an e-beam evaporator. Its thickness was measured to be $\approx$ 100 nm. Then, a textured carbon thin film was deposited onto the titanium layer using a FCVA system (see Section a, page 78 for a description of the FCVA) at a pressure of $\approx 5.10^{-5}$ Torr for a duration of 3 minutes and 58 s. The accelerating voltage applied to the substrate was -300V. The resulting textured carbon film was $\approx$ 140 nm thick.

a Transmission electron microscopy images

TEM and high resolution TEM (HRTEM) images showing the structure of pristine (as-deposited, before annealing) textured carbon are revealed in Figure 3.1. The structure is composed of a semi-crystalline phase, roughly 100 nm in thickness, capped by a mostly amorphous phase roughly 40 nm in thickness. In the semi-crystalline phase (labelled "G" in Figure 3.1 (a)), highly graphitic regions (Figure 3.1 (b)) are separated from each other by amorphous regions. The graphitic planes of the "G" region are arranged perpendicular to the substrate.

488 nm Raman spectra of the pristine textured carbon film yield I(D)/I(G) = 1.02 $\pm$ 0.03, x_G = 1557 $\pm$ 2 cm^{-1} and $FWHM_G$ = 254 $\pm$ 6 cm^{-1}. The width of the G peak is much larger than 100 cm^{-1}, suggesting that the characterized carbon structure belongs to either Stage 2 or Stage 3 of the 3-Stage model proposed by Ferrari *et al.* [74, 124]. The detected average crystal size is below 2 nm (Stage 2 or Stage 3 materials have average crystal sizes below 2 nm), which is an unexpected result considering the HRTEM data showing crystals much larger than 2 nm.

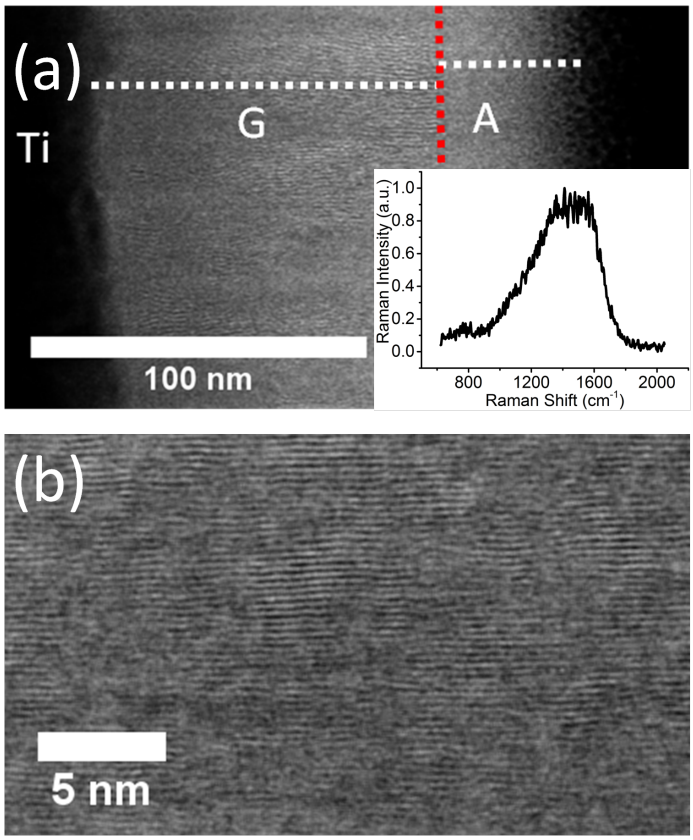

Figure 3.1: TEM characterization of as-deposited textured carbon. (a) Dark-field STEM micrograph showing two sublayers within the un-annealed textured carbon film: a 40 nm-thick amorphous layer ("A") on top of a 100 nm-thick graphitic layer ("G"). Inset: Raman spectrum of as-deposited textured carbon. (b) HR-STEM Dark Field image on a zoomed area from the graphitic "G" layer illustrating the parallel graphitic planes.

b Penetration depth of the 488 nm photons

To understand this discrepancy between the TEM and Raman data, we estimate the penetration depth of the Raman photons. As the film is composed of two phases at different depths in the thin film (from 0 to 40 nm, "A" and from 40 to 140 nm, "G"), a significantly larger fraction of Raman signal could come from the surface layer, which would explain the discrepancy.

One can estimate the penetration depth of light into matter using the Beer-Lambert equation [136]:

$$I(z) = I_0 e^{-\alpha(\omega)z} \tag{3.1}$$

with z the depth of penetration, $I(z)$ the intensity of the light reaching the depth z, I_0 the incident light intensity, $\alpha/2$ the attenuation constant which depends on the angular frequency ω and can be calculated from the imaginary part of the refractive index $k(\omega)$:

$$\alpha(\omega) = 2 * \frac{\omega k(\omega)}{c} \tag{3.2}$$

with c the speed of light in vacuum ($\approx 3.10^8$ m/s).

Hence, by calculating $e^{-\alpha(\omega)z}$, one can estimate the fraction of light $I(z)/I_0$ of angular frequency ω reaching the depth z. The value of $1/\alpha$ gives an estimate of the depth at which 37% of the light intensity remains (*i.e.* has not been absorbed); $1/\alpha$ is called the penetration depth.

Because the crystalline structure of carbon nearest the laser source is closer to that of a-C than to that of graphite (Figure 3.1 (a)), we use estimated values of the imaginary part of the complex index of refraction for a-C at 488 nm [137] (see Table 3.1).

Calculated penetration depth values are typically much smaller than the thickness of the film ($\approx$ 140 nm) with an average of $\approx$ 30 nm (Table 3.1). Therefore, in the considered

Table 3.1: Values of the imaginary part of the index of refraction extracted from [137], and calculated penetration parameters for 488 nm (blue) radiation. ω = 3.86.10^{15} rad/s.

Temperature (°C)	k(ω)	$\alpha(\omega)$	$1/\alpha(\omega)$ (nm)
25	1.003	2.58.10^7	39
200	1.633	4.20.10^7	24
400	1.001	2.58.10^7	39
600	2.347	6.03.10^7	17

conditions (working wavelength of 488 nm, temperatures ranging from 25 to 600 °C), most of the light is absorbed before it reaches half of the depth of the film.

Consequently, most of the photons received by the Raman spectrometer have interacted with the upper-most layer of the film, that is, the "A" layer (Figure 3.1 (a)).

In the capping layer "A", no traces of graphitic crystals are observed in HRTEM images. On the other hand, very large crystalline domains are found in the layer "G" (Figure 3.1 (b)).

Thus, in the 3-Stage model proposed by Ferrari *et al.* [74], the Raman signal of the "A" layer can be interpreted according to Stage 2 or 3, and the "G" layer according to Stage 1. Stage 1 carbon allotropes like the "G" layer have Raman spectra comprising two well-defined D and G peaks, and the full width at half maximum of the G peak is smaller than $\approx$ 100 cm^{-1} [124]. On the other hand, Stage 2 and 3 carbon allotropes like the "A" layer have Raman spectra comprising two overlapping D and G peaks, with large G peak FWHMs (larger than 100 cm^{-1}, see for example the spectrum in the *inset* of Figure 3.1 (a)).

Because of the limited penetration depth of the photons into the structure, the contribution of the "A" layer to the Raman signal is much larger than the contribution of the "G" layer. Hence, it is not surprising that the Raman spectrum of un-annealed textured carbon resembles that of a Stage 2 or 3 material (like "A"), rather than that of a Stage 1 material (like "B").

3.3 Matter removal and amorphization

a Matter removal

After measurement of the output power (see Section a.1, page 96), the sample was placed normally to the laser beam on the piezoelectric stage of the Raman WITec setup (see Figure 2.10) and annealed in ambient conditions.

First, we focused the laser beam onto the surface, at the desired location, at very low powers. Then, we set the power to the desired value, and started annealing the thin film. During the annealing process, a fraction of the light was reflected and collected by the spectrometer; this enabled the *in-situ* monitoring of Raman spectra. We acquired a Raman spectrum every 15 seconds during the annealing process. Faster acquisition was technicaly feasible, however we avoided it as it leads to large noise levels.

When the annealing experiment was over, we turned off the mechanical shutter, hence blocking the laser light, and decreased the laser power. We waited for 10 minutes before opening the shutter again and obtaining new, lower power Raman spectra. The goal of this last step was to uncover whether the Raman signal obtained at the end of the annealing experiment is similar to that obtained after the film has had time to cool down. This proves useful to probe annealing temperatures (as the G peak frequency depends on the temperature [122]) or structural changes occurring during the cooling.

Visual inspection of the laser-annealed surface reveals a disk (Figure 3.2, (a)). Using an AFM, we found that a large amount of matter had been removed during the annealing process (Figure 3.2 (b)). A deep crater is present in the middle (black region circled by a white dashed line in Figure 3.2 (b)), surrounded by a slight bulge (bounded by the two dashed lines in Figure 3.2 (b)).

By characterizing several spots annealed for different amounts of time, we found that the depth of the craters is nearly linearly dependent on the annealing time (Figure 3.2 (c)).

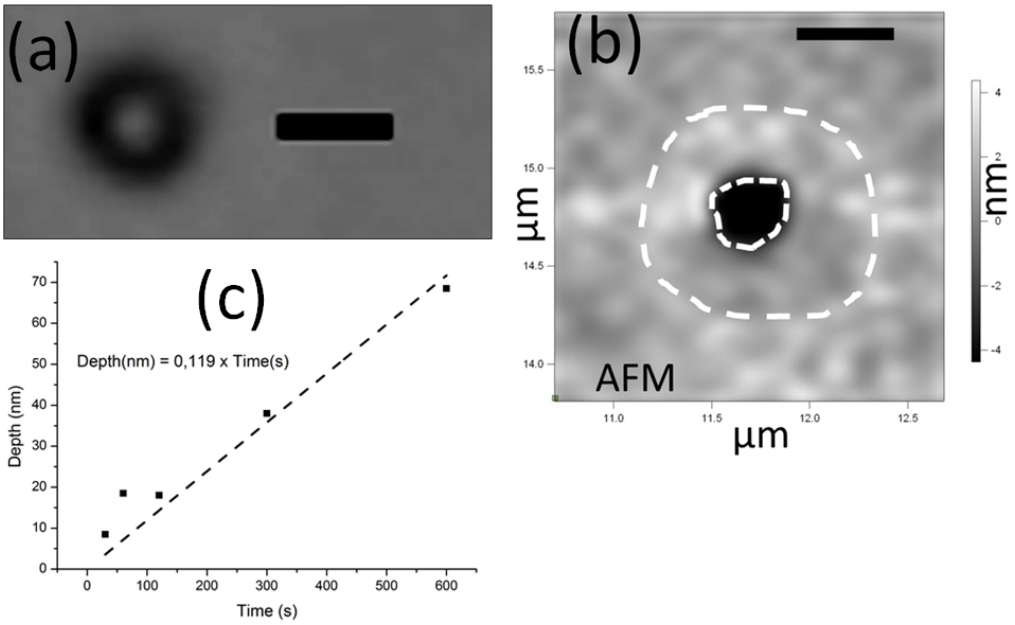

Figure 3.2: Morphology of laser-annealed textured carbon. (a) Optical image (scale bar 1 μm) of a laser-annealed region with energy density $5.9.10^6$ J.mm^{-2}. (b) AFM 2D height image showing a crater (black surrounded by a white dashed line) and a surrounding bulge (marked with a white dashed line) of a laser-annealed region with energy density $1.7.10^7$ J.mm^{-2}. (c) Measured depths as a function of time.

TEM images of two annealed regions confirm the loss of matter (Figure 3.3). In some cases, the matter removal process is found to be efficient enough to remove all of the carbon, down to the titanium layer (Figure 3.3 (c)).

b Amorphization

HRTEM imaging enables to directly visualize the structure of the laser-annealed film. A careful examination of the TEM data shows that during the annealing process, the amount of amorphous matter tends to remain constant, as the frontier between the "A" and "G" layer progresses toward the substrate (Figure 3.3 (b)). This observation implies that the CW laser-annealing process tends to disrupt the crystalline order of the "G" layer, leading to an increasing "A" to "G" fraction as the "G" layer gets thinner during the matter removal process while the thickness of the "A" layer remains roughly constant.

By examining the evolution of Raman spectra *in-situ* during CW laser-annealing, we find that, for the first $\approx$ 1,100 first seconds, the evolution of the structure is correlated with a trend for the I(D)/I(G) ratio values and for the G peak FWHM values: while the I(D)I(G) values decrease (Figure 3.4 (a)), the $FWHM_G$ values increase (Figure 3.4 (b)). Both these trends are expected from the amorphization process. In fact, amorphizing a Stage 2 (or 3) material leads to decreasing I(D)/I(G) values and increasing widths of the peaks [74].

3.4 Graphitization

After reaching a minimum at $\approx$ 1,100 s, both the I(D)/I(G) and G peak position (Figure 3.4 (a)) values increase, while the G peak FWHM values suddenly decrease (Figure 3.4 (b)). These three indicators all point to a graphitization process of the Stage 2 (or 3) material.

By studying the evolution of the Rayleigh scattering intensity as a function of time (Figure 3.4 (c)), we discover that this event occurs concurrently with a drastic increase in

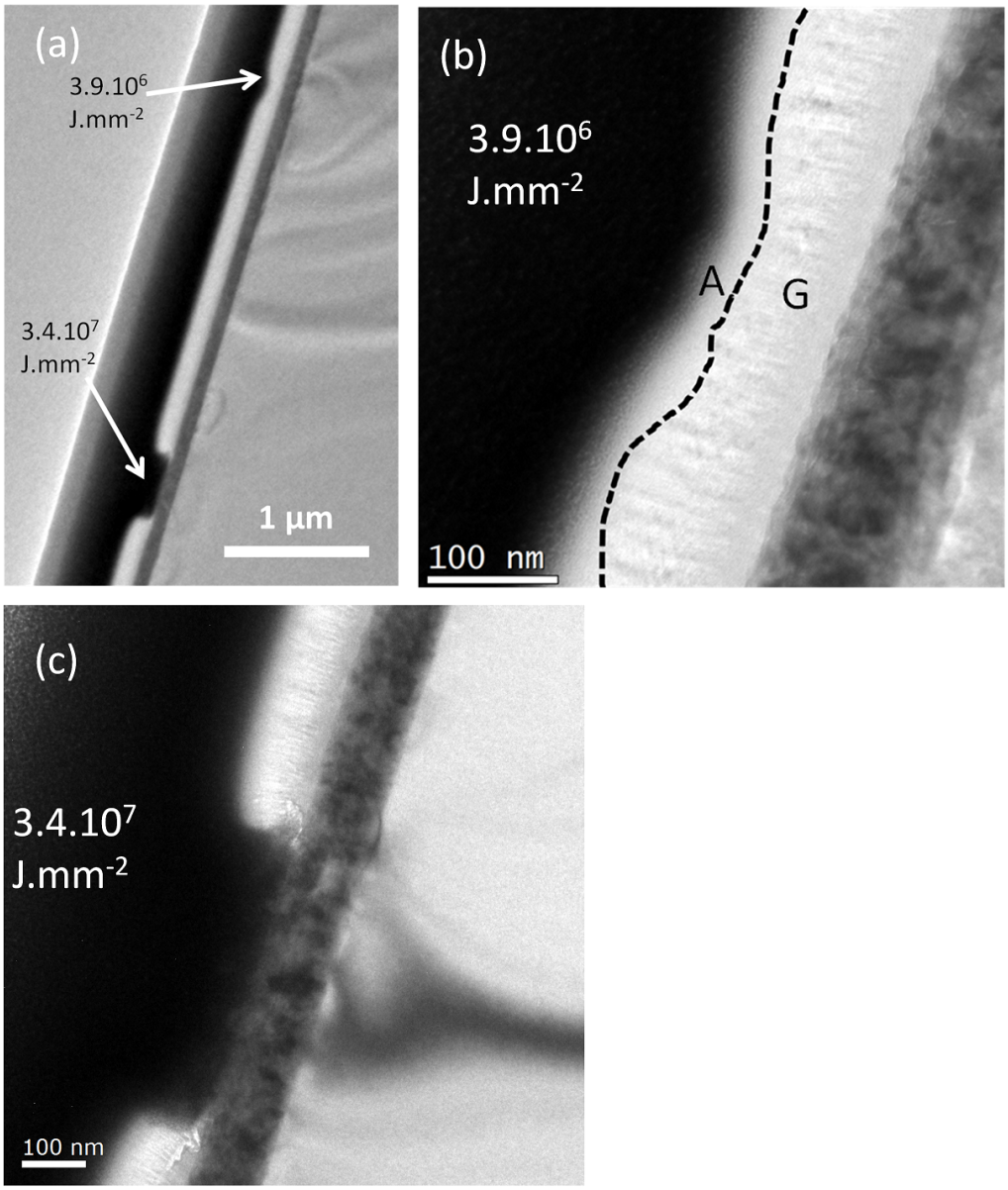

Figure 3.3: (a) Cross-sectional TEM micrograph showing the two craters that have been created by laser-annealing corresponding to two different power densities and durations. (b) TEM micrograph showing the structure of the crater created by annealing with energy density $3.9.10^6$ J.mm^{-2}. The two "G" and "A" sublayers are visible. (c) TEM micrograph showing the structure of the crater created by annealing with energy density $3.4.10^7$ J.mm^{-2}.

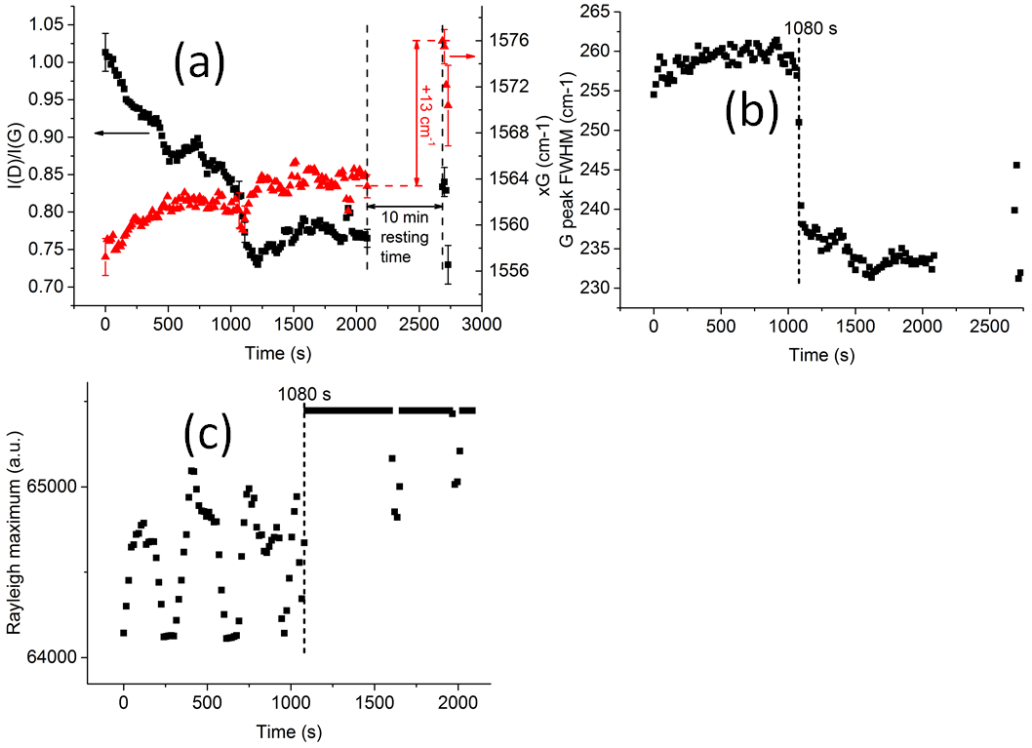

Figure 3.4: (a) Evolution of the I(D)/I(G) ratio (black squares) and G peak position values (red triangles) as a function of time for a film annealed at 16 kW.mm^{-2}. The last four spectra (after 10 min resting time) are taken with much lower Raman power densities to avoid inducing further structural changes. (b) Evolution of the G peak FWHM as a function of time for the same annealing experiment. (c) Evolution of the maximum of the Rayleigh peak as a function of time for the same annealing experiment.

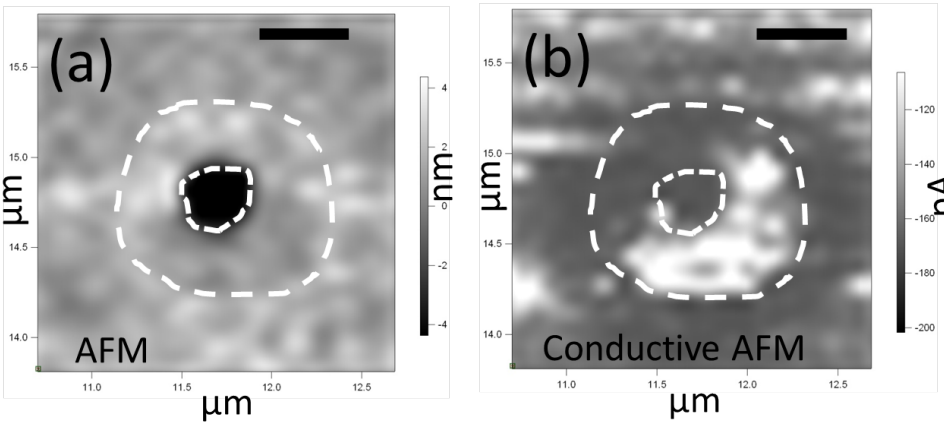

Figure 3.5: conductive AFM data suggest that sp^2 clustering takes place around the crater. ($1.7.10^7$ $J.mm^{-2}$) (a) AFM image. (b) c-AFM image of a laser-annealed crater showing that the highest conduction regions are at the location of the bulge surrounding the hole.

reflectivity of the sample. This sudden increase in reflectivity suggests that at 1,100 s, most of the carbon at the center was removed, effectively uncovering the highly reflective titanium layer, as shown in Figure 3.3 (c).

While most of the laser light was reflected back to the spectrometer, part of the incident light, at the periphery, was absorbed in the surrounding carbon, and the evolution of Raman spectra after 1,100 s enables to probe phenomena occurring there. Thus, the Raman data support a graphitization process occurring in the carbon surrounding the center. CW laser-induced graphitization and its impact on Raman data have already been reported [73, 75, 76]. Therefore, we can conclude from the data discussed so far that while high energy densities lead to matter loss and amorphization, lower energy densities lead to graphitization.

Laser-induced graphitization is interesting for applications such as the drawing of conductive lines in an insulating material. Therefore, we characterized the electrical properties of the laser-annealed film by obtaining a conductivity map of the carbon film with a conductive AFM. The conductive atomic force microscopy data (see Figure 3.5 (b)) show that the hole is surrounded by a conductive region.

A localized conductivity enhancement at regions surrounding the craters was repeatedly

and consistently found after annealing. Moreover, when comparing AFM data with c-AFM data (Figure 3.5 (a) and (b)), we find no evidence of matter loss in the region where the conductivity is enhanced. This discounts the hypothesis that the conductivity enhancement could be due to a smaller thickness of carbon.

On the contrary, there appears to be more matter, as the AFM data show a small bump at the location where the conductivity is enhanced (Figure 3.5 (a)). This localized bump surrounding the hole is reminiscent of a study by Teo *et al.* [58], in which a similar bump was assigned to a graphitization process resulting in a smaller density of the graphitic material.

Thus, conductive AFM and AFM data strongly support the hypothesis that graphitization occurs at the periphery of the annealed region.

Nevertheless, HRTEM images do not enable the direct visualization of graphite crystals at the periphery of the beam (Figure 3.3 (b) and (c)).

Thus, we suggest that the process responsible for the detected changes in the Raman spectra, the density and the electrical conductivity is the formation of sp^2 clusters, rather than a complete formation of graphitic planes. sp^2 clustering is known to lead to an enhancement of the electrical conductivity of amorphous carbon [72]. During thermal annealing, sp^2 clustering was shown to occur before graphitization (see Section b.1.1, page 56).

3.5 Amorphization and matter loss by oxidation

To understand the mechanisms behind all the changes discussed above (matter loss, amorphization, graphitization), it is of interest to estimate the temperatures attained in order to determine the state of the matter during these transformations. Of particular interest is the question of whether these transformations occur in the solid or the liquid

state.

a State of the titanium layer

After annealing, the underlying titanium layer is found to be nearly undamaged, even when the carbon layer is fully removed (Figure 3.3 (c)). Considering the fact that melting or sputtering of carbon should occur at temperatures higher than the melting point of carbon ($\approx$ 4,450 K [138]), both of these processes should lead to significant degradations in the underlying titanium layer (the melting point of titanium is much lower, at $\approx$ 1,941 K). Thus, the removal of matter most likely does not occur through melting or sputtering of carbon. Temperatures much larger than 1,941 K should not be reached near the titanium layer, therefore all the changes discussed above must occur in the solid state.

b Estimation of the annealing temperature

Thanks to our *in-situ* Raman spectroscopy measurements, we may provide an estimate of the temperature reached during laser annealing.

In fact, when the temperature increases in carbon allotropes, it causes a change in the vibration frequency of the phonons associated with the G peak [139, 140]. Consequently, the G peak frequency can be used as a thermometer [122], and there is a linear dependence between the frequency and the temperature, with a coefficient of -0.013 cm^{-1}/K. Using the G peak frequency as a means to estimate the temperature is a valid approach only if no other phenomenon impacting the G peak frequency occurs in the meantime (such as hole doping or mechanical strain [22]).

Here, during the 10 minutes of cooling following the annealing process, the G peak frequency is found to increase drastically, with a difference of 13 cm^{-1} (Figure 3.4 (a)). Calculating an estimate of the temperature by applying the linear coefficient of -0.013 cm^{-1}/K gives a result ΔT = 1,000 K, suggesting that during the annealing process the temperatures rises to $\approx$ 1,300 K.

However, as we will see below, we cannot entirely rule out the influence of other parameters such as hole doping. But the difference in the concentration of dopants due to cooling for ten minutes and its impact on the G peak frequency should be rather limited. Moreover, re-crystallization effects during cooling, which are suggested by a slight increase in the I(D)/I(G) values (Figure 3.4 (a)), may also be responsible of a shift of the G peak to higher values during cooling. Thus, re-crystallization effects may lead to an **over-estimation** of the temperature reached during laser annealing.

Overall, the G peak frequency shift during cooling tends to confirm our hypothesis that the changes observed during annealing are occurring at much lower temperatures than the melting temperature of carbon.

c A mechanism for matter loss and amorphization in the solid state: oxidation

Thus, drastic changes in the structure (amorphization, graphitization) and surface morphology (matter loss) of the textured carbon thin film occur in timescales on the order of minutes, in the solid state and at temperatures much lower than the melting point of carbon.

As the experiments are conducted in air, these transformations can be aided by the presence of oxygen. Gaseous oxygen (O_2) can react in two ways with carbon: it can react with surface C atoms, immediately forming gaseous CO_2 molecules (hence removing carbon atoms from the film), or it can be absorbed by the carbon lattice (possibly disrupting its order) and eventually form gaseous CO molecules [141].

These processes can occur at temperatures much lower than the melting point of carbon. For example, in a study by Liu *et al.*, the oxidation of graphene is found to start at temperatures of 450°C (monolayer graphene) and 600°C (three-layer graphene, similar to bulk graphite). In the same study [142], it is found that the oxidation process strongly hole dopes the carbon structure. A strong hole doping should have an impact on the values of the G peak frequency [22].

d Anomalous G peak frequency increase

A larger concentration of holes in a carbon allotrope leads to a rise of the frequency of the G peak [22]. During *in-situ* Raman characterization, we observed a continuous rise in the frequency of the G peak **that is unexpected if one considers only the structural changes** effectively occurring (amorphization). In fact, following the 3-Stage model of Ferrari *et al.* [74], the continuous rise of the G peak suggests that a graphitization process is taking place, while both the I(D)/I(G) (decreasing) and $FWHM_G$ (rising) data suggest otherwise (amorphization), as discussed above in Section b, page 121.

Therefore, we propose that this "anomalous" G peak frequency rise is due to the hole doping by oxygen atoms induced during the laser-annealing process [142].

Hence, we propose that the transformations observed here are driven by oxidation processes (matter loss by emission of gaseous CO and CO_2, amorphization by absorption of oxygen atoms).

A direct means to test this hypothesis is through the acquisition of energy dispersive X-ray spectroscopy (EDX) maps of the oxygen content in the cross-sections of the films that we obtained for TEM characterization.

e EDX characterization of the oxygen content

We conducted EDX experiments on two craters formed by the absorption of $3.4.10^7$ J.mm^{-2} and $3.9.10^6$ J.mm^{-2} (Figure 3.6).

Figure 3.6 C) shows the oxygen content maps on the small and big craters. A higher oxygen content was detected at the centers of energy for both the small and big craters. In the small crater, oxygen was absorbed in the depth of the carbon film, to depths as large as $\approx$ 30 nm. In the big crater, carbon was removed down to the titanium layer, as already observed in TEM images and confirmed by the carbon elemental map (Figure 3.6 B)). The oxygen elemental map shows that a significant quantity of oxygen atoms has been absorbed at the surface of the titanium layer, strongly suggesting that the titanium layer has been oxidized at its surface. The fact that titanium is oxidized helps explaining why no conductivity enhancement is observed at the center of the craters (*e.g.* Figure 3.5 (b)) even when all the carbon is removed.

Line scans enable to quantify the amount of oxygen that has been adsorbed by carbon during the laser-annealing process. We find that in the small hole, the oxygen content rises from 5% to $\approx$ 20% (Figure 3.6 E)).

Thus, EDX oxygen maps directly confirm the fact that oxidation is occurring during CW laser annealing of textured carbon films. Oxidation explains the matter loss process (as gaseous CO and CO_2 molecules are created, each removing one C atom) and can also

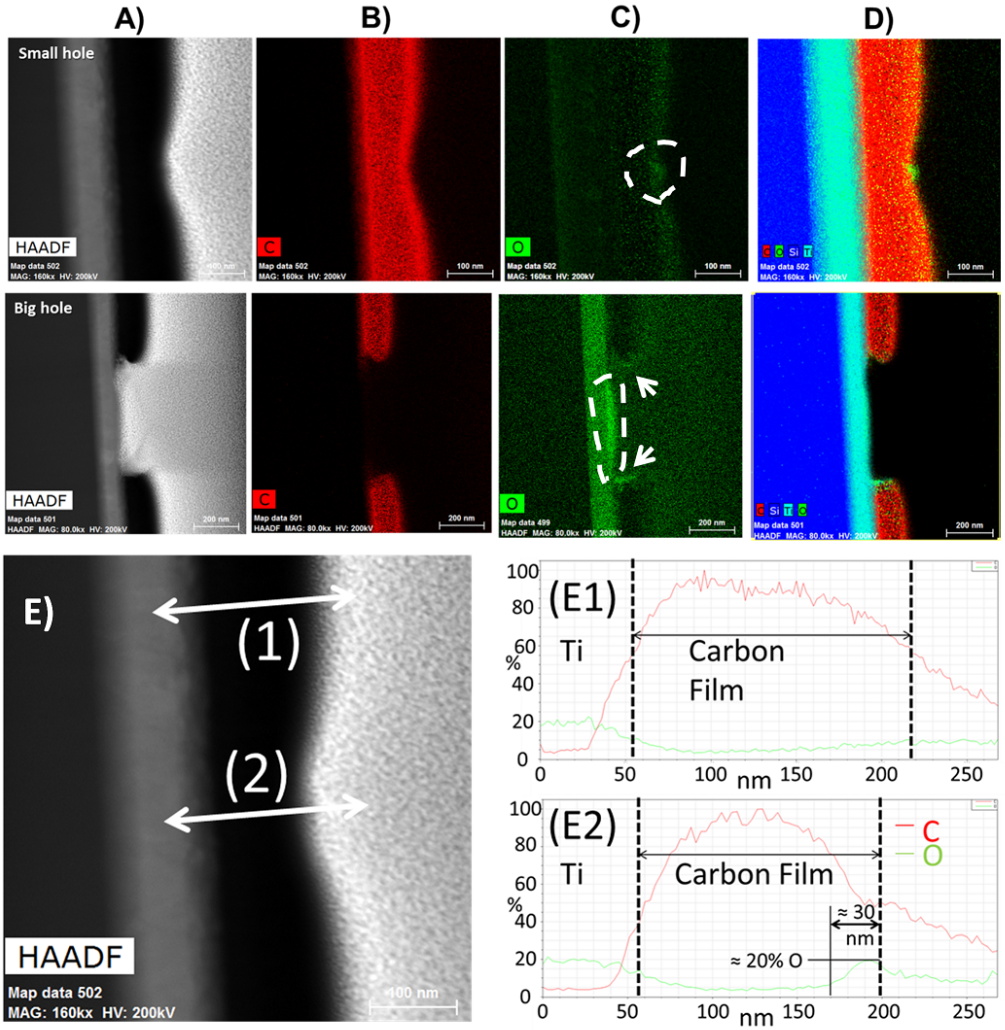

Figure 3.6: EDX chemical mappings on two craters to study the oxygen concentration. Top row: $3.9.10^{6}$.mm^{-2}. Bottom row: $3.4.10^{7}$.mm^{-2}. A) HAADF-STEM micrographs. B) Carbon elemental map. C) Oxygen elemental map. D) Relative map showing the carbon, silicon, titanium and oxygen distributions. E) EDX-STEM line scan analysis on two different positions, far and close to the beam center, for the spot annealed with an energy density of $3.9.10^{6}$ J.mm^{-2}. (E1) Carbon (in red) and oxygen (in green) concentrations recorded along the white arrow labeled (1). (E2) Carbon (in red) and oxygen (in green) concentrations recorded along the white arrow labeled (2).

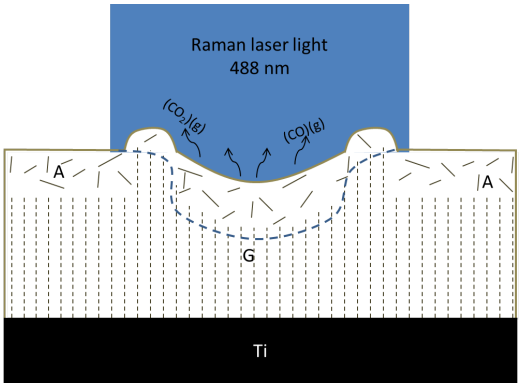

Figure 3.7: Schematic showing the processes occurring during continuous wave laser annealing including graphitization, amorphization, matter loss, oxygen doping and oxidation.

explain the amorphization process. In fact, the oxidation depth ($\approx$ 30 nm) nearly coincides with the depth of amorphization ($\approx$ 40 nm, see Figure 3.3 (b)). Due to their large size, the introduction of oxygen atoms in the carbon lattice may lead to degradations of the structural order [126].

A summary of the processes occurring during continuous wave laser annealing of textured carbon thin films is presented in Figure 3.7.

3.6 Application to continuous-wave laser writing

We demonstrate the capability of the CW laser as a writing tool in Figure 3.8. While satisfying electrical and optical contrast are obtained (Figure 3.8 (a) and (c)), it is hard to see the "NTU" pattern on the 2D height image (Figure 3.8 (b)), suggesting that the optical and electrical contrasts are mostly due to a crystalline change rather than a morphological change. Since the conductivity was enhanced at the laser-annealed locations, we suggest that we locally induced sp^2 clustering during this laser annealing experiment.

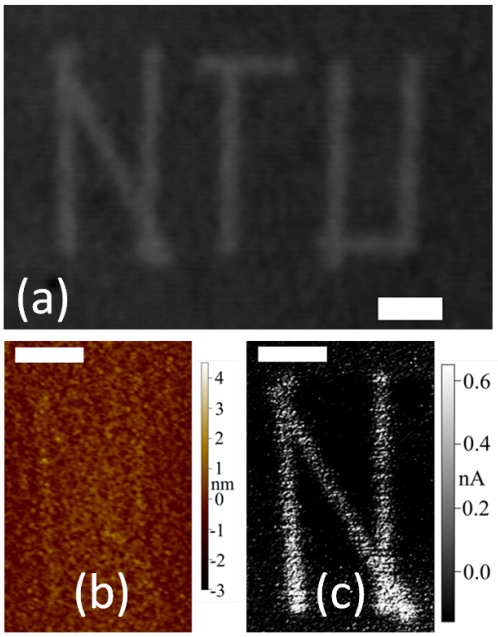

Figure 3.8: Example of a pattern drawn on textured carbon using a CW 488 nm laser beam. (a) Optical image. (b) AFM image (contact mode) of the "N" showing the height of the features. (c) c-AFM image of the "N" showing the conductivity of the features. Scale bars: 2 μm.

Hence, this graphitization process is found to produce very little degradations thanks to the smooth deposition of thermal energy. We also find that regions immediatelly surrounding the craters are smooth, with roughness values of less than 1 nm. CW lasers are a cheap, precise and efficient technology for the writing of patterns in carbon thin films.

3.7 Conclusion

An important goal of this work was to study the structural changes induced by a CW laser. We demonstrated that both **graphitization** and **amorphization** can occur. Moreover, we determined that these changes occur in the solid state, at **temperatures much lower than the melting point of carbon**, resulting in **low surface roughnesses**.

Matter loss was also observed; along with the amorphization, it is driven by **oxidation processes**. Oxygen atoms strongly **hole dope** the carbon, therefore explaining the **anomalous G peak frequency** shift we observe during ***in-situ* Raman characterization of the annealing process**.

Importantly for applications, it is possible to induce different types of structural and morphological changes by tuning the energy density. Matter loss and amorphization occur at higher energy densities than graphitization; the graphitization process is **not driven by oxidation** and **does not result in the growth of large graphitic crystals**. However, it has a strong impact on the electrical properties, resulting in a strong conductivity enhancement.

We demonstrated the potential of CW lasers as **drawing tools** by drawing a pattern made of highly conductive carbon. Moreover, the fact that we could induce phase changes in both directions (graphitization and amorphization) while keeping the surface smooth is promising for **phase change memory applications**.

In the next chapter (Chapter 4), we study the impact of pulsed laser annealing on the structure and surface morphology of textured carbon (pulse duration $\approx$ 5 ns). While

pulsed lasers are more expensive than CW lasers, fast writing and reading is needed for memory applications.

Chapter 4

Graphitization and amorphization of textured carbon by nanosecond laser pulses

4.1 Goals

In Chapter 3, we have shown that both laser-induced graphitization and amorphization of textured carbon can be achieved *via* continuous laser annealing.

Now, we wish to extend the study to pulsed lasers; for applications in data storage, it is necessary to induce reversible changes in shorter timescales than those achieved with CW lasers (on the order of minutes).

While graphitization of carbon films at low to medium energy densities has been demonstrated with pulsed lasers (see Section b.1.3, page 59), the impact of higher energy density pulses has not been studied. We have seen that in the case of silicon, amorphization could be achieved *via* homogeneous solidification at **high energy densities**.

Therefore, one of the objectives of this study is to study the structural changes induced

by high-energy pulsed laser annealing. In particular, achieving amorphization is essential for phase change memory applications.

Another goal of this study is to characterize the degradations induced by the energetic pulses. Achieving a reversible phase change is a first step toward the development of optically controlled phase change memories. But to achieve high performances in terms of cycling ability, degradations must be minimized. At the high energy densities used in this study, large degradations can be expected even though reports on low energy annealing of carbon show limited degradations [143] (Section b.1.3, page 59).

Finally, after a careful study of both the structural changes and the degradations, we want to provide a phenomenological model explaining both; for that purpose, we need to estimate the temperatures that are reached during the laser annealing process. For that purpose, we develop a model of the heat propagation that we solve numerically by using the finite element method.

To summarize, we want to fully assess (reversibility of the phase change, cycling ability, mechanisms of the phase changes and of the degradations) the potential of textured carbon as a phase change memory material whose phase is controlled by the application of nanosecond laser pulses.

4.2 Sample preparation and annealing

a Deposition of textured carbon films

We used a FCVA system (Section a, page 78) to deposit two thin films of textured carbon on previously cleaned silicon substrates. We measured their thicknesses with a Dektak XT profiler.

- the first film was deposited for 9 minutes and the resulting thickness is 310 $\pm$ 120 nm.

- the second film was deposited for 2 minutes and the resulting thickness is 110 $\pm$ 40 nm.

The large measured deviations in thickness come from the deposition technique, as the plasma beam is much more concentrated at its center and the concentration of C^+ ions rapidly decrease at distances from the center of the order of cm.

Both films were deposited at 4.10^{-6} Torr while a -500V bias was applied to the substrate.

Unless otherwise specified, in the rest of the chapter the described results are obtained on the "thick" film (deposited for 9 minutes with a thickness of 310 ± 120 nm).

b Laser annealing

After preparation, the sample was placed on a substrate holder enabling small-range translations in an orthogonal basis (x, y, z) (Figure 2.5).

Then, a single energetic pulse was emitted by the nanosecond laser for each location on the sample. After each annealing experiment, the 3D stage was used to move the sample to avoid overlapping between any two neighboring annealed areas. For each position, the energy density was recorded.

In total, the thicker film (310 $\pm$ 120 nm) was annealed by 41 pulses, while the thinner film (110 $\pm$ 40 nm) was annealed by 24 pulses.

4.3 Characterization of the structural changes

a Raman spectroscopy

a.1 As-deposited textured carbon

Figure 4.1 shows three representative spectra of textured carbon before and after annealing. The spectrum of un-annealed textured carbon consists of three wide peaks close to each other (4.1, bottom). It appears as a single asymmetrical wide peak. By fitting it with three Lorentzian curves, we find that the G peak width is $\approx 268\ cm^{-1}$, leaving no doubt that this carbon allotrope does not belong to the Stage-1 of the 3-Stage model proposed by Ferrari *et al.* (see discussion in Section a.2, page 97). Consequently, in the rest of the discussion, the interpretation of key Raman parameters will be conducted such that:

- an **increase** in the I(D)/I(G) ratio is interpreted as an **increase in the amount of crystalline carbon**.

- a **decrease** in the G peak width is interpreted as **increase in the amount of crystalline carbon**.

- an **increase** in the G peak frequency is interpreted as an **increase in the amount of crystalline carbon**.

a.2 Graphitization

An example of a spectrum of a more crystalline carbon is the middle spectrum of Figure 4.1. As compared to the spectrum of pristine textured carbon, the I(D)/I(G) ratio value rises from 0.69 to 1.18, the G peak frequency rises from 1548 cm^{-1} to 1590 cm^{-1} and the

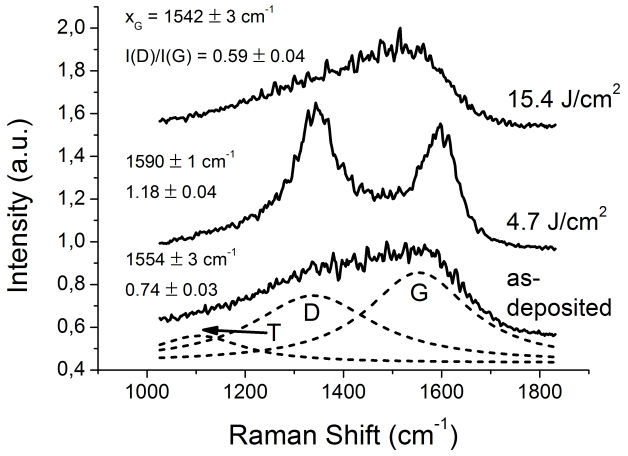

Figure 4.1: Three representative spectra of pristine textured carbon and textured carbon annealed at different energy densities.

G peak width decreases from 268 cm^{-1} to 109 cm^{-1}. Following the 3-Stage model of Ferrari *et al.*, all these changes strongly suggest that a graphitization process has taken place at this location, where the textured carbon film has been annealed with an energy density of 4.7 J/cm^2.

Pulsed laser induced graphitization of amorphous carbon has been extensively described in the literature [57, 81, 82, 84].

a.3 Amorphization

On the other hand, the third spectrum (annealing at 15.4 J/cm^{-2}) displays a shape very similar to that of the spectrum of pristine textured carbon, appearing as a single asymmetrical wide peak (Figure 4.1, top spectrum). Its fitting with the three T, D and G peaks yields I(D)/I(G) = 0.59 (versus 0.69 for pristine textured carbon), x_G = 1542 cm^{-1} (versus 1548 cm^{-1} for pristine textured carbon).

Considering the fact that standard deviations on the values of the I(D)/I(G) ratio and G peak frequency are 0.01 and 1 cm^{-1} (calculated using the Bootstrap method, see Section a.5, page 101), respectively, the changes observed in the third spectrum are signifi-

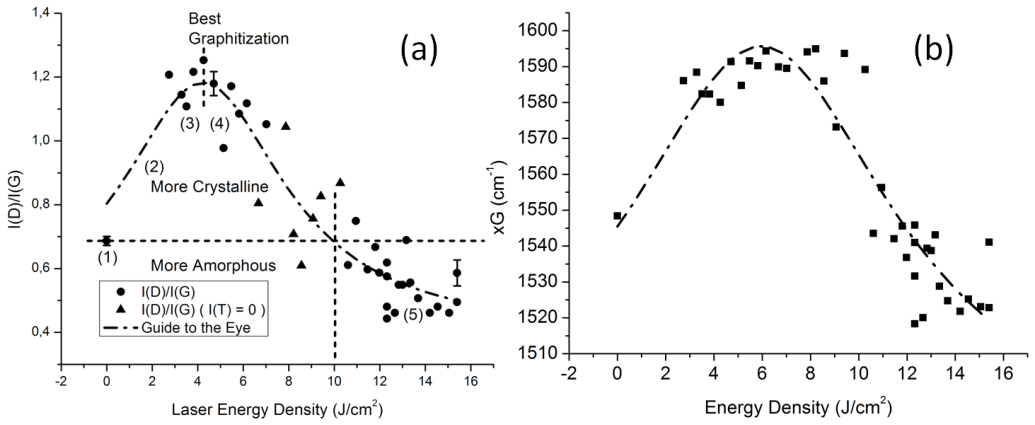

Figure 4.2: (a) Evolution of the I(D)/I(G) ratio values as a function of the energy density of the laser pulse. (b) Evolution of the G peak position values as a function of the energy density of the laser pulse.

cant.

By interpreting the Raman data following the 3-Stage model, the fact that both the I(D)/I(G) and G peak position values decrease significantly as compared to those of the un-annealed film, means that the textured carbon film has gone through an amorphization process during the pulsed annealing experiment.

a.4 From graphitization to amorphization

For a more detailed analysis, Figure 4.2 (a) shows the evolution of the I(D)/I(G) ratio values as a function of the energy density of the pulse. For medium range energies, the I(D)/I(G) ratio values increase significantly, suggesting that a graphitization process is taking place, that gets more efficient as the energy density is increased.

Then, as energy density values rise above $\approx 4\,\mathrm{J/cm^2}$, the I(D)/I(G) values start decreasing until they reach significantly lower values than those extracted for pristine textured carbon. Above $\approx 10\,\mathrm{J/cm^2}$, most data points are significantly below the value for pristine textured carbon. This trend suggests that after $\approx 4\,\mathrm{J/cm^2}$, the graphitization process becomes less efficient, until amorphization takes place, resulting in a film that is more

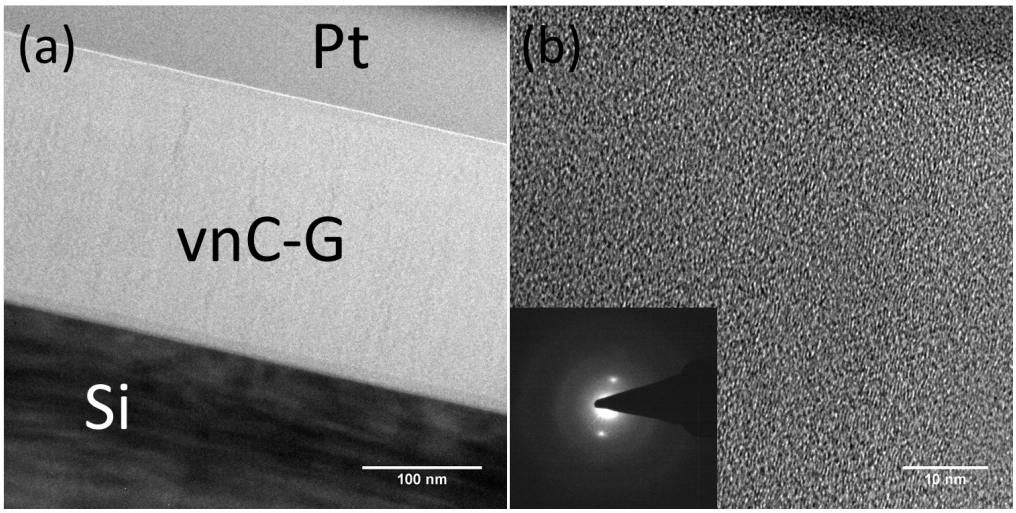

Figure 4.3: TEM characterization of un-annealed textured carbon. (a) TEM micrograph showing the film on top of Si and below the Pt protective layer. Scale bar: 100 nm. (b) HRTEM micrograph showing the vertical graphitic planes. Scale bar: 10 nm. *Inset* SAED pattern showing two dots corresponding to the oriented (002) planes of graphite. The SAED pattern is oriented 90°relative to the displayed HRTEM images.

amorphous than the as-deposited film.

Our interpretation of the I(D)/I(G) data is supported by the evolution of the G peak position as a function of energy density (Figure 4.2 (b)). It follows the same trend.

b Transmission electron microscopy

We obtained HRTEM images of three cross-sections representative of un-annealed, graphitized (one pulse at 4.26 J.cm^{-2}) and amorphized (one pulse at 14.2 J.cm^{-2}) textured carbon.

b.1 As-deposited textured carbon

The structure of the un-annealed film is very uniform, with a measured thickness of $\approx$ 220 nm (Figure 4.3 (a)). It is composed of graphitic planes oriented perpendicular to the substrate, as evidenced by direct visualization on HRTEM images (Figure 4.3 (b)). The presence of two sharp dots on the corresponding SAED pattern (Figure 4.3 (b) *inset*) which correspond to electron diffraction by (002) planes supports the presence of preferentially oriented graphitic crystals.

b.2 Graphitization

Annealing with a medium-energy density pulse (4.26 J/cm^{-2}) affects both the morphology and structure of both the textured carbon film and the silicon substrate (Figure 4.4).

In terms of bonding structure, from the Raman data, a more graphitic structure is expected. At first sight, the difference between un-annealed and graphitized textured carbon is not evident from the HRTEM images (compare Figure 4.3 (b) and Figure 4.4 (b)). Moreover, in both cases, the SAED pattern shows two sharp peaks due to the oriented (002) graphitic planes. Where the atomic structure differs the most is near the surface (Figure 4.4 (c)). There, regions containing graphitic planes oriented with different orientations are observed, evidencing the fact that structural changes occured during the laser annealing process. These crystal structures might be responsible for the enhanced graphitic signal we detected when conducting Raman characterization.

As for the silicon substrate, despite the fact that it is modified on a "large" scale (Figure 4.4 (a)), its structure is still mono-crystalline, suggesting that either it has not melted during annealing, or that it had enough time to re-solidify in an epitaxial manner during cooling.

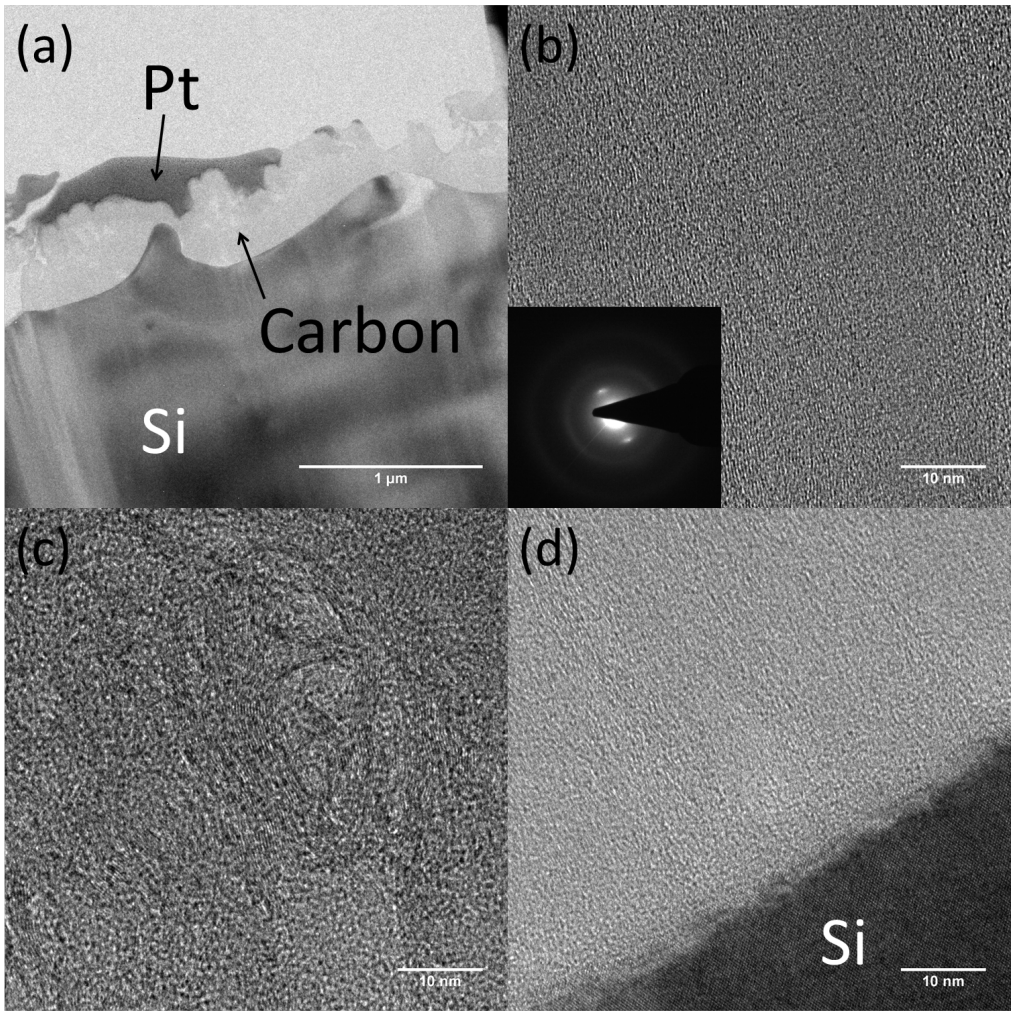

Figure 4.4: TEM characterization of textured carbon annealed by a 4.26 J.cm^{-2} pulse. (a) TEM micrograph showing the film on top of Si and below the Pt protective layer. Scale bar: 100 nm. (b) HRTEM micrograph showing the structure of the film in the middle. Scale bar: 10 nm. *Inset*: SAED pattern showing two dots corresponding to the oriented (002) planes of graphite. (c) HRTEM micrograph showing a region largely modified by the energetic pulse (near the top). Scale bar: 10 nm. (d) HRTEM micrograph showing the structure of the film near the Si substrate. The SAED pattern is oriented 90° relative to the displayed HRTEM images. Scale bar: 10 nm.

b.3 Amorphization

The film annealed at a much larger energy density of 14.2 J.cm^{-2} seems much more regular ("straight") than the film annealed at 4.26 J.cm^{-2}, with a nearly constant thickness of $\approx$ 90 nm (Figure 4.5 (a)), much thinner than the pristine textured carbon film (220 nm), suggesting large matter losses.

From the Raman data, we expect this region to be more amorphous than pristine textured carbon. It is the case, as shown in Figure 4.5 (b). In the whole depth of the film, no graphitic planes are observed in the film. Moreover, the amorphous nature of the annealed film is supported by the SAED pattern showing no distinguishable pattern (Figure 4.5 (b) *inset*).

Nevertheless, we note that we observe carbon crystals at the interface between silicon and carbon. Contrary to the case of graphitic planes in un-annealed textured carbon, these graphitic planes grow **parallel** to the silicon substrate (Figure 4.5 (c)). As these planes are not present in the un-annealed film, their presence after annealing suggests that an epitaxial process takes place during annealing at high energy densities.

To summarize, TEM and HRTEM characterization images enable us to conclude that the phase changes detected by Raman spectroscopy, and especially amorphization, occur in the bulk of the annealed films. Moreover, these images give us information on the state of the silicon/carbon interface and on the microstructure of the silicon substrate. These pieces of information are useful to understand the mechanisms behind phase changes, as will be discussed in Section c, page 162.

c Cycling ability

The fact that we are able to graphitize and to amorphize textured carbon films by pulsed-laser-annealing is of interest for data storage applications. The two states of carbon corresponding to 0 and 1 could be, for example:

- 1 (amorphous)

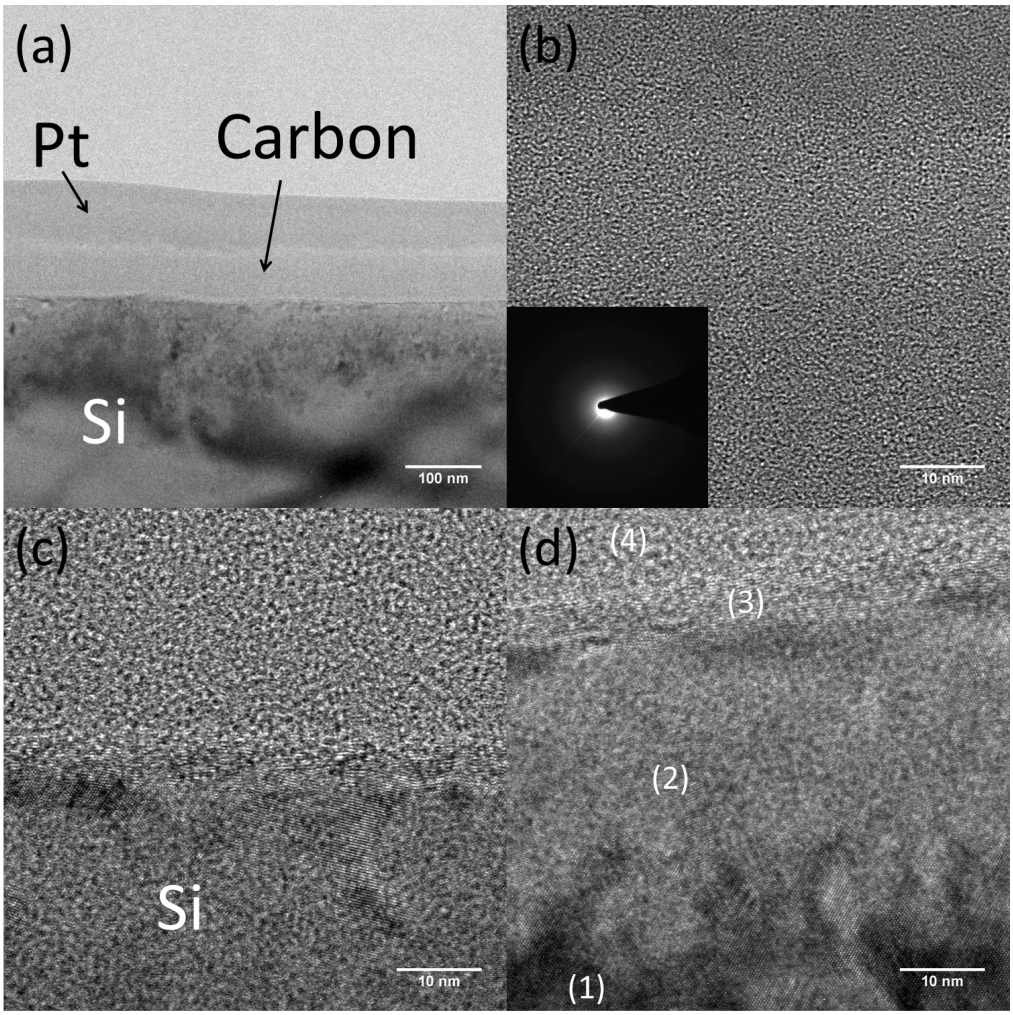

Figure 4.5: TEM characterization textured carbon annealed by a 14.2 J.cm^{-2} pulse. (a) TEM image showing the carbon film on top of the silicon substrate and under the Pt protective layer. Scale bar: 100 nm. (b) HRTEM micrograph showing the amorphous structure of the middle of the film. Scale bar: 10 nm. *Inset*: SAED pattern of the film showing no distinguishable peak. The SAED pattern is oriented 90°relative to the displayed HRTEM images. (c) HRTEM micrograph showing the interface between the substrate and the carbon film. Scale bar: 10 nm. (d) HRTEM micrograph showing the silicon/carbon interface and the depth of the silicon. (1) Mono-crystalline silicon. (2) Poly-crystalline/amorphous silicon. (3) Graphite planes. (d) Amorphous carbon. Scale bar: 10 nm.

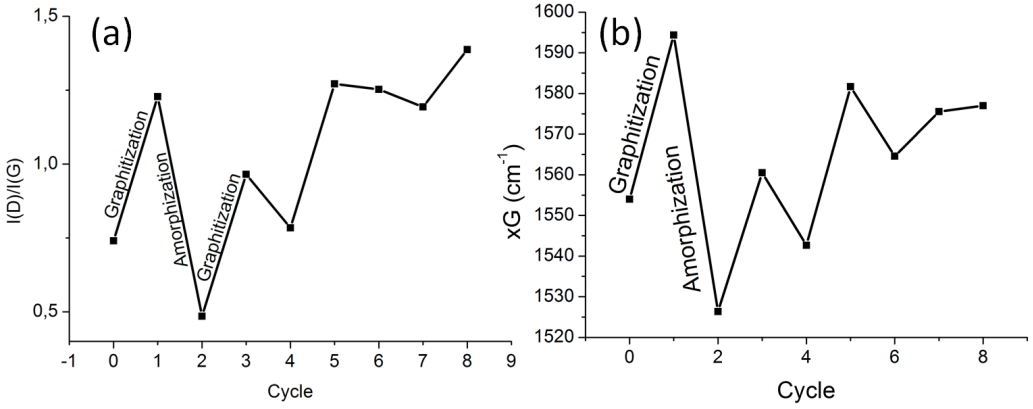

Figure 4.6: Endurance test. (a) Evolution of the I(D)/I(G) ratio value. (b) Evolution of the G peak position value.

- 0 (graphitic)

A state of a textured carbon based memory could be read by several methods. For example:

1) Optical reading. The optical properties of amorphous carbon are different from the optical properties of graphitic carbon (*e.g.* optical reflectivity).

2) Electrical reading. The electrical properties of amorphous carbon are different from the electrical properties of graphitic carbon (*e.g.* electrical resistivity).

Thus, the reversible phase change we demonstrate is promising for optical data storage, and the reading can potentially be done both by optical and electrical means.

Depending on the application, it may be necessary to write and read a number of times, enabling to "re-write" information several times, hence improving the capabilities of our technique for data storage.

However, endurance tests (Figure 4.6) conducted by Raman spectroscopy show that the cycling ability is very limited. After two or three cycles, reversible variations in I(D)/I(G) ratio values or in G peak position becomes small and the device cannot be used as a memory anymore, therefore limiting the potential of our technique for applications requiring a large number of writing/reading cycles.

TEM images, and especially Figure 4.4 (a) and Figure 4.5 (a), show that the annealing process leads to large plastic deformations of the film, the substrate, as well as large matter losses.

To better understand the mechanisms responsible of these degradations, in the next Section, we characterize the state of the surface by SEM.

4.4 Laser-induced degradations

a Roughness increase

Much of the literature on pulsed laser-annealing of carbon thin films focuses on energy densities that are small as compared to those used here. Most studies do not report extensive degradations.

One study [84] reports that pulsed laser annealing leads to a significant increase in the surface roughness of the film upon application of a 0.665 J/cm^2 pulse, from less than 0.2 nm to $\approx$ 3.3 nm (Figure 4.7 (c)). This is a significant jump, however it does not lead to significant issues regarding the electrical characterization of the annealed matter, as reported by the authors. In fact, the team reports a drastic improvement in terms of electrical conductivity (due to laser induced graphitization), even at energy densities leading to these "high" values of the surface roughness.

Here, by comparing the surface state of a textured carbon film annealed at 1.5 $J.cm^{-2}$ (Figure 4.7 (b)) with that of the un-annealed film (Figure 4.7 (a)), we observe the appearance of grain-like surface features of varying sizes. A comparison between these features and those detected by AFM in the study by Xu *et al.* [84] (Figure 4.7 (c)) suggests that these features could be similar in nature.

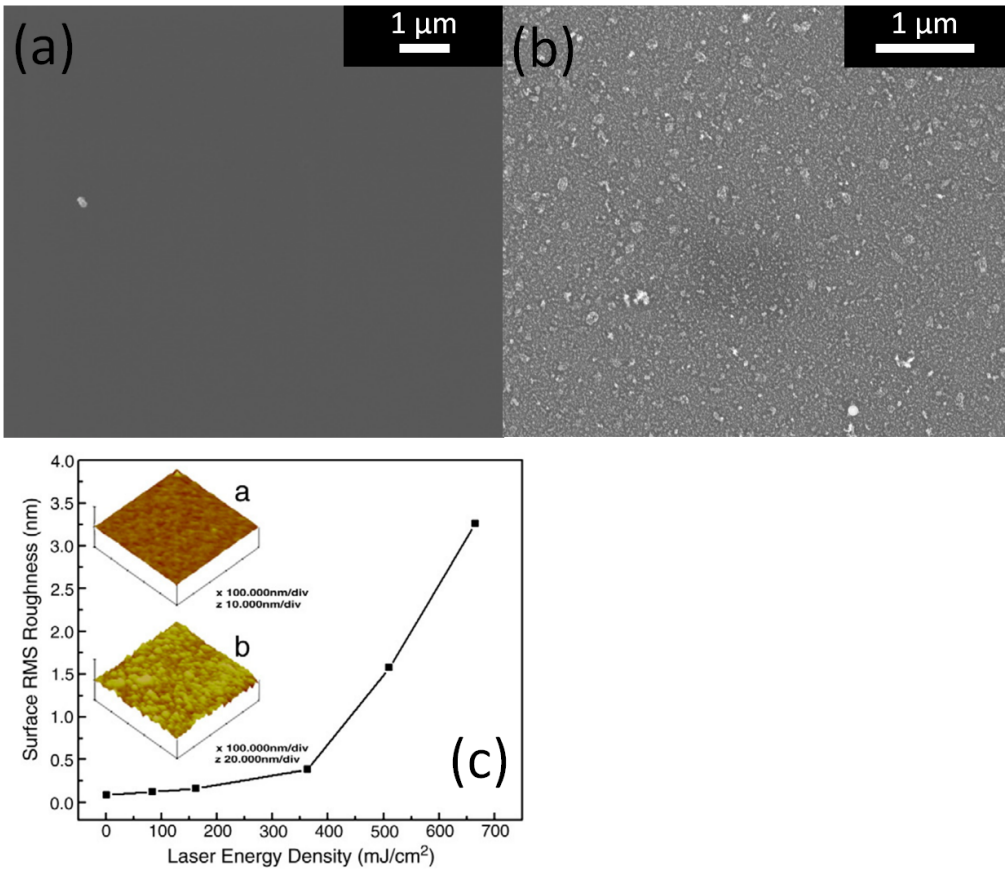

Figure 4.7: Characterization of the surface morphology after laser-annealing at low energy densities. (a) SEM image of the surface of an un-annealed textured carbon film. (b) SEM image of the surface of a textured carbon film annealed by a 1.5 J.cm^{-2} pulse. (c) Evolution of the surface roughness of an amorphous film as a function of the energy density of the pulse (reproduced from [84]).

b Cracks and ripples

At higher energy densities ($\approx$4 J/cm^2), cracks are observed (Figure 4.8 (a) and (c)), revealing the underlying silicon substrate (as evidenced by Raman characterization). Locally, during the annealing process, the carbon film dissociates itself from the silicon substrate (delamination).

Sub-micrometer-sized spheroids are also observed (Figure 4.8 (a)). Similar spheres were observed in [80] after 3.0 J/cm^2 irradiation of graphite (Figure 4.8 (b)). These features were assigned to the hydrodynamic sputtering of carbon caused by the intense heat generated during laser-annealing.

In the thin film only, other features appeared: wave-like surface ripples (Figure 4.8 (c) (d)). Unlike other features that are observed in both films, **they were never observed after laser-annealing of the thick film.**

Except at the locations of the cracks, the surface is entirely covered by the rough carbon thin film, whose morphology comprises bubble-like artefacts. Other artefacts look like empty craters; we hypothesize that these craters were formed by the sputtering of bubbles away from the surface. In some case, these bubbles would fall back to the surface under the form of spheroids [80].

c Sputtering

At higher energy densities, many features which were consisting of bumps or spheroids, transformed into longer, cylindrical features that are either full (wire-like) or empty (tube-like) (Figure 4.9). Spheroids are still present.

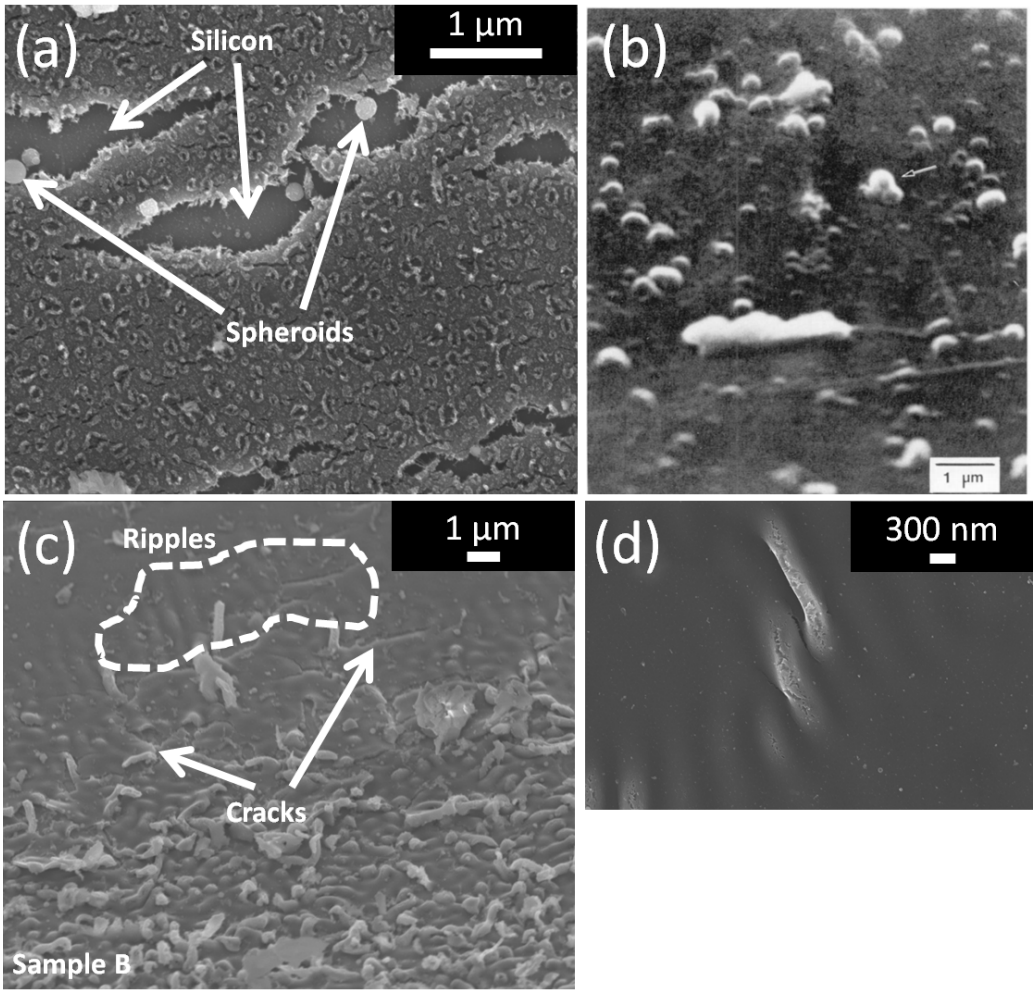

Figure 4.8: (a) SEM micrograph showing the surface morphology of textured carbon after annealing by a 3.9 J/cm^2 pulse. (b) SEM micrograph showing the surface morphology of graphite after annealing by a 30 ns, 3.0 J/cm^2 laser pulse. Reproduced from [80]. (c) SEM micrograph showing wave-like ripples. (d) Higher magnification SEM image of the surface ripples.

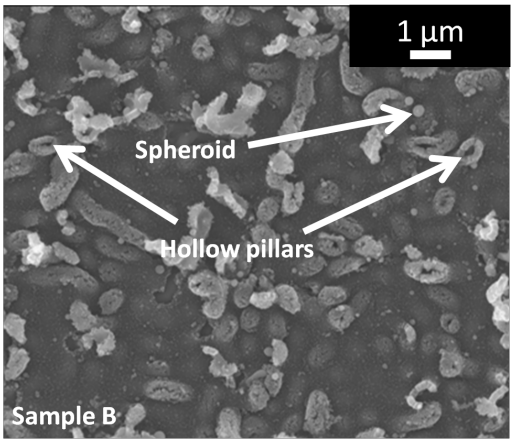

Figure 4.9: SEM micrograph showing the surface morphology of textured carbon after annealing by a 2.3 J/cm^2 pulse.

d Explosive boiling

At even higher energy densities, the surface microstructure drastically transformed, with the appearance of high aspect ratio features consisting in grooves and ridges (Figure 4.10 (a) and (b)). A closer examination of the features reveals that the features themselves are made of spheroids (Figure 4.10 (c)).

At high energy densities, we have seen that the annealing process results in large losses of matter (*e.g.* thickness from $\approx$ 220 nm to $\approx$ 90 nm in the thick film, as discussed in Section b, page 141), in one single pulse. Such rapid matter losses are reminiscent of explosive boiling processes [41] (discussed in b.1.2, page 45). Explosive boiling occurs when very high temperatures are reached in timescales shorter than ≈ 1 μs, which is the case here.

Therefore, the high aspect ratio features (grooves and ridges) are due to explosive boiling. The observed spheroid shapes (Figure 4.10 (c)), on the other hand, have diameters similar to those of the spheroid shapes observed before. This suggests that they were formed at lower temperatures, by normal boiling, when matter remaining after explosive boiling cooled down.

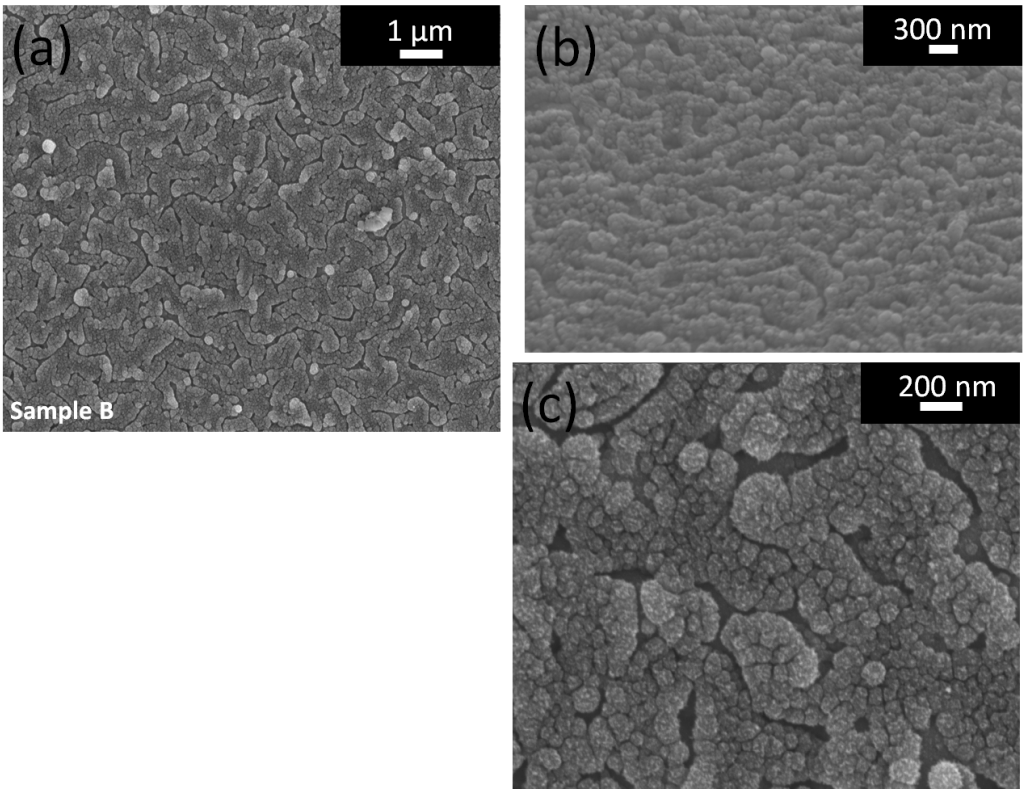

Figure 4.10: (a) SEM micrograph showing the surface morphology of textured carbon after annealing by a 6.7 J/cm^2 pulse. (b) Tilted image (angle = 55 °). (c) Higher magnification image.

Estimates of the temperatures needed for explosive boiling of graphite vary drastically, from 6,710 K to 22,400 K [136]. What is certain is that this process occurs at temperatures much higher than the melting point of carbon ($\approx$ 4,450 K [138]).

Similar boiling processes have been reported in silicon [18].

4.5 Interpretation

a Estimation of the temperature increase during laser-annealing *via* the finite element method

a.1 Initial code

The application of a nanosecond laser pulse to a carbon allotrope such as graphite [144] or amorphous carbon results in a fast and large increase in temperature. The melting point of graphite (4,450 K [138]) is attained at energy densities as low as 0.6 J/cm^2 [144].

We used Cast3M, a free finite element method software developed by the CEA [145], to solve numerically the heat equation in the system during the application of a nanosecond pulse.

For that purpose, we used a Cast3M code written by two students of Ecole Polytechnique, Guillaume Giudicelli and Mathias Lebihain, working under the supervision of Prof. Andrei Constantinescu. The simulation they conducted applied to laser-annealing of graphite (planes horizontally aligned) by a 5 ns, 5 J/cm^2 laser pulse. The values they used for the material parameters were extracted from [144].

Before considering in detail the different parameters that are considered in the model, we looked directly at the results provided by the model at 1 J/cm^2. We found that the melting temperature of carbon is reached and that the surface temperature reaches 4,700 K. This order of magnitude of the temperature is coherent with the results reported in [144].

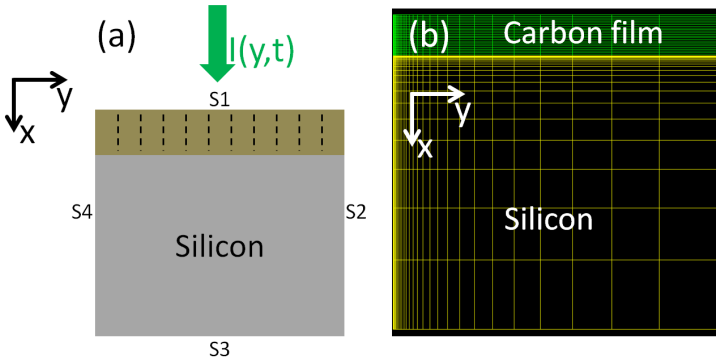

Figure 4.11: Geometry defined in Cast3M. (a) Carbon thin film (x-size = 300 nm, y-size = 100 μm) on top of a silicon substrate (x-size = 2 μm, y-size = 100 μm). (b) Geometry and meshing implemented in Cast3M. The entirety of the simulated structure is not shown as it is too long in the y direction.

a.2 Setting up the simulation: geometry, heat equation, boundary conditions, and physical constants

We then customized the program for our needs. We verified all the values and corrected them when needed. We also changed the simulated orientation of the graphitic planes, as the graphitic planes of textured carbon are oriented perpendicularly to the substrate.

We defined the geometry of the problem and the meshing. We defined two rectangles for the carbon thin film and the silicon substrate, with thicknesses 300 nm and 2 μm, respectively (Figure 4.11). To limit the required computing power, we defined the system in 2 dimensions, with the depth along the x-axis and the width on the y-axis. The width of the thin film/substrate was 100 μm. As most of the energy is absorbed in the thin film, leading to steeper temperature gradients, we defined a finer meshing there as compared to the meshing in the substrate (Figure 4.11 (b)).

The laser source was described as a heat flux varying spatially (y direction) and temporally (t) and entirely absorbed at the surface (x = 0). We also accounted for the reflectivity of the carbon, resulting in the absorption of a fraction of the incident energy. So the inci-

dent heat flux was described in Cast3M as:

$$I(y,t) = (1-R)I_0 f(y)g(t) \tag{4.1}$$

With R the reflectivity coefficient, I_0 the incident energy, f(y) and g(t) two functions varying in y and t, respectively. The surface reflectivity changes when the carbon becomes liquid, so we accounted for that by setting:

$$R_{solid} = 0.3$$

$$R_{liquid} = 0.6$$

The beam profile consists in an ellipse comprising two maxima (Figure 2.6), so we described the spatial profile as a Gaussian with a maximum intensity at y = 0, such that:

$$f(y) = exp(\frac{-y^2}{y_0}) \tag{4.2}$$

The temporal profile is a Gaussian with full-width at half maximum 5 ns. Then:

$$g(t) = \frac{1}{\sigma\sqrt{2\pi}} exp(\frac{-(t-t_0)^2}{2\sigma^2}) \tag{4.3}$$

Where t_0 is the time at which the maximum of the Gaussian is reached (we set it here at 2.5 ns), and σ is a factor impacting the temporal dispersion of the Gaussian, defined such that:

$$FWHM = 2\sqrt{2ln2}\sigma = 2.3548\sigma$$

So the heat flux was defined as:

$$I(y,t) = (1-R)I_0 exp(\frac{-y^2}{y_0})\frac{1}{\sigma\sqrt{2\pi}} exp(\frac{-(t-t_0)^2}{2\sigma^2}) \tag{4.4}$$

The heat equation that was to be solved in Cast3M was written as:

$$\begin{aligned} \rho(T)C_p(T)\frac{\partial T(x,y,T)}{\partial t} = div(\kappa(T).\nabla T) = \frac{\partial}{\partial x}(\kappa_x(T)\frac{\partial T(x,y,T)}{\partial x}) + \\ \frac{\partial}{\partial y}(\kappa_y(T)\frac{\partial T(x,y,T)}{\partial y}) \\ \nabla T(0,y,t) = I(y,t) \text{ on S1 (heat source)} \\ T(x,y,t) = 298K \text{on S2 and S3 (boundary conditions)} \end{aligned} \tag{4.5}$$

To solve the heat equation, we needed to input values of the heat capacity $C_p(T)$, density $\rho(T)$ and thermal conductivity $\kappa(T)$ for both the carbon and the silicon layer. We used values extracted from [144].

For the heat capacity of carbon:

$$C_p(T) = (\frac{1000}{12})(16.299 + 5.262.10^{-3}T - \frac{8.602.10^3}{T^2}) \text{ J/(kg K)}$$

for 298K < T < 1,000 K

$$C_p(T) = (\frac{1000}{12})(24.943 + 4.892.10^{-4}T - \frac{71.156}{T} - \frac{3.649.10^6}{T^2}) \text{ J/(kg K)}$$

for T > 1,000K

$$C_p(T) = 1039 \text{ J/(kg K) for T > 4450 K}$$

And for silicon, $C_p(T) = 700$ J/(kg K).

For the thermal conductivity of carbon:

$$\kappa_{solid/x}(T) = \frac{267.6.10^2}{T} \text{ W/(mK)}$$
$$\kappa_{solid/y}(T) = -0.101 + 181.022T^{-0.53} \text{ W/(mK)}$$
$$\kappa_{liquid}(T) = (\kappa_{solid/y}(T))^{1/3}(\kappa_{solid/x}(T))^{2/3} \text{ W/(mK)}$$

And for silicon, $\kappa = 149$ W/(mK).

For the density values of carbon:

$\rho(T) = 2,250$ kg/m^3 for 298K < T < 4,200K

$\rho(T) = 2,700$ kg/m^3 for T > 4,400K

Linear interpolation for 4,200K < T < 4,400K

And for silicon $\rho(T) = 2330$ kg/m^3

As simulation parameters, we set:

- Simulation time = 30 ns

- Time step = 25 ps

a.3 Solving convergence errors

Solving convergence errors due to the phase change

The students who wrote the initial code reported a failure to simulate the solid -> liquid phase change using the built-in procedure included in Cast3M. For this reason, they modified the value of the heat capacity at temperatures near the melting point, to account for the energy required for the phase change. This technique works, however we found that the phase change procedure works in our case. We changed back the value of the heat capacity accordingly and used the built-in phase change procedure.

Solving convergence errors due to discontinuities in the values of the physical constants

During the phase change, simulation errors occur due to the discontinuity in the values of the physical constants; to minimize these errors, we implemented a smoothing function using a rule of mixtures for the values of the physical parameters (thermal conductivity, specific heat, density) during melting.

If the transition temperature is T_{tr} and if $P_1(T)$ (respectively $P_2(T)$) is the value of the parameter of interest for $T < T_{tr}$ (respectively $T > T_{tr}$), then we used the smoothed function P(T) defined as:

$$P(T) = P_1(T) * S(T) + P_2(T) * (1 - S(T))$$

with S(T) the smoothing function defined as:

$$S(T) = \frac{1}{1 + exp(\alpha(\frac{T}{T_{tr}} - 1))}$$

S(T) is close to 1 for temperatures values below T_{tr}, while it is close to 0 for temperatures above T_{tr}.

This smoothing function enables to avoid discontinuities both in value and in slope; the evolution of critical parameters with the smoothing function is shown in Figure 4.12.

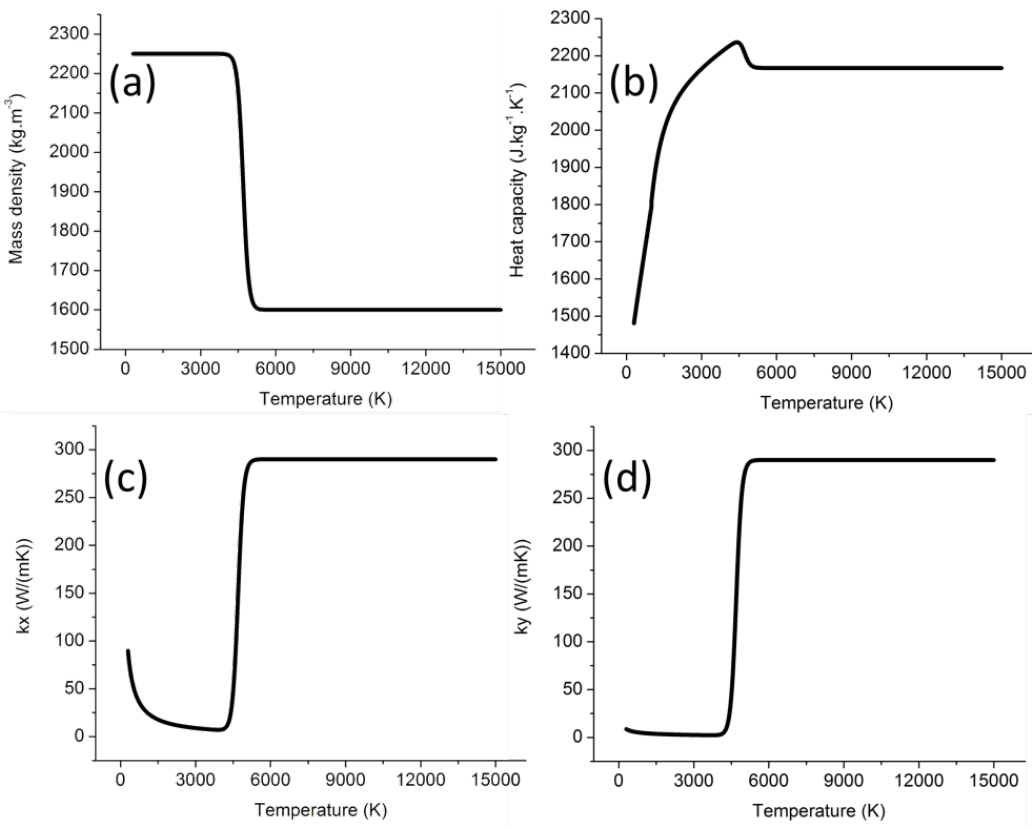

Figure 4.12: Evolution of physical constants as a function of temperature after implementation of the smoothing function. (a) Density of carbon. (b) Heat capacity of carbon. (c) Thermal conductivity of carbon in the x-direction. (d) Thermal conductivity of carbon in the y-direction.

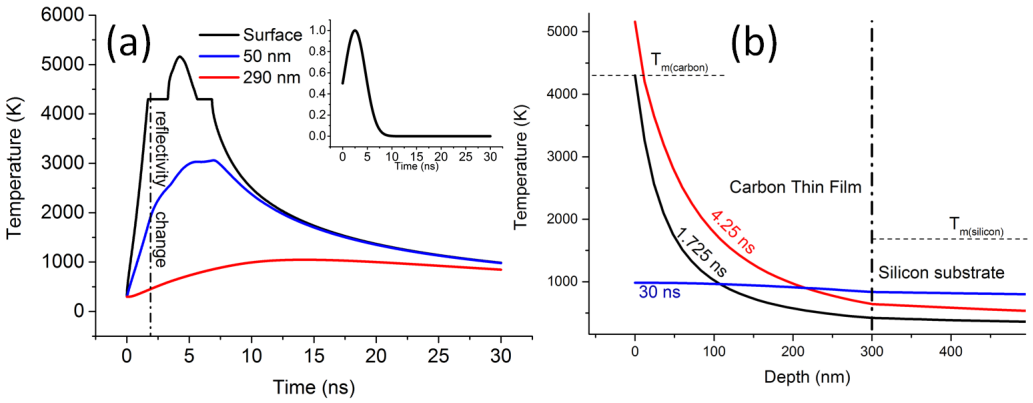

Figure 4.13: Carbon laser-annealing with a 5 ns, 0.6 J/cm^2 pulse. (a) Simulated evolution of the temperature as a function of time for three different depths (surface, 50 nm, 290 nm). (b) Simulated evolution of the temperature as a function of depth for three different times (1.725 ns, 4.25 ns and 30 ns).

a.4 Simulation results

At the end of the simulation, we obtained temperature data at every point of the mesh and at all times from 0 to 30 ns (with 25 ps step). We plotted evolutions of the temperature as a function of time and at specific locations and as a function of location at specific times in Figure 4.13.

First, we note that the melting temperature of carbon (4,450 K) is indeed reached for energy densities as low as 0.6 J/cm^2 (Figure 4.13 black line).

As the surface temperature rises due to the imposed heat flux, it eventually reaches a plateau after 1.7 ns, at 4,450 K. This plateau is due to the melting process, which requires a significant amount of heat to be absorbed as latent heat of fusion. The solid -> liquid phase change occurs at a constant temperature. At roughly the same time, we imposed a reflectivity change in the code to account for the reflectivity difference between the solid and liquid phases of carbon. The liquid phase was set to be more reflective than the solid phase.

After 1.6 ns (at t = 3.3 ns), the temperature starts rising again, above 4,450 K. The surface is now in the liquid state. A maximum temperature of 5,160 K is reached at 4.225 ns.

Then, the temperature starts decreasing again, as the heat input decreases (see Figure 4.13 (a) inset). At 5.675 ns, a new plateau is reached, this time due to the heat provided by the phase change from liquid to solid (recalescence). At 6.825 ns, the surface temperature starts decreasing smoothly again. After 30 ns, the temperature is 985 K.

Studying the evolution of the temperature at a depth of 50 nm (Figure 4.13 (a) blue line) shows that the molten layer is very shallow, as the melting temperature is never reached at a depth of 50 nm. The maximum temperature that is reached at such a depth is 3061 K.

At a depth of 290 nm, very near from the substrate (at depths larger than 300 nm), the temperature never reaches higher than 1,048 K. It is much below the melting point of silicon (1685 K), so the silicon substrate should retain its monocrystalline structure at such low energy densities. In fact, HRTEM images show that the monocrystalline structure of the silicon substrate is mostly intact at energy densities as high as 4.3 J/cm^2 (Figure 4.4 (d)).

Plots of the evolution of the temperature as a function of the depth at different times (Figure 4.13 (b)) shows that very steep thermal gradients occur when the heat input is large. We plotted the temperature evolution at the time of melting the surface layer (1.725 ns, black line), at the time at which a maximum temperature is reached at the surface (4.25 ns, red line) and at the end of the simulation (30 ns, blue line). In the carbon film of thickness 300 nm, thermal gradients are very large: more than 3,870 K over 300 nm at 1.725 ns, and more than 4,510 K over 300 nm at 4.25 ns. Such large thermal gradients should lead to large mechanical stresses, which could be responsible of degradations such as the cracks we observed (Figure 4.8 (a) and (c)).

On the other hand, the plot at 30 ns (Figure 4.13 (b) blue line) shows that the overall temperatures decrease very fast as soon as the heat source is removed. At 30 ns, the thermal gradient along the depth is much lower (149 K over 300 nm), with a maximum temperature of 985 K at the surface. The fact that the temperature decreases drastically in times on the order of tens or hundreds of nanoseconds is critical in explaining why oxidation does not play an important role during laser annealing of carbon by nanosecond pulses. Significant oxidation of carbon typically occurs in times on the order of minutes

[146].

b Interpretation of the observed degradations

Both the literature [144] and our Cast3M simulation suggest that the melting temperature of carbon was reached at energy densities as low as 0.6 J/cm^2. Thus, the range of degradations discussed in Section 4.4 (page 147) appeared when a fraction or all of the carbon film is melted.

There is a continuity between the appearance of surface roughness (Figure 4.7 (b)), bubble-like features (Figure 4.8 (c)), spheroids (Figure 4.8 (a)), empty craters (Figure 4.8 (a)) and empty cylinders (Figure 4.9) which appeared in turn as the energy density of the pulse was increased.

We propose that the roughness increase is due to the nucleation of germs of the liquid phase in a solid matrix; at higher energy densities, the observed bubble-like features are frozen bubbles: when the provided energy was increased, the germs growed to form bubbles (boiling). At even higher energy densities, these bubbles were sputtered away from the surface, resulting in the appearance of craters and empty cylinders at their previous locations. The observed spheroids are bubbles that have fallen back on the surface.

Cracks and delamination are due to thermo-mechanical stresses. While temperatures (and temperature gradients) increase, mechanical stresses due to the different expansions of carbon and silicon rise, leading to delamination and cracking.

On the other hand, the structures observed at very high energy densities (Figure 4.10) are due to explosive boiling, as discussed in Section d, page 151.

c Mechanisms behind the reversible phase change

Considering the fact that a significant volume of carbon goes through a liquid phase during the annealing process, the phase changes occur mostly during the cooling and solidification of molten carbon.

If we draw a comparison with the mechanisms of amorphization of silicon by pulsed laser annealing (Section a.1.4, page 30), here the amorphization process **cannot be quenching**, because quenching is believed to occur at **lower** energy densities than crystallization. Here, amorphization occurs at **higher** energy densities than crystallization.

On the other hand, during pulsed laser annealing of silicon, amorphization *via* homogeneous solidification occurs at **higher** energy densities than crystallization.

Starting from the liquid phase, as the temperature decreases and reaches the solidification point, nuclei of the solid phase start to form [21]. Where and at what frequency these nuclei form depend on the temperature, the temperature homogeneity, and the presence (or absence) of other solid nuclei in the melt, from which crystals can grow epitaxially. After forming, these nuclei need time to grow. The kinetics of growth of the crystalline phase are largely impacted by the presence or absence of crystalline seeds (catalysts).

Thus, if two similar materials cool from the melt at the same speed, one can become crystalline while the other becomes amorphous if the cooling occurs respectively with and without solid crystalline seeds. Crystalline seeds effectively act as templates for the surrounding cooling matter to grow as crystals.

Here, evidence that epitaxial regrowth is a phenomenon drastically impacting the phase change is found in the HRTEM images of textured carbon annealed at high energy densities (Figure 4.5); graphitic planes form on top of the silicon substrate, which itself melts during the annealing process and forms a polycrystalline/amorphous phase during solidification.

Further evidence that the amount of molten material plays a role in the phase change is that at energy densities at which cracks appear (Figure 4.8) and at which the resulting carbon is more graphitic, a fraction of the carbon remains solid, as liquid carbon should completely accommodate the stresses, therefore not resulting in the appearance of cracks. At higher energy densities, the density of cracks drops, supporting the fact that a larger fraction of the carbon melts.

As the energy density increases, the fraction of molten carbon increases as well, leading first to a graphitization process when part of the carbon is melted, and then to an amorphization process when a much larger fraction of the carbon, and part of the silicon, is melted. Considering the temperatures required for explosive boiling, which is a volume process, a very large fraction (or all) of the carbon should be molten when it occurs. At similar energy densities, amorphization is found to occur.

Hence, we propose that, like in silicon, the difference between the graphitization and high-energy amorphization process relies on the amount of molten matter. At small-/medium energy densities, discrete molten regions form in the surrounding solid matrix. When these regions solidify, they are surrounded by solid matter that acts as templates for crystallization. This process is called "heterogeneous solidification" (Figure 4.14).

At higher energy densities, most of the carbon and part of the silicon is melted. Moreover, for higher energy densities the temperatures rise higher and the time spent in the molten state is longer, resulting in a homogeneization of the temperature of the melt. As the melt cools down, it solidifies in the absence of solid seeds acting as crystallization templates. As the temperature is more homoegeneous, all the liquid solidifies at the same time, resulting in a mostly amorphous structure. This process is called "homogeneous solidification" (Figure 4.14).

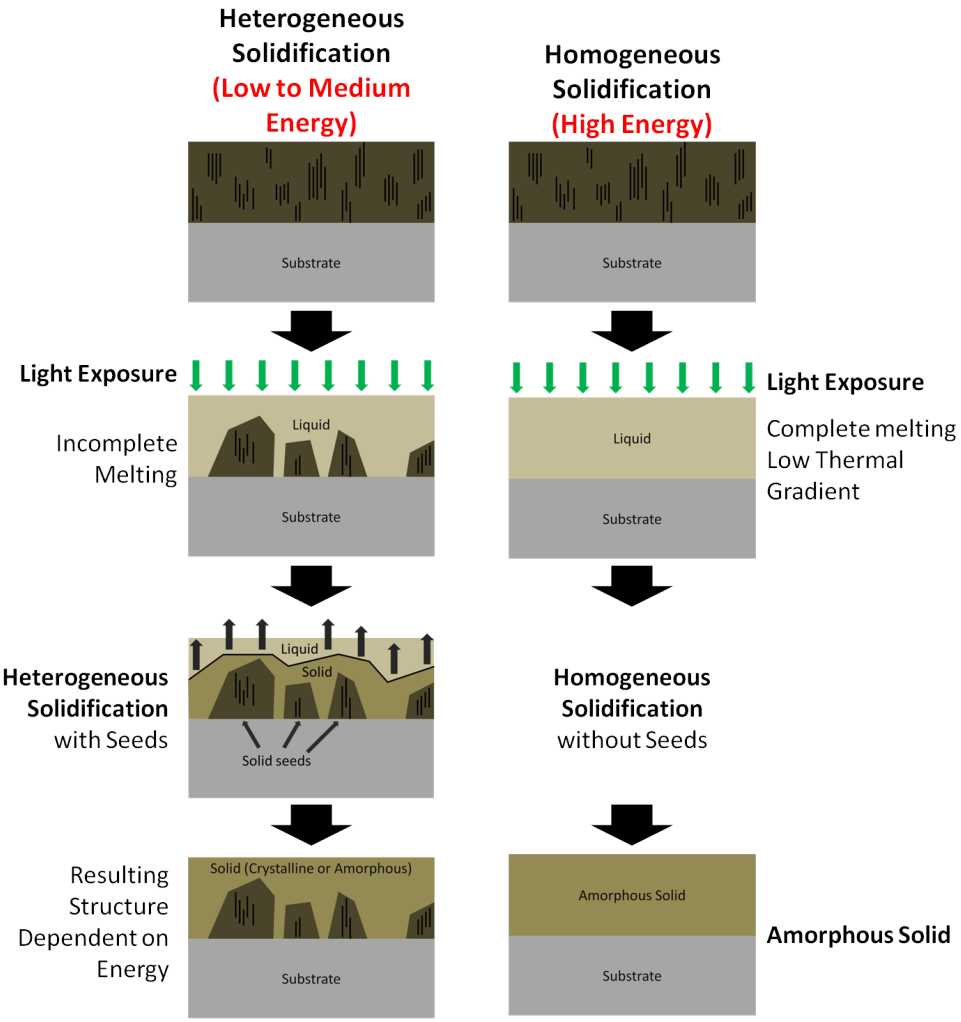

Figure 4.14: Schematic explaining the phase change process.

4.6 Comparison between the thick and thin films

Qualitatively, the trend followed by the I(D)/I(G) ratio values as the pulse energy density is increased is the same for the thin and thick films (Figure 4.15 (a)). However, we observe that the maximum I(D)/I(G) values have higher values in the thick film; moreover, maximum values are reached at higher energy densities. It suggests that more energy is required to obtain optimal graphitization in the thick film. On the other hand, higher I(D)/I(G) values suggest that the maximum graphitic content in the thick film is higher.

These two results can be explained by the phase change model proposed above. In the case of the thick film, more energy is required because the phase changes require partial or total melting in the bulk of the film; hence, a thicker film has a larger volume and requires more energy to melt significantly. The carbon crystallizes during solidification so a significant fraction should be melted to obtain large graphitic crystals *via* heterogeneous solidification. On the other hand, all or most of it should be melted to achieve amorphization *via* homogeneous solidification.

Moreover, if crystals grow from the melt, starting from nuclei dispersed in the volume, their ultimate size will be impacted largely by - other things being equal - the available space. In fact, other growing nuclei, or interfaces, are impeding further growth of the crystals [21]. Thus, more space eventually leads to larger crystals, which are detected by Raman spectroscopy and results in larger I(D)/I(G) ratio values.

This interpretation of the results on the I(D)/I(G) ratio values is also supported by comparing the evolution of the G peak position values for the two films (Figure 4.2 (b)).

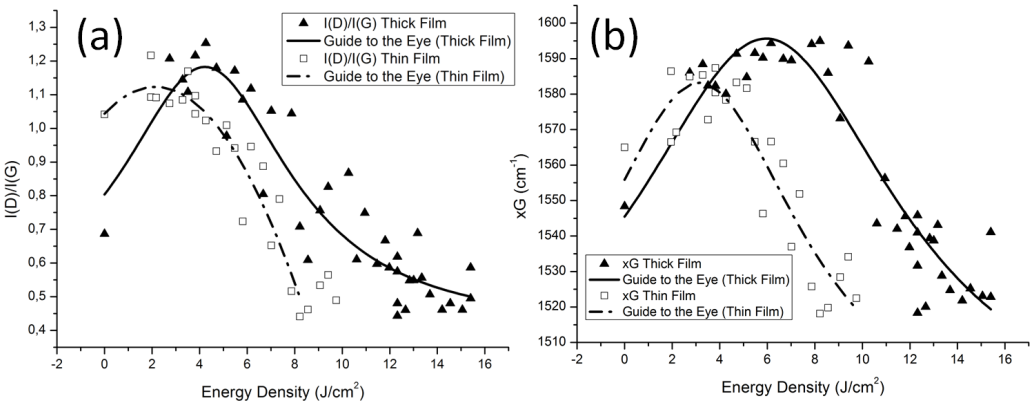

Figure 4.15: (a) Evolution of the I(D)/I(G) ratio as a function of the pulse energy density for the two thin films. (b) Evolution of the G peak position x_G as a function of the pulse energy density for the two thin films.

4.7 Femtosecond laser annealing of textured carbon

a Rationale for setting up a femtosecond laser-annealing experiment

In our study on nanosecond laser-annealing of textured carbon, we showed that we are able to graphitize and amorphize textured carbon by tuning the energy densities. But we also found that the cycling ability is limited due to important degradations, especially at the very high energy densities required for amorphization.

Hence, it would be of high interest for phase-change memory applications, to achieve laser-induced amorphization with low surface degradations. To avoid explosive boiling, we need to avoid reaching very high temperatures [41] while still achieving both graphitization and amorphization.

Ref. [7] discusses the physical processes behind laser-matter interactions and the timescales

required for each process. In particular, it is found that "Carrier-phonon scattering" (thermalization) processes occur on timescales of picoseconds (from 10^{-13} to 10^{-11} s, see Figure 1.2, page 27).

On the other hand, carrier excitation by the incident photons occur on timescales of tens to hundreds of femtoseconds (10^{-14} to 10^{-13} s). The time discrepancy between these two processes results in the possibility to excite a large number of carriers without heating the lattice. When $\approx 10\%$ (or more) of the electrons involved in the bonding of the lattice are excited (removed from bonding orbitals), the atomic structure is destabilized and may lose its configuration at room temperature. This process is demonstrated experimentally in the "melting" of GaAs by femtosecond laser pulses "long before phonon emission can heat the lattice to the melting temperature" [147].

The non-thermal nature of femtosecond laser-annealing, as well as its ability to induce disorder in a crystalline structure, is discussed in a number of other references [148]. Both are of interest to us, as our goal is to induce amorphization at low temperatures. For this reason, we set out to study the femtosecond laser-annealing of textured carbon.

b Femtosecond laser annealing: preliminary results

Details on the femtosecond laser annealing setup can be found in Section e, page 89.

First, we conducted annealing experiments on the silicon substrate; the confocal imaging system enabled direct visualization of the surface state before and after annealing (Figure 4.16). After annealing, a dark disk was found at the energetic centre (Figure 4.16 (b)), which is probably a hole (ablation). It is surrounded by a disk that is darker than the pristine silicon, and that probably corresponds to the "annealing" and "modification (oxidation/amorphization)" regions discussed in [18] (Figure 1.10, page 44).

We then moved on to anneal textured carbon thin films for different times and at dif-

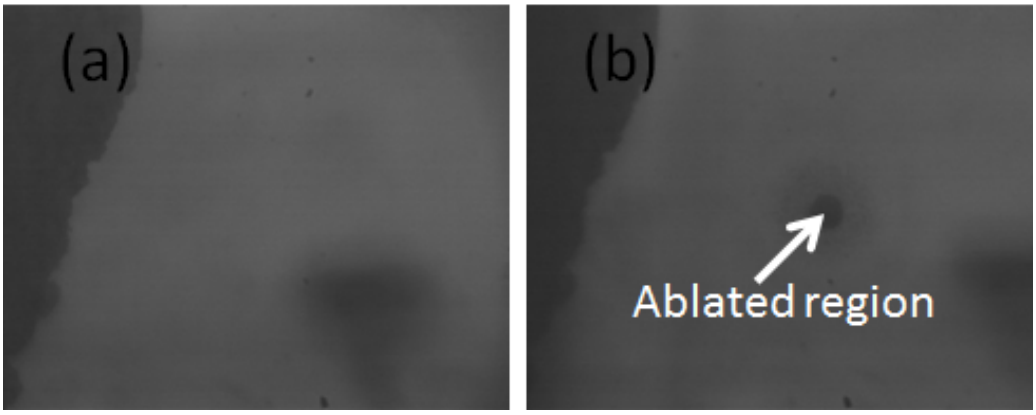

Figure 4.16: Femtosecond laser-annealing of the silicon substrate, during 15 s at 70% of the power output from the polarizer. (a) Image of the surface before annealing. (b) Image of the surface after annealing.

ferent power densities. Preliminary results are displayed in Figure 4.17. Our interpretation of these results is limited, as our efforts on femtosecond laser annealing of textured carbon are just the beginning of efforts conducted by our group on femtosecond laser annealing of carbon allotropes. Ongoing efforts are done by Mr. Ange Maurice, another PhD student at NTU, under the supervision of Prof. Beng Kang Tay.

Figure 4.17 (a) shows the surface state after laser-annealing at different locations for different powers and times. Larger powers and/or times lead to bigger structures. Typically, the geometry of the resulting features resembles the beam profile shown in Figure 2.9 (a), confirming the fact that the focusing of the laser is not ideal.

We also used the movable stage to translate the sample in the plane normal to the laser beam during laser-annealing, in order to obtain the line shown in Figure 4.17 (b). The fringes observed on the larger structures in Figure 4.17 (a) and Figure 2.9 (a) were still present. To characterize the atomic structure of these features rapidly and non-destructively, we used Raman spectroscopy.

The Raman spectra evolve drastically when characterizing matter along the line drawn in Figure 4.17 (b). The first five spectra do not display any carbon peak, most probably because the carbon was completely ablated. Then, from the sixth spectrum, a strong

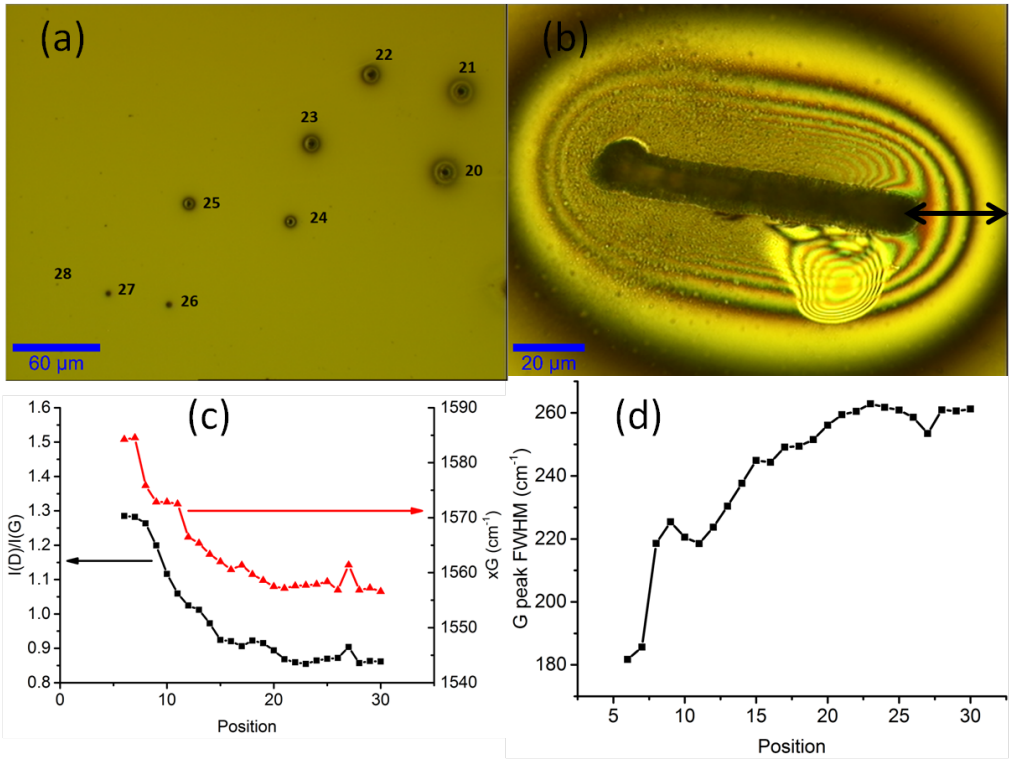

Figure 4.17: Femtosecond laser-annealing of textured carbon. (a) Optical image of laser-annealed locations with different powers and times. (b) Optical image of a laser-annealed location. During annealing, the sample was translated in the plane normal to the laser beam to draw a line. The black arrow indicates the location where several Raman spectra were acquired (Raman mapping). (c) Evolution of the extracted I(D)/I(G) ratio and G peak position as a function of the position on the line defined in (b) (starting from the left). (d) Evolution of the extracted G peak FWHM as a function of the position on the line (starting from the left).

carbon signal is detected, enabling data treatment, fitting and extraction of the critical parameters I(D)/I(G), x_G and $FWHM_G$.

First of all, we note that the width of the G peak is always much larger than 100 cm^{-1}, hinting that the interpretation of the Raman spectra must be done according to Stage 2 or 3 of the 3-Stage model of Ferrari *et al.* [74].

The Raman data seem to indicate that the film is much more graphitic when annealed at higher annealing energies. In fact, Figure 4.17 (c) shows that both the I(D)/I(G) ratio and G peak position values decrease as the Raman signal is mapped from the center of energy to the region outside of the annealed area (decreasing energy density). In Stage-2 of the 3-Stage model, larger values of I(D)/I(G) and x_G indicate a higher graphitic content.

This interpretation is supported unambiguously by the evolution of the G peak width as a function of position (Figure 4.17 (d)). Its increase is typically caused by the decrease of the average crystal size.

b.1 Conclusion of the femtosecond-annealing study

Due to their higher complexity, current femtosecond lasers are more expensive than nanosecond or continuous-wave lasers; consequently, there are few research groups currently using femtosecond lasers to induce phase changes in matter. Hence, commercial femtosecond laser systems are not designed for such applications.

We had to purchase and use several optical components to customize our laser system, effectively making it an efficient femtosecond laser-annealing system. It is now possible to control the power density, translate the sample in three directions, and rapidly image the sample before and after laser-annealing.

Efforts to improve and use the femtosecond laser-annealing setup are still ongoing: recently, there have been new additions to the setup such as a mechanical shutter for better control of the annealing time and a motorized stage with an incremental resolution of 30 nm has been purchased. Another PhD student, Mr. Ange Maurice, is now handling the

femtosecond laser-annealing setup, and is conducting annealing experiments on carbon allotropes.

Regarding the laser-annealing of textured carbon, the preliminary results are neither negative nor encouraging. The main goal is to demonstrate femtosecond laser-induced amorphization with low surface degradations. Preliminary results tend to demonstrate graphitization rather than amorphization, however the energy densities that we used so far are clearly too high to induce changes without degradations. Moreover, the only characterization technique used so far is Raman spectroscopy, a powerful yet limited technique when used alone. For that reason, in this Chapter, we used several other characterization techniques during our study of nanosecond laser-annealing of textured carbon.

More work is needed to reach conclusions. In particular, an interesting study would be to monitor directly the temperature of the film during laser-annealing, by using, for example, an infrared camera. While some references [7, 148] explicitly state that femtosecond laser-annealing is a non-thermal process, it is also a known experimental fact that things can be burnt (exothermal reaction) by femtosecond lasers. A reference [149] also states that the non-thermal behavior is reached only when the repetition rate is low (lower than 10 thousand pulses/second). In our case, the repetition rate is 80 million pulses/second.

4.8 Conclusion

We achieved both **graphitization** and **amorphization** by applying nanosecond laser-pulses on textured carbon thin films. This opens the way toward the **development of optical memories** based on carbon, which could be more resistant to extreme conditions than currently used chalcogenide-based optical memories.

The mechanism behind the reversible phase change relies on crystallization kinetics of carbon in the presence of solid catalysts. When the material cools down in the presence of remaining solid matter, it forms crystals (**heterogeneous solidification**), while when

it cools down without remaining solid matter (**homogeneous solidification**), it remains amorphous (Figure 4.14).

We also found that the **cycling ability is limited**. It is due to the **degradations** induced by the large temperatures, and in particular **phase explosion** at very high energy densities.

For applications requiring large cycling abilities, the degradations have to be minimized. To achieve that, using femtosecond laser pulses rather than nanosecond laser pulses could be a solution, as femtosecond laser pulses are believed to induce far less heating in matter, while still changing its crystalline structure [7, 147].

Chapter 5

A non-volatile graphene memory by planar electro-mechanical switching

5.1 Goals

In the previous two chapters, we demonstrated that carbon thin films can take at least two different crystalline structures (graphitic and amorphous) with different properties, and that their structure can be switched between those two by applying large optical power densities (light pulses).

The goal of this chapter is to demonstrate that another carbon allotrope (graphene) can take **two configurations** when subjected to large electrical energy densities. This would open a route toward the development of **electronic memories**; after demonstrating these two states and for this specific application, we wish to study the **cycling ability**, the **volatility**, the **switching speed**, and the contrast (**I_{ON}/I_{OFF} ratio**).

Then, to be able to assess the "real" potential of our devices, we also need to understand

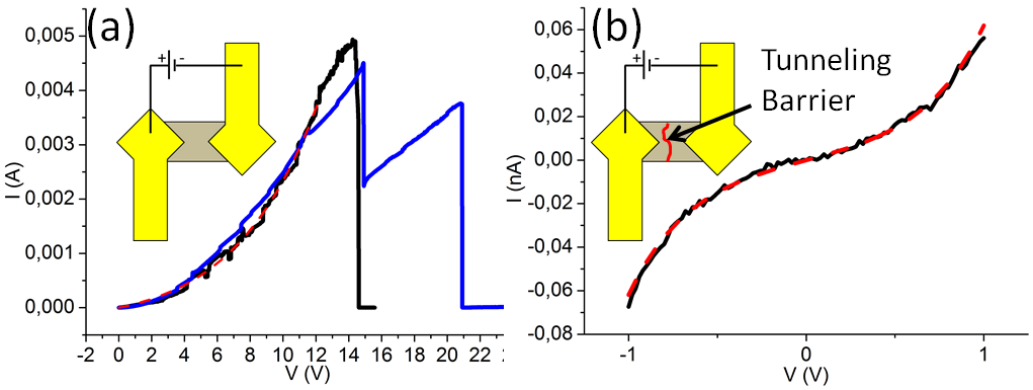

Figure 5.1: (a) Electrical breakdown curves. Blue: vacuum breakdown. Black: air breakdown. Red-dashed: fitting with the VRH model of conduction. *Inset*: schematic showing the device configuration. (b) Low voltage I-V curve of a device after electroforming (black). It is best fitted by a Simmons model of tunneling (red-dashed curve). *Inset*: schematic showing the device configuration, with a red line showing the tunneling barrier.

the **mechanisms leading to this reversible switching**. For that purpose, experimental techniques will be used to **visualize the switching phenomenon**.

Lastly, the development of a **quantitative model** would enable to estimate the optimal performances of our devices to assess their **potential as a competitor to other approaches to memory**.

5.2 Electrical breakdown

a I-V curves before, during and after breakdown

a.1 Pristine devices

Details on the fabrication of the devices are provided in Section c.2, page 84. A schematic representation of a device is shown in the *inset* of Figure 5.1 (a).

When applying a first voltage sweep accross the two electrodes of a device, the current tends to increase in a non-linear manner and small current jumps are observed (especially visible in the black I-V curve in Figure 5.1 (a)).

These current jumps highlight small resistance drops due to current annealing of the contacts and/or the graphene, resulting in the removal of impurities and a decrease in contact resistance [150].

For a perfect graphene lattice and ohmic contacts, a linear trend is expected for the I-V curve; however, it is not what we observe here. The curve is found to be best-fitted by a variable range hopping (VRH) model (Figure 5.1 (a) red dashed).

Raman characterization maps show that the graphene quality is far from homogeneous, with numerous regions of μm size with contrasting colours (brighter or darker, see Figure 5.2 (a)). These contrasts can be partly assigned to multilayer graphene, as acknowledged by Graphene Supermarket (it is stated on their website that more than 90% of the film is mono-layer graphene, while the remaining 10 % is made of "occasional small multilayer islands").

Nevertheless, AFM images after fabrication of the devices show that some regions are much thicker than expected (graphene alone is ≈ 0.34 nm thick), suggesting that a fraction of photoresist deposited during the fabrication steps remains.

The photoresist can readily interact with perfect graphene to form defects [151] acting as traps for the electrons, thus resulting in the non-linear I-V curve (Figure 5.1 (a)). Moreover, as current levels remain high, the density of defects must be low: the effective path for the electrons is comprised of large conductive metallic grains separated by defects, as supported by Raman spectra showing that the defect density is very low (D peak almost 0, *e.g.* Figure 5.2 (c) black bottom curve) and the good fit with the VRH model (Figure 5.1 (a), red dashed line). The VRH conduction model often applies to conductors such as reduced graphene oxide that are composed of conductive crystals separated by defects [152].

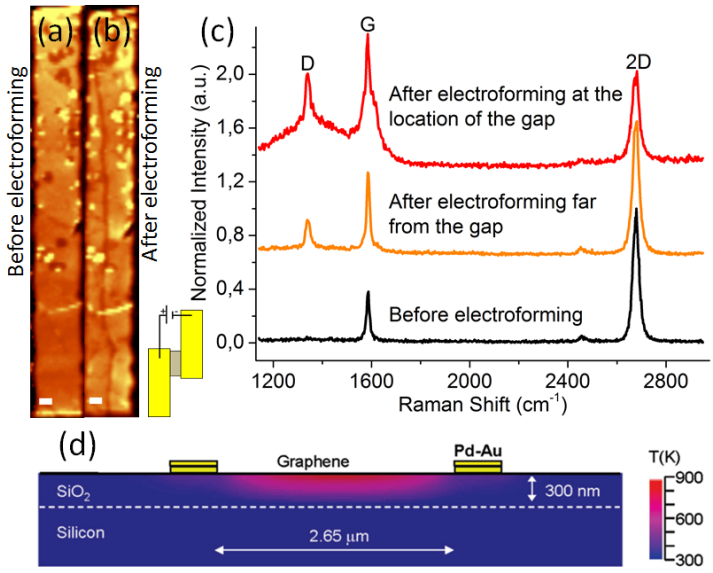

Figure 5.2: Degradations induced in a graphene two-terminal device during electroforming. Raman maps of a device before (a) and after (b) electroforming. The color of each pixel represents the value of the 2D peak intensity. (c) Three representative spectra. (d) Simulation of the temperature field in a graphene FET when the dissipated electronic power equals 161.3 kW.cm^2. Reproduced from [122].

a.2 Electrical breakdown (electroforming)

To summarize, at low to medium voltages, the current keeps on increasing with the voltage, following the VRH model.

Then, we observe a large current drop at high voltages (Figure 5.1 (a)). This current drop can occur in one or several steps. For example, Figure 5.1 (a) shows electroforming data for two devices for which electroforming occurs in one step (in air, black curve) and two steps (in vacuum, blue curve).

Interestingly for applications, this resistance increase was found to be non-volatile. In other words, one can remove the voltage source for a significant amount of time, and measure the resistance of the device again: the measured resistance remains as high as it is right after the current drop.

By contrast, in a volatile switch, this resistance increase would not be permanent.

In the rest of the Chapter, we call this new state of the device the high resistance state (HRS).

a.3 Electrical conduction after electroforming

In a majority of cases, the current levels in devices after electrical breakdown were not detectable, because they are lower than the detection limit of the equipment ($\approx$ 100 fA).

Nevertheless, in some cases, we detected a significant amount of current. For example, Figure 5.1 (b) shows a low voltage I-V curve of a device after electroforming.

The trend of the curve is non-linear, however it cannot be fitted satisfactorily with a VRH conduction model anymore.

We found that the best fit is obtained with a Simmons model for tunneling [153, 154], suggesting that the electroforming step creates an energetic barrier through which charge carriers tunnel.

The Simmons model of tunneling enables to estimate the barrier size and energy. In general, we find that barrier sizes range from 1 to 2 nm, and barrier heights range from $\approx$ 3 to 5 eV. In most devices, currents were undetected because the barrier size is larger than 2 nm, as is also discussed in [155]. Because the current dependence on the width of the barrier is exponential, barrier widths larger than 2 nm invariably lead to negligible amounts of currents.

b Scanning electron microscopy images of the electroformed devices

In a SEM, it is challenging to directly observe the energy barrier. However, we can observe an interesting phenomenon by zooming close to one electrode. Zooming leads to a decrease of the beam size, hence the density of electrons tends to increase. As the concentration of negative charges (electrons) on the surface increases, charging effects may occur: the surface becomes negatively charged and repels the incoming electrons because of Coulomb repulsion. As the incoming electrons do not interact with the surface anymore, fewer informations can be obtained from the microscope image, creating a contrast between areas with charging effects and areas without charging effects.

In our case, charging effects are of interest because they can give information about where the electrons can diffuse when their surface density increases locally. It can be seen in Figure 5.3 (b), where a high contrast is observed between the right and left sides of the flake, that a barrier to the diffusion of electrons exists between the right and the left side of the device.

This barrier crosses the graphene band from one side to the other, inhibiting the current flow and resulting in the drastic resistance increase we observed during voltage sweeping (Figure 5.1 (a)). Overall, the barrier direction (from top to bottom in Figure 5.3 (b)) is perpendicular to the applied electric field (from left to right in Figure 5.3 (b)) but locally, it is following an irregular path with apparently random changes in direction every few μm.

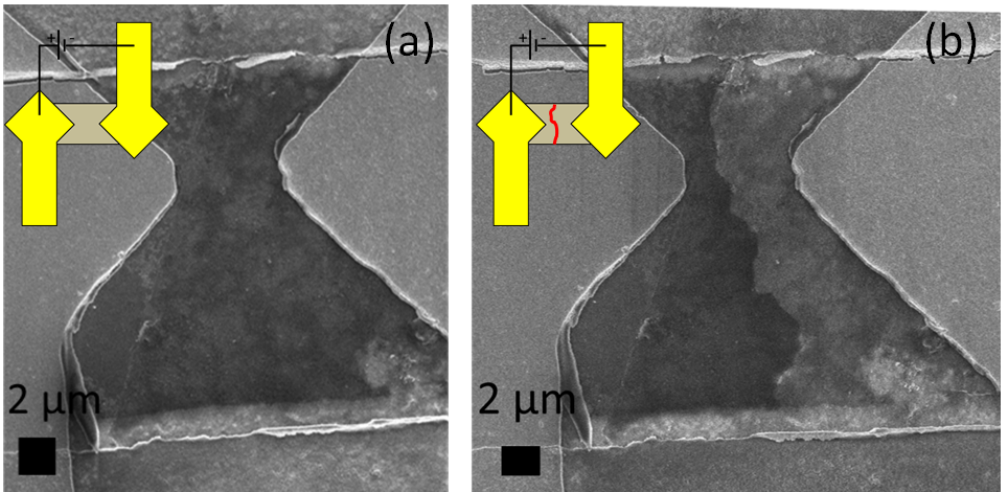

Figure 5.3: SEM image of an electroformed device showing that after electrical breakdown, electrons cannot flow from the right side to the left side of the graphene flake. *Inset*: schematic of the device. The graphene is brown and the electrodes are yellow. (a) Device before electrical breakdown. (b) Device after electrical breakdown. *Inset*: schematic of the device with the energy barrier drawn in red.

Hence, the charging effect in the SEM is a good tool to visualize the shape of the conduction barrier; however, it does not enable to uncover the nature of the barrier because it only shows **where** the electrons stop (not **what** stops them). Moreover, the SEM itself cannot resolve the features of the barrier: without charging effects, the graphene band appears completely homogeneous in the SEM (similar to the image of the pristine device, Figure 5.3 (a)) so we cannot obtain any information about the conduction barrier.

c Raman maps of the electroformed devices

To study the crystalline structure of the energy barrier and the surrounding graphene, we used Raman spectroscopy and obtained maps of the devices before and after electroforming (Figure 5.2 (a) and (b)).

In Raman maps of the intensity of the 2D peak, the energy barrier appears as a dark, irregular line crossing the device from side to side (Figure 5.2 (b)). A darker color means

a lower 2D-peak intensity so the 2D-peak intensity is lower at the location of the barrier.

It is also broader, implying that the quality of the graphene is lower, either because there are more defects in the crystalline structure or because the crystalline structure is disrupted (edges). The evolution of the D and G peaks leads us to the same conclusions: the electroforming process degrades the structure (Figure 5.2 (c)).

Before electroforming, the overall graphene quality iss high, with sharp peaks and a very small D peak. After electroforming, the overall graphene quality is impacted, even away from the conduction barrier: Figure 5.2 (c) shows two representative spectra (before electroforming: bottom, black; after electroforming: middle, orange) of the graphene before and after electroforming.

Thus, the electroforming process leads to degradations of the crystalline structure of graphene: this degradation is more important at the location of the conduction barrier, but it is impacting the whole graphene flake between the electrodes.

The literature on thermal dissipation in graphene FETs [122] discusses the impact of the Joule effect on the temperature field in the graphene (and the substrate) when an electric field is applied accross the graphene. It is found that the highest temperatures are reached at the center of the device, far away from the electrodes which act as heat sinks (Figure 5.2 (d)). Thus, the highest temperatures are reached in the middle, and we note that the conduction barrier tends to appear in the middle of the device as well. This strongly suggests that the electroforming process is assisted by heat, as discussed in other references on electrical breakdown of graphene [108, 109, 122, 155], and CNTs [4, 110, 111].

Using the linear relation between electronic power and maximum temperature provided in the study by Freitag *et al.* [122], we can estimate the temperatures reached during the electrical breakdown of our devices. Our devices break down at power densities of 280 $\pm$ 140 kW.cm^{-2} (vacuum breakdown) and 80 $\pm$ 30 kW.cm^{-2} (air breakdown), which correspond to temperatures of $\approx$ 1300 $\pm$ 750 K (vacuum) and 616 $\pm$ 231 K (air).

Monolayer graphene has been reported to sublimate at temperatures as low as $\approx$ 1,050

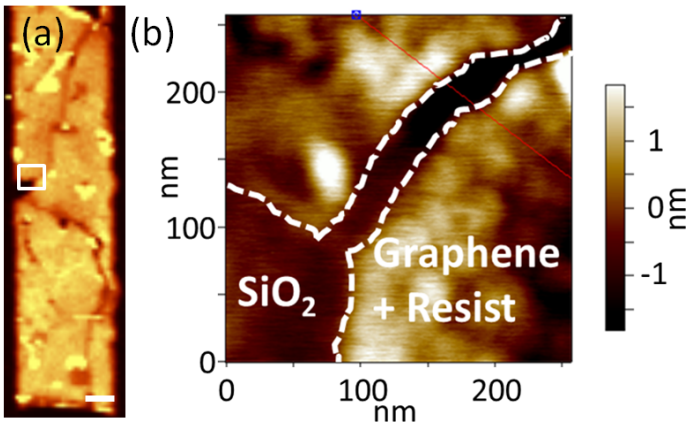

Figure 5.4: AFM characterization of the tunneling barrier. (a) Raman map showing the tunneling barrier. Scale bar: 2 μm. (b) AFM image on the location indicated by the square in the Raman map (a).

K [122] (in vacuum). Moreover, it is etched at lower temperatures in presence of oxygen (450 °C = 723 K) [142]. Thus, we can conclude that the electroforming process occurs at temperatures high enough for substantial sublimation (vacuum) or oxidation (air) to occur.

The lower temperatures needed for oxidation as compared to sublimation in vacuum may explain the discrepancy between the power densities required for electroforming in air and in vacuum. We will obtain more information on the nature of the conduction barrier and on its mechanism of formation by using an AFM to image the barrier and its surroundings.

d Nature of the conduction barrier formed by vacuum electroforming

Figure 5.4 (b) is an AFM image showing the surface morphology of the graphene at the location of the conduction barrier, for a device that has been electroformed in vacuum. The nature of the energy barrier is uncovered: it is a gap into the graphene, whose width varies but is typically on the order of a few tens of nm.

We also found that the electroforming process is energetic enough to induce damages in the SiO_2 substrate. In Figure 5.4 (b), we can deduce the height of the substrate by looking at the lower-left region labelled "SiO_2". By looking at the height profile in the nano-gap, starting from the lower-left region and going to the top-right region, we see that the height is decreasing further, suggesting that the substrate has been excavated by the electroforming process. This finding is consistent with the fact that the graphene structure seems degraded as a whole. The electroforming step is a very energetic process that results in degradation of the graphene and the SiO_2 substrate.

Hence, during vacuum electroforming *via* sublimation of the carbon atoms, a nano-sized gap forms from one side of the graphene band to the other until the electrical conductivity is drastically reduced.

e Nature of the conduction barrier formed by air electroforming

While the Raman signature of the conduction barrier is similar for both vacuum and air electroforming processes (Figure 5.5 (a) and 5.4 (a)), it is much harder to detect the presence of the barrier by atomic force microscopy when the electroforming is done in air (Figure 5.5 (b)). Contrary to the case of vacuum electroforming, plotting the height map does not enable to resolve the conduction barrier (Figure 5.5 (b)).

On the other hand, plotting the phase map rather than the height map enables to visualize the conduction barrier (Figure 5.5 (c)), implying that the matter at the location of the conduction barrier has different mechanical properties.

Thus, while vacuum electroforming occurs through the sublimation of carbon atoms resulting in a "crater" of missing matter, air electroforming occurs without the appearance of such a crater. However, air electroforming also results in a large conductance drop, as well as Raman and AFM phase imaging signatures.

In the presence of oxygen, the material has locally underwent a change which resulted

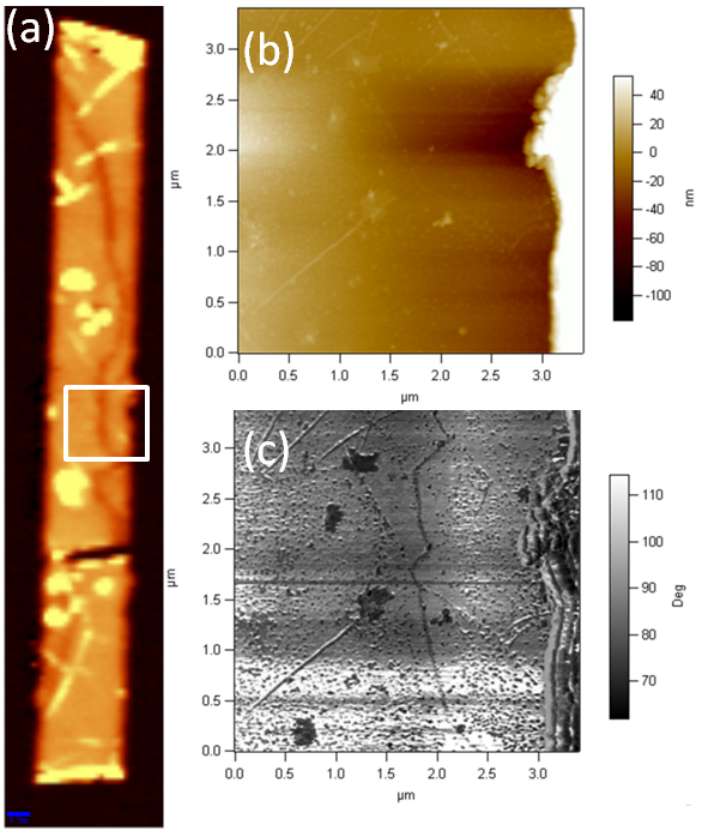

Figure 5.5: Electroforming in air. (a) Raman map of the 2D peak of a device after air electroforming. (b) AFM height image corresponding to the white rectangle area shown in (a). (c) AFM phase image corresponding to the white rectangle area shown in (a).

in a degraded carbon structure and a large drop in conductance. Oxidation of carbon is known to occur through the emission of gaseous CO and CO_2 molecules, but intermediate steps occur which result in the absorption of oxygen atoms and the degradation of the structure, as discussed in Chapter 3.

During air electroforming, carbon atoms are removed *via* the emission of CO and CO_2 molecules and at the same time, oxygen atoms are absorbed. Both these processes (matter loss and oxidation) are impeding the conduction of electrons, as graphene oxide is an electrical insulator [90]. Hence, wherever carbon atoms are missing, resulting in the formation of reactive carbon bonds, oxygen atoms effectively fill the gap. This results

in difficulties in resolving the conduction barrier by AFM, as oxygen (empirical atomic radius = 60 pm) and carbon (empirical atomic radius = 70 pm) atoms have similar dimensions.

Hence, during air electroforming, a conduction barrier forms that is made of oxygen atoms filling the gap created by the emission of gaseous CO and CO_2 molecules. Both the lack of carbon and its oxidation results in a barrier to conduction.

5.3 Memory effect

a Reading and writing

The SET process is the process during which a memory changes its state from a HRS to a low resistance state (LRS). The RESET process is the process during which a memory switches from a LRS to a HRS. The process of switching between two states is called "writing" data. To retrieve the data, it is necessary to "read" the resistance of each memory device. For that, here we typically apply a 1V pulse or sweep (see Figure 5.6 (b) *inset*): such a voltage enables a significant current to flow and be measured to measure the resistance R = V/I while avoiding heating up the device (Joule effect).

First, we focus on ways to SET and RESET devices while applying a voltage sweep to understand the switching mechanism; then, we describe how to SET and RESET devices by applying voltage pulses, which is more interesting for the development of memory applications.

b From HRS to LRS: the SET process

The HRS achieved after electroforming is non-volatile but not definitive. Each device can be returned to a low resistance state (LRS) by applying voltage sweeps and pulses (SET process).

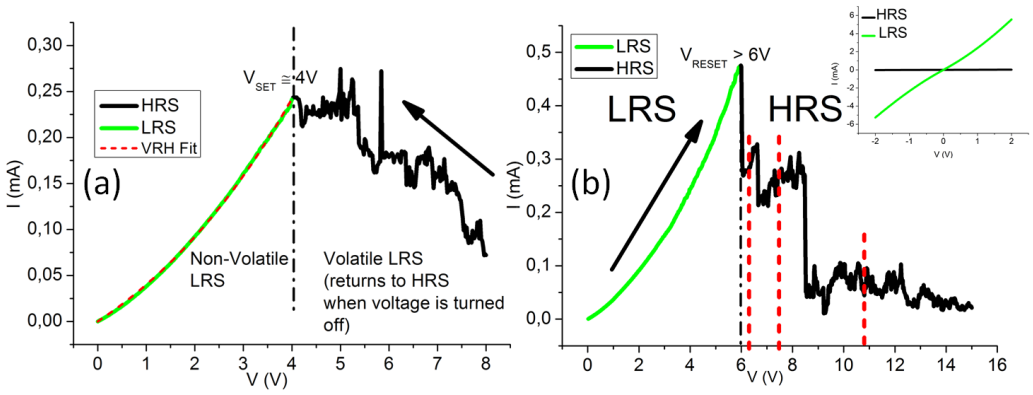

Figure 5.6: SET and RESET processes. (a) SET process. The voltage is swept downward from 8V to 0V and the current is measured. (b) RESET process. The voltage is swept upward from 0V to 15V and the current is measured. *Inset*: Representative low voltage I-V curve of a device in its HRS and in its LRS. Note that it is not the same device as that of (a) and (b).

Figure 5.6 (a) is an I-V curve showing an effective SET process. The voltage was swept downward from 8V to 0V. When the sweep starts (right part of the curve, black line), the device is in its HRS. The first striking feature is that current levels are immediatelly very high (> 0.05 mA) as compared to those reached right after electroforming (less than 1 nA at 1V, Figure 5.1 (b)).

Thus, it seems that the device switches from the HRS to a LRS seemingly instantaneously (faster than the temporal resolution of the equipment).

As the applied voltage keeps on decreasing, the current increases (Figure 5.6 (a)), implying that a process is occurring that reduces the resistance of the device. This process results in a very noisy current increase, as can be seen in the black region of the curve.

This I-V curve is representative of the SET process for all of our devices. We note that if the decreasing voltage sweep is stopped in this black, noisy region, the resistance change is **volatile**. In other words, the device does not retain its LRS if the sweep is stopped, and the device remains in its HRS.

Nevertheless, we are able to obtain a **non-volatile** LRS if, instead of stopping the decreasing voltage sweep in the black region of the curve, we stop it in the green region

(Figure 5.6 (a)). At a threshold voltage (here, $\approx$ 4V), the current stops behaving in a noisy manner and starts decreasing with the voltage in a smooth manner, suggesting that the device is now stabilized in its new state.

The new state of the memory can be read by applying a low voltage and measuring the current. Low-voltage I-V curves of a device in its HRS and its LRS are shown in the *inset* of Figure 5.6 (b).

Electrical conduction in the new LRS is best-described by a VRH mechanism (Figure 5.6 (a), red dashed curve), as is the conduction in the pristine device.

c From LRS to HRS: the RESET Process

We can then get the device back to a HRS by applying an upward voltage sweep (Figure 5.6 (b)). The I-V curve of the RESET process was found to be very similar to that of the electroforming process, even though the current in the right part of the curve (after the initial current drop) was much noisier.

At low voltages, the I-V curve is well-fitted by a VRH model, as the LRS is non-volatile (the device is still in the same state as it was at the end of the SET process). At higher voltages, the current drops abruptly, typically in several steps. Even at the first current drop, the new resistance state is non-volatile. However, the resulting resistance might not be as high as that obtained after electroforming if the voltage is stopped too soon. Multiple resistance states can be obtained by stopping the RESET process at different voltages. For example, three different high resistance states can be expected from the RESET process shown in Figure 5.6 (b) if the voltage is stopped at the three different voltages labelled with red dashed lines. In the remaining discussion, we call all of these intermediate states "HRS" and we will not study in detail these resistance variations.

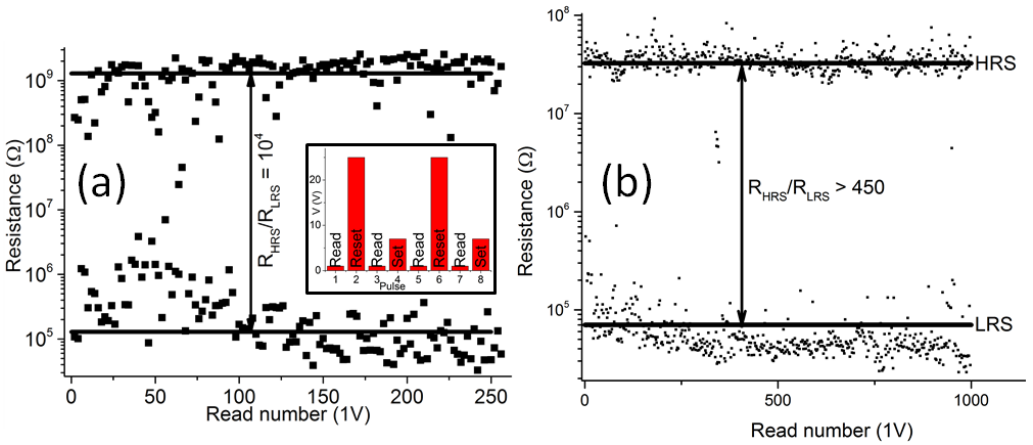

Figure 5.7: Endurance tests on two devices. (a) More than 100 cycles are achieved. V_{read} = 1V (10 ms) , V_{SET} = 7V (1s), V_{RESET} = 25V (10 ms). (b) 500 cycles are achieved. V_{read} = 1V (10 ms) , V_{SET} = 7V (10 ms), V_{RESET} = 27V (10 ms).

d Switching with voltage pulses

Most applications require devices to switch ON (LRS) and OFF (HRS) rapidly. The fastest possible excitation is a single voltage pulse (ideally, a Dirac delta function), so we set out to switch our devices with voltage pulses rather than sweeps.

Alongside SET and RESET pulse voltages, a reading pulse voltage has to be defined, which is used to read the resistance state without changing it.

Moreover, from the voltage sweep data, we find that the RESET voltage must be defined higher than the SET voltage. For example, for the device switched in Figure 5.6 (a) and (b), the SET voltage is $\approx$ 4 V and the RESET voltage is > 6V. To obtain a HRS with a resistance as high as possible, it is better to apply much higher voltage pulses.

Hence: $V_{read} < V_{SET} < V_{RESET}$.

e Endurance and I_{ON}/I_{OFF} ratio values

e.1 Principle

Figure 5.7 (a) is a graph presenting the results of an endurance test, during which voltage pulses were applied subsequently in the following sequence:

- V_{read} (1V): read the resistance

- V_{SET} (7V): from HRS to LRS

- V_{read} (1V): read the resistance

- V_{RESET} (25V): from LRS to HRS

Here, the device starts the sequence in the HRS so the first resistance value read at V_{read} (1V) is high (HRS). Then, a V_{SET} (7V) pulse is applied, switching the device from its HRS to its LRS. A second V_{read} pulse is then applied to measure the new resistance state (LRS). Then, a V_{RESET} (25V) pulse is applied to switch the device from its LRS to its HRS. The sequence is then repeated.

Figure 5.7 (a) displays the resistance values read at V_{read} (not at V_{SET} or V_{RESET}). The goal of this test is to evaluate how many times devices can switch before failing.

e.2 Results

This particular device could switch more than 100 times, which might be performant enough for some long-term data storage applications (similar to the use we make of a DVD), but not performant enough for computing applications (*e.g.* SRAM, DRAM or Flash). If these memories are used for computing applications, a better understanding of the failure mechanism, and how to control it, must be achieved.

e.3 Limitations and Solutions

The cycling ability of devices tends to increase for lower I_{ON}/I_{OFF} values. As discussed above, the HRS can be controlled by setting different values of V_{RESET} (see Figure 5.6 (b), red dashed lines). Hence the I_{ON}/I_{OFF} can be controlled. As devices tend to be more durable for lower values of the I_{ON}/I_{OFF} ratio, a trade-off between cycling ability and I_{ON}/I_{OFF} ratio must be made, depending on the application. The best endurance test we conducted so far shows that a device can be switched more than 500 times with I_{ON}/I_{OFF} ratio values above 450 (Figure 5.7 (b)).

Other than the limited endurance, we also observed a large variability in the resistance levels, both high and low. It is especially striking in Figure 5.7 (a), especially for the first ≈ 50 cycles.

If this variability is intrinsic to the functioning of our devices and cannot be corrected, it strongly limits the field of applications of our memory devices. In fact, current computers rely on error-free algorithms to achieve their best performances: silicon transistors are so reliable that algorithms relying on virtually no reading or writing error can perform well, even when the number of calculations reach billions of iterations. This is a huge issue for graphene-based nano-gap devices, but not only, as other memory devices are performing well but cannot offer the same kind of reliability that silicon transistors do.

The semiconductor industry is well aware of this issue, which also limits the field of applications of current approaches to memory relying on silicon transistors (`http://spectrum.ieee.org/semiconductors/processors/the-era-of-errortolerant-computing`) and approaches relying on probability rather than pure determinism are proposed to design error-tolerant circuits in the near future. This would enable to diminish the power consumption of circuits, as much more power is required to insure 100% reading and writing accuracy, as compared to, say, 99% accuracy. This evolution parallels the shrinking of devices to dimensions where quantum effects start taking place; quantum phenomena are intrinsically random, as opposed to classical phenomena, effectively making predicting the outcome of a single event with 100% accuracy

impossible.

e.4 Possible Causes of the Limitations

We recall that high energies are deployed during the electroforming process, as evidenced by degradations to the graphene structure and SiO_2 substrate; moreover, the similarity between their I-V curves suggests that the RESET and electroforming processes share similar attributes. It suggests that each V_{RESET} pulse degrades the device, eventually leading to failure. Logically then, the usage of lower V_{RESET} values enable longer tests, because they degrade the device less at each cycle. A better understanding of the switching mechanisms is necessary and described below.

5.4 Development of an electro-mechanical model

a Closing the nano-gap

To develop a detailed model of operation for our devices, we need a basic understanding of the writing steps (SET, RESET) as well as the static states (HRS, LRS) and how they achieve their stability (non-volatility).

Some consistent facts are:

- in the HRS, a nano-gap is opened, impeding conduction

- in the LRS, the conduction mechanism is the same as that in pristine graphene (VRH)

- resistance values in the LRS can be very low (see Figure 5.6 (b), *inset*, for a device where R $\approx$ 500 Ω in the LRS). We have not studied in detail the experimental conditions for which small LRS resistance values are obtained.

- for switching, the required duration of SET pulses is longer than that of RESET pulses, especially if high I_{ON}/I_{OFF} ratio values are required (Figure 5.7).

For large currents to flow in the LRS, there are two possible paths. Either the current flows through the SiO_2 substrate, or it flows through the graphene (see Section c.2.1, page 70 for a detailed discussion).

It is believed that SiO_2 switching occurs through the growth and shrinking of silicon nanocrystals, with slowest reported switching speeds of 500 ns.

In this study, the switching speed is much slower, either for the SET or the RESET process, with values on the order of 10 ms for the fastest devices (20,000 times slower). Pulse durations on the order of the second were often required to achieve switching (*e.g.* the duration of the SET pulse in Figure 5.7 (a) is 1s).

The timescales required here are more in line with those reported in [85] and [87] (see Table 1.6 page 72), where the reported switching mechanism is reversible movements of the graphene flakes. Moreover, as discussed in Section c.2.1, page 70, Zhang *et al.* unambiguously showed that the switching of a graphene nano-gap device was occuring entirely through the movements of the graphene flakes [87].

Finally, the fact that the conduction mechanism (VRH) was the same in the pristine devices and in the LRS is consistent with a conduction through the graphene in both cases.

For these reasons, we believe that the switching mechanism shown here is linked to conduction through graphene in the LRS, and that the susbtrate plays no central role in the switching.

a.1 AFM characterization of the nano-gap

A way to test this hypothesis is through AFM characterization of the nano-gap both in the LRS and in the HRS. If conduction in the LRS occurs through the graphene, the nano-gap should be found to be much smaller in the LRS as opposed to the HRS. AFM images of the nano-gap before and after RESET are shown in Figure 5.8.

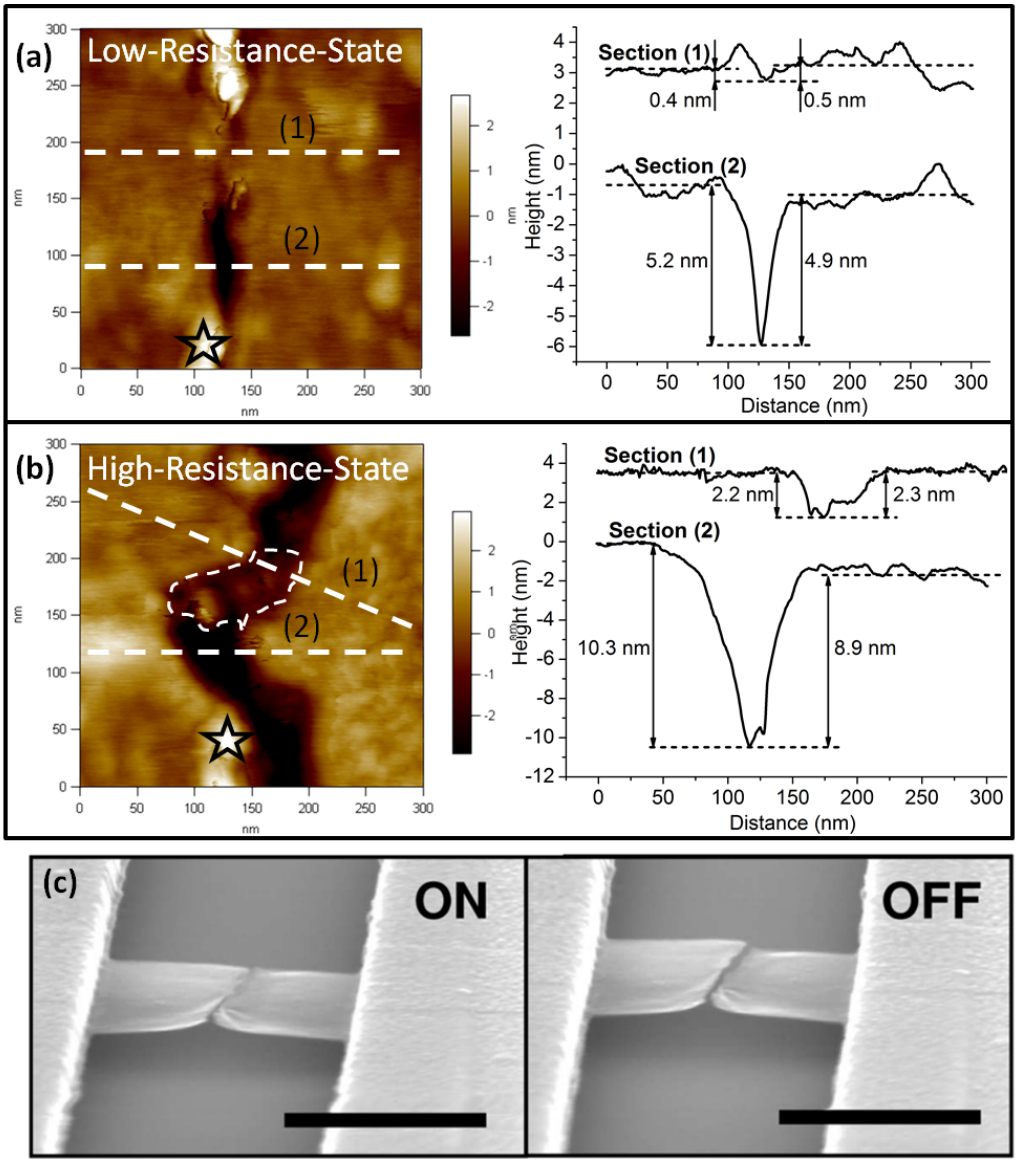

Figure 5.8: AFM images of a nano-gap before and after RESET. (a) AFM image and corresponding sections of a nano-gap in the LRS. (b) AFM image and corresponding of a nano-gap in the HRS. (c) SEM images of a suspended graphene device in the LRS (left) and HRS (right). Reproduced from [87].

Figure 5.8 shows that the gap is much larger in the HRS as compared to the LRS. Moreover, it seems likely that the two graphene flakes in the LRS are connected at some locations. For example, section (1) shows a small valley 0.5 nm deep at the location of the nano-gap, which is $\approx$ 5 nm deep everywhere else. This valley is most probably made of graphene crossing the gap.

What is clear from Figure 5.8 is that the two graphene flakes (separated by the nano-gap) move during switching, either toward each other during the SET process, or apart from each other during the RESET process. These characterization results are qualitatively similar to those reported in [87], where SEM images show that two suspended graphene flakes are moving toward each other (SET) or apart (RESET) (Figure 5.8 (c)).

a.2 Forces controlling the reversible movements around the nano-gap

This reversible movement of the graphene flakes can be explained by either mechanical forces pulling them toward each other, or thermal effects leading them to expand.

During the SET process, temperatures remain low (*i.e.* close to room temperature) as long as the nano-gap is opened, because only tunneling currents are flowing (and the heat generated equals RI^2). Moreover, if stretching is induced by heating, the coefficient of thermal expansion of graphene must be positive. However, it has been shown [156] that for temperatures below 1,000 K, the coefficient of thermal expansion of graphene is negative. Hence, for all temperatures below 1,000 K, the graphene should shrink, resulting in a larger nano-gap. Thus, the thermal hypothesis is unlikely.

Another option is that the graphene flakes move toward and apart from each other because electrical forces are applied to them. In particular, the system comprising the insulating nano-gap surrounded by graphene can be considered as a capacitor. When a voltage is applied accross a capacitor, attractive forces rise due to the Coulomb attraction between the charges that are accumulating on both sides of the insulator. These attractive forces could be responsible of the SET process; they would be opposed by

mechanical forces opposing both the stretching of the graphene (elastic forces) and the movement of graphene relative to the SiO_2 substrate (friction forces). Such mechanical forces could be responsible of the RESET process.

a.3 Development of a quantitative model

Let us develop a quantitative model accounting for these forces to check the validity of this hypothesis.

a.3.1 Parallel plate capacitor

As a voltage is applied across the insulating nano-gap, positive and negative charges accumulate on opposite sides, giving rise to an attractive electrostatic force due to Coulomb forces between opposite charges. For a parallel-plate capacitor, this force is expressed as:

$$F_{elec} = \frac{\varepsilon_0 A V^2}{2d^2} \tag{5.1}$$

Where ε_0 is the vacuum permittivity ($8.85.10^{-12}$ F/m), A is the surface area of one plate (in m^2), V the applied voltage (in V) and d the size of the nano-gap (in m) (Figure 5.9 (a)).

The attractive electrostatic force tends to accelerate the two graphene flakes toward each other. However, before a graphene flake moves, static friction forces opposing this acceleration have to be overcome. Static friction forces can be expressed as:

$$F_{friction} = fWL \tag{5.2}$$

Where f is the coefficient of friction of the graphene/SiO_2 interface ($0.1.10^6$ Pa [157]), W is the width of the flake (in m), and L is its length (in m) (Figure 5.9 (a)).

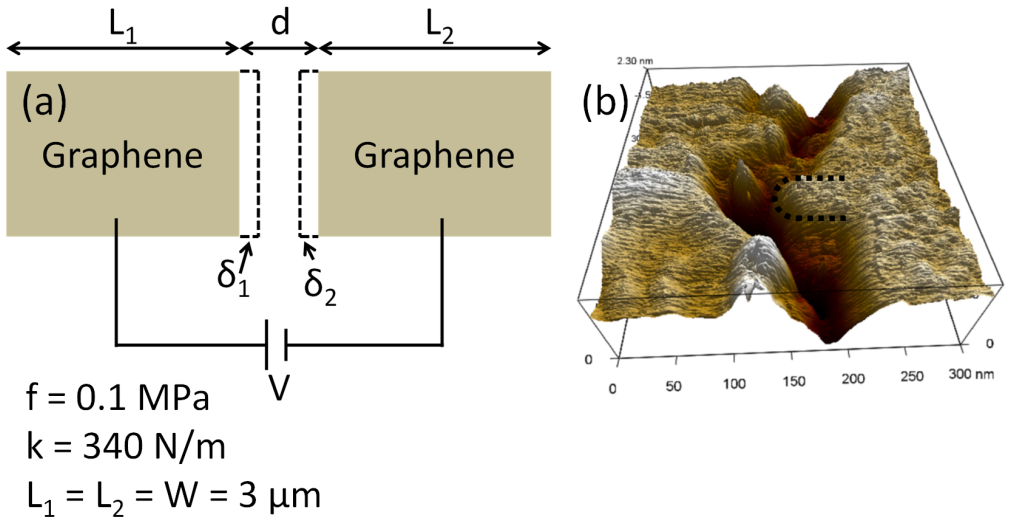

Figure 5.9: (a) Schematic showing the idealized system described by the model. (b) 3D AFM image of the nano-gap and the two graphene flakes. Black short dashed line: a $\approx$ 50 nm rectangle capped by a $\approx$ 25 nm circle is used to estimate the field enhancement factor of such a sharp feature *via* the equation of Edgcombe and Valdre.

In the meantime, if the electrostatic forces are stronger than the static friction, as graphene flakes start moving and stretch toward each other, they act like springs that are characterized by their spring constant k (340 N/m [157]). Elastic forces hence arise, opposing either the stretching or the compression of the flakes around an equilibrium position where elastic forces are nil:

$$F_{elastic} = \frac{kW\delta}{L} \tag{5.3}$$

Where δ is the deformation of the graphene flake (in m) with respect to its initial position (Figure 5.9 (a)).

a.3.2 Field-enhancement factor

Now that we set up a basic model for a parallel plate capacitor, an extra term called the field enhancement factor γ must be added to the electrostatic force to account for the fact

that our graphene devices are not made of two parallel flakes, but rather, two flakes with irregular nanometer-sized features (Figure 5.9 (b)).

Sharp features can drastically enhance the electrical field locally. Moreover, the fact that graphene is a 2D material with a very small height may also enhance the electrical field [158, 159].

Estimating a correct value of the enhancement factor is a difficult task because one must account for shapes that are a few nanometers in size. It is especially challenging in our case, as sharp features may be located anywhere on the length of the gap (few microns).

To estimate a value of the field-enhancement factor based on the geometry of the field-enhancement feature, Edgcombe and Valdre [160] provide an equation applying to cylindrical shapes (such as CNTs) terminated by a sphere.

$$\gamma = 2 + 0.7\frac{L}{r} \tag{5.4}$$

Where L is the length of the cylinder (in m) and r the radius of the sphere (in m).

Applying this equation to a cylinder of 50 nm length terminated by a sphere of 25 nm diameter (see Figure 5.9 (b), short dashed line), we calculate a field-enhancement-factor of ≈ 5.

This factor is taken into account in the expression of the electrostatic force, as the electrostatic force depends on the electric field.

In order to provide the new expression of the electrostatic force, we now use indices 1 and 2 to describe the two-flake system shown in Figure 5.9 (a). For example, δ_1 refers to the deformation of the graphene flake on the left (Figure 5.9 (a)). δ_2 applies to the other graphene flake on the right of the nano-gap. Indices also apply to forces and other parameters when necessary.

Taking into account the field enhancement factor and indices, the electrostatic force can now be expressed as:

$$F_{elec1/2} = \frac{\gamma^2 \varepsilon_0 A V^2}{2(d - \delta_1 - \delta_2)^2} \tag{5.5}$$

And the elastic force:

$$F_{elastic1/2} = \frac{kW\delta_{1/2}}{L} \tag{5.6}$$

Before the flakes start moving, the attractive force must overcome the static friction force, that is:

$$F_{elec1/2} > F_{friction1/2} \tag{5.7}$$

Which is equivalent to:

$$V_{threshold} > \frac{d}{\gamma}\sqrt{\frac{2fL_{1/2}}{\varepsilon_0 h}} \tag{5.8}$$

To estimate whether the electro-mechanical model explains the switching observed experimentally, we solve the static equilibrium equations - that are (2 equations, 1 for each flake, and 2 inequations):

$$\sum F = F_{elec1/2} - F_{friction1/2} - F_{elastic1/2} = 0 \tag{5.9}$$

for

$$\delta_1 + \delta_2 < d \, and \, V > V_{threshold} \tag{5.10}$$

If no solution $\delta_1 + \delta_2 < d$ is found for $V > V_{threshold}$, it means that the only solutions are for $\delta_1 + \delta_2 > d$, which is a pull-in situation where the flakes accelerate toward each other until the gap is closed.

Details of the calculations are provided in Appendix B.

We find values for $V_{\text{pull-in}}$:

$$V_{max} = V_{pull-in} = \sqrt{\frac{8}{27}\frac{kWd^3}{\gamma^2\epsilon_0 WhL_{eff}}(1 + \frac{f_{eff}L_{eff}^2}{kd})^3} \tag{5.11}$$

For any values of V > $V_{pull-in}$, $\sum F = F_{elec1/2} - F_{friction1/2} - F_{friction1/2} > 0$ for any couple $\delta_1 + \delta_2$, so as long as the two flakes are not in contact (*i.e.* as long as $\delta_1 + \delta_2 < d$) they keep on accelerating toward each other due to the increasing electrostatic force. They eventually end up overlapping each other, hence establishing an electrical contact.

We calculate values of the pull-in voltage $V_{pull-in}$ for different values of the field enhancement factor and for a device architecture such that: $W = L_1 = L_2 = 3$ μm (Figure 5.10).

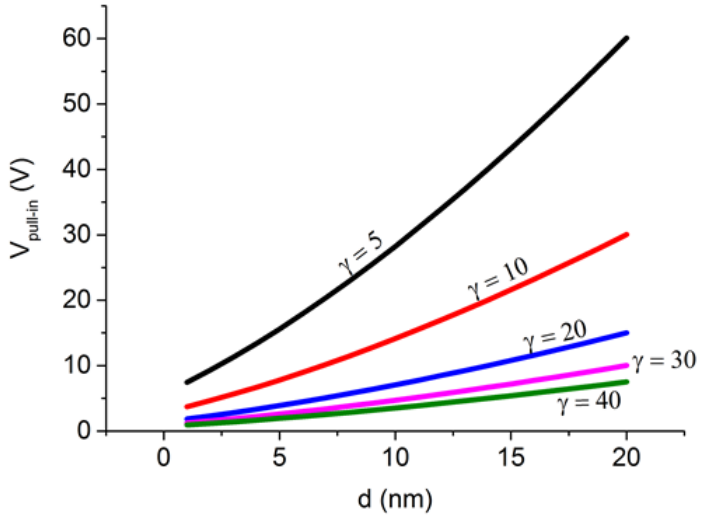

Figure 5.10: Evolution of the pull-in voltage as a function of the gap size, for different values of the field-enhancement factor γ.

For $\gamma = 5$, values of the pull-in voltage increase fast as the initial gap size increases. For d = 20 nm, the required pull-in voltage equals $\approx$ 60 V, which is much larger than the values required experimentally to turn a switch ON.

On the other hand, for smaller values of the nano-gap, values of the pull-in voltage are smaller. For example, for a gap of 2 nm, the required pull-in voltage is $\approx$ 9V. A gap size of 2 nm is much smaller that the gap we observed with the atomic force microscope (Figure 5.8); however, in some cases the AFM data do not agree with the electrical data, because we detect tunneling current in the HRS and estimate a gap size of $\approx$ 2 nm by fitting with the Simmons model of tunneling (Figure 5.1 (b)).

There are two reasons why the AFM and electrical data may suggest different gap sizes:

1) Fitting the electrical data enable to correctly estimate the minimum size of the gap. The discrepancy with the AFM data comes from the fact that we only characterize a limited area of the gap by AFM. Thus, we might not observe the location at which the gap size is the smallest. In fact, the geometry of the gap is very irregular, with sharp features and varying widths. If this hypothesis is true, then it is correct to estimate the pull-in voltage at a gap size of 2 nm. Moreover, it is possible that the AFM does not have

the lateral resolution to resolve a 2 nm wide gap.

2) The irregular geometry of the gap and sharp features lead to a large field enhancement factor, hence changing the "effective size" of the gap (as seen by the electrons). Hence, by fitting the electrical data, we estimate a much smaller size than the real one because the Simmons model for tunneling does not account for field enhancement by sharp features. If this hypothesis is true, it is necessary to use a bigger value of the field-enhancement factor γ. In fact, the calculated field enhancement factor value of 5 is valid for a cylinder-shape (3D sharp feature). Mono-layer is quasi 2D, which should lead to an even larger field enhancement.

A larger value of the field enhancement factor for a bigger gap leads to low values of the pull-in voltage. For example, with a value of the field-enhancement factor of 40 and a gap of 20 nm, the required pull-in voltage is 8V. Calculated values of the pull-in voltage for different field enhancement factors and gap sizes are displayed in Figure 5.10.

b Stability in the LRS

Graphene acts like a spring with a spring constant k (0.1 MPa). If this "spring" is at rest when the nano-gap is opened, it is not at rest when the nano-gap is closed, and elastic forces will work to re-open the nano-gap.

However, the two-terminal switches developed in this thesis are non-volatile, which means that the nano-gap remains closed even when the electrostatic forces are removed. Thus, there is a force that counteracts the action of elastic forces and keeps the gap closed. In traditional nano-electromechanical switches, this force is the van der Waals force between the two contacting structures [107].

Let us propose that the two graphene flakes are in contact along the entire length of the nano-gap, that is, W (Figure 5.9 (a)). Then, the van der Waals adhesion force between the two sides equals:

$$F_{vdw} = \alpha h W \tag{5.12}$$

Where α is the adhesion force per unit area between the two graphene flakes equalling $6.6.10^{-15}\ N/\text{Å}^2 = 6.6.10^5\ N/m^2$ [161], and h and W are the height and width of the graphene flake, respectively.

The condition for gap re-opening when the electrical power is removed is:

$$max(F_{elastic1/2}) > F_{vdw} \tag{5.13}$$

For the elastic force, we need to account for the maximum value between the two values of the elastic force (one for each flake). We rewrite the inequality:

$$max(\frac{\delta_{1/2}}{L_{1/2}}) > \frac{\alpha h}{k} \tag{5.14}$$

We test this inequality for the symmetrical case, where $\delta_{1/2} = \frac{d}{2}$ and $L_{1/2} = 3\mu m$. It is found that for all values of the **gap size d above 1 nm**, the elastic forces are much larger than the van der Waals forces, implying that the **stability is not achieved by the van der Waals forces** between the two graphene flakes.

c Formation of covalent bonds

The electro-mechanical model we developed satisfactorily explains the switching from the HRS to the LRS. However:

1) It does not satisfactorily explain the switching from the LRS to the HRS. Typically, non-volatile electro-mechanical switches rely on attractive electrostatic forces to SET and repulsive electrostatic forces to RESET [107]. Here, we only apply attractive electrostatic forces as a voltage drop is applied across the two flakes.

2) The SiO_2 substrate is damaged by the electroforming process and subsequent switching cycles, suggesting that high temperatures are reached. If the entire switching is purely electro-mechanical, temperatures should remain low. The same issue has puzzled other researchers [87] when they found that the switching behavior of their devices was dependent on the temperature, hence "ruling out a purely electromechanical switching mechanism".

3) The graphene is also damaged by the electroforming process, supporting the fact that high temperatures are reached.

4) The LRS is non-volatile, despite the fact that van der Waals forces are too weak to keep the two graphene flakes attached to each other, as discussed above.

5) To reach a non-volatile LRS state, the power must be kept ON for a significant duration (on the order of the second, see Figure 5.7 and Figure 5.6 (a)), while purely electromechanical switches have been predicted to switch faster than 1 ns [106].

These facts suggest that while the switching is driven by electro-mechanical forces, another process is behind the stability in the LRS. This stabilization process occurs during the noisy rise in current plotted in black in Figure 5.6 (a) and it is not complete as long as the green part of the curve is not reached.

Barreiro *et al.* [162] have shown that two overlapping graphene flakes can fuse if enough current flows from one flake to the other (Figure 5.11). With the help of the electromechanical model developed above, we have shown that during the SET process, the two graphene flakes accelerate toward each other until they contact each other, and since they need a certain time to reach their static position (the speed cannot get to 0 immediately), it is very likely that they end up overlapping each other, exactly like in Figure 5.11 (b). Then, the current increases drastically, with the highest resistance (hence the largest amount of heat) at the location where the two flakes contact each other. It is thus very likely that here, the mechanism behind the stability in the LRS is the punctual fusing of the two graphene flakes, or at least the formation of covalent bonds, hence effectively forming conductive bridges.

To conclude, the functioning of our devices can be explained by considering two processes:

- a purely electro-mechanical mechanism is behind the switching.

- the non-volatility in the LRS is warranted by the formation of covalent bonds, while the non-volatility in the HRS is warranted by the elastic and friction forces opposing the movement of the graphene from its equilibrium position.

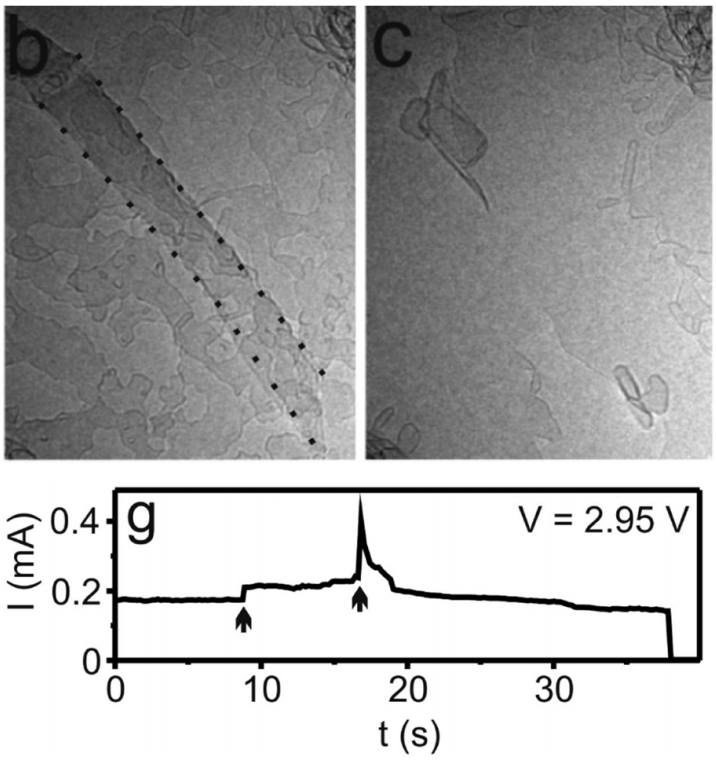

Figure 5.11: TEM images and I-V curve showing the fusing of two overlapping flakes, reproduced from [162]. (b) The two overlapping flakes before fusing. (c) After fusing. (g) Current as a function of time for V = 2.95 V. The second arrow (between 15 and 20s) corresponds to the fusing of the two graphene flakes.

A schematic of our model is shown in Figure 5.12. Figure 5.12 (a) shows the state of the device in the HRS: the gap is opened and the current flows by tunneling. Figure 5.12 (b) shows the SET proces: a voltage is applied accross the nano-gap, resulting in the accumulation of opposite charges at both sides of the gap. These opposite charges attract each other, hence creating an attractive force between the two flakes. When this force is large enough to close the nano-gap, the conduction is restored at some places, resulting in high temperatures and punctual fusing of the flakes. Conductive bridges are formed, restoring the VRH conduction of the graphene (LRS, Figure 5.12 (c)). Finally, by applying a large electric field accross the device in its LRS, heat is generated at the locations of the bridges, eventually leading to breaking of the covalent bonds (Figure 5.12 (d)). When the bonds are broken, the elastic forces lead the gap to re-open, and the device gets back to its HRS (Figure 5.12 (a)).

d Dynamics of the two-flake system

Ignoring friction forces, we can estimate the resonant frequency of a spring with spring constant k:

$$\omega = \sqrt{\frac{k}{m}} = \sqrt{\frac{k}{\rho h W L}} \tag{5.15}$$

ω equals $\approx$ 7.3.10^9 rad.s^{-1} $= 1.2.10^9$ Hz for the parameters chosen above (Figure 5.9) and $\rho = 2.1$ g.cm^{-3}. At this frequency, an entire switching cycle lasts for 0.83 ns, which is in line with theoretical predictions of switching speeds for nano-electro mechanical switches [106].

Despite the fact that we ignore the impact of friction forces, this estimate of the switching speed supports the idea that switching in itself is much faster than the time required to reach stability in the LRS.

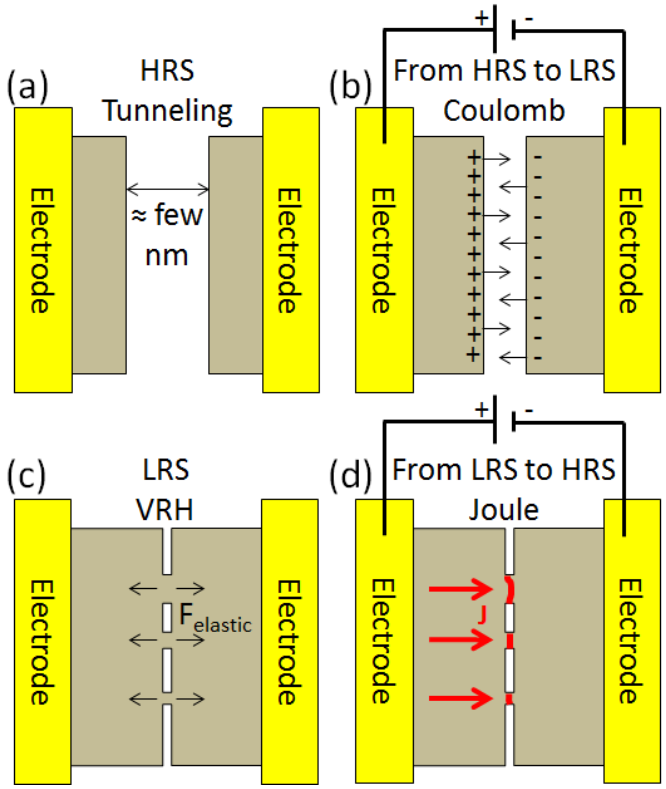

Figure 5.12: Schematic of the switching. (a) In the HRS, the nano-gap is large and electrical conduction is through electron tunneling. (b) SET process: closing of the nano-gap *via* the Coulomb attraction forces. (c) State of the device in the LRS. Graphene bridges are made during the SET process. The current flows through them. (d) RESET process. The Joule effect provides enough energy to break the bridges, and the elastic forces then open the gap.

e Pure Electro-Mechanical Switching

For the graphene two-terminal devices we developed in this Chapter to be competitive as an alternative to Flash or DRAM, switching speeds and cycling ability must be greatly improved. We found that both the low switching speed and cycling ability are due to the need to form and break covalent bonds at each switching cycle.

Nevertheless, our model also predicts that non-volatility can be reached **without covalent bonds** at the condition that the nano-gap is less than 1 nm in width.

It has been shown that creating very small nano-gaps (less than 2 nm) *via* controlled electrical breakdown is possible [155]. Therefore, using the same electrical breakdown technique to make two-terminal planar electro-mechanical graphene-based memory devices could lead to much faster and endurant devices.

However, issues about the variability remain, even if we achieve a purely electro-mechanical switching approach. As the nano-gap size must remain smaller than 1 nm in length to enable switching without covalent bonds, we can expect significant tunneling currents to flow in the devices even in the OFF state. These currents would be the equivalent of the subthreshold currents plaguing silicon transistors at very small channel lengths, leading to power losses and, more importantly, a large variability in the resistance value of the high resistance state. The amount of current flowing by tunneling is exponentially dependent on the distance. Even a very small change in distance (say, 0.1 nm) could lead to a large change in resistance. If that is the case, we would have either to greatly diminish the effective resistance contrast in our algorightms, to account for any such variation and enable 100% accuracy, or to design error-tolerant circuits. As discussed in Section e.3, page 189, at dimensions where quantum mechanics play an important role, purely deterministic approaches are bound to fail.

5.5 Conclusion

We have developed graphene-based devices that **can take two (or more) configurations** such that their resistance drastically changes in a **non-volatile** manner. I_{ON}/I_{OFF} ratio values of as high as $\mathbf{10}^4$ are achieved (cycling ability ≈ 100) and cycling abilities of **500 cycles** are achieved (with $I_{ON}/I_{OFF} > 450$). While these are promising results, the **switching speeds are very low** (fastest 10 ms) as compared to those of other current approaches to memory.

For the mechanism enabling the SET switching (from HRS to LRS), we hypothesized that it is the **closing of the nano-gaps** created during the electrical breakdown of the graphene devices. We used an AFM to visualize the state of the nano-gap both in the HRS and in the LRS: **the nano-gap is smaller in the LRS as compared to the HRS**, with some regions possibly connected by graphene.

To assess the "real" potential of our devices, we provided a way to estimate the important metrics that can be achieved; in particular, our memories must be drastically improved in terms of switching speed and endurance. We started by calculating the attractive electrical forces required to close the nano-gap, and found that **they are sufficient to close it**, at the SET voltages typically used during our experiments.

However, **the non-volatility could not be explained by our model** accounting only for the electrostatic, van der Waals, friction and elastic forces. The model also **did not satisfactorily explain the low switching speed**, as much faster speeds should be achieved with a purely electro-mechanical graphene-based switch.

Several clues suggest that the stability in the LRS is warranted by **covalent bonds connecting the two flakes** surrounding the nano-gap in the LRS.

Forming and destroying covalent bonds at each step is **costly in terms of energy and time**. Therefore, to improve our devices, another way to achieve stability must be found: one lead is to create much smaller gaps during the electrical breakdown (less than 1 nm wide). In that case, **our model predicts that the stability could be guaranteed by the**

van der Waals forces alone and that **switching speeds comparable to DRAM could be achieved**.

Conclusion

In this thesis, we studied the mechanisms leading to strong changes in carbon allotropes when submitting them to large optical and electrical power densities, and we showed how these changes can be used for applications.

First, in Chapter 1, we discussed the **state of the art in terms of both optical and electronic memory** and how both technologies rely on **constant improvements in terms of performances and of memory architecture**. As Moore's law is expected to fail soon, and chalcogenides can only be used at low temperatures, **allotropes of carbon are expected to play a growing role for memory applications**. We introduced the carbon allotropes that we consider in this thesis (**graphene and textured carbon**) for both electronic and optical memory applications. We discussed the particular **challenges** we wish to address, which inhibit the progress in the development of carbon-based electronic and optical memories.

Then, in Chapter 2, we described the experimental methods that are used to solve these challenges. For optical memory applications, carbon thin films are **deposited** on silicon, and a good **understanding and control of the lasers** is necessary to understand the mechanisms leading to the phase changes. After the transformations, **characterization tools** are used to study the structure and the morphology of the thin films. For electronic memories, **electronic devices based on graphene are fabricated**. We use optical lithography coupled to **graphene removal** and **electrode deposition** techniques; to understand the operation of our devices, **controllable electrical excitations** are applied, and the **quality** of the graphene is monitored **at every step** (before and after switch-

ing).

In Chapter 3, we studied in detail the impact of high-power continuous laser annealing on the crystalline structure and morphology of textured carbon. Three drastic changes are observed at different power densities: graphitization, **amorphization** and **matter loss**. While graphitization has been reported previously in the literature, amorphization and matter loss are seldom discussed. Moreover, the mechanism behind graphitization, as well as its consequences on the electrical properties of the carbon thin film, are poorly understood. We are able to demonstrate experimentally that continuous-wave laser annealing leads to an **enhanced electrical conductivity**, opening a direct route toward using continuous-wave lasers as a **tool to pattern conductive lines**, while keeping the damage levels low. Moreover, we demonstrated that these structural changes occur at temperatures much lower than the melting point of carbon (**solid-state crystallization**), hence explaining the **low levels of surface degradations** when graphitization is achieved. The amorphization and matter loss processes are also found to occur in the solid state, suggesting that oxygen plays an important role in these mechanisms; this fact is confirmed experimentally, as **we detect higher concentrations of oxygen** at the locations of the matter removal and amorphization. Matter removal occurs through the **emission of gaseous CO and CO_2 molecules**, while amorphization occurs through the **degradation of the crystalline structure by the absorption of oxygen atoms**. Finally, we demonstrate the **potential of continuous-wave lasers as tools to draw patterns** by precisely drawing a conductive pattern. In the same manner, amorphous lines or trenches could be drawn easily by tuning the power density.

Then, in Chapter 4, we studied the impact of nanosecond laser pulses on the crystalline structure and surface morphology of textured carbon. While at low and medium energy densities, graphitization is found to occur as reported in the literature, at high energy densities we uncover an **amorphization process**. We then directly demonstrate **cycling ability**, thus opening the way toward the **development of optically-controlled carbon phase change memories**. However, the cycling ability is found to be rather limited, so we conduct a study of the surface degradations induced by the energetic laser pulses to understand this limitation. At low energy densities, **grains of limited sizes** grow on the

surface, which can be compared to the roughness increase discussed in the literature on low energy pulsed annealing of carbon thin films. While these grains grow in size when the energy density increases, at a fixed energy density we observe **cracks and ripples**. Then, the grains form **bubble-like features**, and at higher energy densities we observe **full and hollow cylinders** suggesting that sputtering processes are occuring. Finally, at the highest energy densities, we observe **high aspect ratio structures** also made of smaller bubble-like features. To help explaining the mechanisms behind these important structural and morphological changes, we develop a **finite-element-model of the temperature field** during the laser-annealing process. With it, we find that the melting temperature of carbon is reached at energy densities lower than the minimum energy density we use in the study. Hence all the detected changes, whether structural or morphological, occur while at least **a fraction of the carbon film is in the molten state**. Thus, we propose that the grains and bubbles are **growing nuclei of the liquid phase** that are frozen during cooling. The cracks are due to large thermal gradients locally leading to large structural stresses and **thermo-mechanical failure**. Cracks disappear as more matter is molten, hence relieving the stresses. Ripples, on the other hand, are due to **light - plasmons interactions at the surface of the silicon substrate** underneath the carbon film. At higher energy densities, the carbon bubbles are vaporized, hence creating **sputtering** traces such as full and hollow cylinders. Finally, at much higher energy densities, **explosive boiling** occurs, resulting in large matter losses and high aspect ratio features. The bubbles are due to **secondary sputtering processes** occuring after the explosion.

To explain the reversible phase change, we propose a model accounting for the state of the matter during solidification. A **heterogeneous solidification** (large thermal gradients during solidification, obtained after low to medium energy density annealing) leads to an interface-controlled solidification. The solid-liquid interface can act as a template (catalyst) for crystallization hence resulting in graphitization. On the other hand, a **homogeneous solidification** (low thermal gradient during solidification obtained after high energy density annealing) leads to a nearly simultaneous solidification of the whole film, resulting in catalyst-free solidification and amorphization.

To develop optically-controlled memories with large cycling abilities, it would be necessary to achieve phase changes while minimizing thermal damages; because some re-

ports discuss the non-thermal amorphization of matter *via* femtosecond laser annealing, we setup **a fully-functional femtosecond laser annealing bench**. While **preliminary results** on femtosecond laser-annealing of textured carbon are neither encouraging nor negative, another PhD student is already working with the laser for carbon laser-annealing applications.

Finally, in Chapter 5, we discuss the development of **high I_{ON}/I_{OFF} non-volatile graphene-based two-terminal memories**. After fabrication of the devices, to make them switcheable, we first use an **electrical breakdown step** that results in the formation of a **nano-sized gap** (2 nm < size < 50 nm). Depending on the environment, the mechanism behind this breakdown is either **sublimation** (higher power) or **oxidation** (lower power). After breakdown, most devices do not conduct a detectable electrical current, except for some ≈ 1 GΩ devices for which current flows *via* **tunneling**. Nano-gap devices can then be returned to a **non-volatile LRS** by applying an electric field. Finally, they can be **returned to a non-volatile HRS** by applying a higher electric field. In the literature, two main switching mechanisms are proposed for nano-gap devices: one is based on the SiO_2 substrate, whereby metallic silicon nanocrystals grow/shrink depending on the applied electric fields; the other is based on reversible movements of the conductive material on top of the SiO_2 substrate (*e.g.* graphene). Because the switching characteristics of our devices are closer to those whose switching has been explained by the reversible movements of graphene, we decide to **experimentally test this hypothesis *via* visualization of the nano-gap both in the HRS and the LRS**. We find that **the nano-gap is smaller in the LRS as compared to the HRS** which tends to confirm our hypothesis.
To confirm this hypothesis further and quantitatively understand the performances of our devices and their potential as a competitor to current approaches, **we develop a quantitative model of the switching**. The mechanism for SET is **Coulomb attraction**: the nano-gap acts as the insulator of the capacitor formed by the two graphene flakes on either side of the gap; therefore, applying an electric field leads to the build-up of an attractive force. On the other hand, the RESET process is driven by **elastic recoil forces** that oppose the stretching of the graphene. The model also takes into account **friction forces** due to the interface between the graphene and the SiO_2 substrate. An

important conclusion extracted from the exploitation of the model is that it does not predict the observed non-volatility nor the observed degradations to the structure of the graphene, as well as the slow switching speed we uncovered experimentally. On the other hand, all of these phenomena can be explained by accounting for the **fusing of the two graphene flakes** that requires high temperatures and longer times and is sufficient to **insure non-volatility**. While the formation of covalent bonds is an advantage for our devices because it garanties the non-volatility, it is a drawback in terms of switching speed and energy consumption. Nevertheless, our model predicts that **non-volatility could be obtained in a purely electro-mechanical device** (without the need for covalent bonds) if the nano-gap width is smaller than ≈ 1 nm. Comparable sizes of nano-gaps have already been demonstrated in the literature by using specific electrical breakdown methods: these nano-gap formation methods could be used to develop **very fast non-volatile electro-mechanical switches**. The fact that our devices have a planar configuration (as opposed to a suspended configuration) may enable to obtain all the advantages of electro-mechanical switches (resistance to high temperatures, to external electric fields, high I_{ON}/I_{OFF}, high switching speed) without their drawbacks (mechanical failure).

Perspectives

The work presented in this thesis significantly improves our understanding of the mechanisms leading to degradations of carbon allotropes when they are submitted to large power densities. It provides useful informations related to the durability of materials and devices in "normal" (*i.e.* lower energy density) conditions. For example, to predict the durabilitiy of a device at a temperature T_1 (*e.g.* room temperature), studies at a temperature T_2 significantly higher than T_1 are typically used. Higher temperature studies (at T_2) lead to "accelerated ageing", hence they enable to predict what can happen in the long term to a material/device at lower temperatures (T_1).

On the other hand, many types of degradations occur specifically at high powers. In the scientific literature, most studies focus on low power densities, because they are the most common for applications, and they lead to lower degradations; usually, degradations are a problem that has to be avoided. By contrast, in this thesis, we demonstrate that high power density phenomena can be used for applications.

In Chapter 3, we demonstrate that continuous-wave laser annealing can be used as a patterning tool for carbon allotropes; those patterns can be either more crystalline, more amorphous, or made of holes (matter removal). Our work is an important demonstration; however, further improvements to the technique can be achieved both in understanding structural change phenomena and in mastering the operational aspects of the tool.

In terms of understanding, we find that all the phenomena occur in the solid state, with amorphization and matter loss aided by oxidation. The solid-state graphitization pro-

cess does not lead to large graphitic crystals but rather to small sp^2 clusters.
It is discussed in the literature, and shown here, that these clusters may lead to drastic changes in the electrical and optical properties of carbon; but how so? What type of electrical conduction can we expect from such clusters? And as a consequence of the type of conduction: what maximum I_{ON}/I_{OFF} (between graphitized and un-graphitized regions) current ratio values can we expect?
To improve the operational aspects of the tool, it would be of interest to study the reversibility of the phase change: after we have made the carbon film more graphitic, can we make it more amorphous (and *vice-versa*)? Can we induce amorphization without matter loss? Answering those two questions is critical to know whether we can reversibly rewrite conductive patterns or if this technique is only useable once.
Lastly, today many applications require ever smaller features, achieving the same functions in ever smaller areas. Can we write patterns smaller than what we demonstrate here? The minimum beam size of lasers is typically limited by diffraction effects. However, in the last few years, many different demonstrations (many involving light-plasmons interactions) of light matter interactions at sizes much smaller than the diffraction limit have been reported: can we use such interactions to draw patterns at a fraction of the diffraction-limited beam size?
Those studies would enable to assess the potential of continuous wave lasers as a tool capable of drawing patterns that are smaller than the beam size of the laser, in a reversible manner; a better understanding of the transformations and of their impact on the properties of matter would enable to more precisely predict the impact of the drawing and to tune the power densities to achieve the desired transformations in a more precise manner.

In Chapter 4, for the first time, we achieve reversible phase changes in textured carbon by using a nanosecond laser. However, the cycling ability is rather limited due to the degradations induced by the high energy pulses. Therefore, it is necessary to limit the amount of degradations. To do so, the transformations should be achieved at lower temperatures than those attained in our study. It has been reported in the scientific literature that it is possible to induce low-temperature amorphization in some materials by using femtosec-

ond laser pulses. Consequently, we believe it would be of interest to thouroughly study the structural and morphological changes induced to textured carbon by a femtosecond laser pulse. Today, little is known about femtosecond laser pulse - matter interactions, and it is very difficult to predict the impact of such interactions. If, like what has been demonstrated with other materials, textured carbon amorphization can be achieved with a femtosecond laser pulse, the cycling ability of optically controlled phase change memories based on textured carbon should be drastically improved.

As we just discussed, the results in both chapters 3 and 4 have fundamental as well as practical value. Another interesting practical question is whether the phase changes observed here can be achieved in "real-world" applications. In this thesis, we used lasers that are rather bulky because we the need for miniaturization was not a priority in the laboratory. But for some applications such as, for example, optical data storage in space, volume and weight are very high stakes due to the very high costs associated with sending cargo in orbit or beyond. It is clear that sending powerful enough lasers in space is possible, as the laser of the ChemCam system on the Curiosity Rover currently exploring the surface of Mars has a power of ≈ 1 GW/cm^2, similar to the laser used in Chapter 4 and higher than the laser used in Chapter 3. So we know it is possible, but the cost obviously was not a primary issue for the Curiosity mission. Therefore, it would be of interest to work with manufacturers of cheaper, smaller laser sources to study whether a small, cheap system can function. The goal would not be to replace Blu-Ray systems but to realize cheap optical data storage systems working in places where the conditions are extreme (*e.g.* high temperatures, radiations) such as space or nuclear power plants.

Finally, in Chapter 5, we develop non-volatile graphene-based two-terminal memories with current ratios of 10^4 (100 cycles) and higher. Their operation relies on the reversible, electrically-controlled movements of graphene flakes separated by a nano-sized gap. While promising, these devices demonstrate switching speeds and cycling abilities much lower than theoretically predicted for nano-electro-mechanical switches. It is because of the need to create and destroy covalent bonds at each switching cycle. These covalent bonds are necessary to achieve non-volatility in the low resistance state. However, in

the quantitative model we developed in this thesis, we found that non-volatility can also be achieved without covalent bonds, provided that the nano-gap is smaller than 1 nm in width. In the literature, an electrical breakdown technique has been reported than enables the fabrication of nano-sized gaps in graphene bands with average width lower than 2 nm. It would be of interest to implement this technique and try it with the nano-gap memories we developed: theoretically, a purely electro-mechanical operation (without covalent bonds) would enable our devices to switch as fast as volatile DRAM while retaining non-volatility.

Overall, the results discussed in this thesis show that using high power densities and studying their impact on the structure and morphology of carbon allotropes enables to develop innovative applications. While these large power densities cannot be used during operation of ubiquitous applications, they can be used to form devices for ubiquitous use (*e.g.* electroforming of graphene electro-mechanical switches) or to fabricate devices that can be used in much rougher conditions (*e.g.* optical disks in Space). While we demonstrated the concept for three applications (laser writing in Chapter 3, optical memory in Chapter 4 and electrical memory in Chapter 5), the performance of these applications could be improved by further studies on their mechanisms of operation.

Author's publications

Peer-reviewed journal articles

L. Loisel, I. Florea, C-S. Cojocaru, B.K. Tay, B. Lebental, Oxidation-Based Continuous Laser Writing in Vertical Nano-Crystalline Graphite Thin Films, *Scientific Reports* 6, 26224 (2016). **doi**: 10.1038/srep26224

L. Loisel, M. Châtelet, G. Giudicelli, M. Lebihain, Y. Yang, C-S. Cojocaru, A. Constantinescu, B.K. Tay, B. Lebental, Graphitization and Amorphization of Nano-Crystalline Graphite Using High-Energy Nanosecond Laser Pulses, *Carbon* 105, 227-232 (2016). **doi**: 10.1016/j.carbon.2016.04.026

L. Loisel, A. Maurice, S. Vezzoli, C-S. Cojocaru, B.K. Tay, B. Lebental, A high performance non-volatile graphene memory by planar electro-mechanical switching, to be submitted.

Oral presentations at conferences (speaker)

L. Loisel, B. Lebental, M. Châtelet, Y. Yang, C-S. Cojocaru, B.K. Tay, Nanosecond-laser-induced graphitization and amorphization of thin nano-crystalline graphite films, *E-MRS Spring 2014*, Lille.

L. Loisel, A. Maurice, B. Lebental, S. Vezzoli, C-S. Cojocaru, B.K. Tay, A Non-Volatile Graphene-Based Planar Electro-Mechanical Switch, *SPIE Nanoscience + Engineering 2015*, San Diego.

Conference proceedings

L. Loisel, A. Maurice, B. Lebental, S. Vezzoli, C-S. Cojocaru, B.K. Tay, A graphene-based non-volatile memory, *Proceedings SPIE 9552, Carbon Nanotubes, Graphene, and Emerging 2D Materials for Electronic and Photonic Devices VIII*. **doi**: 10.1117/12.2188110

Bibliography

[1] MarketsandMarkets. Non volatile memory market worth 40.2 billion dollars by 2020, 2014. URL http://www.marketsandmarkets.com/PressReleases/non-volatile-memory.asp.

[2] MarketsandMarkets. Next generation memory market by technology (nonvolatile memory (mram, fram, pcm, and rram), volatile memory (dram (tram, ttram, and others) and sram (zram and others), application and geography, global forecast to 2013 2020, 2015. URL http://www.marketsandmarkets.com/Market-Reports/Memristor-Memory-Market-632.html.

[3] Sumio Iijima. Helical microtubules of graphitic carbon. *nature*, 354(6348):56–58, 1991. ISSN 0028-0836.

[4] Philip G. Collins, M. Hersam, M. Arnold, R. Martel, and Ph Avouris. Current saturation and electrical breakdown in multiwalled carbon nanotubes. *Physical Review Letters*, 86(14):3128–3131, 2001. URL http://link.aps.org/doi/10.1103/PhysRevLett.86.3128. PRL.

[5] J Feinleib, SC Moss, and SR Ovshinsky. Rapid reversible light induced crystallization of amorphous semiconductors. *Applied Physics Letters*, 18(6):254–257, 1971. ISSN 0003-6951.

[6] G. I. Meijer. Who wins the nonvolatile memory race? *Science*, 319(5870):1625–1626, 2008. doi: 10.1126/science.1153909. URL http://www.sciencemag.org/content/319/5870/1625.short.

[7] SK Sundaram and Eric Mazur. Inducing and probing non-thermal transitions in semiconductors using femtosecond laser pulses. *Nature Mater.*, 1(4):217–224, 2002. ISSN 1476-1122. doi: 10.1038/nmat767.

[8] Simone Raoux and Matthias Wuttig. *Phase change materials: science and applications*. Springer Science & Business Media, 2010. ISBN 0387848746.

[9] S. Hudgens and B. Johnson. Overview of phase-change chalcogenide nonvolatile memory technology. *MRS Bulletin*, 29(11):829–832, 2004. ISSN 1938-1425. doi: doi: 10.1557/mrs2004.236. URL http://dx.doi.org/10.1557/mrs2004.236.

[10] B. Stritzker, A. Pospieszczyk, and J. A. Tagle. Measurement of lattice temperature of silicon during pulsed laser annealing. *Physical Review Letters*, 47(5):356–358, 1981. URL http://link.aps.org/doi/10.1103/PhysRevLett.47.356. PRL.

[11] A. G. Cullis, H. C. Webber, N. G. Chew, J. M. Poate, and P. Baeri. Transitions to defective crystal and the amorphous state induced in elemental si by laser quenching. *Physical Review Letters*, 49(3):219–222, 1982. URL http://link.aps.org/doi/10.1103/PhysRevLett.49.219. PRL.

[12] Michael O. Thompson, J. W. Mayer, A. G. Cullis, H. C. Webber, N. G. Chew, J. M. Poate, and D. C. Jacobson. Silicon melt, regrowth, and amorphization velocities during pulsed laser irradiation. *Physical Review Letters*, 50(12):896–899, 1983. URL http://link.aps.org/doi/10.1103/PhysRevLett.50.896. PRL.

[13] Michael O. Thompson, G. J. Galvin, J. W. Mayer, P. S. Peercy, J. M. Poate, D. C. Jacobson, A. G. Cullis, and N. G. Chew. Melting temperature and explosive crystallization of amorphous silicon during pulsed laser irradiation. *Physical Review Letters*, 52(26):2360–2363, 1984. URL http://link.aps.org/doi/10.1103/PhysRevLett.52.2360. PRL.

[14] R. F. Wood, D. H. Lowndes, and J. Narayan. Bulk nucleation and amorphous phase formation in highly undercooled molten silicon. *Applied Physics Letters*, 44(8):770–772, 1984. doi: doi:http://dx.doi.org/10.1063/1.

94912. URL http://scitation.aip.org/content/aip/journal/apl/44/8/10.1063/1.94912.

[15] T Sameshima and S Usui. Pulsed laser induced amorphization of silicon films. *Journal of applied physics*, 70(3):1281–1289, 1991. ISSN 0021-8979.

[16] James S. Im, H. J. Kim, and Michael O. Thompson. Phase transformation mechanisms involved in excimer laser crystallization of amorphous silicon films. *Applied Physics Letters*, 63(14):1969–1971, 1993. doi: doi:http://dx.doi.org/10.1063/1.110617. URL http://scitation.aip.org/content/aip/journal/apl/63/14/10.1063/1.110617.

[17] T. Sameshima and S. Usui. Pulsed laser induced melting followed by quenching of silicon films. *Journal of Applied Physics*, 74(11):6592–6598, 1993. doi: doi:http://dx.doi.org/10.1063/1.355097. URL http://scitation.aip.org/content/aip/journal/jap/74/11/10.1063/1.355097.

[18] J Bonse, S Baudach, J Kruger, W Kautek, and M Lenzner. Femtosecond laser ablation of silicon modification thresholds and morphology. *Applied Physics A*, 74(1):19–25, 2002. ISSN 0947-8396.

[19] P. L. Liu, R. Yen, N. Bloembergen, and R. T. Hodgson. Picosecond laser induced melting and resolidification morphology on si. *Applied Physics Letters*, 34(12):864–866, 1979. doi: doi:http://dx.doi.org/10.1063/1.90703. URL http://scitation.aip.org/content/aip/journal/apl/34/12/10.1063/1.90703.

[20] Raphael Tsu, Rodney T. Hodgson, Teh Yu Tan, and John E. Baglin. Order-disorder transition in single-crystal silicon induced by pulsed uv laser irradiation. *Physical Review Letters*, 42(20):1356–1358, 1979. URL http://link.aps.org/doi/10.1103/PhysRevLett.42.1356. PRL.

[21] Melvin Avrami. Kinetics of phase change. i general theory. *The Journal of Chemical Physics*, 7(12):1103–1112, 1939. doi: doi:http://dx.doi.org/10.1063/1.1750380. URL http://scitation.aip.org/content/aip/journal/jcp/7/12/10.1063/1.1750380.

[22] Gill Lee. The quest for a universal memory. *IEEE Spectrum*, 2012.

[23] J. Joshua Yang, Dmitri B. Strukov, and Duncan R. Stewart. Memristive devices for computing. *Nat Nano*, 8(1):13–24, 2013. ISSN 1748-3387. URL http://dx.doi.org/10.1038/nnano.2012.240. 10.1038/nnano.2012.240.

[24] H-SP Wong, Simone Raoux, SangBum Kim, Jiale Liang, John P Reifenberg, Bipin Rajendran, Mehdi Asheghi, and Kenneth E Goodson. Phase change memory. *Proceedings of the IEEE*, 98(12):2201–2227, 2010. ISSN 0018-9219.

[25] H. S. P. Wong, Lee Heng-Yuan, Yu Shimeng, Chen Yu-Sheng, Wu Yi, Chen Pang-Shiu, Lee Byoungil, F. T. Chen, and Tsai Ming-Jinn. Metal oxide rram. *Proceedings of the IEEE*, 100(6):1951–1970, 2012. ISSN 0018-9219. doi: 10.1109/JPROC.2012.2190369.

[26] Stanford R Ovshinsky. Reversible electrical switching phenomena in disordered structures. *Physical Review Letters*, 21(20):1450, 1968.

[27] Matthias Wuttig. Phase-change materials: Towards a universal memory? *Nat Mater*, 4(4):265–266, 2005. ISSN 1476-1122. URL http://dx.doi.org/10.1038/nmat1359. 10.1038/nmat1359.

[28] Matthias Wuttig and Noboru Yamada. Phase-change materials for rewriteable data storage. *Nat Mater*, 6(11):824–832, 2007. ISSN 1476-1122. URL http://dx.doi.org/10.1038/nmat2009. 10.1038/nmat2009.

[29] D. Loke, T. H. Lee, W. J. Wang, L. P. Shi, R. Zhao, Y. C. Yeo, T. C. Chong, and S. R. Elliott. Breaking the speed limits of phase-change memory. *Science*, 336(6088):1566–1569, 2012. doi: 10.1126/science.1221561. URL http://www.sciencemag.org/content/336/6088/1566.abstract.

[30] Feng Xiong, Albert D. Liao, David Estrada, and Eric Pop. Low-power switching of phase-change materials with carbon nanotube electrodes. *Science*, 332(6029):568–570, 2011. doi: 10.1126/science.1201938. URL http://www.sciencemag.org/content/332/6029/568.abstract.

[31] Blaise Fanning, Shekoufeh Qawami, Raymond S Tetrick, and Frank T Hady. Multi-level memory with direct access, 2011.

[32] Rainer Waser and Masakazu Aono. Nanoionics-based resistive switching memories. *Nat Mater*, 6(11):833–840, 2007. ISSN 1476-1122. URL http://dx.doi.org/10.1038/nmat2023. 10.1038/nmat2023.

[33] Rainer Waser, Regina Dittmann, Georgi Staikov, and Kristof Szot. Redox-based resistive switching memories nanoionic mechanisms, prospects, and challenges. *Advanced Materials*, 21(25-26):2632–2663, 2009. ISSN 1521-4095. doi: 10.1002/adma.200900375. URL http://dx.doi.org/10.1002/adma.200900375.

[34] L. Chua. Memristor-the missing circuit element. *IEEE Transactions on Circuit Theory*, 18(5):507–519, 1971. ISSN 0018-9324. doi: 10.1109/TCT.1971.1083337.

[35] ITRS. International technology roadmap for semiconductors - 2011 edition - emerging research devices. Report, 2011.

[36] Chen Yang Yin, L. Goux, S. Clima, B. Govoreanu, R. Degraeve, G. S. Kar, A. Fantini, G. Groeseneken, D. J. Wouters, and M. Jurczak. Endurance retention trade off on hfo2 metal cap 1t1r bipolar rram. *Electron Devices, IEEE Transactions on*, 60(3):1114–1121, 2013. ISSN 0018-9383. doi: 10.1109/TED.2013.2241064.

[37] Myoung Jae Lee, Chang Bum Lee, Dongsoo Lee, Seung Ryul Lee, Man Chang, Ji Hyun Hur, Young-Bae Kim, Chang-Jung Kim, David H. Seo, Sunae Seo, U. In Chung, In Kyeong Yoo, and Kinam Kim. A fast, high-endurance and scalable non volatile memory device made from asymmetric ta2o5-x tao2-x bilayer structures. *Nat Mater*, 10(8):625–630, 2011. ISSN 1476-1122. doi: http://www.nature.com/nmat/journal/v10/n8/abs/nmat3070.html#supplementary-information. URL http://dx.doi.org/10.1038/nmat3070. 10.1038/nmat3070.

[38] K. L. Wang, J. G. Alzate, and P. Khalili Amiri. Low-power non-volatile spintronic memory: Stt-ram and beyond. *Journal of Physics D: Applied Physics*, 46(7):074003, 2013. ISSN 0022-3727. URL http://stacks.iop.org/0022-3727/46/i=7/a=074003.

[39] Diao Zhitao, Li Zhanjie, Wang Shengyuang, Ding Yunfei, Panchula Alex, Chen Eugene, Wang Lien-Chang, and Huai Yiming. Spin-transfer torque switching in magnetic tunnel junctions and spin-transfer torque random access memory. *Journal of Physics: Condensed Matter*, 19(16):165209, 2007. ISSN 0953-8984. URL http://stacks.iop.org/0953-8984/19/i=16/a=165209.

[40] Brian R Tull, James E Carey, Eric Mazur, Joel P McDonald, and Steven M Yalisove. Silicon surface morphologies after femtosecond laser irradiation. *Mrs Bulletin*, 31 (08):626–633, 2006. ISSN 1938-1425.

[41] Antonio Miotello and Roger Kelly. Critical assessment of thermal models for laser sputtering at high fluences. *Appl. Phys. Lett.*, 67(24):3535–3537, 1995. ISSN 0003-6951. doi: 10.1063/1.114912.

[42] Robert F. Service. Is silicon's reign nearing its end? *Science*, 323(5917):1000–1002, 2009. doi: 10.1126/science.323.5917.1000. URL http://www.sciencemag.org/content/323/5917/1000.short.

[43] S. Anthony. Intel forges ahead to 10nm, will move away from silicon at 7nm, 2015. URL http://arstechnica.com/gadgets/2015/02/intel-forges-ahead-to-10nm-will-move-away-from-silicon-at-7nm/.

[44] Paul S. Peercy. The drive to miniaturization. *Nature*, 406(6799):1023–1026, 2000. ISSN 0028-0836. URL http://dx.doi.org/10.1038/35023223. 10.1038/35023223.

[45] A. K. Geim and K. S. Novoselov. The rise of graphene. *Nature Mater.*, 6(3):183–191, 2007. ISSN 1476-1122. doi: 10.1038/nmat1849. URL http://dx.doi.org/10.1038/nmat1849. 10.1038/nmat1849.

[46] T. Durkop, S. A. Getty, Enrique Cobas, and M. S. Fuhrer. Extraordinary mobility in semiconducting carbon nanotubes. *Nano Letters*, 4(1):35–39, 2004. ISSN 1530-6984. doi: 10.1021/nl034841q. URL http://dx.doi.org/10.1021/nl034841q.

[47] Savas Berber, Young-Kyun Kwon, and David Tomanek. Unusually high thermal

conductivity of carbon nanotubes. *Physical Review Letters*, 84(20):4613–4616, 2000. URL http://link.aps.org/doi/10.1103/PhysRevLett.84.4613. PRL.

[48] Phaedon Avouris, Zhihong Chen, and Vasili Perebeinos. Carbon-based electronics. *Nature Nanotech.*, 2(10):605–615, 2007. ISSN 1748-3387. doi: 10.1038/nnano.2007.300. URL http://dx.doi.org/10.1038/nnano.2007.300. 10.1038/nnano.2007.300.

[49] K. S. Novoselov, A. K. Geim, S. V. Morozov, D. Jiang, Y. Zhang, S. V. Dubonos, I. V. Grigorieva, and A. A. Firsov. Electric field effect in atomically thin carbon films. *Science*, 306(5696):666–669, 2004. doi: 10.1126/science.1102896. URL http://www.sciencemag.org/content/306/5696/666.abstract.

[50] Antonio Castro Neto, Francisco Guinea, and Nuno Miguel Peres. Drawing conclusions from graphene. *Physics World*, 19(11):33, 2006. ISSN 0953-8585.

[51] Xu Du, Ivan Skachko, Anthony Barker, and Eva Y. Andrei. Approaching ballistic transport in suspended graphene. *Nat Nano*, 3(8):491–495, 2008. ISSN 1748-3387. doi: http://www.nature.com/nnano/journal/v3/n8/suppinfo/nnano.2008.199_S1.html. URL http://dx.doi.org/10.1038/nnano.2008.199. 10.1038/nnano.2008.199.

[52] Alexander A. Balandin, Suchismita Ghosh, Wenzhong Bao, Irene Calizo, Desalegne Teweldebrhan, Feng Miao, and Chun Ning Lau. Superior thermal conductivity of single-layer graphene. *Nano Letters*, 8(3):902–907, 2008. ISSN 1530-6984. doi: 10.1021/nl0731872. URL http://dx.doi.org/10.1021/nl0731872.

[53] Changgu Lee, Xiaoding Wei, Jeffrey W. Kysar, and James Hone. Measurement of the elastic properties and intrinsic strength of monolayer graphene. *Science*, 321(5887):385–388, 2008. doi: 10.1126/science.1157996. URL http://www.sciencemag.org/content/321/5887/385.abstract.

[54] M Shakerzadeh, N Xu, M Bosman, BK Tay, X Wang, EHT Teo, H Zheng, and H Yu. Field emission enhancement and microstructural changes of carbon films by single pulse laser irradiation. *Carbon*, 49(3):1018–1024, 2011. ISSN 0008-6223. doi: 10.1016/j.carbon.2010.11.010.

[55] Maziar Shakerzadeh, GC Loh, N Xu, WL Chow, CW Tan, C Lu, Ray Chin Chong Yap, Dunlin Tan, Siu Hon Tsang, and Edwin Hang Tong Teo. Re ordering chaotic carbon: Origins and application of textured carbon. *Adv. Mater.*, 24(30):4112–4123, 2012. ISSN 1521-4095. doi: 10.1002/adma.201104991.

[56] Maziar Shakerzadeh, MK Samani, Narjes Khosravian, Edwin Hang Tong Teo, M Bosman, and Beng Kang Tay. Thermal conductivity of nanocrystalline carbon films studied by pulsed photothermal reflectance. *Carbon*, 50(3):1428–1431, 2012. ISSN 0008-6223.

[57] M. Shakerzadeh, E. H. T. Teo, A. Sorkin, M. Bosman, B. K. Tay, and H. Su. Plasma density induced formation of nanocrystals in physical vapor deposited carbon films. *Carbon*, 49(5):1733–1744, 2011. ISSN 0008-6223. doi: http://dx.doi.org/10.1016/j.carbon.2010.12.059. URL `http://www.sciencedirect.com/science/article/pii/S0008622310009383`.

[58] EHT Teo, A Bolker, R Kalish, and C Saguy. Nano-patterning of through-film conductivity in anisotropic amorphous carbon induced using conductive atomic force microscopy. *Carbon*, 49(8):2679–2682, 2011. ISSN 0008-6223. doi: 10.1016/j.carbon.2011.02.055.

[59] Xu Shi, David Ian Flynn, Beng Kang Tay, and Hong Siang Tan. Filtered cathodic arc source, 2000.

[60] Xu Shi, Tu Yu Qiang, Tan Hong Siang, Beng Kang Tay, and William I. Milne. Simulation of plasma flow in toroidal solenoid filters. *Plasma Science, IEEE Transactions on*, 24(6):1309–1318, 1996. ISSN 0093-3813. doi: 10.1109/27.553196.

[61] David Ian Flynn, Xu Shi, Hong Siang Tan, and Beng Kang Tay. Ignition means for a cathodic arc source, 2001.

[62] Siu Hon Tsang, Naiyun XU, Hang Tong Edwin Teo, and Beng Kang Tay. Apparatus for the generation of nanocluster films and methods for doing the same, 2015.

[63] X. Shi, B. K. Tay, and S. P. Lau. The double bend filtered cathodic arc technology and its applications. *International Journal of Modern Physics B*, 14(02n03):

136–153, 2000. doi: doi:10.1142/S0217979200000145. URL http://www.worldscientific.com/doi/abs/10.1142/S0217979200000145.

[64] DWM Lau, DG McCulloch, MB Taylor, JG Partridge, DR Mckenzie, NA Marks, EHT Teo, and BK Tay. Abrupt stress induced transformation in amorphous carbon films with a highly conductive transition phase. *Physical review letters*, 100(17): 176101, 2008.

[65] Qing Zhang, S. F. Yoon, Rusli, H. Yang, and J. Ahn. Influence of oxygen on the thermal stability of amorphous hydrogenated carbon films. *Journal of Applied Physics*, 83(3):1349–1353, 1998. doi: doi:http://dx.doi.org/10.1063/1.367311. URL http://scitation.aip.org/content/aip/journal/jap/83/3/10.1063/1.367311.

[66] N. M. J. Conway, A. C. Ferrari, A. J. Flewitt, J. Robertson, W. I. Milne, A. Tagliaferro, and W. Beyer. Defect and disorder reduction by annealing in hydrogenated tetrahedral amorphous carbon. *Diamond Relat. Mater.*, 9(3 6):765–770, 2000. ISSN 0925-9635. doi: 10.1016/S0925-9635(99)00271-X. URL http://www.sciencedirect.com/science/article/pii/S092596359900271X.

[67] V. Kulikovsky, P. Bohac, C. Vorli, A. Deineka, D. Chvostova, A. Kurdyumov, and L. Jastrabi. Oxidation of graphite-like carbon films with different microhardness and density. *Surface and Coatings Technology*, 174 175(0):290–295, 2003. ISSN 0257-8972. doi: http://dx.doi.org/10.1016/S0257-8972(03)00593-0. URL http://www.sciencedirect.com/science/article/pii/S0257897203005930.

[68] Kazuyuki Takai, Meigo Oga, Hirohiko Sato, Toshiaki Enoki, Yoshimasa Ohki, Akira Taomoto, Kazutomo Suenaga, and Sumio Iijima. Structure and electronic properties of a nongraphitic disordered carbon system and its heat-treatment effects. *Phys. Rev. B: Condens. Matter*, 67(21):214202, 2003. doi: 10.1103/PhysRevB.67.214202. URL http://link.aps.org/doi/10.1103/PhysRevB.67.214202. PRB.

[69] D. G. McCulloch, J. L. Peng, D. R. McKenzie, S. P. Lau, D. Sheeja, and B. K. Tay. Mechanisms for the behavior of carbon films during annealing. *Phys. Rev.*

B: Condens. Matter, 70(8):085406, 2004. doi: 10.1103/PhysRevB.70.085406. URL http://link.aps.org/doi/10.1103/PhysRevB.70.085406. PRB.

[70] A. C. Ferrari, B. Kleinsorge, N. A. Morrison, A. Hart, V. Stolojan, and J. Robertson. Stress reduction and bond stability during thermal annealing of tetrahedral amorphous carbon. *J. Appl. Phys.*, 85(10):7191–7197, 1999. doi: 10.1063/1.370531. URL http://scitation.aip.org/content/aip/journal/jap/85/10/10.1063/1.370531.

[71] AI Savvatimskiy. Measurements of the melting point of graphite and the properties of liquid carbon (a review for 1963 2003). *Carbon*, 43(6):1115–1142, 2005. ISSN 0008-6223. doi: 10.1016/j.carbon.2004.12.027.

[72] J. O. Orwa, I. Andrienko, J. L. Peng, S. Prawer, Y. B. Zhang, and S. P. Lau. Thermally induced sp2 clustering in tetrahedral amorphous carbon (tac) films. *J. Appl. Phys.*, 96(11):6286–6297, 2004. doi: 10.1063/1.1808918. URL http://scitation.aip.org/content/aip/journal/jap/96/11/10.1063/1.1808918.

[73] M. Bowden, D. J. Gardiner, and J. M. Southall. Raman analysis of laser annealed amorphous carbon films. *J. Appl. Phys.*, 71(1):521–523, 1992. doi: 10.1063/1.350691. URL http://scitation.aip.org/content/aip/journal/jap/71/1/10.1063/1.350691.

[74] A. C. Ferrari, A. Libassi, B. K. Tanner, V. Stolojan, J. Yuan, L. M. Brown, S. E. Rodil, B. Kleinsorge, and J. Robertson. Density, sp3 fraction, and cross-sectional structure of amorphous carbon films determined by x-ray reflectivity and electron energy-loss spectroscopy. *Physical Review B*, 62(16):11089–11103, 2000. URL http://link.aps.org/doi/10.1103/PhysRevB.62.11089. PRB.

[75] R. W. Lamberton, S. M. Morley, P. D. Maguire, and J. A. McLaughlin. Monitoring laser induced microstructural changes of thin film hydrogenated amorphous carbon (a-ch) using raman spectroscopy. *Thin Solid Films*, 333:114–125, 1998. ISSN 0040-6090. doi: 10.1016/S0040-6090(98)00848-7. URL http://www.sciencedirect.com/science/article/pii/S0040609098008487.

[76] J. Z. Wan, Fred H. Pollak, and Benjamin F. Dorfman. Micro raman study of diamondlike atomic-scale composite films modified by continuous wave laser annealing. *J. Appl. Phys.*, 81(9):6407–6414, 1997. doi: 10.1063/1.364421. URL http://scitation.aip.org/content/aip/journal/jap/81/9/10.1063/1.364421.

[77] T. Venkatesan, D. C. Jacobson, J. M. Gibson, B. S. Elman, G. Braunstein, M. S. Dresselhaus, and G. Dresselhaus. Measurement of thermodynamic parameters of graphite by pulsed-laser melting and ion channeling. *Phys. Rev. Lett.*, 53(4):360–363, 1984. doi: 10.1103/PhysRevLett.53.360. URL http://link.aps.org/doi/10.1103/PhysRevLett.53.360. PRL.

[78] A. M. Malvezzi, N. Bloembergen, and C. Y. Huang. Time-resolved picosecond optical measurements of laser-excited graphite. *Phys. Rev. Lett.*, 57(1):146–149, 1986. doi: 10.1103/PhysRevLett.57.146. URL http://link.aps.org/doi/10.1103/PhysRevLett.57.146. PRL.

[79] D.H. Reitze, X Wang, H Ahn, and MC Downer. Femtosecond laser melting of graphite. *Phys. Rev. B: Condens. Matter*, 40(17):11986, 1989. doi: 10.1103/PhysRevB.40.11986.

[80] J Steinbeck Speck, J Steinbeck, and MS Dresselhaus. Microstructural studies of laser irradiated graphite surfaces. *J. Mater. Res.*, 5(05):980–988, 1990. ISSN 2044-5326. doi: 10.1557/JMR.1990.0980.

[81] Leona C Nistor, J Van Landuyt, VG Ralchenko, TV Kononenko, Elena D Obraztsova, and VE Strelnitsky. Direct observation of laser-induced crystallization of ac: H films. *Applied Physics A*, 58(2):137–144, 1994. ISSN 0947-8396.

[82] Y. Miyajima, A. A. D. T. Adikaari, S. J. Henley, J. M. Shannon, and S. R. P. Silva. Electrical properties of pulsed uv laser irradiated amorphous carbon. *Appl. Phys. Lett.*, 92(15):152104–152104–3, 2008. ISSN 0003-6951. doi: 10.1063/1.2908208.

[83] E. Cappelli, C. Scilletta, S. Orlando, V. Valentini, and M. Servidori. Laser annealing of amorphous carbon films. *Appl. Surf. Sci.*, 255(10):5620–5625, 2009. ISSN 0169-

4332. doi: 10.1016/j.apsusc.2008.10.062. URL http://www.sciencedirect.com/science/article/pii/S0169433208021326.

[84] Naiyun Xu, Hang Tong Edwin Teo, Maziar Shakerzadeh, Xincai Wang, Chee Mang Ng, and Beng Kang Tay. Electrical properties of textured carbon film formed by pulsed laser annealing. *Diamond Relat. Mater.*, 23:135–139, 2012. ISSN 0925-9635. doi: 10.1016/j.diamond.2012.01.016.

[85] Brian Standley, Wenzhong Bao, Hang Zhang, Jehoshua Bruck, Chun Ning Lau, and Marc Bockrath. Graphene-based atomic-scale switches. *Nano Letters*, 8(10): 3345–3349, 2008. ISSN 1530-6984. doi: 10.1021/nl801774a. URL http://dx.doi.org/10.1021/nl801774a.

[86] Congli He, Zhiwen Shi, Lianchang Zhang, Wei Yang, Rong Yang, Dongxia Shi, and Guangyu Zhang. Multilevel resistive switching in planar graphene/sio2 nanogap structures. *ACS Nano*, 6(5):4214–4221, 2012. ISSN 1936-0851. doi: 10.1021/nn300735s. URL http://dx.doi.org/10.1021/nn300735s.

[87] Hang Zhang, Wenzhong Bao, Zeng Zhao, Jhao-Wun Huang, Brian Standley, Gang Liu, Fenglin Wang, Philip Kratz, Lei Jing, and Marc Bockrath. Visualizing electrical breakdown and on/off states in electrically switchable suspended graphene break junctions. *Nano letters*, 12(4):1772–1775, 2012. ISSN 1530-6984.

[88] Emil B. Song, Bob Lian, Sung Min Kim, Sejoon Lee, Tien-Kan Chung, Minsheng Wang, Caifu Zeng, Guangyu Xu, Kin Wong, Yi Zhou, Haider I. Rasool, David H. Seo, Hyun-Jong Chung, Jinseong Heo, Sunae Seo, and Kang L. Wang. Robust bi-stable memory operation in single-layer graphene ferroelectric memory. *Applied Physics Letters*, 99(4):042109, 2011. doi: doi:http://dx.doi.org/10.1063/1.3619816. URL http://scitation.aip.org/content/aip/journal/apl/99/4/10.1063/1.3619816.

[89] Hu Young Jeong, Jong Yun Kim, Jeong Won Kim, Jin Ok Hwang, Ji-Eun Kim, Jeong Yong Lee, Tae Hyun Yoon, Byung Jin Cho, Sang Ouk Kim, Rodney S. Ruoff, and Sung-Yool Choi. Graphene oxide thin films for flexible nonvolatile

memory applications. *Nano Letters*, 10(11):4381–4386, 2010. ISSN 1530-6984. doi: 10.1021/nl101902k. URL http://dx.doi.org/10.1021/nl101902k.

[90] C. L. He, F. Zhuge, X. F. Zhou, M. Li, G. C. Zhou, Y. W. Liu, J. Z. Wang, B. Chen, W. J. Su, Z. P. Liu, Y. H. Wu, P. Cui, and Run-Wei Li. Nonvolatile resistive switching in graphene oxide thin films. *Applied Physics Letters*, 95(23):232101, 2009. doi: doi:http://dx.doi.org/10.1063/1.3271177. URL http://scitation.aip.org/content/aip/journal/apl/95/23/10.1063/1.3271177.

[91] Hong Seul Ki, Kim Ji Eun, Kim Sang Ouk, Choi Sung-Yool, and Byung Jin Cho. Flexible resistive switching memory device based on graphene oxide. *Electron Device Letters, IEEE*, 31(9):1005–1007, 2010. ISSN 0741-3106. doi: 10.1109/LED.2010.2053695.

[92] Simone Bertolazzi, Daria Krasnozhon, and Andras Kis. Nonvolatile memory cells based on mos2/graphene heterostructures. *ACS Nano*, 7(4):3246–3252, 2013. ISSN 1936-0851. doi: 10.1021/nn3059136. URL http://dx.doi.org/10.1021/nn3059136.

[93] Augustin J. Hong, Emil B. Song, Hyung Suk Yu, Matthew J. Allen, Jiyoung Kim, Jesse D. Fowler, Jonathan K. Wassei, Youngju Park, Yong Wang, Jin Zou, Richard B. Kaner, Bruce H. Weiller, and Kang L. Wang. Graphene flash memory. *ACS Nano*, 5(10):7812–7817, 2011. ISSN 1936-0851. doi: 10.1021/nn201809k. URL http://dx.doi.org/10.1021/nn201809k.

[94] T. J. Echtermeyer, Max C. Lemme, M. Baus, B. N. Szafranek, A. K. Geim, and H. Kurz. Nonvolatile switching in graphene field-effect devices. *Electron Device Letters, IEEE*, 29(8):952–954, 2008. ISSN 0741-3106. doi: 10.1109/LED.2008.2001179.

[95] Nagase Masao, Hibino Hiroki, Kageshima Hiroyuki, and Yamaguchi Hiroshi. Graphene-based nano-electro-mechanical switch with high on/off ratio. *Applied Physics Express*, 6(5):055101, 2013. ISSN 1882-0786. URL http://stacks.iop.org/1882-0786/6/i=5/a=055101.

[96] Kaveh M. Milaninia, Marc A. Baldo, Alfonso Reina, and Jing Kong. All

graphene electromechanical switch fabricated by chemical vapor deposition. *Applied Physics Letters*, 95(18):183105, 2009. doi: doi:http://dx.doi.org/10.1063/1.3259415. URL http://scitation.aip.org/content/aip/journal/apl/95/18/10.1063/1.3259415.

[97] Sung Min Kim, Emil B. Song, Sejoon Lee, Sunae Seo, David H. Seo, Yongha Hwang, R. Candler, and Kang L. Wang. Suspended few-layer graphene beam electromechanical switch with abrupt on-off characteristics and minimal leakage current. *Applied Physics Letters*, 99(2):023103, 2011. doi: doi:http://dx.doi.org/10.1063/1.3610571. URL http://scitation.aip.org/content/aip/journal/apl/99/2/10.1063/1.3610571.

[98] Peng Li, Zheng You, and Tianhong Cui. Graphene cantilever beams for nano switches. *Applied Physics Letters*, 101(9):093111, 2012. doi: doi:http://dx.doi.org/10.1063/1.4738891. URL http://scitation.aip.org/content/aip/journal/apl/101/9/10.1063/1.4738891.

[99] Zhiwen Shi, Hongliang Lu, Lianchang Zhang, Rong Yang, Yi Wang, Donghua Liu, Haiming Guo, Dongxia Shi, Hongjun Gao, Enge Wang, and Guangyu Zhang. Studies of graphene-based nanoelectromechanical switches. *Nano Research*, 5(2):82–87, 2012. ISSN 1998-0124. doi: 10.1007/s12274-011-0187-9. URL http://dx.doi.org/10.1007/s12274-011-0187-9.

[100] Yang Chai, Yi Wu, Kuniharu Takei, Hong-Yu Chen, Shimeng Yu, Philip CH Chan, Ali Javey, and H-SP Wong. Nanoscale bipolar and complementary resistive switching memory based on amorphous carbon. *Electron Devices, IEEE Transactions on*, 58(11):3933–3939, 2011. ISSN 0018-9383.

[101] Fu Di, Xie Dan, Feng Tingting, Chenhui Zhang, Jiebin Niu, Qian He, and Liu Litian. Unipolar resistive switching properties of diamondlike carbon-based rram devices. *Electron Device Letters, IEEE*, 32(6):803–805, 2011. ISSN 0741-3106. doi: 10.1109/LED.2011.2132750.

[102] Abu Sebastian, Andrew Pauza, Christophe Rossel, Robert M Shelby, Arantxa Fraile Rodriguez, Haralampos Pozidis, and Evangelos Eleftheriou. Resistance

switching at the nanometre scale in amorphous carbon. *New Journal of Physics*, 13 (1):013020, 2011. ISSN 1367-2630.

[103] Franz Kreupl, Rainer Bruchhaus, Petra Majewski, Jan B Philipp, Ralf Symanczyk, Thomas Happ, Christian Arndt, Mirko Vogt, Roy Zimmermann, and Axel Buerke. Carbon based resistive memory. *arXiv preprint arXiv:0901.4439*, 2009.

[104] Hamed Dadgour, Muhammad M. Hussain, and Kaustav Banerjee. A new paradigm in the design of energy efficient digital circuits using laterally actuated double gate nems, 2010.

[105] H.F. Dadgour and K. Banerjee. Hybrid nems cmos integrated circuits: a novel strategy for energy efficient designs, 2009. URL http://digital-library.theiet.org/content/journals/10.1049/iet-cdt.2008.0148.

[106] Owen Y. Loh and Horacio D. Espinosa. Nanoelectromechanical contact switches. *Nat Nano*, 7(5):283–295, 2012. ISSN 1748-3387. URL http://dx.doi.org/10.1038/nnano.2012.40. 10.1038/nnano.2012.40.

[107] Thomas Rueckes, Kyoungha Kim, Ernesto Joselevich, Greg Y. Tseng, Chin-Li Cheung, and Charles M. Lieber. Carbon nanotube-based nonvolatile random access memory for molecular computing. *Science*, 289(5476):94–97, 2000. doi: 10.1126/science.289.5476.94. URL http://www.sciencemag.org/content/289/5476/94.abstract.

[108] Raghunath Murali, Yinxiao Yang, Kevin Brenner, Thomas Beck, and James D. Meindl. Breakdown current density of graphene nanoribbons. *Applied Physics Letters*, 94(24):–, 2009. doi: doi:http://dx.doi.org/10.1063/1.3147183. URL http://scitation.aip.org/content/aip/journal/apl/94/24/10.1063/1.3147183.

[109] Lee KyeongJae, A. P. Chandrakasan, and Jing Kong. Breakdown current density of cvd-grown multilayer graphene interconnects. *Electron Device Letters, IEEE*, 32 (4):557–559, 2011. ISSN 0741-3106. doi: 10.1109/LED.2011.2108259.

[110] Albert Liao, Rouholla Alizadegan, Zhun-Yong Ong, Sumit Dutta, Feng Xiong, K. Jimmy Hsia, and Eric Pop. Thermal dissipation and variability in electrical breakdown of carbon nanotube devices. *Physical Review B*, 82(20):205406, 2010. URL http://link.aps.org/doi/10.1103/PhysRevB.82.205406. PRB.

[111] Philip G. Collins, Michael S. Arnold, and Phaedon Avouris. Engineering carbon nanotubes and nanotube circuits using electrical breakdown. *Science*, 292(5517): 706–709, 2001. doi: 10.1126/science.1058782. URL http://www.sciencemag.org/content/292/5517/706.abstract.

[112] Jun Yao, Lin Zhong, Zengxing Zhang, Tao He, Zhong Jin, Patrick J. Wheeler, Douglas Natelson, and James M. Tour. Resistive switching in nanogap systems on sio2 substrates. *Small*, 5(24):2910–2915, 2009. ISSN 1613-6829. doi: 10.1002/smll.200901100. URL http://dx.doi.org/10.1002/smll.200901100.

[113] Jun Yao, Zhengzong Sun, Lin Zhong, Douglas Natelson, and James M. Tour. Resistive switches and memories from silicon oxide. *Nano Letters*, 10(10):4105–4110, 2010. ISSN 1530-6984. doi: 10.1021/nl102255r. URL http://dx.doi.org/10.1021/nl102255r.

[114] Jun Yao, Lin Zhong, Douglas Natelson, and James M. Tour. Silicon oxide: A non-innocent surface for molecular electronics and nanoelectronics studies. *Journal of the American Chemical Society*, 133(4):941–948, 2011. ISSN 0002-7863. doi: 10.1021/ja108277r. URL http://dx.doi.org/10.1021/ja108277r.

[115] Jun Yao, Jian Lin, Yanhua Dai, Gedeng Ruan, Zheng Yan, Lei Li, Lin Zhong, Douglas Natelson, and James M. Tour. Highly transparent nonvolatile resistive memory devices from silicon oxide and graphene. *Nat Commun*, 3: 1101, 2012. doi: http://www.nature.com/ncomms/journal/v3/n10/suppinfo/ncomms2110_S1.html. URL http://dx.doi.org/10.1038/ncomms2110. 10.1038/ncomms2110.

[116] Jun Yao, Lin Zhong, Douglas Natelson, and James M. Tour. In situ imaging of the conducting filament in a silicon oxide resistive switch. *Scientific Reports*, 2:242, 2012. doi: 10.1038/srep00242http://www.nature.com/articles/

srep00242#supplementary-information. URL http://dx.doi.org/10.1038/srep00242.

[117] Albert D. Liao, Paulo T. Araujo, Runjie Xu, and Mildred S. Dresselhaus. Carbon nanotube network-silicon oxide non-volatile switches. *Nat Commun*, 5, 2014. doi: 10.1038/ncomms6673. URL http://dx.doi.org/10.1038/ncomms6673.

[118] B. K. Tay, Z. W. Zhao, and D. H. C. Chua. Review of metal oxide films deposited by filtered cathodic vacuum arc technique. *Mater. Sci. Eng., R*, 52(1 3):1 48, 2006. ISSN 0927-796X. doi: 10.1016/j.mser.2006.04.003. URL http://www.sciencedirect.com/science/article/pii/S0927796X06000271.

[119] N. Xu, S. H. Tsang, E. H. T. Teo, and B. K. Tay. Formation of thick textured carbon film using filtered cathodic vacuum arc technique. *Nanoelectronics Conference (INEC), 2013 IEEE 5th International*, pages 78–80, 2013. ISSN 2159-3523. doi: 10.1109/INEC.2013.6465959.

[120] Xuesong Li, Weiwei Cai, Jinho An, Seyoung Kim, Junghyo Nah, Dongxing Yang, Richard Piner, Aruna Velamakanni, Inhwa Jung, Emanuel Tutuc, Sanjay K. Banerjee, Luigi Colombo, and Rodney S. Ruoff. Large-area synthesis of high-quality and uniform graphene films on copper foils. *Science*, 324(5932):1312–1314, 2009. doi: 10.1126/science.1171245. URL http://www.sciencemag.org/content/324/5932/1312.abstract.

[121] Xuesong Li, Yanwu Zhu, Weiwei Cai, Mark Borysiak, Boyang Han, David Chen, Richard D. Piner, Luigi Colombo, and Rodney S. Ruoff. Transfer of large-area graphene films for high-performance transparent conductive electrodes. *Nano Letters*, 9(12):4359–4363, 2009. ISSN 1530-6984. doi: 10.1021/nl902623y. URL http://dx.doi.org/10.1021/nl902623y.

[122] Marcus Freitag, Mathias Steiner, Yves Martin, Vasili Perebeinos, Zhihong Chen, James C. Tsang, and Phaedon Avouris. Energy dissipation in graphene field-effect transistors. *Nano Letters*, 9(5):1883–1888, 2009. ISSN 1530-6984. doi: 10.1021/nl803883h. URL http://dx.doi.org/10.1021/nl803883h.

[123] F. Tuinstra and J. L. Koenig. Raman spectrum of graphite. *J. Chem. Phys.*, 53(3): 1126–1130, 1970. doi: 10.1063/1.1674108. URL http://scitation.aip.org/content/aip/journal/jcp/53/3/10.1063/1.1674108.

[124] Andrea Carlo Ferrari and John Robertson. Raman spectroscopy of amorphous, nanostructured, diamond like carbon, and nanodiamond. *Philos. Trans. R. Soc. London, Ser. A*, 362(1824):2477–2512, 2004. ISSN 1364-503X. doi: 10.1098/rsta.2004.1452.

[125] Benjamin Frank, Ali Rinaldi, Raoul Blume, Robert SchlÃ¶gl, and Dang Sheng Su. Oxidation stability of multiwalled carbon nanotubes for catalytic applications. *Chemistry of Materials*, 22(15):4462–4470, 2010. ISSN 0897-4756. doi: 10.1021/cm101234d. URL http://dx.doi.org/10.1021/cm101234d.

[126] Sebastian Osswald, Mickael Havel, and Yury Gogotsi. Monitoring oxidation of multiwalled carbon nanotubes by raman spectroscopy. *J. Raman Spectrosc.*, 38(6): 728–736, 2007. ISSN 1097-4555. doi: 10.1002/jrs.1686. URL http://dx.doi.org/10.1002/jrs.1686.

[127] Scilab : Logiciel open source gratuit de calcul numerique, (windows 7, version 5.5.0), 2014. URL http://www.scilab.org.

[128] Bradley Efron and Robert Tibshirani. Bootstrap methods for standard errors, confidence intervals, and other measures of statistical accuracy. *Statistical science*, pages 54–75, 1986. ISSN 0883-4237.

[129] Daisuke Shindo and Hiraga Kenji. *High-resolution electron microscopy for materials science*. Springer Science & Business Media, 2012. ISBN 4431684220.

[130] Victor Abdelsayed, Sherif Moussa, Hassan M. Hassan, Hema S. Aluri, Maryanne M. Collinson, and M. Samy El-Shall. Photothermal deoxygenation of graphite oxide with laser excitation in solution and graphene-aided increase in water temperature. *J. Phys. Chem. Lett.*, 1(19):2804–2809, 2010. ISSN 1948-7185. doi: 10.1021/jz1011143. URL http://dx.doi.org/10.1021/jz1011143.

[131] Lei Huang, Yang Liu, Le-Chun Ji, Yi-Qun Xie, Tao Wang, and Wang-Zhou Shi. Pulsed laser assisted reduction of graphene oxide. *Carbon*, 49(7):2431–2436, 2011. ISSN 0008-6223. doi: http://dx.doi.org/10.1016/j.carbon.2011.01.067. URL http://www.sciencedirect.com/science/article/pii/S0008622311001047.

[132] Yonglai Zhang, Li Guo, Shu Wei, Yinyan He, Hong Xia, Qidai Chen, Hong-Bo Sun, and Feng-Shou Xiao. Direct imprinting of microcircuits on graphene oxides film by femtosecond laser reduction. *Nano Today*, 5(1):15–20, 2010. ISSN 1748-0132. doi: 10.1016/j.nantod.2009.12.009. URL http://www.sciencedirect.com/science/article/pii/S1748013210000046.

[133] Carlos Rios, Matthias Stegmaier, Peiman Hosseini, Di Wang, Torsten Scherer, C. David Wright, Harish Bhaskaran, and Wolfram H. P. Pernice. Integrated all-photonic non-volatile multi-level memory. *Nature Photon.*, 2015. ISSN 1749-4893. doi: 10.1038/nphoton.2015.182. URL http://dx.doi.org/10.1038/nphoton.2015.182.

[134] Veronica Strong, Sergey Dubin, Maher F. El-Kady, Andrew Lech, Yue Wang, Bruce H. Weiller, and Richard B. Kaner. Patterning and electronic tuning of laser scribed graphene for flexible all-carbon devices. *ACS Nano*, 6(2):1395–1403, 2012. ISSN 1936-0851. doi: 10.1021/nn204200w. URL http://dx.doi.org/10.1021/nn204200w.

[135] Denis A. Sokolov, Kristin R. Shepperd, and Thomas M. Orlando. Formation of graphene features from direct laser-induced reduction of graphite oxide. *J. Phys. Chem. Lett.*, 1(18):2633–2636, 2010. ISSN 1948-7185. doi: 10.1021/jz100790y. URL http://dx.doi.org/10.1021/jz100790y.

[136] NM Bulgakova and AV Bulgakov. Pulsed laser ablation of solids: transition from normal vaporization to phase explosion. *Appl. Phys. A*, 73(2):199–208, 2001. ISSN 0947-8396. doi: 10.1007/s003390000686.

[137] B. J. Stagg and T. T. Charalampopoulos. Refractive indices of pyrolytic graphite, amorphous carbon, and flame soot in the temperature range 25Â° to 600Â°c. *Com-*

bust. Flame, 94(4):381–396, 1993. ISSN 0010-2180. doi: 10.1016/0010-2180(93)90121-I. URL http://www.sciencedirect.com/science/article/pii/001021809390121I.

[138] J. Steinbeck, G. Dresselhaus, and M. S. Dresselhaus. The properties of liquid carbon. *International Journal of Thermophysics*, 11(4):789–796, 1990. ISSN 0195-928X. doi: 10.1007/BF01184345. URL http://dx.doi.org/10.1007/BF01184345.

[139] D. B. Fischbach and M. Couzi. Temperature dependence of raman scattering by disordered carbon materials. *Carbon*, 24(3):365–369, 1986. ISSN 0008-6223. doi: 10.1016/0008-6223(86)90239-3. URL http://www.sciencedirect.com/science/article/pii/0008622386902393.

[140] H. D. Li, K. T. Yue, Z. L. Lian, Y. Zhan, L. X. Zhou, S. L. Zhang, Z. J. Shi, Z. N. Gu, B. B. Liu, R. S. Yang, H. B. Yang, G. T. Zou, Y. Zhang, and S. Iijima. Temperature dependence of the raman spectra of single-wall carbon nanotubes. *Appl. Phys. Lett.*, 76(15):2053–2055, 2000. doi: 10.1063/1.126252. URL http://scitation.aip.org/content/aip/journal/apl/76/15/10.1063/1.126252.

[141] Chaoen Li and Trevor C. Brown. Carbon oxidation kinetics from evolved carbon oxide analysis during temperature-programmed oxidation. *Carbon*, 39(5):725–732, 2001. ISSN 0008-6223. doi: 10.1016/S0008-6223(00)00189-5. URL http://www.sciencedirect.com/science/article/pii/S0008622300001895.

[142] Li Liu, Sunmin Ryu, Michelle R. Tomasik, Elena Stolyarova, Naeyoung Jung, Mark S. Hybertsen, Michael L. Steigerwald, Louis E. Brus, and George W. Flynn. Graphene oxidation: Thickness-dependent etching and strong chemical doping. *Nano Lett.*, 8(7):1965–1970, 2008. ISSN 1530-6984. doi: 10.1021/nl0808684. URL http://dx.doi.org/10.1021/nl0808684.

[143] Naiyun Xu, Siu Hon Tsang, Edwin Hang Tong Teo, Xincai Wang, Chee Mang Ng, and Beng kang Tay. Effect of initial sp3 content on bonding structure evolution of amorphous carbon upon pulsed laser annealing. *Diamond and Related Materials*, 30 (0):48–52, 2012. ISSN 0925-9635. doi: http://dx.doi.org/10.1016/j.diamond.2012.

09.008. URL http://www.sciencedirect.com/science/article/pii/S0925963512002002.

[144] J Steinbeck, G Braunstein, MS Dresselhaus, T Venkatesan, and DC Jacobson. A model for pulsed laser melting of graphite. *J. Appl. Phys.*, 58(11):4374–4382, 1985. ISSN 0021-8979. doi: 10.1063/1.335527.

[145] CEA. Cast3m. http://www-cast3m.cea.fr/index.php, 2015.

[146] Zhiyou Du, Adel F. Sarofim, John P. Longwell, and Charles A. Mims. Kinetic measurement and modeling of carbon oxidation. *Energy Fuels*, 5(1):214–221, 1991. ISSN 0887-0624. doi: 10.1021/ef00025a035. URL http://dx.doi.org/10.1021/ef00025a035.

[147] P. Saeta, J. K. Wang, Y. Siegal, N. Bloembergen, and E. Mazur. Ultrafast electronic disordering during femtosecond laser melting of gaas. *Physical Review Letters*, 67(8):1023–1026, 1991. URL http://link.aps.org/doi/10.1103/PhysRevLett.67.1023. PRL.

[148] A. Rousse, C. Rischel, S. Fourmaux, I. Uschmann, S. Sebban, G. Grillon, Ph Balcou, E. Forster, J. P. Geindre, P. Audebert, J. C. Gauthier, and D. Hulin. Non-thermal melting in semiconductors measured at femtosecond resolution. *Nature*, 410(6824):65–68, 2001. ISSN 0028-0836. doi: http://www.nature.com/nature/journal/v410/n6824/suppinfo/410065a0_S1.html. URL http://dx.doi.org/10.1038/35065045. 10.1038/35065045.

[149] Vitali E. Grudzev and Anastasia S. Gruzdeva. Thermal and nonthermal effects in femtosecond laser ablation and damage of transparent materials, 2000. URL http://dx.doi.org/10.1117/12.407310. 10.1117/12.407310.

[150] Joel Moser, Amelia Barreiro, and Adrian Bachtold. Current-induced cleaning of graphene. *Applied Physics Letters*, 91(16):163513, 2007. ISSN 0003-6951.

[151] Yaping Dan, Ye Lu, Nicholas J. Kybert, Zhengtang Luo, and A. T. Charlie Johnson. Intrinsic response of graphene vapor sensors. *Nano Lett.*, 9(4):1472–1475, 2009.

ISSN 1530-6984. doi: 10.1021/nl8033637. URL http://dx.doi.org/10.1021/nl8033637.

[152] Cristina Gomez-Navarro, R. Thomas Weitz, Alexander M. Bittner, Matteo Scolari, Alf Mews, Marko Burghard, and Klaus Kern. Electronic transport properties of individual chemically reduced graphene oxide sheets. *Nano Letters*, 7(11):3499–3503, 2007. ISSN 1530-6984. doi: 10.1021/nl072090c. URL http://dx.doi.org/10.1021/nl072090c.

[153] John G. Simmons. Generalized formula for the electric tunnel effect between similar electrodes separated by a thin insulating film. *Journal of Applied Physics*, 34(6):1793–1803, 1963. doi: doi:http://dx.doi.org/10.1063/1.1702682. URL http://scitation.aip.org/content/aip/journal/jap/34/6/10.1063/1.1702682.

[154] Ferry Prins, Amelia Barreiro, Justus W. Ruitenberg, Johannes S. Seldenthuis, Nuria Aliaga-Alcalde, Lieven M. K. Vandersypen, and Herre S. J. van der Zant. Room-temperature gating of molecular junctions using few-layer graphene nanogap electrodes. *Nano Letters*, 11(11):4607–4611, 2011. ISSN 1530-6984. doi: 10.1021/nl202065x. URL http://dx.doi.org/10.1021/nl202065x.

[155] Cornelia Nef, Laszlo Posa, Peter Makk, Wangyang Fu, Andras Halbritter, Christian Schonenberger, and Michel Calame. High-yield fabrication of nm-size gaps in monolayer cvd graphene. *Nanoscale*, 6(13):7249–7254, 2014. ISSN 2040-3364. doi: 10.1039/C4NR01838A. URL http://dx.doi.org/10.1039/C4NR01838A.

[156] Duhee Yoon, Young-Woo Son, and Hyeonsik Cheong. Negative thermal expansion coefficient of graphene measured by raman spectroscopy. *Nano Letters*, 11(8):3227–3231, 2011. ISSN 1530-6984. doi: 10.1021/nl201488g. URL http://dx.doi.org/10.1021/nl201488g.

[157] Alexander L. Kitt, Zenan Qi, Sebastian RÃ©mi, Harold S. Park, Anna K. Swan, and Bennett B. Goldberg. How graphene slides: Measurement and theory of strain-dependent frictional forces between graphene and sio2. *Nano Letters*, 13

(6):2605–2610, 2013. ISSN 1530-6984. doi: 10.1021/nl4007112. URL http://dx.doi.org/10.1021/nl4007112.

[158] Zhiming Xiao, Juncong She, Shaozhi Deng, Zikang Tang, Zhibing Li, Jianming Lu, and Ningsheng Xu. Field electron emission characteristics and physical mechanism of individual single-layer graphene. *ACS Nano*, 4(11):6332–6336, 2010. ISSN 1936-0851. doi: 10.1021/nn101719r. URL http://dx.doi.org/10.1021/nn101719r.

[159] Hisato Yamaguchi, Katsuhisa Murakami, Goki Eda, Takeshi Fujita, Pengfei Guan, Weichao Wang, Cheng Gong, Julien Boisse, Steve Miller, Muge Acik, Kyeongjae Cho, Yves J. Chabal, Mingwei Chen, Fujio Wakaya, Mikio Takai, and Manish Chhowalla. Field emission from atomically thin edges of reduced graphene oxide. *ACS Nano*, 5(6):4945–4952, 2011. ISSN 1936-0851. doi: 10.1021/nn201043a. URL http://dx.doi.org/10.1021/nn201043a.

[160] C. J. Edgcombe and U. ValdrÃ¨. Experimental and computational study of field emission characteristics from amorphous carbon single nanotips grown by carbon contamination. i. experiments and computation. *Philosophical Magazine Part B*, 82 (9):987–1007, 2002. ISSN 1364-2812. doi: 10.1080/13642810208218357. URL http://dx.doi.org/10.1080/13642810208218357.

[161] John Cumings, Philip G. Collins, and A. Zettl. Materials: Peeling and sharpening multiwall nanotubes. *Nature*, 406(6796):586–586, 2000. ISSN 0028-0836. URL http://dx.doi.org/10.1038/35020698. 10.1038/35020698.

[162] A. Barreiro, F. Borrnert, M. H. Rummeli, B. Buchner, and L. M. K. Vandersypen. Graphene at high bias: Cracking, layer by layer sublimation, and fusing. *Nano Letters*, 12(4):1873–1878, 2012. ISSN 1530-6984. doi: 10.1021/nl204236u. URL http://dx.doi.org/10.1021/nl204236u.

Appendix A

Scilab codes for parameter extraction and noise error calculations from Raman data sets

Listing A.1: Scilab code used to fit the Raman data with three Lorentzian curves and extract the desired parameter values

```
// Sum of three Lorentzian peaks and a horizontal baseline
function y=lorentz1(x, p)
a=p(1)  // Baseline
b=p(2)   // Amplitude Lorentz 1
c=p(3)   // x0 Lorentz 1   D peak
d=p(4)   // Tau Lorentz 1
e=p(5)   // Amplitude Lorentz 2
f=p(6)   // x0 Lorentz 2   G peak
g=p(7)   // Tau Lorentz2
```

```
h=p(8)  // Amplitude Lorentz 3
i=p(9)   // x0 Lorentz 3   T peak
j=p(10)  // Tau Lorentz 3

// Definition of the function
y=((x-c)^(2)+0.25*d^2)^(-1)*(0.5*b*d)+d+((x-f)^(2)+0.25*g^2)
    ^(-1)*(0.5*e*g) +((x-i)^(2)+0.25*j^2)^(-1)*(0.5*h*j)
endfunction

function e=G(p, z)     // Function to calculate the error at each
     iteration
x=z(1)
y=z(2)
e=y-lorentz1(x,p)
endfunction

p0=[100;10;1350;200;10;1580;200;5;1060;200] // Initialization

[p,err]=datafit(G,Z,p0)     // Calculation of the parameters (
    Least Square Method)
```

Listing A.2: Scilab code used to generate data subsets

```
taille=size(var1);                                  // How many
    data points in the initial set (var1)?

bootnum=20;                                         // Number of
    data subsets to generate (20)
datanum=taille(1);                                  // Number of
    random indexes generated per subset (equal to the number of
    data points)
bootdata=zeros(datanum,2*bootnum);                  // All the
```

```
    generated data will go into this matrix

for j=1:bootnum                                    // For each
    data subset iteration

bootrand=round((datanum-1)*rand(datanum,1));       // Vector of
    random indexes between 0 and N-1

bootrand=gsort(bootrand,'g','i');                  // Sorting the
    generated indexes in the growing order
bootrand=bootrand+1;                               // To avoid
    indexes = 0 so now indexes are between 1 and N

for i=1:datanum
bootdata(i,(2*j-1))=var1(bootrand(i),1); // Values of the Raman
    Shifts corresponding to the generated indexes
bootdata(i,(2*j))=var1(bootrand(i),2);   // Values of the Raman
    Intensities corresponding to the generated indexes
end

end
clear i j;
// All the data are in the matrix bootdata
```

Appendix B

Electro-mechanical model for graphene memories: calculation of the pull-in voltage

To find values of $\delta_1 + \delta_2$ that solve the static equilibrium conditions, we write:

$$\begin{aligned} \frac{\gamma^2 \varepsilon_0 A V^2}{2(d-\delta_1-\delta_2)^2} - fWL_1 - \frac{kW\delta_1}{L_1} = 0 \\ \frac{\gamma^2 \varepsilon_0 A V^2}{2(d-\delta_1-\delta_2)^2} - fWL_2 - \frac{kW\delta_2}{L_2} = 0 \end{aligned} \tag{B.1}$$

We multiply both equations by L_1 and L_2, respectively, and add them to obtain:

$$\frac{(L_1+L_2)\gamma^2 \varepsilon_0 A V^2}{2(d-\delta_1-\delta_2)^2} - fW(L_1^2+L_2^2) - kW(\delta_1+\delta_2) = 0 \tag{B.2}$$

Which can also be written as:

$$\frac{\gamma^2 \varepsilon_0 A V^2}{2(d-(\delta_1+\delta_2))^2} - \frac{fW(L_1^2+L_2^2)(L_1+L_2)}{(L_1+L_2)^2} - \frac{kW(\delta_1+\delta_2)}{L_1+L_2} = 0 \tag{B.3}$$

So the equation of static equilibrium of the two flakes is equivalent to the equation of static equilibrium of a single flake with effective length $L_{eff} = L_1 + L_2$ and effective

friction parameter $f_{eff} = \frac{L_1^2+L_2^2}{(L_1+L_2)^2}$, for a displacement equal to $\delta_1 + \delta_2$.

$$\frac{\gamma^2 \varepsilon_0 A V^2}{2(d-(\delta_1+\delta_2))^2} - f_{eff} W L_{eff} - \frac{kW(\delta_1+\delta_2)}{L_{eff}} = 0 \tag{B.4}$$

$$\frac{\gamma^2 \varepsilon_0 A V^2}{2d^2} = f_{eff} W L_{eff} (1 - \frac{(\delta_1+\delta_2)}{d})^2 + \frac{kWd}{L_{eff}} \frac{(\delta_1+\delta_2)}{d} (1 - \frac{(\delta_1+\delta_2)}{d})^2 \tag{B.5}$$

To simplify the calculations, we define the polynomial P(X) such that:

$$A = f_{eff} W L_{eff}$$
$$B = \frac{kWd}{L_{eff}}$$
$$X = \frac{(\delta_1+\delta_2)}{d}$$
$$C = \frac{\gamma^2 \varepsilon_0 A V^2}{2d^2}$$

Thus the equation of static equilibrium is equivalent to:

$$P(X) = A(1-X)^2 + BX(1-X)^2 = C \tag{B.6}$$

We look for solutions of this equation for which:

$$0 < X < 1$$

Finding a real value of X verifying this inequation would mean that at the first static equilibrium, the flakes have moved toward each other without completely closing the gap.

By calculating the derivative of P(X) with respect to X, one can find its maximum value reached at X such that P'(X)=0. We find that:

$$\forall X \in [0,1] P(X) \leqslant \frac{4B(\frac{A}{B}+1)^3}{27} = \frac{4}{27} \frac{kWd}{L} (1 + \frac{fL^2}{kd})^3 = P_{max} \tag{B.7}$$

This gives us the maximum value of P(X) for which the equilibrium condition has a solution.

Thus:

$$P_{max} = \frac{4}{27} \frac{kWd}{L} (1 + \frac{fL^2}{kd})^3 = \frac{\gamma^2 \varepsilon_0 A V_{max}^2}{2d^2} \tag{B.8}$$